

Modern Aspects of Electrochemistry 55

Stojan S. Djokić *Editor*

# Biomedical Applications

 Springer

# MODERN ASPECTS OF ELECTROCHEMISTRY

---

No. 55

*Series Editors:*

Ralph E. White  
Department of Chemical Engineering  
University of South Carolina  
Columbia, SC 29208

Constantinos G. Vayenas  
Department of Chemical Engineering  
University of Patras  
Patras 265 00  
Greece

*Managing Editor:*

Maria E. Gamboa-Aldeco  
1107 Raymer Lane  
Superior, CO 80027

For further volumes:  
<http://www.springer.com/series/6251>

Previously from Modern Aspects of Electrochemistry

### **Modern Aspects of Electrochemistry No. 53**

## **Applications of Electrochemistry and Nanotechnology in Biology and Medicine II**

Edited by Noam Eliaz, Professor of Engineering at Tel-Aviv University

Topics in Number 53 include:

- Fundamental studies of electron tunneling between electrodes and proteins
- Electron transfer kinetics at oxide films on metallic biomaterials
- How adsorption of organic molecules and ions depends on surface crystallography of the metal electrode
- Studying and modifying biomaterial surfaces with high resolution using the scanning electrochemical microscope
- Electrochemical method for high-throughput screening of enzymatic activity

### **Modern Aspects of Electrochemistry No. 54**

## **Electrochemical Production of Metal Powders**

Edited by Stojan S. Djokić, Professor of Chemical & Materials Engineering at the University of Alberta

Topics in Number 54 include:

- General theory of disperse metal electrodeposition
- Electrodeposition of pure metal powders e.g., Cu, Ag, Pb, Co, Fe and Ni
- Formation of porous Cu electrodes by constant and periodically changing regimes of electrolysis
- Morphology, phase and chemical composition of electrodeposited Co-Ni, Fe-Ni and Mo-Ni-O powders
- Electrodeposition of dispersed nanoparticles
- Electroless deposition of metal powders from aqueous solutions

Stojan S. Djokić  
Editor

# Biomedical Applications

 Springer

Editor  
Stojan S. Djokić  
Elchem Consulting, Ltd.,  
Edmonton, AB, Canada

ISSN 0076-9924

ISBN 978-1-4614-3124-4

ISBN 978-1-4614-3125-1 (eBook)

DOI 10.1007/978-1-4614-3125-1

Springer New York Heidelberg Dordrecht London

Library of Congress Control Number: 2012943075

© Springer Science+Business Media New York 2012

This work is subject to copyright. All rights are reserved by the Publisher, whether the whole or part of the material is concerned, specifically the rights of translation, reprinting, reuse of illustrations, recitation, broadcasting, reproduction on microfilms or in any other physical way, and transmission or information storage and retrieval, electronic adaptation, computer software, or by similar or dissimilar methodology now known or hereafter developed. Exempted from this legal reservation are brief excerpts in connection with reviews or scholarly analysis or material supplied specifically for the purpose of being entered and executed on a computer system, for exclusive use by the purchaser of the work. Duplication of this publication or parts thereof is permitted only under the provisions of the Copyright Law of the Publisher's location, in its current version, and permission for use must always be obtained from Springer. Permissions for use may be obtained through RightsLink at the Copyright Clearance Center. Violations are liable to prosecution under the respective Copyright Law.

The use of general descriptive names, registered names, trademarks, service marks, etc. in this publication does not imply, even in the absence of a specific statement, that such names are exempt from the relevant protective laws and regulations and therefore free for general use.

While the advice and information in this book are believed to be true and accurate at the date of publication, neither the authors nor the editors nor the publisher can accept any legal responsibility for any errors or omissions that may be made. The publisher makes no warranty, express or implied, with respect to the material contained herein.

Printed on acid-free paper

Springer is part of Springer Science+Business Media ([www.springer.com](http://www.springer.com))

# Preface

Research in electrochemical science and technology has brought about tremendous achievements. Beyond the traditional applications in electronics, energy devices, aerospace, and automotive areas, developments in electrochemistry are very important for many practical biomedical applications. In particular, developments related to medical devices, implants, sensors, antimicrobially active materials, drug delivery systems, etc. have significantly advanced in the past few decades.

The aim of this volume of *Modern Aspects of Electrochemistry* is to review the electrochemical aspects of the latest developments of various materials used in biomedical applications.

Competent scientists/researchers in their respective fields from all around the world were invited to write this volume.

In Chapter 1, by Ingrid Milošev, properties of CoCrMo alloy for biomedical applications are thoroughly analyzed. This alloy is one of the most important alloys used in orthopedic and dental implantology, due to its hardness, high wear resistance, and superior corrosion resistance under physiological conditions. The chapter discusses the electrochemical characterization of CoCrMo alloy under various conditions simulating physiological circumstances, and results *in vitro* and *in vivo* obtained thus far are critically evaluated. In addition, Milošev discusses in detail the tribocorrosion behavior of CoCrMo alloys, which is of tremendous significance for orthopedic implants. It is believed that this chapter will bring to the readers basic concepts and open a new window for future directions related to the biomedical applications of CoCrMo alloys.

Chapter 2 by Magagnin, Cojocar, and Secondo is devoted to the exploitation of electroless methods for generating metallic nanostructures

for biomedical technologies. Electroless deposition is a very viable route for the synthesis of metallic nanostructures. This chapter discusses electroless deposition of Au, Ag, Cu, Ni, Co, etc. for a number of biomedical applications. Applications to sensors and microdevices, preparation and use of nanostructured metals for supporting and wiring biomolecules for DNA analysis, and disease screening are discussed. The use of nanostructures, such as nanorods and nanoparticles, is analyzed in view of their potential applications to nano-biotechnology. Metallic nanostructures, developed via electroless deposition, may in the future play a fundamental role in the understanding of different interactions of biological systems at the nanolevel.

Sannakaisa Virtanen discusses corrosion behavior, surface modification, and biocompatibility of biodegradable Mg alloys in Chapter 3. Magnesium and its alloys are very attractive for applications as biodegradable implants, since they readily corrode in body fluids. On the other hand, the corrosion products, namely Mg(II) ions, are considered to be nontoxic. This chapter analyzes basic concepts of Mg corrosion vis a vis possible biomedical applications as implants. Hydrogen evolution, an increase in pH in the vicinity of the corroding surface, and nonuniform propagation of dissolution of Mg are analyzed. Importantly for the present volume of *Modern Aspects of Electrochemistry*, Virtanen discusses surface modifications in order to tailor the degradation and biological performance of Mg alloys. Conversion coatings, e.g.,  $\text{MgF}_2$ , Ca-phosphate coatings, protein coatings, or self-assembled monolayers as possibilities for the surface modification of Mg alloys are analyzed.

Chapter 4 by Norman, Thakur, and Thundat provides an overview of the current literature on combined electrochemical–microcantilever measurements, which may have significant applications in the biomedical field. These devices have the potential to exhibit fast and reliable detection of small concentrations of molecules in biofluids. Nanoscale actuators are needed for a wide range of applications such as robotics, artificial muscles, prosthetic, micromechanical, and microfluidic devices. They can be operated under physiological conditions, making them particularly well suited for biomedical applications. As this chapter clearly states, in order to achieve improved performance for biomedical applications, development of microcantilever sensors that allow for measurements in complex real-life samples must be continued in the future.

In Chapter 5 by Djokić, treatments of various surfaces with silver and its compounds for biomedical applications are described. The antimicrobial properties of silver are well known. Silver or its compounds have been applied as coatings for devices used as topical wound dressings, urinary catheters, endotracheal tubes, cardiac valves, etc. In this chapter, electrochemical, chemical, and physical treatments of various surfaces with silver and their antimicrobial properties for biomedical applications are discussed.

This new volume of Modern Aspects of Electrochemistry brings to scientists, engineers, and students new concepts and summarized results related to surface treatments for biomedical applications, which may have significant influence for future practical applications.

Edmonton, AB, Canada

Stojan S. Djokić



# Contents

<b>1</b>	<b>CoCrMo Alloy for Biomedical Applications.....</b>	<b>1</b>
	Ingrid Milošev	
<b>2</b>	<b>Electroless Synthesis of Metallic Nanostructures for Biomedical Technologies.....</b>	<b>73</b>
	Luca Magagnin, Paula Cojocaru, and Francesco Secundo	
<b>3</b>	<b>Biodegradable Mg Alloys: Corrosion, Surface Modification, and Biocompatibility.....</b>	<b>101</b>
	Sannakaisa Virtanen	
<b>4</b>	<b>Microcantilever Sensors: Electrochemical Aspects and Biomedical Applications.....</b>	<b>127</b>
	Lana Norman, Garima Thakur, and Thomas Thundat	
<b>5</b>	<b>Surface Treatments with Silver and Its Compounds for Biomedical Applications.....</b>	<b>173</b>
	Stojan S. Djokić	
	<b>Index.....</b>	<b>205</b>



# Contributors

**Paula Cojocar** Dip. Chimica, Materiali e Ing. Chimica G. Natta, Politecnico di Milano, Milano, Italy

**Stojan S. Djokić** Elchem Consulting Ltd., Edmonton, AB, Canada

**Luca Magagnin** Dip. Chimica, Materiali e Ing. Chimica G. Natta, Politecnico di Milano, Milano, Italy

**Ingrid Milošev** Jožef Stefan Institute, Ljubljana, Slovenia  
Valdoltra Orthopaedic Hospital, Ankaran, Slovenia

**Lana Norman** Department of Chemical and Materials Engineering, University of Alberta, Edmonton, AB, Canada

**Francesco Secondo** Istituto di Chimica del Riconoscimento Molecolare, CNR, Milano, Italy

**Garima Thakur** Department of Chemical and Materials Engineering, University of Alberta, Edmonton, AB, Canada

**Thomas Thundat** Department of Chemical and Materials Engineering, University of Alberta, Edmonton, AB, Canada

**Sannakaisa Virtanen** Department of Materials Science and Engineering (WW-4), Institute for Surface Science and Corrosion, University of Erlangen-Nuremberg, Erlangen, Germany



# Chapter 1

## CoCrMo Alloy for Biomedical Applications

Ingrid Milošev

### 1.1 Introduction

Metallic materials used in biomedical applications have become increasingly important as the number of various implanted devices, e.g., orthopedic, cardiovascular, dental, and ophthalmological implants, constantly increases. In addition to titanium-based alloys and stainless steel, cobalt–chromium–molybdenum alloy (CoCrMo) is one of the most important materials used in orthopedic applications, i.e., total hip replacements. The increasing number of implanted hip replacements is the result of the prolongation of the average life expectancy and an active lifestyle in older age. Among the diseases of the joint that in most cases require surgical treatment, osteoarthritis is the most important. After implantation of a hip prosthesis, pain is reduced and the functionality of the joint is recovered. The average lifetime of the implanted prosthesis is about 15 years. Compared to implants used in the 1970s, the lifetime of contemporary hip prostheses progressively increases because of progress in surgical techniques, treatment, material manufacturing, and quality control. The ultimate goal is to produce hip prostheses

---

I. Milošev (✉)

Jožef Stefan Institute, Jamova c. 39,  
Ljubljana SI-1000, Slovenia

Valdoltra Orthopedic Hospital,  
Jadranska c. 31, Ankaran SI-6280, Slovenia  
e-mail: Ingrid.Milosev@ijs.si

that would endure the average postsurgical lifetime of more than 20 years and enable the patient to live an active lifestyle without pain. To achieve this goal, understanding alloy behavior *in vitro* and *in vivo* is crucial.

As metallic materials were introduced into biomedical applications in the 1940s–1950s, it was recognized that corrosion resistance is of special importance. Early *in vitro* studies were performed in saline and simulated physiological solutions, first mainly as static experiments. Retrieval studies soon showed that some corrosion or corrosion-initiated localized damage occurred at the metal components, and *in vitro* studies were then conducted in a way to study possible localized phenomena. In this chapter, the progress of early electrochemical studies is summarized. It was also recognized early that the passivity of an alloy to be used in the human body is based on the formation of a thin passive film, but its characteristics were not known in detail. As the applications of CoCr-based alloys in orthopedics intensified, the interest in these materials increased as well. More sophisticated electrochemical and surface analytical techniques were introduced in the late 1990s and 2000s. In this chapter, these studies are reviewed, including the most important results concerning the composition, structure, and thickness of the passive oxide layer formed at the CoCrMo alloy surface in simulated physiological solutions. The majority of results are related to simple saline simulated physiological solutions. The effect of phosphate ions is described in detail. It was recognized, however, that a simple saline solution does not entirely mimic *in vivo* conditions and that the effect of biomolecules should be taken into account. As a model for biomolecules, the effect of a complexing agent is discussed, followed by the effect of proteins, mainly albumin. The formation and distribution of organometallic compounds, as the most important compounds formed between metal ions and proteins *in vivo*, is presented. It becomes clear that to approach closely an *in vivo* situation, *in vitro* experiments should be conducted in media containing biomolecules and living cells.

Tribocorrosion experiments can be regarded as a bridge between the *in vitro* and *in vivo* situation. These experiments, conducted in various media with special emphasis on the change in wear mechanism caused by the presence of proteins, are presented. Finally, studies performed on retrieved metal components are described to identify the types of corrosion processes *in vivo*.

## 1.2 CoCrMo Alloys and Their Properties

### 1.2.1 *Development and Chemical and Physical Properties of Cobalt-Based Alloys*

Alloying of cobalt was developed most notably by E. Haynes at the beginning of the twentieth century. Haynes developed a series of cobalt–chromium alloys named Stellites [1]. In 1913, cobalt–chromium–tungsten alloys (CoCrW) were patented. In the 1930s the cobalt-based alloy Vitallium was patented and used for the manufacture of parts for aircraft engines. In the original specification, it contained 30% Cr, 7% W, and 0.5% C; later the tungsten was replaced by 5% Mo. A similar alloy was developed also by Krupp in Germany. The composition of these older alloys—Stellites, Vitallium, and HS—is given in Table 1.1. Molybdenum is added to refine grain size, enhance solid solution strengthening, and increase corrosion resistance. The composition of CoCrMo alloys has not changed significantly since that time. The largest change is related to the stricter control of the content of carbon and, consequently, the more homogeneous distribution of hard carbide grains and increased abrasion resistance of the alloy. There are six ISO 5832 (International Organization for Standardization) standards for Co-based alloys, which correspond to various compositions and manufacturing processes. Four of these are mainly used in orthopedics [2–5]. Today, the cast and wrought alloys ISO 5832-4 and 5832-12 are primarily used in orthopedics. According to the American Standards for Testing and Materials (ASTM) classifications, these alloys are denoted as F-75 and F-1537,

**Table 1.1** Composition of original Co-based alloys [1]

Alloy	Composition/wt (%)								
	Co	Cr	Mo	Ni	Fe	Mn	W	C	Si
Stellite 1 CoCrW	50	33					13	2.5	
Stellite 8 CoCrMo	63	30	6					0.2	
Vitallium CoCrMo	62.5	30	5			0.5		0.5	0.2
HS-21 CoCrMoNi	Bal.	27–30	5–7	2–5	0.75	1		0.2–0.35	
HS-25 CoCrNi	Bal.	19–21		9–11	3	2		0.05–0.15	

respectively. These two alloys have almost identical composition but differ in microstructure. There are two types of wrought alloys, low- and high-carbon, which differ in carbon content. Other Co-based alloys include CoCrWNi and CoNiCrMo wrought alloys, but these alloys are less appropriate for use in orthopedics because of their poor wear properties [6, 7]. Moreover, these two alloys contain nickel, which raises concerns about biological reactivity.

Cast alloys have a chromium-rich matrix and larger grains. With hot isostatic pressing, the grain size can be reduced to 8  $\mu\text{m}$ . Cast alloys exhibit an inhomogeneous, large-grained, cored microstructure. The dendritic regions are Co rich, whereas the interdendritic regions can be a quaternary mixture consisting of various Co-rich, Cr-rich, and Cr- and Mo-rich phases [1]. Wrought alloys have a face-centered cubic structure that exhibits an austenitic microstructure with finely distributed small block carbides.

Cobalt-based alloys are very tough materials. They can be described as wear- and corrosion resistant and are stable at elevated temperatures. Many properties stem from the crystallographic nature of cobalt, the formation of a solid solution with chromium and molybdenum, and consequent formation of extremely hard carbides [1, 7]. Co-based alloys exhibit relatively high density ( $8.9 \text{ g cm}^{-3}$ ) and high elastic modulus (210–253 GPa). These properties are less attractive compared to Ti-based alloys, which exhibit lower density ( $4.5 \text{ g cm}^{-3}$ ) and an elastic modulus (110 GPa) closer to that of bone. However, a combination of high corrosion resistance, wear resistance, high hardness (300–400 Vickers hardness), and ultimate strength (655–1,300 GPa) is the basis for the applications of Co-based alloys in joint replacements [7].

### ***1.2.2 Use of CoCrMo Alloys in Orthopedics***

In addition to its use in engineering, in the 1930s Vitallium was also used for the preparation of metallic dental casting as an alternative to gold alloys, which had already become very expensive [1]. Vitallium was introduced to orthopedics by Smith-Peterson in 1937 [1]. At about the same time, H. Bohlman, using the work of Venable and Stuck, designed a corrosion-resistant short stem made of Vitallium [7]. In 1938 Philip Wiles designed the first total hip arthroplasty made of stainless steel [2]. A steel ball was secured to the femur with a bolt and a stainless steel acetabular liner was secured with screws.

This design was rather disappointing because the stainless steel used at that time was insufficiently corrosion resistant. Long-stemmed prostheses appeared in the 1950s and provided less stress concentration. The design of the Wiles prosthesis was adopted in 1951 by G.K. McKee and J. Watson-Farrar, at first using stainless steel, and later a CoCrMo alloy. This design was a so-called metal-on-metal combination comprising a metal femoral head articulating within a metal acetabular inlay. The cast CoCrMo alloy was considered satisfactory for total hip replacements [8]. In the mid-1960s, poly(methyl methacrylate) (PMMA) cement was used for fixation in hip arthroplasty for the first time. The relatively high torque and frictional forces resulted in the generation of metallic debris and early loosening. In 1960, John Charnley developed a “low friction” arthroplasty using an acetabular shell made of polytetrafluoroethylene (PTFE, Teflon). Unfortunately, this design resulted in early failures because of the poor wear resistance of PTFE. Charnley then replaced PTFE with high-density polyethylene, which was not as friction free as PTFE but much more wear resistant. The femoral component was made of stainless steel and had a 22-mm head [9]. The prototype of this prosthesis was developed in 1962 and still remains the gold standard of hip arthroplasty with metal-on-polyethylene articulation. The basic Charnley design was later modified by Muller (so-called Charnley–Muller prostheses) [10]. Stainless steel was replaced by CoCrMo alloy, and the prostheses had a variable neck size and larger head size. The Charnley prosthesis, which was the basic archetype, was followed by hundreds of different designs and modifications. In the past 15 years, CoCrMo alloy has been mainly used as a bearing surface, i.e., for the manufacture of the femoral head in metal-on-polyethylene bearings where it articulates against the interior of a polyethylene cup, and for the manufacture of femoral head and acetabular inlay in metal-on-metal bearings of total joint replacements and surface replacements.

### **1.3 Early In Vitro Investigations and Relationship to In Vivo Failures**

The high corrosion resistance of a metal or alloy to be used in the human body as a dental or orthopedic implant was immediately recognized as one of the most important prerequisites. “High strength materials with extreme inertness are required,” as was noted by Hoar

and Mears [11]. None of the implant materials is perfect in the sense of fulfilling all mechanical, chemical, and safety requirements completely. Because body fluids, such as blood, plasma, and lymph, all contain a considerable concentration of chloride ions, it was important to recognize under which conditions the breakdown of passivity may occur *in vivo* [11]. The authors emphasized that “even if no visible breakdown occurs, i.e., the metal is in the passive state, perhaps in many years *in vivo* transfer of metal to surrounding tissue may be appreciable” [11].

Hoar and Mears investigated various stainless steel, CoCrMo, and Ti-based alloys in 0.17 M NaCl and Hanks’ physiological balanced salt solution [11]. Hanks’ “physiological” or balanced salt solution fairly closely imitates (from the chemical aspect) the fluid in muscle and bone [12]. Resting potentials (potential of an isolated specimen after 480 h in stagnant solution open to the air) and breakdown potentials (at which the anode showed a sharp increase of current when potential was gradually raised) were measured. Stainless steels exhibit breakdown potentials ~50–150 mV below the resting potential. Thus, film breakdown can always be expected where these alloys are used in aerated solutions of 0.17 M chloride content. The resting potential for Vitallium was 0.5 V, far less negative than the breakdown potential at 0.87 V. Thus, film breakdown is very unlikely. Titanium alloys exhibit breakdown potentials >6 V, which is far more positive than the resting potential in the range of 0.3–0.5 V. However, under abrasion, scratching, or crevice conditions, healing of the oxide layer by repassivation may take some time. In a crevice, the long and narrow electrolytic path between it and the surface cathode may lead to such a large ohmic drop through the solution that its repassivation is not possible. The authors concluded that stainless steels (even of the higher Cr–Ni quality) are “unlikely to resist all breakdown by pitting when exposed to the body fluids (or other media containing chloride) indefinitely; cobalt-based alloys may well withstand such exposure for long times; titanium and (especially) some of its alloys should withstand such exposure for an indefinite period” [11].

A.T. Kuhn reviewed corrosion of CoCr alloys in aqueous environments, among them also physiological media (0.9% NaCl and Ringer’s solution) [13]. The literature data were divided into the following categories: simple corrosion, stress corrosion, crevice corrosion and pitting, fretting corrosion, couple corrosion, and corrosion *in vivo*. Various CoCr alloys (Wironit, Vitallium, and Wironium) that were immersed for 2 months in solution containing  $9 \text{ g l}^{-1}$  NaCl

in an open beaker at 37°C showed only minimal corrosion (less than 0.2 ppm) [14]. Although the alloy was not susceptible to stress corrosion, crevice and pitting corrosion were observed. Co-based alloys become more susceptible to crevice corrosion as Ni content increases from 0% to 25%. Alloys with at least 20% Cr were more crevice attack resistant when Mo content was 5% or more. The resistance of Co-based alloy to pitting was high [15], but fretting corrosion may harm the passive oxide layer.

Corrosion rates of metals *in vivo* based on the concentration of metal ions in surrounding tissue after implantation in animals are much higher than *in vitro* [16, 17]. This conclusion was achieved by the authors presumably for two reasons. The first reason is chemical; i.e., the composition of the environment is more corrosive than that found in a simulated physiological solution. The second reason is that crevice conditions are somewhat established by the surrounding tissue. Therefore, in the following studies the occurrence of possible corrosion processes under specific circumstances, e.g., crevice and galvanic corrosion, was investigated in more detail. Alloys of cast CoCrMo, wrought CoCrMo, wrought CoNiCrMo, and Ti-6Al-4V alloys were incorporated in specimens simulating couple and crevice corrosion conditions [18]. The specimens were implanted in dogs for 30 months. No substantial evidence of corrosion activity on the surfaces of the metal was observed, except for a tarnish film on the titanium alloy when coupled to a cast CoCrMo alloy. Because the tarnish film was not observed *in vitro*, the authors concluded that *in vitro* studies alone are not completely definitive and that a prosthetic device which is a composite of the cast CoCrMo and Ti-6Al-4V alloys may be inappropriate [18].

The use of combinations of dissimilar metals in multi-alloy hip prostheses leads to conditions in which galvanic corrosion may appear. To check this possibility, cyclic polarization curves were measured for individual and coupled CoCrMo and Ti-6Al-4V alloys in 0.9% NaCl [19]. Galvanic coupling did not significantly enhance corrosion tests. The resistance of CoCrMo alloy to pitting and crevice corrosion was even improved by coupling to titanium alloy. No exaggerated corrosion caused by the coupling was noted on retrieved Sivash prostheses that incorporated both these alloys [19]. Based on potential versus time curves measured in isotonic saline solution of low pH (1.5) to accelerate corrosion, a conclusion was reached that CoCrMo alloys should not be used in combination with stainless steel but may be used in combination with titanium alloy [20]. The specimens

were fabricated from a CoCrMo alloy (HS21) cylinder force fit in a large titanium alloy, or a stainless steel cylinder, to give a surface-to-area ratio of 1:4 and a crevice between metals. As similar results were obtained by other authors [21, 22], it was concluded that the corrosion rate in a stable passive region is not significantly increased by coupling; thus, what is of interest is how coupling affects the resistance of the alloys to pitting or accelerated general corrosion, i.e., to local or general passive film breakdown.

Potentiostatic polarization curves for individual specimens in 0.9% NaCl (pH 7) showed that stainless steel is very susceptible to pitting [21]. No pitting was observed for Co- and Ti-based alloys, although the Co-based alloy indicated possible susceptibility to pitting or crevice corrosion [21]. Lucas et al. investigated susceptibility of surgical CoCr alloy to pitting corrosion in vitro and in vivo [23]. The in vitro study comprised cyclic polarization curves in 0.9% NaCl at 37°C at pH 7.0 under both aerated and deaerated conditions. Current hysteresis, as a typical feature of pitting corrosion according to the protection potential theory, was observed only for alloy passivated in phosphoric acid, but not for a nonpassivated alloy. However, no evidence of pitting corrosion was revealed. Also, the examination of the nonbearing surface of hip prostheses made of cobalt alloy after in vivo implantation up to 6 years showed no features uniquely identified as the result of pitting corrosion. Casting microporosity was observed on retrieved femoral heads, which could mistakenly be identified as pitting corrosion. Because passivating treatment either changed the surface chemistry of the oxide layer or increased it, it was hypothesized that current hysteresis is related to the breakdown of this preestablished passive film followed by a repassivation. This behavior should not be associated with pitting corrosion as is normally taken to be the case by application of the protection potential theory. Based on these results, it was concluded that CoCrMo alloy will not undergo pitting under static conditions. However, when the alloy is either severely cold worked or subjected to fretting or a cyclic loading condition, pitting corrosion has been observed in vitro [24, 25].

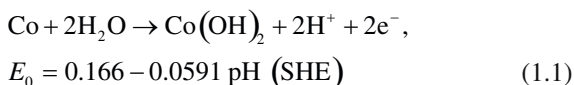
Forged CoCrMo alloy exhibited higher resistance to pitting and crevice corrosion in media containing chlorides than cast alloy, which was ascribed to a more homogeneous and finer-grained structure [26]. This alloy also exhibits total resistance to stress corrosion cracking in the elastic and even plastic range. Under movements of parts made of forged and cast alloys, no galvanic corrosion was observed, as both the cast and forged alloys remained in the stable passive state.

## 1.4 Electrochemical Studies on Individual Metals in Simulated Inorganic Physiological Solution

In their early study, Hoar and Mears emphasized that the extremely slow release of cobalt and titanium into the surrounding environment is caused by the passage of cations through their passivating oxide film, without breakdown [11]. It was also noted that all the alloys protect themselves by formulation of a passive film [27]. In this chapter the properties of the passivating oxide layer formed on CoCrMo alloy under simulated physiological solution in the light of more recent studies and sophisticated electrochemical and surface analytical techniques are discussed. First, electrochemical behavior of the individual metal components—Co, Cr, and Mo—of the CoCrMo alloy is presented. The effect of the presence of chloride ions, which are abundantly present in simulated physiological solutions, is also discussed. Then, the results for the CoCrMo alloy are presented, accompanied by discussion of the effect of particular metal components.

### 1.4.1 Electrochemical Studies on Cobalt

Cyclic voltammograms (CVs) for Co metal recorded in 0.9% NaCl (NaCl), simulated Hanks' physiological solution (SPS), and phosphate buffer solution (PBS) are depicted in Fig. 1.1. The composition of the solutions used is given in Table 1.2. CVs recorded in chloride-based solutions—NaCl and SPS—are very similar, with much shorter passive range compared to nonchloride-containing phosphate buffer. Let us first discuss the behavior in the latter solution. The CV shows typical features of anodic behavior of cobalt in alkaline solutions, which is relatively complex and depends on the potential range. It can be divided into active dissolution, passivity, transpassivity, and oxygen evolution [30, 31, 43–47]. At pH 7–10, the primary passivity is caused by the formation of CoO or, more likely, the hydrated oxide,  $\text{Co}(\text{OH})_2$ :



The shape of active/passive transition (the height of the anodic peak) and the extent of the passive region are dependent on the

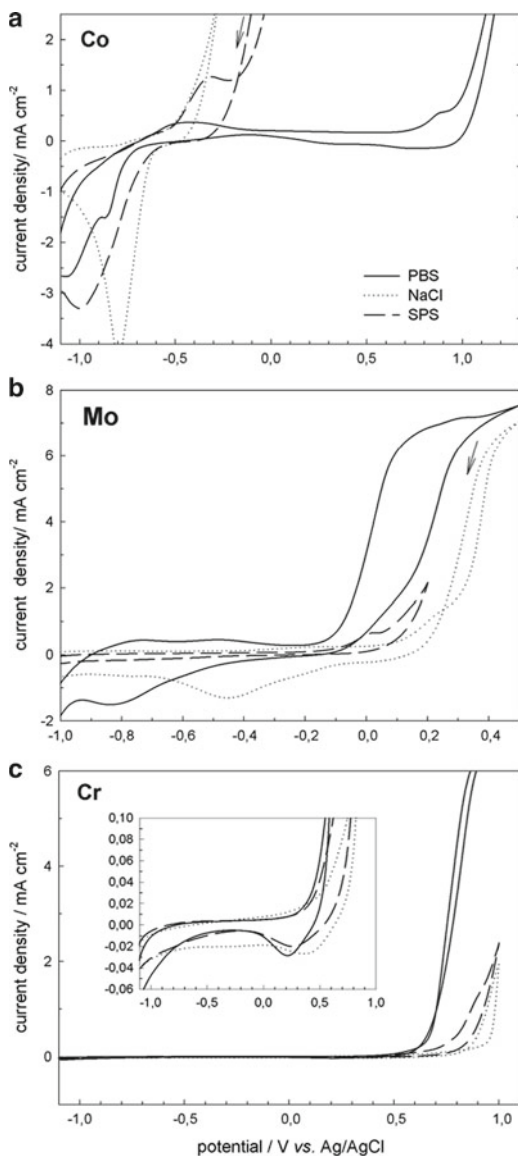


**Fig. 1.1** Cyclic voltammograms (CV) recorded for cobalt (a), molybdenum (b), and chromium (c) in 0.9% NaCl, simulated Hanks' physiological solution (SPS), and phosphate buffer solution (PBS).  $dE/dt = 50 \text{ mV s}^{-1}$ . *Inset* in (c) depicts CV with expanded current density scale

**Table 1.2** Composition of various media used to study the behavior of CoCrMo alloy

Solution (pH) <sup>a</sup>	Composition	References
0.9% NaCl, pH=7.4 (adjusted by conc. HCl and conc. NaOH)	9.08 g l <sup>-1</sup> NaCl	This work
0.14 M NaCl, pH=7.4 (adjusted by conc. HCl and conc. NaOH)	8.2 g l <sup>-1</sup> NaCl	[28]
0.14 M NaCl, pH=7.4 (adjusted by conc. HCl and buffered via the use of Tris <sup>b</sup> )	8.2 g l <sup>-1</sup> NaCl	[29]
Hanks' simulated physiological solution (SPS), pH=7.4 (adjusted by 1 M NaOH, nonbuffered)	8 g l <sup>-1</sup> NaCl, 0.4 g l <sup>-1</sup> KCl, 0.35 g l <sup>-1</sup> NaHCO <sub>3</sub> , 0.25 g l <sup>-1</sup> NaH <sub>2</sub> PO <sub>4</sub> ·H <sub>2</sub> O, 0.19 g l <sup>-1</sup> CaCl <sub>2</sub> ·2H <sub>2</sub> O, 0.19 g l <sup>-1</sup> MgCl <sub>2</sub> , 0.06 g l <sup>-1</sup> MgSO <sub>4</sub> ·7H <sub>2</sub> O, 1 g l <sup>-1</sup> glucose	[This work, 30–38]
Simulated physiological fluid (SBF), pH=7.4 (adjusted by conc. HCl and buffered via use of Tris)	0.14 M NaCl, 1 mM KH <sub>2</sub> PO <sub>4</sub> , 2.5 mM CaCl <sub>2</sub> , 3 mM KCl, 1.5 mM MgSO <sub>4</sub> , 4.2 mM NaHCO <sub>3</sub> , 0.5 mM Na <sub>2</sub> SO <sub>4</sub>	[29]
Saline phosphate buffer solution (SPBS), pH=7.4	0.14 M NaCl, 1 mM KH <sub>2</sub> PO <sub>4</sub> , 3 mM KCl, 10 mM Na <sub>2</sub> HPO <sub>4</sub>	[28, 39, 40]
Saline phosphate buffer solution (SPBS), pH=7.4	8 g l <sup>-1</sup> NaCl, 0.2 g l <sup>-1</sup> KCl, 1.15 g l <sup>-1</sup> Na <sub>2</sub> HPO <sub>4</sub> , 0.2 g l <sup>-1</sup> KH <sub>2</sub> PO <sub>4</sub>	[41]
Phosphate buffer solution (PBS), pH=7.4	0.1 M Na <sub>2</sub> HPO <sub>4</sub> ·H <sub>2</sub> O, 0.1 M K <sub>2</sub> HPO <sub>4</sub>	[This work, 42]

<sup>a</sup>Not additionally buffered<sup>b</sup>Tris, tris(hydroxymethyl)aminomethane

composition of the solution and pH. In KOH solutions, the height of the anodic peak was linearly dependent on the concentration of KOH [45]. In borate solutions of different pHs (from 7.45 to 11.0), the height of the anodic peak decreased with increasing pH, indicating that the Co(OH)<sub>2</sub> layer became more protective [43]. In PBS the broad passivity region extends from -0.2 V to 0.8 V Ag/AgCl (Fig. 1.1); current density is independent of potential. In borate buffer, three different regions were recognized depending on the potential in the passive region: primary, secondary, and tertiary passivity [43].

Primary passivity is related to the formation of CoO or, more likely,  $\text{Co}(\text{OH})_2$ . The thickness of this layer, 2.5 nm, is almost independent of potential in the passive region. In the second half of the passive region, a bilayered oxide,  $\text{CoO}/\text{Co}_3\text{O}_4$ , is formed [43–45, 47]. The outer layers of the oxide film, largely  $\text{Co}(\text{OH})_2$ , are converted to the more passive cobalto-cobaltic oxide [44]:



At even more positive potentials (1.3–0.059 pH), in the tertiary passive region bilayered oxide  $\text{CoO}/\text{Co}_2\text{O}_3$  (cobaltous/cobaltic) is formed, leading to the lowest values of current density in the passive region [43].



The thickness of this layer increases with potential from 1.5 to 3.5 nm. Burke et al. reported that at about 0.6 V (RHE) a hydrous Co(II) film is gradually converted to Co(III)-containing species as  $\text{Co}_3\text{O}_4$ ,  $\text{Co}_2\text{O}_3$ , and  $\text{CoOOH}$  [44]. The final anodic transition occurs just before oxygen gas evolution:



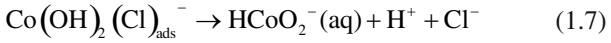
Transpassive dissolution occurs at 1.1 V (SHE) and is nearly independent of pH [43].

Other authors differed between the primary and secondary passivity region in borate buffer (pH=9.3) [47–49]. The primary region was ascribed to the formation of Co(II) oxide/hydroxide with thickness between 1.0 nm [47] and 2.5 nm [30, 43]. Secondary passivity in the transpassive region is caused by formation of Co(III) species ( $\text{Co}_3\text{O}_4$ ). It is reflected in a significant increase in oxide thickness up to 4 nm [43, 47] and 6 nm [48, 49].

In PBS, two reduction peaks appear, at  $-0.88$  V and  $-1.05$  V (Fig. 1.1a). Up to the anodic potential limit of 0.2 V, the peak at  $-1.05$  V was the only cathodic peak. For more positive anodic limits, the peak at  $-0.88$  V appears as well. These results suggest a two-layered film structure. It was proposed that the outer layer is first reduced to hydrated  $\text{Co}^{2+}$  ions before the inner CoO layer is reduced to metallic cobalt [43].

In the presence of chloride ions, the behavior of cobalt changes considerably. In 0.05 M KOH the values of corrosion density increased

linearly with  $c_{\text{NaCl}}$ , indicating increased dissolution [45]. The authors proposed that the increase in  $\text{Cl}^-$  concentration leads to the dissolution of the outer  $\text{Co(III)}$  oxide layer according to the following reactions:



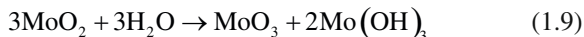
During the anodic sweep in NaCl and SPS, the oxidation of cobalt starts at approximately  $-0.8$  V (Fig. 1.1a). The passive range in SPS is established at  $-0.4$  V without an active/passive transition. It extends to  $-0.3$  V in NaCl, and to  $-0.1$  V in SPS, where the current density starts to increase at the breakdown potential,  $E_b$ . Compared to PBS, where the passive range extends up to 0.8 V, the presence of chloride ions thus significantly narrows the passive region of cobalt. At potentials more positive than  $E_b$ , current hysteresis is observed in both NaCl and SPS solutions, indicating that under these conditions cobalt is subjected to localized pitting corrosion. However, the passive range in SPS is approximately 200 mV more positive, indicating a higher resistance to localized breakdown compared to NaCl solution. The reason for this behavior clearly lies in the solution composition. Namely, SPS contains phosphate ions that obviously incorporate in the oxide layer and thus contribute to the passivation process, similar to what Burke et al. suggested for chloride-free solutions [44]. The anodic sweep was markedly different in neutral phosphate solution ( $\text{pH}=7$ ) where the first anodic peak was omitted compared to more alkaline NaOH solution ( $\text{pH}=13$ ) [44]. One possible explanation would be that the activity of the cobalt oxide decreases with decreasing pH. Another possible explanation is the formation of an insoluble cobalt compound, presumably phosphate, before the formation of  $\text{CoO/Co(OH)}_2$ . The formation of this compound is supported by the fact that the peak potential is located 30 mV more negative than the equilibrium potential of  $\text{Co(OH)}_2$  formation. The formation of insoluble cobalt phosphate, or at least the incorporation of phosphate ions into the oxide layer, may lead to the reduced activity of cobalt oxide in phosphate solution [30, 44]. A similar mechanism seems to be valid in phosphate- and chloride-containing phosphate solution (Fig. 1.1a).

Other ions present in SPS may act as promoters of pitting corrosion of cobalt [32]. For example, bicarbonate ions (also present in SPS) are aggressive toward  $\text{Co(II)}$  oxide film and cause pitting of the metal [50]. The passive layer is composed of both  $\text{CoCO}_3$  and  $\text{Co(OH)}_2$ .

Under the influence of  $\text{HCO}_3^-$  ions, the dissolution of  $\text{CoCO}_3$  results in the formation of  $\text{Co}(\text{CO}_3)_{2-3}$  in the upper range of the Co(II) region. At higher potentials where Co(III) is formed in the oxide film, the metal passivates, and bicarbonate causes relatively little film breakdown.

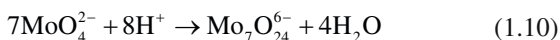
### 1.4.2 Electrochemical Studies on Molybdenum

CVs for Mo metal recorded in NaCl, SPS, and PBS are depicted in Fig. 1.1b. Compared to Co, Mo metal shows rather different behavior in all three solutions. In nonchloride-containing alkaline solutions, the behavior of Mo is rather complex. The presence of different molybdenum species on the metal surface with increasing electrode potential after polarization in 0.5 M NaOH solution was confirmed by X-ray photoelectron spectroscopy (XPS) [51]. In the lower potential range molybdenum(III) species are formed ( $\text{Mo}(\text{OH})_3$ ), which are gradually transformed to Mo(IV) oxide,  $\text{MoO}_2$ . The formation of species of different valence may be observed in PBS as two anodic peaks appear at  $-0.65$  V and  $-0.4$  V (see Fig. 1.1b). The oxidation of Mo(III) and Mo(IV) oxides occurring in the transpassive range, which in PBS begins at  $-0.1$  V, results in the formation of Mo(VI) species [51]. At the same time the XPS peak assigned to Mo(III) increases, which the authors ascribed to the disproportionation reaction, e.g.,



In the reverse cycle in PBS, a cathodic peak appears at  $-0.8$  V (Fig. 1.1b).

The passivity of molybdenum in 0.15 M NaCl was ascribed to the formation of  $\text{MoO}_2$  or  $\text{Mo}_2\text{O}_3$ , presumably the former, which starts at  $-0.6$  V (Ag/AgCl) and protects the surface up to about 0 V (Ag/AgCl) [52]; this agrees well with the curve for NaCl presented in Fig. 1.1b. The composition of the oxide film was confirmed by surface-enhanced Raman spectroscopy (SERS) [52]. After oxidation at potentials higher than  $-0.1$  V, the presence of molybdate and/or heptamolybdate species has been identified [52]. In aqueous solutions, molybdate is in equilibrium with heptamolybdate:



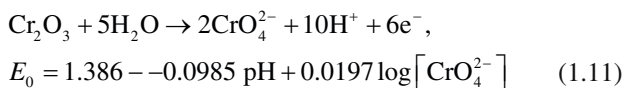
Although the curves recorded for Mo in NaCl and SPS are more similar than that in PBS, they differ in several features. The potential limiting the passive region is most positive in NaCl and shifts to more negative values in SPS and PBS. The transpassive peak is more pronounced in phosphate-containing solution, as reported also by Wang et al. [52]. In NaCl, a current hysteresis appears, indicating the process of localized corrosion. In the reduction cycle, a cathodic peak forms at about  $-0.45$  V for anodic potential limits more positive than  $0.5$  V and may be thus related to the reduction of molybdate species.

### 1.4.3 *Electrochemical Studies on Chromium*

CVs for Cr metal recorded in NaCl, SPS, and PBS are depicted in Fig. 1.1c. CVs are similar to those for Mo but extend to more positive potentials. In the passive range, Cr metal shows quite similar CVs in all three solutions regardless of the presence of chloride ions. The lack of an active–passive peak indicates that the air-formed layer is not easily removed by cathodic reduction or that the chromium surface is immediately passivated upon immersion in the electrolyte. The passivation is the result of the formation of chromium(III) oxide, as confirmed by X-ray photoelectron spectroscopy (XPS) in sulfuric acid [53, 54], SERS in  $0.15$  M NaCl [55], and by X-ray absorption near edge structure (XANES) in sulfuric acid, borate buffer, and sodium hydroxide [56]. The thickness of the passive layer was estimated at a few nanometers and increases linearly with potential: from  $0.5$  to  $2.5$  nm in sulfuric acid [53], from  $0.3$  to  $1.2$  nm in boric acid solution (pH  $6.48$ – $8.42$ ) [57], and from  $1.0$  to  $3.5$  nm in sulfuric acid [54]. The layer grows according to the high field mechanism. Electrochemical capacitance is inversely proportional to the applied potential. Thus, the passive layer behaves as a simple dielectric with a dielectric constant of  $\sim 25$  and an ionic resistivity of  $\sim 10^{13}$   $\Omega$  cm. Comparison of SER spectra of well-crystallized  $\text{Cr}_2\text{O}_3$  and that of the passive layer formed in  $0.15$  M NaCl showed that the passive layer is highly disordered with a spectrum that closely matches amorphous  $\text{Cr}_2\text{O}_3$  [55]. Some  $\text{Cr}(\text{OH})_3$  was also present. Other authors also confirmed that the passive layer of chromium is highly hydrated [53, 54, 57]. Moffat and Latanision proposed that it consists of chromic ions bridged together by a network of water, hydroxide, and oxide ligand [53]. Haupt and Strehblow proposed a  $\text{Cr}_2\text{O}_3$  matrix containing

some water [54]. Seo et al. [57] proposed that the passive layer equals  $\text{Cr}_2\text{O}_3$  and that only the uppermost layer is hydrated.

At  $E > 0.5$  V, Cr undergoes transpassive oxidation accompanied by the formation of species of higher valence. According to thermodynamics [58], the oxidation to Cr(III) to chromate  $\text{CrO}_4^{2-}$  is expected in neutral and alkaline solutions, whereas dichromate species  $\text{Cr}_2\text{O}_7^{2-}$  are formed in acidic solution. Both chromate and dichromate species are highly soluble in an aqueous environment. Based on the surface analytical data from XPS [53, 54], XANES [56], and SERS [55], it is now clearly established that the transpassive oxidation of chromium (III) oxide results in the formation of  $\text{CrO}_4^{2-}$  species according to the reaction:



Schmuki et al. used XANES to investigate the oxide on Cr in borate buffer (pH 8.4) [56]. The Cr(VI) species was detected in the film at potentials more negative than the potential of transpassive dissolution. The Cr(VI) is trapped as  $\text{CrO}_4^{2-}$  in the outermost part of the film, possibly as a consequence of O anion inward migration. The fraction of the Cr(VI) in the oxide film was found to be about 3%.

As the anodic potential limit exceeds 0.4 V, a small reduction peak appears at 0.2 V (Fig. 1.1c), indicating that the layer becomes redox active with the solid state reduction of a higher valence species, i.e., Cr(VI) to Cr(III) [53, 59]; this correlates with the transition of the electrode capacitance at the same potential [53]. The charge associated with this peak increases with the potential and the peak potential shifts to more positive values [53]. Interestingly, Metikoš-Huković and Ceraj-Cerić proposed that, at  $\sim 0.1$  V saturated calomel electrode in borate buffer pH 8.2, a solid state transformation of p-type  $\text{Cr}_2\text{O}_3$  to n-type  $\text{CrO}_2$  occurs [60]. Similar behavior as for pure chromium metal is observed on stainless steels, where passivity is largely based on the formation of  $\text{Cr}_2\text{O}_3$  oxide as an inner part of the passive layer [61–63].

Cr spontaneously passivates and yields a broad passivity region extending from  $-1.0$  V to  $0.4$  V in PBS and  $0.5$  V in SPS and NaCl (Fig. 1.1c). In none of these solutions is chromium subjected to localized pitting corrosion, as was the case with Co metal. Thus, the  $\text{Cr}_2\text{O}_3$  layer is highly protective even in chloride-containing solutions. The potential at which the current density starts to increase at the end of the passive region is most negative for PBS and most positive for

NaCl. Another detail worth mentioning is the shape of the curve in the transpassive region where the formation of higher-valence species occurs. In NaCl, once the current density starts to increase at the end of the passive region, it increases progressively. In SPS and PBS, a shoulder/peak is observed at 0.9 V and 0.8 V, respectively (Fig. 1.1c). Similar behavior is observed for Mo metal. Thus, phosphate ions shift the onset of the transpassive range to more negative potentials, presumably because of the formation of Mo and Cr phosphate, which then leads to increased formation of higher-valence species, as explained in Sect. 1.5.

## 1.5 Electrochemical Studies on CoCrMo Alloy in Simulated Inorganic Physiological Solution

### 1.5.1 *Composition, Thickness, and Structure of the Oxide Layer*

CVs for CoCrMo alloy and individual metal constituents in SPS are depicted in Fig. 1.2. Cobalt and molybdenum show a much narrower range of passivation than chromium and alloy, which show similar behavior. As for chromium metal, CoCrMo alloy passivates spontaneously in air, resulting in the formation of a thin (1.8-nm) oxide film containing mainly  $\text{Cr}_2\text{O}_3$ , with a minor contribution from Co and Mo oxides, as confirmed by XPS [33, 64]. Because this layer cannot be reduced cathodically, it remains at the surface of the alloy also upon immersion in the electrolyte. The air-formed molybdenum species disappear quickly in 0.15 M NaCl and are replaced by  $\text{Co}(\text{OH})_2$ , and  $\text{Cr}_2\text{O}_3$  may be partially transformed into  $\text{Cr}(\text{OH})_3$  [64].

Because of the presence of this spontaneously formed oxide layer, the alloy reaches passivity without going through an active–passive transition. The passive range extends from  $-0.9$  V and extends up to  $0.5$  V (Fig. 1.2). In the cathodic cycle, a small peak at  $0.2$  V is observed for anodic potential limits more positive than  $0.4$  V. The absence of cathodic peaks corresponding to the reduction of Co and Mo oxides (as observed for metals) indicates that the formation of these oxides is strongly suppressed by the formation of chromium oxide.

Composition, thickness, and structure of the oxide layer formed by electrochemical oxidation were investigated by XPS. The investigations

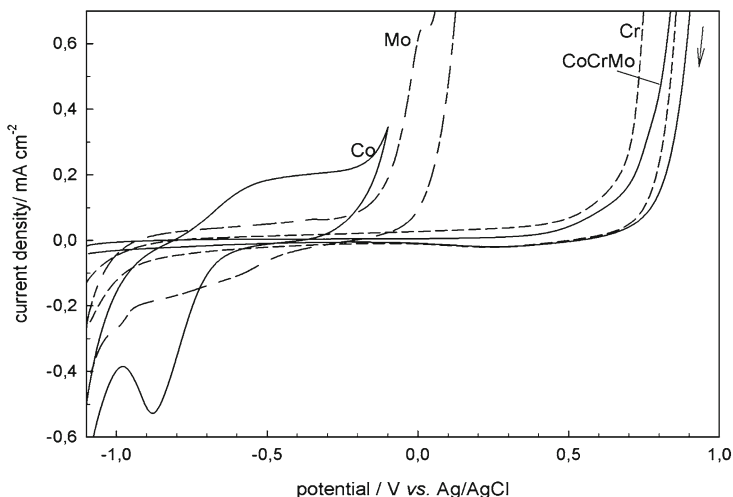


**Fig. 1.2** Cyclic voltammograms recorded for cobalt, molybdenum, chromium, and CoCrMo alloy in simulated Hanks' physiological solution (SPS).  $dE/dt=50 \text{ mV s}^{-1}$

were performed in a close correlation to the polarization curve of CoCrMo alloy recorded in SPS (Fig. 1.3). In the cathodic region the current is dominated by the reduction of water and, partially, of dissolved oxygen. As already mentioned, there is no active/passive transition and the passive range is established immediately following the Tafel region. The passive range extends from  $-0.3 \text{ V}$  to approximately  $0.6 \text{ V}$ , at which potential it is interrupted by the current density increase. At  $0.75 \text{ V}$  a current peak appears, related to the transpassive oxidation. This process is followed by oxygen evolution at higher potentials. Based on the XPS spectra recorded at various potentials according to the polarization curve the composition of the oxide film is determined. The results are expressed as cationic fractions deduced from deconvoluted XPS spectra. In the lower potential range,  $E \leq 0.3 \text{ V}$ , the passive film consists predominantly of  $\text{Cr}_2\text{O}_3$  and  $\text{Cr}(\text{OH})_3$  (Fig. 1.4) [29, 33, 64]. This layer is hydrated, as evidenced from the shape of the oxygen O1s XPS peak, which contains a significant amount of  $\text{OH}^-$  content [29, 33].

Between  $-0.3 \text{ V}$  and  $0.3 \text{ V}$ , the oxide layer thickness increases linearly with potential with a rate of  $1.5 \text{ nm V}^{-1}$  (Fig. 1.3). It reached  $3.1 \text{ nm}$  at  $0.3 \text{ V}$ . Thickness of the oxide film formed in SPS as a function of potential obtained by various methods is presented in Fig. 1.5.

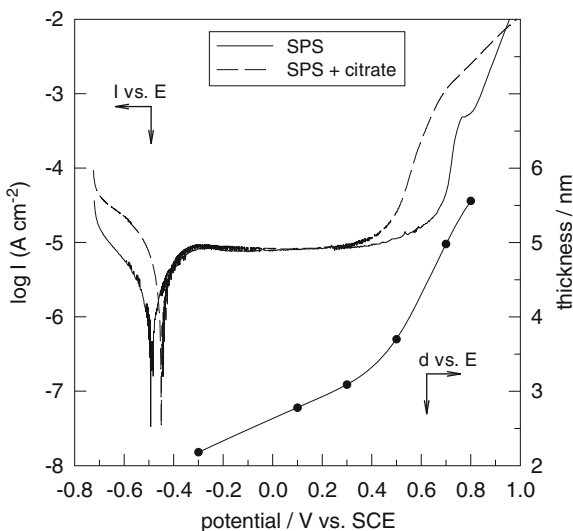


**Fig. 1.3** Polarization curves recorded for CoCrMo alloy in simulated Hanks' physiological solution with and without the addition of 0.05 M Na citrate as complexing agent.  $dE/dt=1 \text{ mV s}^{-1}$ . The thickness of the oxide layer deduced from XPS data is given on the right-hand y-axis (Reprinted from I. Milošev and H.-H. Strehblow, *Electrochim. Acta* 48 (2003) 2767, with permission from Elsevier [33])

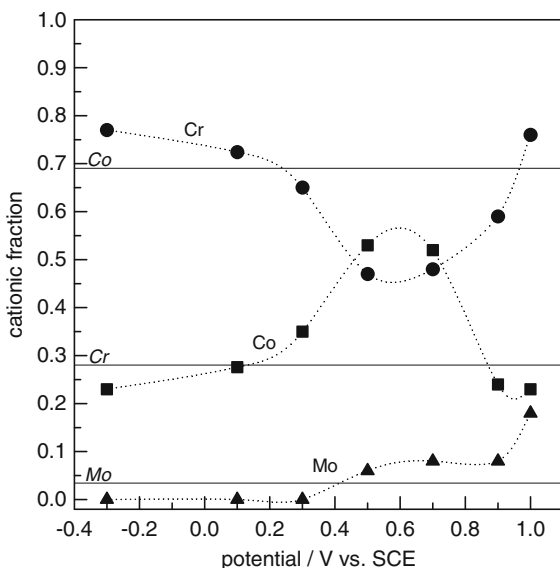


**Fig. 1.4** Cationic composition of the passive layer after oxidation of CoCrMo alloy in simulated Hanks' physiological solution as a function of oxidation potential. *Thin lines* denote the atomic fractions for Co, Cr, and Mo in the bulk alloy (Reprinted from I. Milošev and H.-H. Strehblow, *Electrochim. Acta* 48 (2003) 2767, with permission from Elsevier [33])

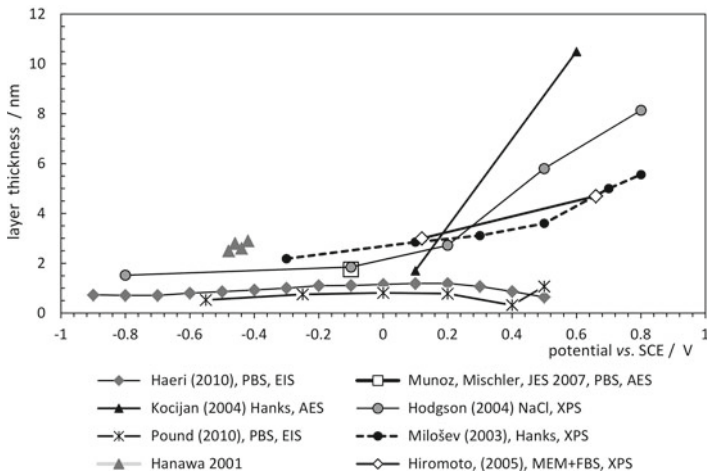


**Fig. 1.5** Comparison of literature data reported for thickness of oxide layer formed on CoCrMo alloy in various simulated physiological solutions deduced by XPS, AES, and EIS methods. Note that the results reported by Hanawa et al. correspond to the autoclaved samples and samples immersed in Hanks' solution, MEM+fetal serum, and L929 cells (the potential at the scale is thus arbitrarily chosen)

Hodgson et al. also observed that, up to 0.2 V, the oxide thickness increases moderately with the potential at a rate of approximately  $1.0 \text{ nm V}^{-1}$  [29]. This increase in thickness is almost entirely related to the increase in  $\text{Cr}_2\text{O}_3/\text{Cr}(\text{OH})_3$  thickness. Although chromium amounts to 28wt% in the base alloy, it accounts for the predominant cationic fraction in the oxide layer (Fig. 1.4) and protects the underlying alloy. The degree of protectiveness can be confirmed by the two orders of magnitude higher value of polarization resistance for CoCrMo alloy compared to pure cobalt (and three times higher than for pure chromium) [30, 34, 65]. Electrochemical impedance spectroscopy (EIS) measurements performed at various potentials in accordance with the polarization curves show that the polarization resistance increased markedly with increasing potential and reaches a maximum value at the middle of the passive range [30].

At potentials more positive than 0.3 V, there are significant changes in the composition and thickness of the oxide layer. In this range (at about 0.5 V), the current density starts to increase, first

gradually, and then abruptly, and thus limits the passive state (Fig. 1.3). These changes in current density are related to the changes in composition and thickness of the oxide film. Namely, in this potential range both Co and Mo oxides enter the passive layer (Fig. 1.4), whereas in the lower potential range cobalt and molybdenum remain unoxidized, and their oxidation starts at  $E \geq 0.3$  V. Co is present mainly as CoO and Mo as MoO<sub>3</sub>. At 0.6 V, cobalt content reaches a maximum of 55% and then decreases again at higher potentials. Similar results were reported by Hodgson et al., with low cobalt concentration at  $E < 0.5$  V, reaching a maximum of ~20% at 0.5 V, and then decreasing again [29]. The incorporation of cobalt in the film formed on CoCrMo in saline phosphate buffer solution (SPBS) was detected at 0.25 V Ag/AgCl but not in the film formed at 0.007 V [41]. These results indicate that cobalt is released mainly into the solution and does not significantly contribute to oxide growth.

Up to 0.5 V the cationic fraction of molybdenum is very small, but it increases at higher potentials, reaching approximately 10% (Fig. 1.4) [29, 33]. Although Milošev and Strehblow detected only Mo(VI) species [33], Hodgson et al. reported that both Mo(IV) and Mo(VI) were detected at lower potentials, but that Mo(IV) tend to disappear at  $E \geq 0.5$  V and only Mo(VI) remained [29]. In contrast, Li et al. reported that the passive film formed on CoCrMo alloy in 0.15 M NaCl is generated of only Cr and Co species, and no Mo species were detected in the film [64].

Formation and incorporation of Mo- and especially Co-oxides into the passive layer at  $E > 0.3$  V is accompanied by a significant increase in layer thickness (Fig. 1.5). In this potential range it increases more steeply, with a rate of 4.8 nm V<sup>-1</sup> [33] and 10 nm V<sup>-1</sup> [29].

The existence of different regions recognized in polarization and surface analytical measurements were corroborated also by electrochemical impedance measurements which showed that the surface oxide formed on MP35N alloy (Co–35Ni–20Cr–9Mo) undergoes two distinct changes as the potential is increased in phosphate-buffered saline [66]. The first change at 0.4 V SCE located at the end of passive range was associated with solid state oxidation reactions involving the conversion of Cr(III) to Cr(VI) and of Co(II) to Co(III). At this potential a significant change increase in oxide capacitance occurred, in agreement with reported changes in layer thickening rate (Fig. 1.5) [29, 33]. The second change was at about 0.6–0.7 V (SCE), corresponding to the release of chromate and nickel ions [66].

The third region in the polarization curve corresponds to the transpassive region at  $E > 0.7$  V, where the current density abruptly increases with potential (Fig. 1.2). This behavior, consistent with the transpassive oxidation observed for chromium metal [53, 54, 56], is related to the formation of Cr(VI) species, as evidenced by the chromium Cr 2p XPS peak at 578.7 eV. Change in oxide composition is reflected in the change in EIS parameters at this potential [66]. At the same time the content of cobalt decreases again, indicating that the majority of oxidized cobalt is released to solution (Fig. 1.4). The formation of a certain amount of  $\text{Co}_2\text{O}_3$  and/or  $\text{Co}_3\text{O}_4$  in the transpassive range cannot be excluded, but their identification is ambiguous because of the small chemical shift between Co(III) and Co(IV) species and to the low Co content in the passive layer [33]. In the reverse cycle, a cathodic peak is observed at 0.2 V (Fig. 1.2). This peak is observed only for anodic potential limits more positive than 0.4 V (Fig. 1.1c), indicating that it is related to the solid state reduction of Cr(VI) species, consistent with the behavior of chromium metal [53].

Changes in the passive layer occurring during primary and secondary passivity were monitored by a method for simultaneously evaluating both the polarization and impedance behavior [67]. Small incremental steps in potential (50 mV every 10 or 100 s) are applied to an electrochemical interface and the current response is collected digitally. The data are subjected to a numerical Laplace transform technique to obtain the frequency dependent admittance (reciprocal impedance) of the interface. Using this method it was observed that the oxide film formed on CoCrMo alloy in 0.9% NaCl solution already begins to thin at 0.2 V (Ag/AgCl), i.e., at potentials well below the breakdown potential typically reported for this alloy, i.e.,  $E > 0.5$  V (Ag/AgCl). This technique was further developed by introducing voltage-dependent EIS using time-domain techniques and non-ideal time-transient function, the generalized Cauchy-Lorentz function and dispersion parameter, which is a measure of the non-ideality of the surface, and KWV-Randles function [68]. These changes in thickness were related to distinct and sudden change in morphology, as evidenced by electrochemical atomic force microscopy (ECAFM) [69] and scanning electrochemical microscopy (SECM) studies [70]. In ECAFM, the sample is placed in a fluid of the atomic force microscope (AFM) cell, which is under electrochemical control. In the range from  $-1.0$  to  $-0.5$  V (Ag/AgCl), the surface remains free of oxide and exhibits a polished appearance (Fig. 1.6).

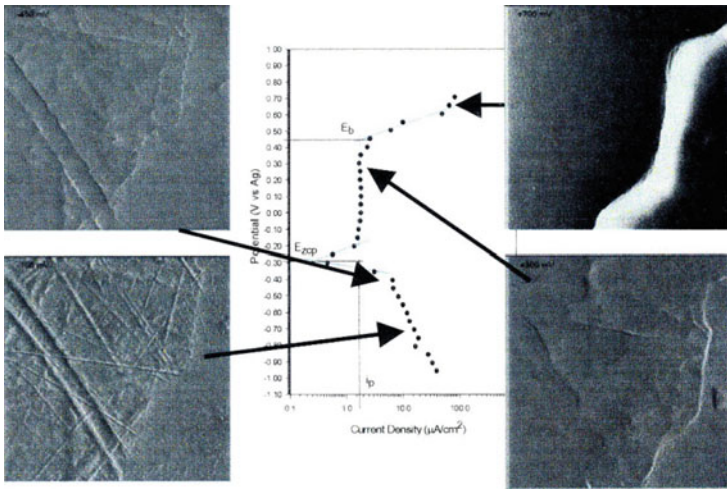


**Fig. 1.6** ECAFM results for a cast CoCrMo alloy in PBS. In the *center* is the potentiostatic polarization curve; the AFM images (in deflection mode) are shown at various electrode potentials (Reprinted from J. Gilbert, Z. Bai, J. Baeriger, and S. Megremis, *Medical Device Materials: Proceedings of the Materials and Processes for Medical Devices Conference*, ASM International, Anaheim, 2004, p. 139, with permission from ASM International [69])

For  $E > -0.5$  V (Ag/AgCl), the oxide overgrows the surface, fills in many of the minor scratches, and becomes smooth and flat. The film continues to develop until about 0.3 V, at which point the film suddenly begins to undergo breakdown. By 0.5 V the film has completely broken down and transpassive behavior is taking place. This change in morphology at 0.3 V may be related to a change in chemistry of the oxide layer as well, i.e., incorporation of Co- and Mo-oxide in the layer [28, 29, 33].

In-depth distribution and thickness of the passive oxide layer can be revealed using XPS in combination with sputter depth profiling. Sputter depth profiling of the passive layers formed on CoCrMo alloy in SPS at two different oxidation potentials, i.e., 0.1 V and 0.6 V, confirmed that the Co- and Mo-oxides are located primarily at the oxide–electrolyte interface (Fig. 1.7). Sputter depth profiles were presented separately for oxide and metal components of individual metals. At the surface, chromium oxide is the major constituent of the passive layer; i.e., it is enriched in the layer compared to its bulk

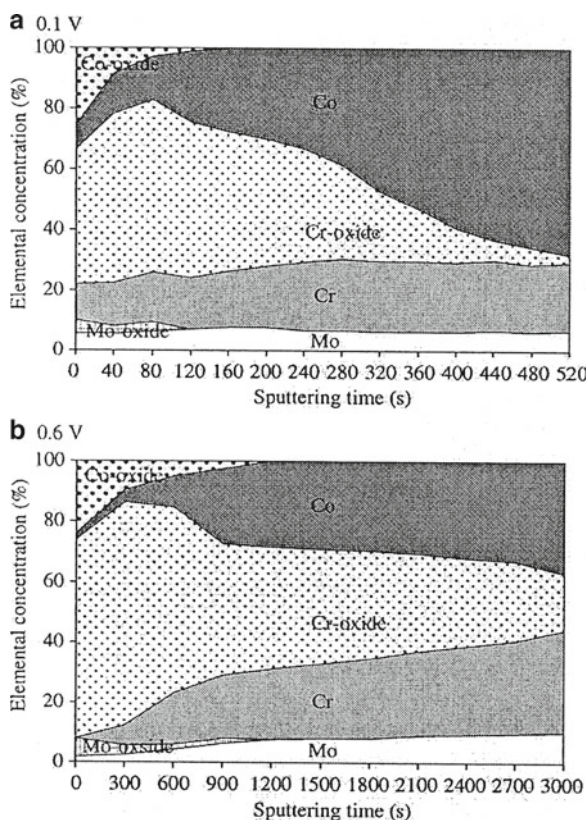


**Fig. 1.7** Depth profiles of CoCrMo alloy after oxidation at 0.1 V (a) and 0.6 V (b) for 1 h in simulated Hanks' physiological solution as a function of sputtering time. Sputtering time relative to  $Ta_2O_5$  standard is  $0.01 \text{ nm s}^{-1}$  (Reprinted from A. Kocijan, I. Milošev, and B. Pihlar, *J. Mater. Sci. Mater. Med.* 15 (2004) 643, with permission from Springer [38])

content. Cobalt oxide is present in approximately 25%, whereas molybdenum oxide is present as a minor constituent in about 5%. After oxidation at 0.1 V, Co-oxide is detected up to 0.8-nm depth (Fig. 1.7a). Once the Co- and Mo-oxides are sputtered away, the composition of inner part of the layer is revealed. The oxide thickness was determined as 2.1 nm relative to  $Ta_2O_5$  as the intensity of the oxygen signal decrease to one half. After oxidation at 0.6 V, the thickness of the oxides increases significantly (Fig. 1.7b). Both Co- and

Mo-oxides are present primarily at the outermost surface up to 12 nm depth. After sputtering the outermost layer, the content of Cr in the passive layer formed at 0.6 V remains practically unchanged across the whole passive layer. The thickness of the layer formed at 0.6 V was determined as 13.5 nm (Fig. 1.5) [35].

To complement and correlate the electrochemical processes occurring at the solid surface and those resulting in the dissolution, measurements of dissolved metal ions in solutions are carried out. In the lower potential range, where the formation of  $\text{Cr}_2\text{O}_3/\text{Cr}(\text{OH})_3$  predominates, electrochemical oxidation for 2 h at  $-0.1$  V in 0.14 M NaCl detected only small amounts of Co, as measured by inductively coupled plasma mass spectrometry (ICP-MS) [29]. Dissolved Cr and Mo could not be detected indicating that the dissolution of these elements is below the detection limit of the method used. Oxidation at potentials within the transpassive range, 0.75 V, however, strongly accelerated dissolution (about 300-fold compared to passive range). All alloying elements were now detected in the electrolyte. The ratio of dissolved alloying elements was near to the stoichiometric composition of the alloy. However, periodic cycling between two potentials in the passive region ( $-0.2$  V/ $0.2$  V), and especially between reducing and passivating potentials ( $-0.8$  V/ $-0.1$  V), leads to the selective dissolution of cobalt. Therefore, the active dissolution potential is mainly dominated by the cobalt component of the alloy. Smith and Gilbert revealed that during transpassive oxidation the Co:Cr:Mo molar ratio in the solution was 82% Co to 14% Cr to 5% Mo, i.e., significantly greater than the alloy concentration (75% Co, 28% Cr, and 5% Mo), thus implying preferential dissolution of Co [70].

It was suggested that Cr and Mo precipitate at the sample surface as hydrated oxides or oxychlorides and the Co ions remain solvated in solution, explaining the elevated Co levels compared to the alloy.

Similar results were reported for accelerated corrosion of vitalium in 0.9% saline solution and 10% solution of calf serum in saline [71]. After accelerated corrosion, performed at 500 mV (SCE) for 30 min, cobalt was rapidly excreted from the alloy in a higher concentration compared to that in bulk alloy.

The solubility and electrochemical behavior of CoCrMo alloy in SPS is dependent on pH [32, 34, 72]. Concentrations of dissolved metals after 30 days immersion in SPS of pH 2.0 and 6.8 were measured for CoCrMo alloy and its metal constituents Co, Cr, and Mo using inductively coupled plasma mass spectrometry (ICP-MS) [32, 34].

At pH 6.8, the concentration of dissolved cobalt decreased from  $608.0 \mu\text{g cm}^{-2}$  for Co metal to  $0.734 \mu\text{g cm}^{-2}$  for alloy, i.e., four orders of magnitude. A similar result was observed for molybdenum: the concentration of dissolved molybdenum decreased from  $64.3 \mu\text{g cm}^{-2}$  for Mo metal to  $0.040 \mu\text{g cm}^{-2}$  for alloy. In contrast, the concentration of dissolved chromium remained very low, i.e.,  $0.004 \mu\text{g cm}^{-2}$  for Cr metal and  $0.040 \mu\text{g cm}^{-2}$  for the alloy. This finding suggested that the oxide films formed on cobalt and molybdenum metals are much more soluble than those formed on Cr and CoCrMo alloy. By lowering the pH, the dissolution of both Co and Cr was increased by about 80% [34].

### 1.5.2 Effect of Phosphate Ions

In this section, the effect of phosphate ions in simulated physiological solution on the electrochemical behavior of CoCrMo alloy is analyzed. The discussion of the results for the alloy is based on those for individual metal components presented in Sect. 1.4. CVs for CoCrMo alloy recorded in NaCl, SPS, and PBS are shown in Fig. 1.8.

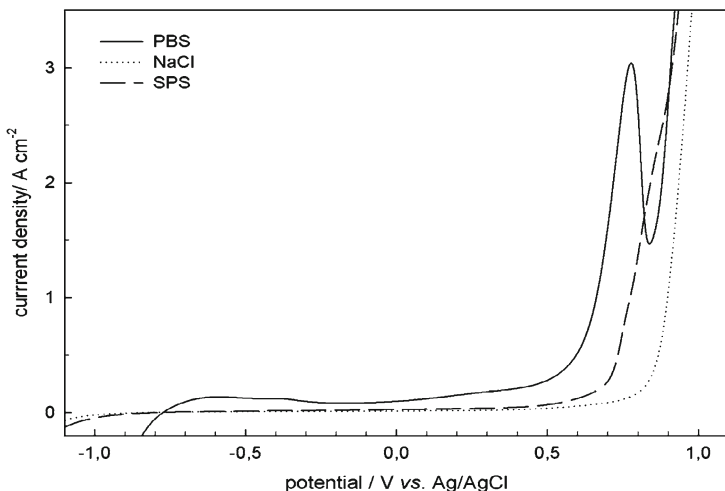
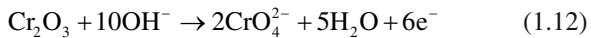


**Fig. 1.8** Anodic part of cyclic voltammograms (VCVs) recorded for CoCrMo alloy in 0.9% NaCl, simulated Hanks' physiological solution (SPS), and phosphate buffer solution (PBS).  $dE/dt=50 \text{ mV s}^{-1}$

The alloy behaves most similarly to chromium, and to a certain extent also to molybdenum (Fig. 1.1). The most pronounced differences between CVs are observed in the transpassive range. Phosphate ions induce an increase in current density and a shift in the onset of transpassive range to more negative potentials. In PBS, a pronounced peak at 0.8 V is formed. In SPS, which also contains phosphate ions, onset of transpassivity is shifted to more positive values. A shoulder, rather than a peak, appears at 0.88 V. In NaCl, the potential of the current density increase is shifted to even more positive values. Once the increase is started, it proceeds steadily, without a peak or shoulder. The features observed in the transpassive range are obviously related to the composition of solution, i.e., presence of phosphate ions and formation of metal phosphates, e.g., orthophosphate  $\text{CrPO}_4$  and metaphosphate  $\text{Mo}(\text{PO}_3)_3$ . It was observed experimentally that the peak in the transpassive region increases with increasing phosphate concentration [42]. Because this peak is mainly related to the formation of Cr(VI) species, it implies that increasing phosphate concentration leads to a higher production of chromate ions. This hypothesis was corroborated experimentally by measuring the concentration of  $\text{CrO}_4^{2-}$  by UV/vis absorption spectroscopy during 4 h oxidation at 0.74 V (SCE) in PBS [42]. The transpassive dissolution of chromium oxide starts with the dissolution of  $\text{Cr}_2\text{O}_3$  via reaction (1.12). In the presence of phosphate ions, reaction (1.13) takes place and leads to the formation of an additional amount of chromate ion, as evidenced also by increased current density of the peak in the transpassive region.



Increased formation of  $\text{CrO}_4^{2-}$  species at higher PBS concentration might be thus explained by the presence of a  $\text{CrPO}_4$  underlayer beneath the  $\text{Cr}_2\text{O}_3$  oxide. Interestingly, the deposition of chromium orthophosphate was identified experimentally after exposure of CoCrMo pellets to human serum [73] and in vivo in the periprosthetic tissue of hip prostheses [74].

Various types of phosphate solutions, with or without chloride ions added, are presented in Table 1.2. The difference in behavior of CoCrMo alloy in 0.14 M NaCl solution and saline phosphate buffer (SPBS) was investigated by Muñoz and Mischler [28]. In both solutions the EIS diagrams exhibit a typical passive state shape characterized

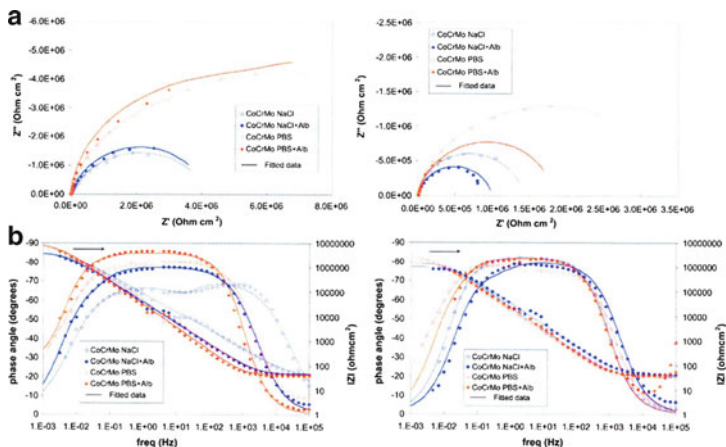


**Fig. 1.9** Nyquist plots (a) and Bode plots (b) of CoCrMo in different solutions at  $-0.1$  V vs. SCE and OCP, pH 7.4, and  $37^\circ\text{C}$  (Reprinted from A. Igual Muñoz and S. Mischler, *J. Electrochem. Soc.* 154 (2007) C562, with permission from The Electrochemical Society [28])

by high impedance values with capacitive behavior (Fig. 1.9). The equivalent circuit implied two time constants in series. One time constant was attributed to the oxide resistance ( $R_{in}$ )/capacitance ( $C_{in}$ ) parallel combination across the oxide and the second is attributed to the charge transfer resistance ( $R_{out}$ )/double-layer capacitance ( $C_{out}$ ) parallel combination.

At the open circuit potential, OCP, and potential in the passive range ( $-0.1$  V SCE), the addition of phosphate increased the value of  $R_{out}$  as well as  $CPE_{out}$ . The increase in  $R_{out}$  was much higher at the potential in the passive region ( $-0.1$  V SCE) than at the OCP, i.e., two to three orders of magnitude compared to a slight increase at the OCP. Therefore, the outer layer formed in the presence of phosphate increases the corrosion resistance. This effect was related to the formation of a phosphate-rich layer covering the electrode surface and blocking the mass transport of oxygen or reaction products to and from the electrode surface. Indeed, the presence of phosphate in the oxide layer was confirmed by XPS [28]. In the passive region in SPBS, the resistance of the outer layer exceeds that of the inner layer, whereas in the NaCl solution the resistance of the inner layer remains significantly larger than that of the outer layer, indicating that the kinetics remains under mass-transport control through the oxide film.

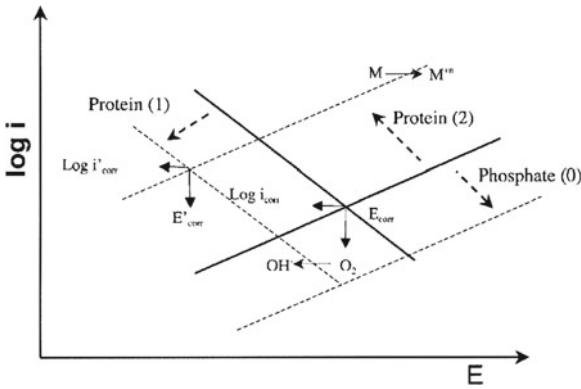


**Fig. 1.10** Mixed potential theory applied to interpret the effect of albumin and phosphates on CoCrMo corrosion potential and corrosion current. Phosphate ions act as anodic inhibitors (*arrow 0*). Albumin acts as a cathodic inhibitor (*arrow 1*) but can accelerate the anodic oxidation of the metal by binding metal ions (*arrow 2*) (Reprinted from A. Igual Muñoz and S. Mischler, *J. Electrochem. Soc.* 154 (2007) C562, with permission from The Electrochemical Society [28])

Besides potential, immersion time (1–24 h) is also an important parameter: it modifies the interface behavior of CoCrMo alloy by increasing the resistance of the film in phosphate-containing solution [39]. The presented results suggest that the addition of phosphate modifies the nature of the inner passive film at OCP but apparently not at  $-0.1$  V, i.e., in the passive region.

A corrosion mechanism was proposed taking into consideration the mixed potential theory to interpret the effect of phosphate on corrosion current and corrosion potential (Fig. 1.10). The adsorption of phosphate decreases the corrosion current density and shifts the potential to more positive values. Therefore, it acts as an anodic inhibitor. The concentration of phosphate ions affects the formation of oxide layer on CoCrMo alloy, as evidenced by EIS data reflecting the adsorption and blockage of surface by phosphate ions at the electrode–electrolyte interface [42]. Charge transfer resistance,  $R_{ct}$ , changed as a function of phosphate concentration and immersion time [42]; it increased from  $280 \text{ k}\Omega \text{ cm}^2$  (2 h; 0.05 M PBS) to  $1,230 \text{ k}\Omega \text{ cm}^2$  (8 h 40 min; 0.1 M PBS), indicating that the presence of the phosphate ions is governing the corrosion behavior of CoCrMo alloy. The addition of calf serum produced no significant effect, which is in contrast to titanium, where the competition between the adsorption mechanisms of proteins and those relating to phosphate ions was evident [75].

### 1.5.3 Addition of Complexing Agents

A simple inorganic solution cannot completely mimic the *in vivo* situation. The complexing agent (such as EDTA and citrate) constitutes a simple model of physiological conditions in which serum proteins *in vivo* complex metal ions [76]. Studies on stainless steel in the presence of ethylenediaminetetraacetic acid (EDTA) and citrate have shown that metal cations tend to form soluble complexes, leaving behind a thinner and depleted passive layer [35–37]. The addition of a complexing agent caused an increase in the current density recorded for CoCrMo alloy in SPS (Fig. 1.3). At the same time, decreased content of cobalt in the passive layer was observed as a consequence of the complexation reaction of dissolved Co cations [31, 38]. Not only the composition but also the thickness of the passive film is strongly affected by the addition of a complexing agent. In EDTA containing SPS, significant changes occur (compare Figs. 1.7 and 1.11). In the absence of a complexing agent, the thickness of the oxide layer on CoCrMo alloy formed in SPS at 0.1 V and 0.6 V was 2.1 nm and 13.5 nm, respectively; addition of EDTA caused a decrease in thickness to 1.6 nm and 7.5 nm [38].

Stimulation of the anodic dissolution process was found to be strongly related to the stability constant of the complex and the metal involved [31, 38]. Citrate is a complexing agent for  $\text{Co}^{2+}$  with the stability constant of  $\log K_{\text{st}} = 5$  [77]. Co forms strong complexes with EDTA, with logarithms of stability constant of  $\text{Co}^{2+}$  16.3 and  $\text{Co}^{3+}$  41.4 [77]. Indeed, EDTA induces stronger stimulation of anodic process on Co than citrate [31]. No literature data exist for stability constants for complexes of Mo with EDTA; however, a similar effect is observed as for Co, indicating that the addition of a complexing agent strongly affects the dissolution of Mo as well. Theoretically, EDTA may form very strong complexes also with  $\text{Cr}^{3+}$  ions [77], but because of the very slow dissolution of the strongly protective  $\text{Cr}_2\text{O}_3$  layer, the amount of Cr(III) species available for complexing is small.

A phase diagram of the layer formation, electric transfer, and dissolution with complex formation is presented in Fig. 1.12. Anodic oxidation of the alloy yields the formation of the various cations  $\text{Me}^{z+}$ , which become part of a passivation oxide layer. The cations may be transferred across the oxide–electrolyte interface, thus leading to the corrosion rate of metal (reaction 1). Oxide growth requires the formation of  $\text{O}^{2-}$  ions at the oxide–electrolyte interface. These ions may migrate within the oxide under the influence of the high

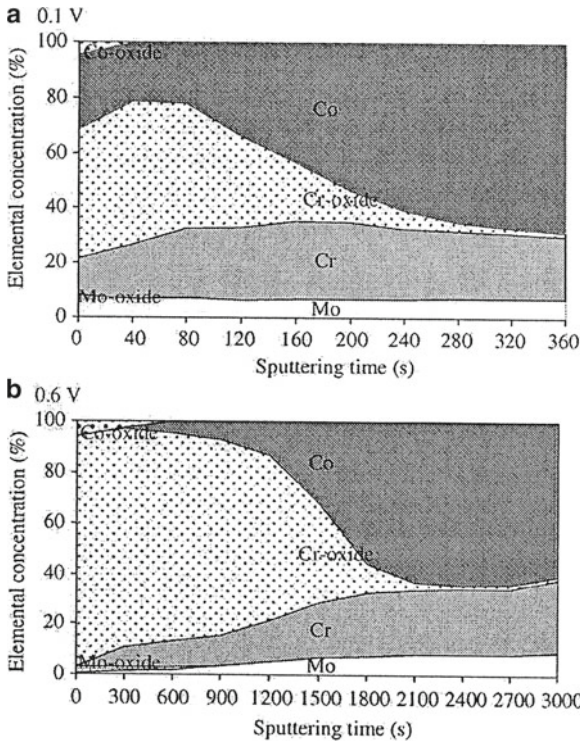


**Fig. 1.11** Depth profiles of CoCrMo alloy after oxidation at 0.1 V (a) and 0.6 V (b) for 1 h in simulated Hanks' physiological solution containing 50 mM EDTA as a function of sputtering time. Sputtering time relative to  $\text{Ta}_2\text{O}_5$  standard is  $0.01 \text{ nm s}^{-1}$  (Reprinted from A. Kocijan, I. Milošev, and B. Pihlar, *J. Mater. Sci. Mater. Med.* 15 (2004) 643, with permission from Springer [38])

electrical field strength of some  $10^6 \text{ V cm}^{-1}$  to the metal surface to grow new oxide at both sites (reaction 2). Electron transfer across the passive layer (reaction 3) is required for oxide formation and corrosion in the passive state through the action of an oxidant such as dissolved oxygen or hydrogen ions. Complexing of cations with  $\text{X}^-$ , e.g., citrate, enhances the dissolution rate of cations according to reaction (4). Complex formation reduces their positive charge, thus decreasing the activation energy for their transfer from the  $\text{O}^{2-}$  matrix of the oxide. The fast formation of complexes with a high stability constant is therefore the reason for an increased dissolution rate and the related thinning of the oxide layer.

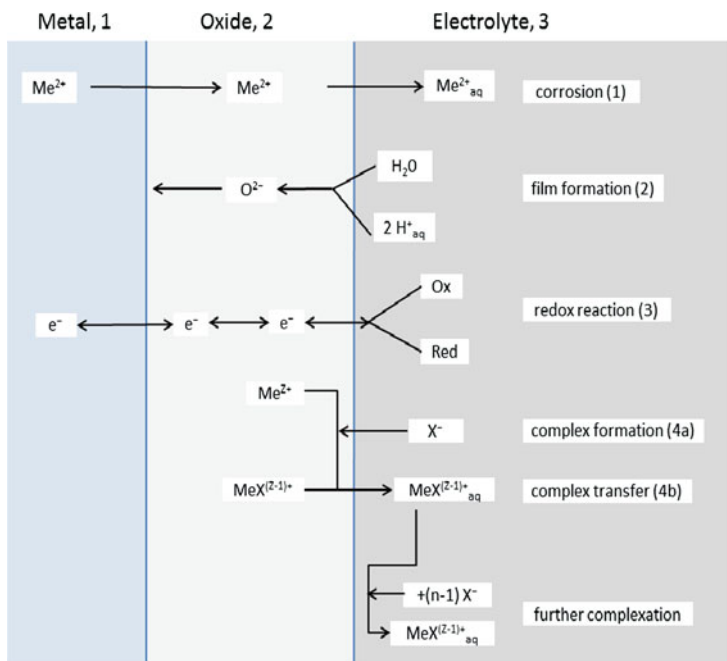


**Fig. 1.12** Phase diagram of a passive film showing corrosion (1), film formation (2), redox reaction (3), and dissolution with complex formation, transfer, and further complexation (4a, 4b)

## 1.6 Electrochemical Studies of CoCrMo Alloy in Simulated Physiological Solution Containing Biomolecules

### 1.6.1 Effect of Proteins

In the previous section, the effects of inorganic anions and complexing agents were discussed. In this section, the effect of proteins, or more particularly albumin, playing the most significant role is discussed. Albumin is generally regarded to mean serum albumin or plasma albumin. The word albumin is used to describe any protein or a group of proteins that are water soluble, moderately soluble in concentrated salt solutions, and experience heat denaturation. Albumins are

commonly found in blood plasma and are unique among plasma proteins in that they are not glycosylated. Human serum albumin is the most abundant protein in human blood plasma. It comprises about half of the blood serum protein and is mainly responsible for the maintenance of blood pH and osmotic pressure. The reference range for albumin concentrations in blood is 3.4–5.4 g per 100 ml. Its serum half-life is approximately 20 days; it has a molecular mass of 67 kDa, its isoelectric point at 25°C is 4.7, and dimension is  $14 \times 4 \times 4 \text{ nm}^3$  [78]. Albumin when ionized in water at pH 7.4, as found in the body, is negatively charged. According to X-ray crystallographic data, the albumin structure is predominately  $\alpha$ -helical (67%), with the remaining polypeptide occurring in turns and extended or flexible regions between subdomains with no  $\beta$ -sheets. Albumin comprises three homologous domains that assemble to form a heart-shaped molecule [79]. When heated, albumin goes through two structural stages. The first stage (up to 65°C) is reversible; the second stage (>65°C) is irreversible but does not necessarily result in a complete destruction of the ordered structure. The onset temperature of conformation change is 58.1°C. Above 65°C,  $\beta$ -sheets are formed. Perhaps the most outstanding property of albumin is its ability to bind reversibly with an incredible variety of ligands such as fatty acids, hematin, bilirubin, charged aromatic compounds, cysteine, glutathione, and various metals. Because of these properties, serum albumin, mostly bovine serum albumin (BSA), is considered as a model protein in biocompatibility studies.

The effect of adding BSA ( $0.5 \text{ g l}^{-1}$ ) to 0.14 M NaCl and SPBS on polarization curves is presented in Fig. 1.13 [28]. In NaCl, the addition of albumin slightly increases the current density in the whole potential range, but this increase is more pronounced in SPBS, especially in the cathodic region. In SPBS, the addition of albumin shifts the corrosion potential to more negative values and increases the corrosion current density. The addition of  $0.5 \text{ g l}^{-1}$  BSA to SPBS increased the value of  $i_{\text{corr}}$  approximately fivefold. Because the value of  $i_{\text{corr}}$  is higher in pure NaCl solution than in SPBS, the addition of the same BSA concentration to NaCl solution induces a smaller increase, i.e., from 9.6 to  $11.5 \mu\text{A cm}^{-2}$  [28].

It is evident that both phosphate ions and albumin play a significant role in the electrochemical properties of the metal–oxide–electrolyte interface. Both species specifically competitively adsorb on the alloy surface, which is not surprising because at pH 7.4 albumin is negatively charged as phosphate ions. Thus, both species compete for

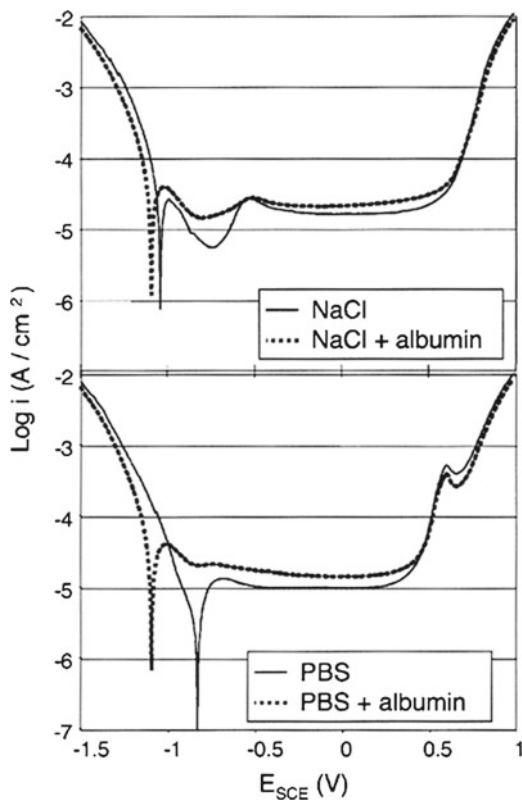


**Fig. 1.13** Potentiodynamic curves for CoCrMo alloy in 0.14 M NaCl and PBS solutions with or without 0.05 g l<sup>-1</sup> albumin (pH 7.4, 37°C) (Reprinted from A. Igual Muñoz and S. Mischler, *J. Electrochem. Soc.* 154 (2007) C562, with permission from The Electrochemical Society [28])

adsorption. However, their effect on corrosion is quite different. The corrosion mechanism was proposed and presented in Fig. 1.10. Albumin acts as a cathodic inhibitor because its adsorption impedes the access of the oxidant to the metal surface. At the same time it increases the dissolution rate of metal because it limits the adsorption of phosphate, thus accelerating corrosion. Although phosphate retains its inhibitive behavior at the OCP, the effect of albumin is different at OCP compared to its behavior at -0.1 V, i.e., in the passive range (Fig. 1.9). At OCP albumin completely suppresses the effect of phosphate whereas in the passive range it has no significant effect [28].

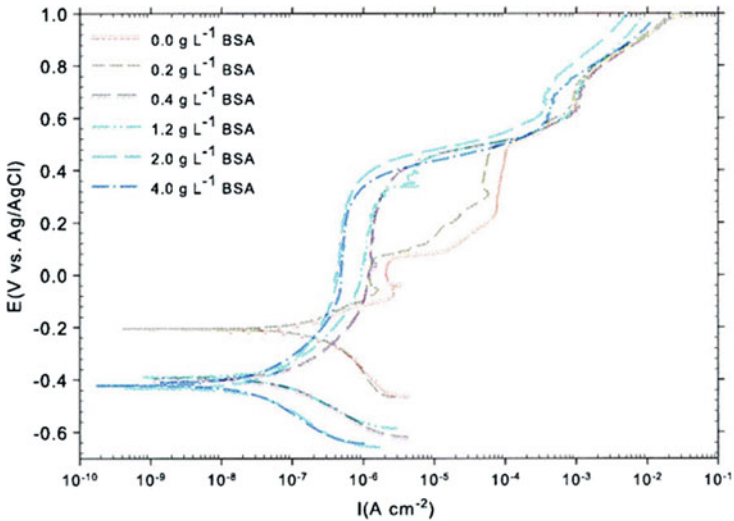


**Fig. 1.14** Potentiodynamic polarization curves of Co–28Cr–6Mo in PBS solutions and various BSA concentrations (0–4 g l<sup>-1</sup>) from -0.25 V to 1 V versus Ag/AgCl with a scan rate of 0.167 mV s<sup>-1</sup> in aerated conditions at 37°C and pH of 7.4 (Reprinted from S. Karimi, T. Nikchi, and A. Alfantazi, *Corrosion Sci.* 53 (2011) 3262, with permission from Elsevier [41])

Auger profiles of CoCrMo layer oxidized at -0.1 V (passive range) show a double-layer structure with an inner oxide layer covered by an adsorption layer (outer layer) containing albumin [28]. As a result of adsorption, larger effects of phosphate ions and albumin are expected on the electrical properties of the outer layer. Indeed, the capacitance of the outer layer is increased by a factor of 10 and 5, respectively. Although albumin increases the  $R_{\text{out}}$  resistance by a factor of 50 in the NaCl solution, the phosphate has a much larger impact and increases the resistance of the outer layer by three orders of magnitude. Albumin is less efficient in reducing the reaction rate, probably because its larger size does not allow the formation of a compact film, as is the case of a phosphate-rich layer.

Karimi et al., on the other hand, observed a significant effect of BSA in the passive range as well (Fig. 1.14) [41]. The addition of BSA was studied in the broad concentration range from 0.2 to 4.0 g l<sup>-1</sup> in SPBS at 37°C. For concentrations  $\geq 0.4$  g l<sup>-1</sup>, the addition of BSA strongly affected the polarization curves by shifting the corrosion potential to more negative values and decreasing the cathodic current

**Table 1.3** Activation energy values ( $E_a$ /kJ/mol) obtained from the potentiodynamic curves and EIS results on a CoCrMo alloy at temperatures from 298 to 333 K in different NaCl solutions

	Potentiodynamic curves	EIS
NaCl	49.4	34.5
NaCl+5 mg l <sup>-1</sup> BSA	28.8	31.5
NaCl+20 mg l <sup>-1</sup> BSA	29.5	30.5
NaCl+50 mg l <sup>-1</sup> BSA	28.3	32.6
NaCl+500 mg l <sup>-1</sup> BSA	45.2	43.1

BSA Bovine serum albumin

Source: Reprinted from C. Valero Vidal, A. Olmo Juan, and A. Igual Muñoz, *Colloids Surf. B: Biomaterials* 80 (2010) 1, with permission from Elsevier [40]

density. Therefore, BSA acts as the cathodic inhibitor. The addition of BSA strongly decreased the current density in the second half of the passive range, i.e., for  $E > 0.1$  V, which is related to the introduction of Co-oxide in the film. In the absence of BSA, no cobalt was detected in the oxide layer formed at 0.007 V (Ag/AgCl) (mid-passive range), but in the presence of 4.0 g l<sup>-1</sup> BSA, cobalt (1.7at.%) was detected in the layer, as analyzed by XPS [41]. The increase in cobalt content could be explained by the adsorption of BSA to the surface of alloys and its affinity to react with cobalt [73]. In the solution containing BSA, a lower concentration of chloride and phosphorus were also detected. It seems that protein acts as a negatively charged barrier film and blocks anions, such as chloride and phosphate, from reaching the surface.

To investigate the adsorption mechanism, dependence on temperature and BSA concentration from 0.005 to 0.5 g l<sup>-1</sup> was studied in 0.14 M NaCl [40]. This concentration range is smaller compared to that studied by Karimi et al. (0.2–4.0 g l<sup>-1</sup>) [41]. With increasing temperature and BSA concentration (up to 0.05 g l<sup>-1</sup>), the corrosion rate,  $i_{\text{corr}}$ , increased. The activation energy,  $E_a$ , of the corrosion process was obtained from linear variation of the rate of metal dissolution reaction assigned as corrosion current density,  $i_{\text{corr}}$ , with temperature (Arrhenius equation) (Table 1.3). The highest activation energy was obtained in NaCl solution, 49.4 kJ mol<sup>-1</sup>, and it decreased when adding 0.005, 0.02, and 0.05 g l<sup>-1</sup> BSA to around 28 kJ mol<sup>-1</sup>. Hence, the addition of BSA to the saline solution caused a decrease in the corrosion activation energy of 21 kJ mol<sup>-1</sup>, which indicates that the adsorption of protein to the CoCrMo surface and subsequent formation of a complex with metal ions from the passive film reduced the activation energy

and enhanced the corrosion rate of the alloy [80, 81]. Thus, by the addition of BSA, a less protective layer was formed on the CoCrMo surface than in pure saline solution. This observation further indicates that the adsorption of BSA molecules onto the CoCrMo surface occurred by a charge transfer mechanism, probably chemisorption [82], in agreement with the results obtained by Omanovic et al. for adsorption behavior of serum proteins albumin and fibrinogen on Ti [83], albumin on stainless steel [80], and  $\beta$ -lactoglobulin on stainless steel [81].

When the concentration of the BSA was increased to  $0.50 \text{ g l}^{-1}$ , the activation energy increased again (Table 1.3). Obviously, different electrochemical behavior occurs in high and low BSA-containing solutions. Similar behavior was observed by Alfonso et al. [84] on stainless steel: at lower BSA concentration the complexing effect of BSA was predominant and favored metal dissolution, whereas at a higher BSA concentration the predominant effect was the adsorption of the protein on the surface.

The adsorption of proteins onto the CoCrMo surface has been described by the Langmuir isotherm:

$$\Gamma = \frac{B_{\text{ADS}} \Gamma_{\text{max}} c}{1 + B_{\text{ADS}} c} \quad (1.14)$$

where  $c$  ( $\text{mol cm}^{-3}$ ) is the equilibrium concentration of the adsorbate in the bulk solution,  $\Gamma$  ( $\text{mol cm}^{-2}$ ) is the amount of protein adsorbed, i.e., surface concentration,  $\Gamma_{\text{max}}$  ( $\text{mol cm}^{-2}$ ) is the maximum value of  $\Gamma$ , and the parameter  $B_{\text{ADS}}$  ( $\text{cm}^3 \text{ mol}^{-1}$ ) reflect the affinity of the adsorbate toward adsorption sites [80, 81, 83]. Equation (1.14) can be rearranged to give

$$\frac{c}{\Gamma} = \frac{1}{B_{\text{ADS}} \Gamma_{\text{max}}} + \frac{c}{\Gamma_{\text{max}}} \quad (1.15)$$

A plot of  $c/\Gamma$  versus concentration should give a straight line with parameters  $\Gamma_{\text{max}}$  and  $B_{\text{ADS}}$  derived from the slope and intercept, respectively. Saturated surface concentration  $\Gamma_{\text{max}}$  increases with temperature, indicating strong adsorption of BSA toward the CoCrMo surface.  $B_{\text{ADS}}$  shows some scatter in data but strongly increases at 333 K, indicating a higher affinity of the denatured structure of BSA molecules in the bulk solution for the surface, possibly resulting in multilayer adsorption [80, 81, 83].

The calculated values of Gibbs free energy of adsorption,  $\Delta G_{\text{ADS}}$ , range from  $-51.3 \text{ kJ mol}^{-1}$  at 298 K to  $-57.2 \text{ kJ mol}^{-1}$  at 333 K. Such high values again indicate that the molecules have a strong adsorption of BSA onto the CoCrMo surface, i.e., chemisorption. Enthalpy,  $\Delta H_{\text{ADS}} = 2.04 \text{ kJ mol}^{-1}$ , and entropy,  $\Delta S_{\text{ADS}} = 176 \text{ J mol}^{-1}$ , of adsorption suggested that the adsorption process of BSA onto the CoCrMo surface is an endothermic process and that the molecule suffers structural changes when adsorbing on the metallic surface. The structure and hence dimensions of the molecule change when the protein adsorbs onto a surface. The induced structural changes can lead to a considerably entropy gain, which appears to be a driving force for the adsorption of BSA [83].

The ability of the surface to induce conformational changes or denaturation of proteins is important to the biocompatibility of a given material [85]. Several factors can drive the protein adsorption process:

- (a) Electrostatic protein–protein and surface–protein interactions, which may be repulsive or attractive
- (b) Dehydration of the surface and protein
- (c) Structural changes in the protein

Changes of conformation are generally more important on hydrophobic than on hydrophilic surfaces; i.e., a protein molecule with low conformational stability (soft protein), such as albumin, adsorbs on a great variety of surfaces (hydrophilic or hydrophobic), even under adverse electrostatic conditions. In contrast, high stability protein (hard protein) adsorbs mainly on hydrophobic surfaces. On hydrophilic surfaces, the hard protein adsorbs only under favorable electrostatic interactions. Furthermore, interactions between proteins and surfaces, resulting in adsorption, can be affected by a number of factors, such as temperature, conformation of the protein in solution and its bulk concentration, pH, ionic strength, and the surface characteristics of the material onto which adsorption occurs [86, 87].

The effect of BSA adsorption as a function of medium (pure water,  $\text{pH} = 8 - 8.4$ , and 0.1 M PBS,  $\text{Na}_2\text{HPO}_4 + \text{NaH}_2\text{PO}_4$ ,  $\text{pH} = 7$ ) and material (chromium and molybdenum) was investigated by Pradier et al. [88]. Significant changes in adsorption of BSA were observed in PBS compared to water, as indicated by amide bands in Fourier transform infrared reflection–adsorption spectra (FT-IRRAS) (Figs. 1.15 and 1.16). In pure water, short times of immersion (a few minutes) resulted in higher BSA adsorption on Cr than on Mo. For longer

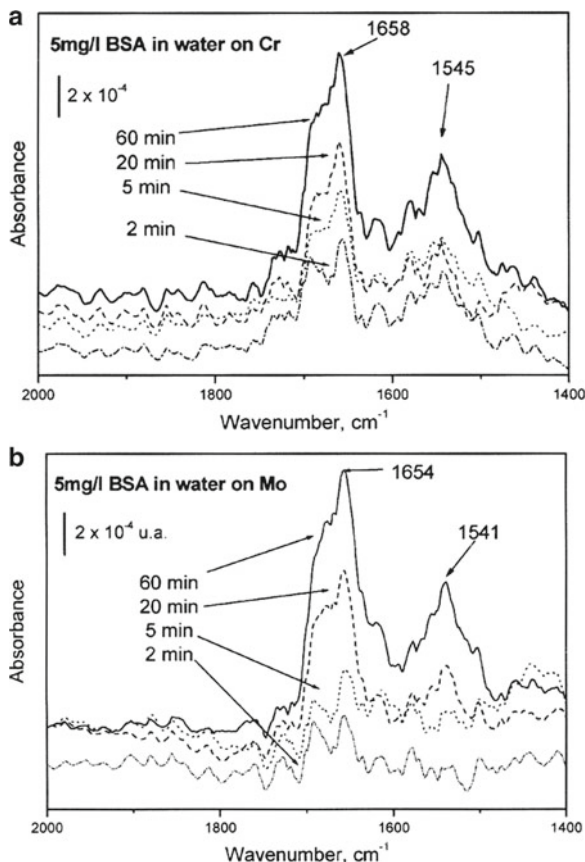


**Fig. 1.15** IRRAS spectra of chromium and molybdenum surfaces after immersion in a  $5 \text{ mg l}^{-1}$  BSA–water solution for 2, 5, 20, and 60 min. The samples were rinsed and dried before analysis (Reprinted from C.M. Pradier, F. Kármán, J. Telegdi, E. Kálman, and P. Marcus, *J. Phys. Chem.* 107 (2003) 6766, with permission from ACS Publications [88])

times (20 min, 1 h), the amount of BSA was similar on both surfaces (Fig. 1.15). Spectra show peaks ascribed to vibration modes  $\nu_{\text{C=O}}$  and  $\nu_{\text{C-N}}, \delta_{\text{N-H}}$ , centered at  $1,658 \text{ cm}^{-1}$  and  $1,545 \text{ cm}^{-1}$ , respectively (amide I and amide II). These peptide-characteristic signals increase with immersion time. The band at a maximum at  $1,658 \text{ cm}^{-1}$  can be fitted with two components at  $1,680 \text{ cm}^{-1}$  and  $1,658 \text{ cm}^{-1}$ . The former is characteristic of  $\beta$ -turns and bends of partially unfolded BSA molecules, and the latter is ascribed to H-bonded Co in  $\alpha$ -helices and

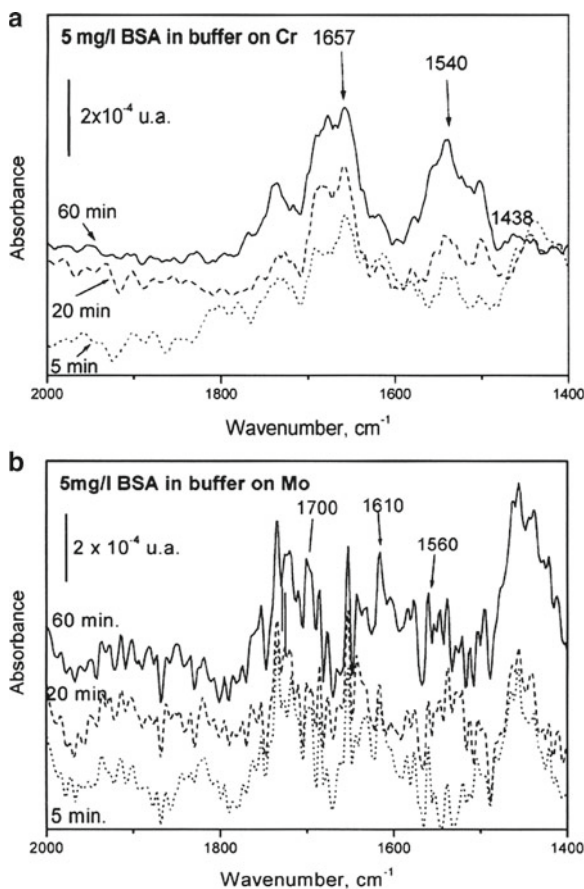


**Fig. 1.16** IRRAS spectra of chromium and molybdenum surfaces after immersion in a 5 mg l<sup>-1</sup> BSA-phosphate buffer solution for 5, 20, and 60 min. The samples were rinsed and dried before analysis (Reprinted from C.M. Pradier, F. Kármán, J. Telegdi, E. Kálman, and P. Marcus, *J. Phys. Chem.* 107 (2003) 6766, with permission from ACS Publications [88])

suggests the presence of packed hydrophobic helical domains. With increasing immersion time the component at 1,658 cm<sup>-1</sup> significantly increases, indicating the tendency to form dense peaks of proteins on chromium; a similar trend was not observed on Mo. Significant changes in adsorption of BSA were observed in PBS (Fig. 1.16). A strong decrease (factor ~3) of the amide bands was observed in comparison to the results obtained in pure water (Fig. 1.15).

XPS analysis was also explored to study the chemical composition of the metal surface [88]. After immersion in water containing 20 mg l<sup>-1</sup> BSA, the chromium surface was covered by a thin layer of Cr(OH)<sub>3</sub>, whereas Mo was covered by oxide MoO<sub>2</sub>. Deconvolution of the carbon signal confirmed that chemically intact (and not decomposed) BSA molecules were adsorbed at the surface. A nitrogen peak at 400.9 eV confirmed the presence of amine or amide groups of the protein. In the presence of phosphate, the adsorption was strongly diminished, indicating that adsorbed phosphates block the adsorption of BSA. Reyes et al. reported that the BSA diffusion coefficient decreased by a factor of 4 in a 0.1 M phosphate-buffered solution compared to pure water [89]; this is a kinetic parameter that explains a low rate of BSA adsorption from a phosphate-containing solution.

Finally, the data show conformational changes of the BSA molecules that are different on two substrates: the BSA structure is more compact on Cr than on Mo. There are several possible reasons. At pH in the range 7–8.3, both surfaces are presumably negatively charged. Chromium is covered by a hydroxide layer, although the layer on Mo is only slightly hydroxylated. It is assumed that the BSA internal structure is reorganized to optimize its interactions with the hydrophilic Cr surface. Lu and Park showed that the  $\alpha$ -helix structure is favored on hydrophilic surfaces [90]. The authors proposed the following main difference in the adsorption mechanism of BSA on Cr and Mo [88]. When coming in contact with the metal surface, negatively charged BSA molecules undergo partial unfolding to present a maximal number of positive groups such as the N-terminal and lysine residue toward the surface: this occurs on both Cr and Mo during the first 20 min of immersion. Further adsorption of proteins tends to proceed so as to minimize the surface energy in two possible ways. One path is to occupy the free surface areas, which probably occurs on Mo. The other possibility is the formation of a second layer of proteins on top of the already attached ones. This mechanism is predominant on Cr because it enables the formation of a more compact helical structure, as experimentally observed on Cr.

### ***1.6.2 Formation of Organometallic Compounds and Distribution of Proteins***

It was early recognized that organic molecules play an important role in the behavior of metals and alloys in a physiological environment.

After implantation, the first event of the interaction between tissues and the metallic device is the adsorption of plasma constituents, especially proteins, onto the metal surface. Proteins encounter the surface depending upon the product of their concentration and their self-diffusion velocity, which is approximately inversely related to the square root of their molecular weight [76]. Thus, protein–surface interactions *in vivo* or *in vitro* from mixed solutions can be regarded as a succession of events. The early arrivers (low molecular weight/high concentration) are potentially displaced by late arrivers (high molecular weight/low concentration). This process, known as the Vroman effect, implies that even after the total surface concentration of protein reaches a steady-state value, the composition of the film at the interface continues to change.

Svare et al. showed that the presence of cysteine inhibited the electrochemical passivation of nickel and improved the passivation tendency of copper [91]. Proteins, including albumin, had little or no effect on passivation of these metals. Relatively few studies have considered the effect of proteins on the electrochemical (corrosion) behavior of metals. The majority of these studies have been performed on stainless steels [35, 92–95]. Proteins increased the corrosion rate of the stainless steel and commercially pure (c.p.) titanium but did not have an effect on Ti–6Al–4V alloy [93]. Stainless steels were subjected to pitting corrosion in the presence of proteins [92].

Proteins can have a significant effect on the passivation behavior of individual metals and alloys because they can act as complexing agents for dissolved metal ions, thus stimulating the dissolution rate of a base alloy and, consequently, suppressing the formation of the protective oxide layer (see Sect. 1.5). Iron and stainless steel AISI 304 were susceptible to localized corrosion in the presence of complexing agent and various proteins (albumin,  $\gamma$ -globulin, transferrin, and fibrinogen) [35]. All proteins, and especially complexing agent EDTA, increased the dissolution of individual metals and alloys. The effect of particular proteins differed on various metals and alloys, which is probably related to different stability constants of complexes between individual metal ions and various proteins. These constants are known for complexes between complexing agents such as EDTA and individual metal ions (Sect. 1.5), and for complexes between individual amino acids and metal ions [96], but are far less well known for complexes between proteins and metal ions.

In the following text the effects of protein on metal dissolution, predominant products, site of formation, binding to proteins, and route of distribution are discussed. The dissolution of metal ions and their distribution and binding to proteins have been studied by combination of immersion tests *in vitro* with metal powders, metal salts, or corrosion products, or *in vivo* by injecting metal salts into animals. Concentration of released metals and their binding to proteins was then determined by analytical methods. The mechanism was also analyzed in the serum of patients with hip replacements.

Metal salt solutions ( $\text{CrCl}_3$  and  $\text{CoCl}_2$ ) were incubated with 1:20 dilution of murine serum proteins for 24 h [97]. Free metal was then removed by dialysis and the percentage of protein-bound metal ions was measured. Chromium and cobalt have similar protein-binding affinity and bind to protein in proportion to the added concentration ratio. The form taken by the corrosion products of CoCrMo metal powder upon dissolution in serum *in vitro* and *in vivo* in rats was studied by Woodman et al. [98]. Concentrations of dissolved metals were much higher in serum solution compared to saline (factor of 10). The predominant form of corrosion products of chromium are organometallic complexes with proteins. Two principal serum protein peaks were observed:  $\alpha_2$  macroglobulin and albumin [98]. In general, organometallic compounds have two components: one is an organic moiety, and the other is the metallic moiety [76]. The association between the two can be weak or strong, i.e., from chelation, coordination, to ligand formation. The production of the organometallic compounds by implants is controlled by a dynamic equilibrium established between the alloy and the intermediate organometallic compound, as well as between the alloy and inorganic ions. The release of chromium was strongly dependent on the surface area of the powder whereas cobalt release was not. The reason for this behavior lies in the fact that the organometallic complex may form either on the surface or in solution. If it is formed on the surface, then the ratio of the implant surface area available for equilibrium will govern both the formation rate and the equilibrium concentration, as is apparently the case for complexes formed between chromium and serum proteins [98]. The complexing is controlled at the interface of the metallic spheres with the serum, and any increase in surface area of powder will increase the equilibrium concentration of those metals released from the alloy. If the complex forms preferentially in solution, then only the rate of formation is affected, as is apparently the case for

cobalt. The increase in surface area will not produce any increase in equilibrium concentration. Instead, cobalt may complex in solution.

The rate of corrosion depends on the rate of removal of the intermediate organometallic compound [76]. If more is removed by the deposition in tissues, then corrosion could proceed at an increased rate. Because the removal of the intermediate compound is a rate-limiting step, differences seen between biological response to powder and bulk implants probably reflect different surface (interface) reaction conditions.

In the presence of 0.1% bovine albumin and fibrinogen, increased dissolution of copper was observed, whereas the dissolution of chromium showed only a small increase [95]. It seems that different metals behave differently in the presence of different proteins. Two mechanisms may be operative: proteins may abstract metals ions from the oxidized layer, or they can act as catalysts, oxidizing the metals with internal disulfate groups, and forming a protein-metal complex, with the disulfide bonds being subsequently reformed by oxidation with oxygen. Although in many cases this would not lead to a loss of structure by the protein, repeated activity of this nature is likely to lead to cross-linking and precipitation. Because albumin is a smaller and more flexible molecule than fibrinogen, and contains free sulfhydryl groups, it is reasonable to expect that cross-linking will occur more readily with albumin than fibrinogen (despite that it is less stable in solution).

Different metals bind differently not only to proteins but also to cells [99]. Nickel almost exclusively binds to albumin and not to cells, whereas cobalt binds to cells and albumin. The valence of chromium affects its binding ability.  $\text{Cr}^{3+}$  from  $\text{CrCl}_3$  binds to cells in very small quantities, whereas  $\text{Cr}^{6+}$  from  $\text{K}_2\text{Cr}_2\text{O}_7$  binds strongly to cells. All the metals (Ni, Co, Cr) bind strongly to albumin, which is the most abundant protein in serum and tissue. The fact that metals bind to albumin means that they could become widely distributed in the body, which helps to explain the dissemination of the corrosion products from the site of implant. This predicted behavior was confirmed in *in vivo* experiments in which metal salts or corrosion products generated by fretting corrosion of stainless steel were injected in hamsters and the concentration of nickel, cobalt, and chromium in the serum, attached to red cells, and attached to white cells was determined [100]. Metals are transported rapidly from the intramuscular site with high levels in the blood by 2 h. The level of metal in the

blood varied considerably with nickel being transported in high concentration to the blood, chromium with a valence of 6+ being transported to the blood at intermediate concentrations, and cobalt and chromium with a valence of 3+ being transported less to the blood. The highest amount of cell binding was observed with chromium 6+. Cobalt showed negligible binding to blood cells. When all the metal salts injected together were compared with the individual salts injected alone, there was no difference.

These results indicated that each metal behaves independently of the presence of other metals. Metals behave differently in the presence of different proteins, but dependently on pH, i.e., protein charge [94]. As Zwitter ions, proteins have a positive charge in solution acidic to their isoelectric point (pI) and a negative charge in solution basic to their pI. The average pI of albumin is 4.5; gamma globulin has a wide range of isoelectric points with an average at 8. Although alteration of pH in saline solution (pH 3, 5, and 8) did not affect the corrosion rate, in protein solutions significant changes were observed. In protein solution acidic to the pI, the presence of positively charged albumin did not alter the corrosion rate as compared to that in saline. However, the presence of negatively charged proteins in solutions basic to their pI decreased the degree of corrosion. In saline solution, the release of nickel and chromium was proportional to their composition in the alloy, but in the albumin solutions at pH 5 and 8, the Ni:Cr ratio was significantly higher, indicating a preferential release of nickel.

Determination of the specific protein carrier of metal degradation products is an essential component in the assessment of the long-term biological effects of total joint replacement devices [101]. The process of protein adsorption onto the surface of biomaterials is dynamic. More prevalent serum proteins such as albumin initially dominate the biofilm that forms immediately upon implantation through reaction of the metal surface with proteins, forming a proteinaceous film. Initially adsorbed proteins are then replaced over time with less abundant proteins that have greater affinity for the implant surface, such as immunoglobulin [76, 102]. The kinetics of metal release from, and protein binding to, Co- and Ti-based alloy spherical particles during a 1-week immersion in human serum was investigated [101]. Cr was released from Co-based alloy at an order of magnitude higher than the release of Ti from Ti-based alloys. Obviously, there is a higher binding capacity of human serum for Cr from Cr-based alloy, relative

to Ti from Ti-based alloys. Both Cr and Ti released from Co- and Ti-based alloys exhibited a bimodal binding pattern, preferential binding to both low molecular weight proteins (<32 kDa) and to higher molecular weight proteins in the 180- to 250-kDa range. In the range between 77 and 140 kDa only Cr was found, indicating that there were distinct differences in the biofilm composition between the two alloys.

This mechanism was checked in human serum from patients without and with joint replacements containing elevated serum levels of Cr and Ti [102]. Cr and Ti were bound to serum proteins within specific molecular weight ranges in both patient groups. Two molecular ranges were found to bind Cr (at  $\approx 70$  and  $\approx 180$  kDa) in patients with CoCr prostheses, whereas a single molecular weight range (at  $\approx 70$  kDa) was found to bind Ti in patients with Ti alloy prostheses. Higher molecular weight proteins dominated by immunoglobulins ( $\approx 180$  kDa) have the greatest affinity for Cr. This metal-protein binding was reproduced in vitro by adding  $\text{CrCl}_3$  at concentrations of  $\approx 100$  and 1,000 ppb Cr, which are orders of magnitude higher than that in the serum of patients with CoCr implants ( $\approx 3$  ppb Cr). This finding suggests that protein binding is initiated in the periprosthetic space where metal concentrations are typically two to three orders of magnitude higher than that observed systemically in the serum.

### ***1.6.3 Effect of Biomolecules and Cell Cultures***

The existence of biomolecules and cells influences the interface behavior between metal and solution and should be taken into account when evaluating the corrosion phenomena and biocompatibility of metals. A biomolecule adsorption layer containing proteins and cells probably forms on the surface of the metal, and it is of interest to determine its role and properties.

In fetal bovine serum, which contains a number of inorganic compounds, various proteins, hormones, insulin, and other compounds, the CoCrMo alloy exhibited higher corrosion resistance than in 0.1 M sulfate solution [103, 104]; this was concluded based on the measurements of polarization resistance, which was higher in serum than in inorganic solution. Furthermore, the OCP value was more negative for about 250 mV. Considering the difference in pH of 1.1

between the two solutions (7.1 for serum and 6.0 for sulfate solution), a shift of about 60 mV could be expected. This higher difference could be explained by the rate of oxygen reduction (cathodic reaction), which is significantly lower in serum than in inorganic solution. This fact could be the reason why the OCP recorded in serum remains more negative. The lower oxygen reduction current in serum can be attributed to an increase in corresponding Tafel slope or to a decrease in the exchange current density. The adsorption of organic species from serum onto the electrode surface may cause the blocking of terminal oxygen atoms at the interface passive film–electrolyte, which, consequently, hinders the charge transfer responsible for the passive film dissolution.

To more closely simulate the *in vivo* conditions and to study the effect of cell cultures, Hiromoto et al. developed an electrolytic cell that enabled the electrochemical measurements to be performed during culturing cells on specimens [105]. The passive region of the CoCrMo alloy was not significantly affected by the composition of the solution, i.e., inorganic ions in the Hanks' solution and proteins and amino acids in the E-MEM+FBS solution (Eagle's minimum essential medium with 10vol% fetal bovine serum) did not apparently affect its corrosion resistance [106]. The oxide layer was enriched in Cr and Mo oxides regardless of the medium tested. After oxidation up to 0.12 V (SCE), i.e., at the beginning of the passive region, the thickness of the oxide layer formed in MEM+FBS solution was 3.0 nm, comparable to other solutions (Fig. 1.5). In the transpassive region changes were observed depending on the solution composition. The concentrations of Cr and Mo were smaller than in the primary passive film and the thickness was greater. It seems that the reactions in this region are accelerated by the presence of inorganic ions such as  $\text{H}_x\text{PO}_4^{n-}$  and  $\text{SO}_4^{2-}$  and biomolecules, or difference in pH, or both. In MEM, the preferential dissolution of cobalt may occur as a result of the preferential binding to serum proteins, leading to the relative increase of Cr concentration in the film. After oxidation to 0.665 V (SCE), i.e., in the region of the transpassive peak, the thickness of the oxide layer increased to 4.7 nm (Fig. 1.5). The thickness of the surface layers formed at CoCrMo in various solutions under various conditions is quite similar.

The electrochemical behavior of CoCrMo alloy was investigated in different biological solutions including urine, serum, and joint fluid [107]. The alloy exhibits only a small passive region in joint

fluid and serum but a much larger region in urine. The corrosion current densities are comparable in three biological solutions, at a range of 1.65–2.59  $\mu\text{A cm}^{-2}$ , and smaller than that reported for 0.14 M NaCl solution, 9.6  $\mu\text{A cm}^{-2}$  [28]. Based on the cyclic polarization measurements it was concluded that the susceptibility to pitting corrosion differs in the three solutions, being the highest in serum.

To study the effect of a different medium on the composition and thickness of the surface layer formed on CoCrMo, specimens were prepared by five treatments [108]:

1. Polishing in deionized water, and autoclaving at 121°C
2. Immersion in Hanks' solution for 7 days
3. Immersion in a cell culture medium [MEM+FBS: Eagle's MEM containing 10% fetal bovine serum (FBS)]
4. Incubation with cultured cells (MEM+FBS+L929 mouse fibroblast cells)

The surface films were then investigated using XPS. The composition of the surface layer differed from the bulk composition and was in all cases enriched in Cr and depleted in Co. In Hanks', MEM+FBS, and L929 specimens Ca and P were detected, indicating the formation of calcium phosphate. The Ca:P ratio was 0.7, smaller than that on Ti under the same condition (1:3). After immersion in Hanks' and cell culture media, cobalt was not detected in the surface film, indicating that during immersion preferential dissolution of cobalt occurred, leading to the enrichment of surface oxide with chromium(III) oxide. In addition to chromium, the film contained molybdenum. The thickness of the film did not change significantly in the presence of cells and proteins and ranged between 2.5 nm for a polished specimen and 2.9 nm for an autoclaved specimen (Fig. 1.5). A possible explanation is that adsorbed proteins did not form a complete layer but rather a rough and porous layer that did not contribute to the calculated thickness evaluated from the XPS intensity ratios. The degree of layer hydration was also dependent on the medium: autoclaving led to dehydration and oxidation with enrichment in chromium. In body fluids, cobalt is completely dissolved, and the chromium oxide is formed, containing a small amount of molybdenum oxide. A calcium layer was formed on the top surface.

It was hypothesized that not only macrophage cells but their release-reactive chemical species (RCS) alter the surface oxide composition of CoCrMo alloy *in vitro* [109]. As-polished and passivated CoCrMo samples were incubated for 3 days in cell culture

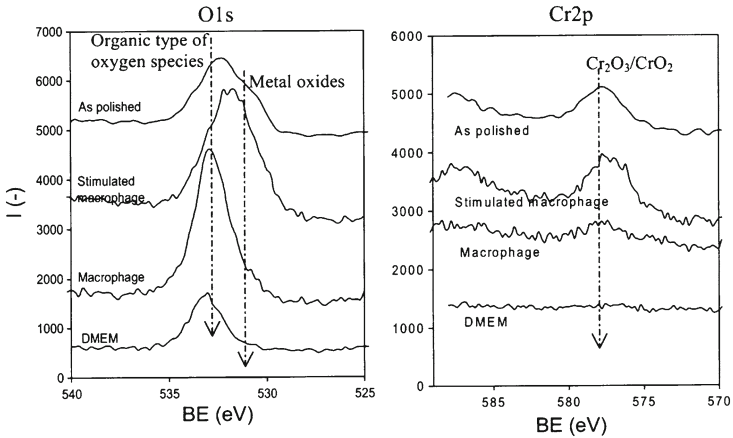


**Fig. 1.17** Examples of the O and Cr high-resolution spectra for As-polished and passivate Co–Cr–Mo samples and samples after 3 days exposure to cell culture medium, culture medium with nonactivated cells, and culture medium with LPS+IFN- $\gamma$ -activated macrophage cells. In general, peaks decreased with medium and increased again with nonactivated and activated macrophage cells (Reprinted from H.-Y. Lin and J.D. Bumgardner, *Biomaterials* 25 (2004) 1233, with permission from Elsevier [109])

medium (Dulbecco's modified Eagle medium (DMEM)+1 mM Na-pyruvate+10% FBS+1 $\times$  antibiotic-antimycotic+2 mM L-glutamin) in an incubator at 37°C. A polished and passivated sample contained C, O, Co, Cr, and Mo (Fig. 1.17), which corresponds to the presence of surface oxides. The decrease in Co, Mo, and Cr signals after 3 days in DMEM was attributed to absorption of proteins from the culture medium. After being cultured with macrophage cells, the intensities of Cr and O recovered. Cells were activated by supplementing the medium with 0.05  $\mu\text{g ml}^{-1}$  interferon- $\gamma$  and 5  $\mu\text{g ml}^{-1}$  lipopolysaccharide. This stimulation of cells to release NO and other RCS induced further increase in peak intensities. Cell attachment may have limited protein deposition on the surface, and thus the oxides were revealed after cell removal. It was postulated that the RCS ( $\text{H}_2\text{O}_2$ ,  $\text{O}_2^-$ , and NO) released by activated cells influenced a further oxidation of the alloy surface. Perhaps oxygen formed by reduction of  $\text{H}_2\text{O}_2$  further reacted with metal, or  $\text{H}_2\text{O}_2$  participated in

the formation of hydroxyl radicals in the presence of metal or metal ions, thus promoting oxidation.

These data demonstrate that the surface oxide composition varied with *in vitro* environments. Changes in the composition of the alloy surface over time by cells are important for the understanding of host–material interactions and the release of corrosion products. Further evidence on the action of biomolecules is presented by Lewis et al. [73, 110]. CoCrMo pellets were immersed in human serum, fetal bovine serum (FBS), synovial fluid, and water for 5 days, and the composition of the surface film was studied by time-of-flight–secondary ion mass spectrometry (TOF-SIMS) technique. The composition and thickness of the layers formed differed considerably between different solutions. Serum produced a mixed composition of  $\text{Cr}_2\text{O}_3 \cdot x\text{H}_2\text{O}$ ,  $\text{Co}(\text{OH})_2 \cdot x\text{H}_2\text{O}$ ,  $\text{Cr}(\text{OH})_3 \cdot x\text{H}_2\text{O}$ ,  $\text{CrPO}_4 \cdot x\text{H}_2\text{O}$ , and  $\text{Co}_3(\text{PO})_4 \cdot x\text{H}_2\text{O}$  within a thick deposit of calcium phosphate. The thickness of both oxide/hydroxide (25 nm) and calcium phosphate layers was the thickest (30 nm) in this solution. Compared to human serum, chromium phosphate and a second layer of cobalt hydroxide were absent in the FBS. The thickness of both oxide and phosphate layers were smaller than in serum (10 and 20 nm, respectively). The synovial fluid sample had a thin layer (1.5 nm) of  $\text{Cr}_2\text{O}_3 \cdot x\text{H}_2\text{O}$  and an insignificant deposit of calcium phosphate, whereas the water sample had a passive layer (3–3.5 nm) of  $\text{Cr}(\text{OH})_3 \cdot x\text{H}_2\text{O}$  at the surface and  $\text{Cr}_2\text{O}_3 \cdot x\text{H}_2\text{O}$  as the inner layer. Deposits of calcium phosphate on the sample surface immersed in serum contained Co and Cr ions. It seems that Co and Cr migrated from the bulk metal surface and were trapped in serum deposits. Chromium existed as oxide, hydroxide, and phosphate, whereas the cobalt was present predominantly as phosphate and hydroxide: this may account for the composition of wear debris from CoCr implants, which are predominantly hydroxy-phosphate compounds [74]. In synovial fluid, insignificant deposits of calcium phosphate were formed, which was ascribed to the possible action of proteoglycans, pyrophosphates, phospholipids, lubricin, and superficial zone protein (SZP). Circulation of these compounds around the implant may inhibit calcium phosphate deposition and therefore contribute to osteolysis.

The composition of the medium affected metal dissolution [73, 110]. Protein increased the dissolution of Cr and decreased the dissolution of Co; i.e., the samples immersed in synovial fluid had the highest Cr and the lowest Co concentrations [73]. The fact that proteins have greater affinity for Cr than for Co explains why dissolved Cr is higher

in synovial fluid than in PBS and water. Effective complexing of metal cations with proteins leads to a thinning of the oxide layer, similar to the mechanism presented in Sect. 1.5.

## 1.7 Tribocorrosion

Tribocorrosion can be defined as an irreversible transformation of a material resulting from simultaneous physicochemical and mechanical surface interactions occurring in a tribological contact [111]. During tribocorrosion the material is thus subjected to friction, lubrication, wear, and corrosion. Orthopedic implants are typical examples of such systems. Materials degradation from simultaneous chemical and mechanical effects may occur under a variety of conditions (1) sliding (two- and three body), leading to corrosive wear, wear-accelerated corrosion, and chemomechanical polishing; (2) fretting (two- and three body), leading to fretting corrosion; (3) rolling in ball bearings, causing corrosive wear; and (4) impingement, causing erosion corrosion and impingement attack. Fretting is a special type of tribological contact involving a reciprocating motion of small amplitude (a few micrometers) and is highly relevant for orthopedic applications involving sliding joints [112].

Electrochemical behavior of CoCrMo alloy in the active state in acidic and alkaline buffered solutions was studied before, during, and after mechanical disruption of the passive film [113]. The measurements were performed in a tribo-electrochemical microcell consisting of a microcapillary filled with the electrolyte solution and containing a rotating ceramic tube that rubs the electrode surface. At acidic pH cobalt and chromium oxidize, giving the bivalent aqueous ions Co(II) and Cr(II) as primary oxidation products, while the cathodic partial reaction is the hydrogen evolution reaction. At alkaline pH, cobalt and chromium originate the oxide species CoO and CrO whereas the oxygen electronation reaction supplies the oxidation current. The repassivation rate at neutral pH is lower than at pH 4.0, because the coprecipitation of cobalt oxide species hinders the formation of the  $\text{Cr}_2\text{O}_3$ .

There has been much debate to identify whether high carbon (HC) or low carbon (LC) content CoCrMo alloy was more appropriate for metal-on-metal bearings of artificial hip implants. The main difference between the two alloys is the presence of chromium carbides in

the HC alloy that increase hardness but may affect the corrosion stability by depleting the metal matrix in chromium [114]. The relevant literature has been reviewed recently [115]. The literature results were not straightforward and indicate that the role of carbides is complex and depends on the prevailing wear mechanism (abrasion, fatigue) on their wear resistance and cohesion to the matrix.

In tribocorrosion it is common to distinguish two contributions to material removal: mechanical wear and wear-accelerated corrosion [116]. The former mechanism corresponds to the release of metal particles by abrasion action of the alumina ball. The latter results from the removal of the passive film and subsequent enhanced metal oxidation. The total wear corresponds to the sum of the wear-accelerated volume,  $V_{\text{mech}}$ , and the metal volume lost by wear-accelerated corrosion,  $V_{\text{chem}}$ , according to

$$V_{\text{tot}} = V_{\text{chem}} + V_{\text{mech}} \quad (1.16)$$

The  $V_{\text{chem}}$  can be calculated from the wear track current  $I_{\text{sliding}}$  using Faraday's law:

$$V_{\text{chem}} = \frac{I_{\text{sliding}} t M}{n F \rho} \quad (1.17)$$

where  $M$  is the atomic mass,  $n$  is the charge number for the oxidation reaction (2.36),  $F$  is the Faraday constant,  $\rho$  is the density of the alloy ( $7.44 \text{ g cm}^{-3}$ ), and  $t$  is the duration of the sliding. Tribocorrosion behavior of low- and high-carbon CoCrMo alloys sliding against an alumina ball was measured in four different simulated body fluids [NaCl, and saline phosphate buffer (SPBS) with and without albumin] [115]. The total wear was determined using a noncontact laser scanning profilometer;  $V_{\text{mech}}$  was calculated as a difference between the wear volume and the chemical volume. The total wear volumes and chemical and mechanical wear volumes are compared in Fig. 1.18. Wear ranking depends significantly on the test electrolyte: the HC alloy wears more than the LC in the NaCl and in the SPBS+albumin solutions, whereas no significant differences are observed in other electrolytes. When differences appear between alloys, this is mainly caused by a difference in mechanical wear (Fig. 1.18c), which is more pronounced in the HC alloy. Thus, in NaCl and NaCl+albumin the dissolution rate seems to be mainly controlled by the alloy composition. As in the HC alloy, a significant part of Cr is bound in  $\text{Cr}_{21}\text{Mo}_2\text{C}_6$  carbides, and the Cr-depleted matrix is more prone to corrosion.

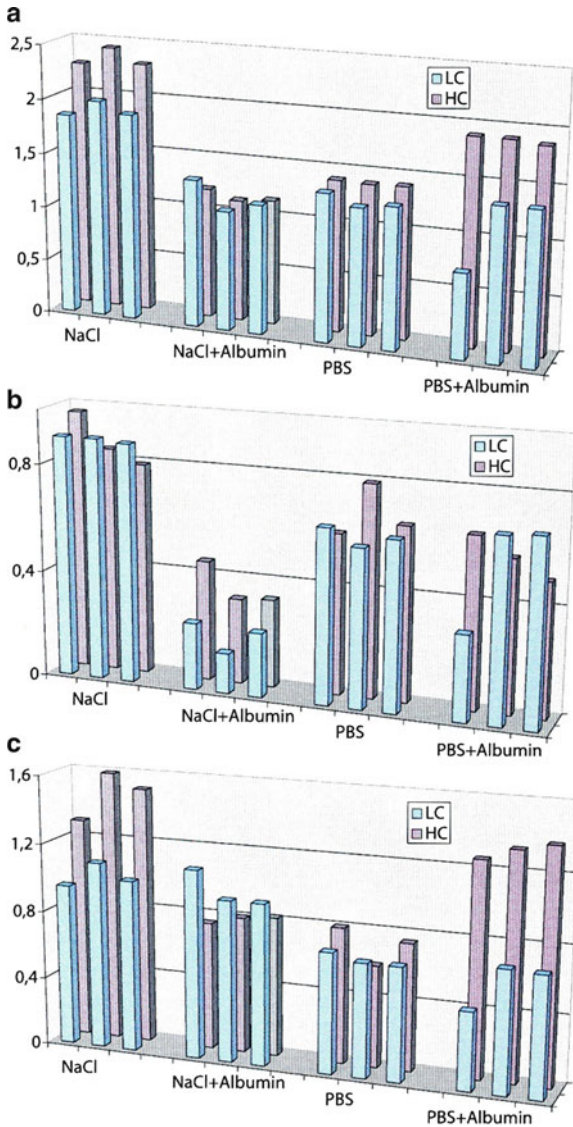


**Fig. 1.18** Total wear volume (a), chemical wear volume (b), and mechanical wear volume (c) of low-carbon (LC) and high-carbon (HC) CoCrMo alloys in simulated body fluids. Normal load is 1.2 N; applied potential is  $-0.1 V_{SCE}$  (Reprinted from A. Igual Muñoz and S. Mischler, *J. Mater. Sci. Mater. Med.* 22 (2011) 437, with permission from Springer [115])

Moreover, hard carbides released as loose debris particles inside the contact provoke abrasion. In phosphate-containing solution, the role of solution chemistry becomes more pronounced, which could be related to the enhancement of corrosion by sliding, as well as to surface chemical effects affecting third-body wear. It seems that the presence of albumin limits the adsorption of inhibitive phosphate ions and consequently increased significantly corrosion of both alloys in SPBS.

Besides solution chemistry, the tribocorrosion rate of CoCrMo alloy varied with the applied potential [117]. Under cathodic conditions wear was negligible, whereas it critically increased under passive conditions and increased with increasing potential. Cyclic mechanical removal of the passive film followed by its repassivation contributes to its higher damage. Figure 1.19 shows typical optical images of the wear tracks in 0.14 M NaCl and bovine solution (BS). At the cathodic potential of  $-1.0$  V (Ag/AgCl), the wear track is generally smooth because the wear proceeds mainly through mechanical removal of particles. At  $-0.5$  V some scratches were observable in the wear track. At more anodic potentials, grain boundary dissolution was noticed in NaCl solution and only above  $0.75$  V in BS. At potentials within the passive region ( $0.05$  and  $0.5$  V), the values of  $V_{\text{tot}}$  were higher in BS than in NaCl solution, the consequence of higher values of  $V_{\text{mech}}$  in BS solution. The amount of wear debris increased with increasing potential, and the amount of particles was always higher outside the track in NaCl solution, whereas in BS, i.e., in the presence of proteins, wear particles were mainly entrapped in the scratches. Therefore, the wear pattern is affected by the solution chemistry. It was suggested that the incorporation of proteins into the passive layer possibly modifies the surface charge and the repulsion forces acting between particles. In NaCl, the repassivation was sufficiently fast to allow them to form a disperse and small third body. Wear particles thus formed were less compacted. In protein-containing solution, metallic particles formed by mechanical wear can agglomerate, and larger particles abrade the surface, producing greater damage [118]. It is likely that the release of  $\text{Co}^{2+}$  ions leads to enhanced binding of proteins under sliding, and charge transfer at the metal–solution interface is reduced by the formation of corrosion products, i.e.,  $\text{Co}_3(\text{PO}_4)_2 \cdot 2\text{H}_2\text{O}$  or an organometallic complex [117, 118].

Under tribological contact the contact zone became more active than the rest of surface and increases the corrosion rate; corrosion rates 20–60 times higher were observed under sliding than under static

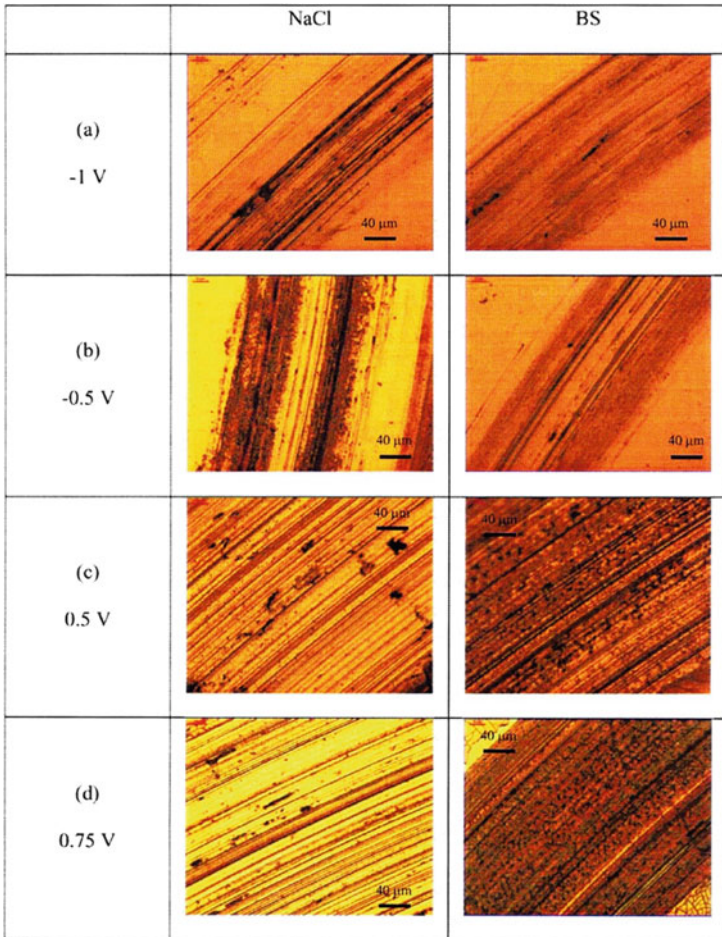


**Fig. 1.19** Optical images of the wear tracks of CoCrMo alloy in NaCl and BS at different applied potentials:  $-1 \text{ V}_{\text{Ag}/\text{AgCl}}$  (a),  $-0.5 \text{ V}_{\text{Ag}/\text{AgCl}}$  (b),  $0.5 \text{ V}_{\text{Ag}/\text{AgCl}}$  (c), and  $0.75 \text{ V}_{\text{Ag}/\text{AgCl}}$  (d). Normal load 5 N, pH 7.4, and  $37^\circ\text{C}$  (Reprinted from A. Igual Muñoz and L. Casabán Julian, *Electrochim. Acta* 55 (2010) 5428, with permission from Elsevier [117])

conditions [119]. The active zone is constantly rubbed by mechanical forces, thus repeatedly removing the protective passive film or semi-protective adsorbed film and promoting charge transfer. Combined effect of wear and corrosion on low- and high-carbon CoCrMo alloy

in various simulated physiological media (0.3% NaCl, 50% bovine serum, and DMEM) was studied in a tribo-electrochemical cell under sliding contact conditions [120, 121]. A silicon nitride ball was used as a counterface material at a normal load of 80 N. Under static conditions, the composition of the medium strongly affects the susceptibility of the CoCrMo alloy toward corrosion: the breakdown potential is most positive in saline solution, shifts to more negative values in DMEM (containing amino acids), and is the most negative for bovine serum. It is postulated that the increased binding of proteins and amino acids to chromium, and especially cobalt, is responsible for a premature loss of passivity. Under sliding conditions, the corrosion-related damage, primarily the effect of corrosion of wear, represented a significant part of the overall tribocorrosion process, which was dependent on the composition of the solution. Corrosion accounted for between 22% and 47% of the total volume loss, the remainder being attributed to mechanical wear. For both alloys, high- and low-carbon, the corrosion-related damage was the smallest in saline, higher in serum, and the highest in DMEM conditions [120, 121].

The nature of the film formed during tribocorrosion in different media was investigated by XPS and contact angle measurements [119, 121]. A protein adsorption layer 3–4 nm thick was formed in the wear scars for high-carbon CoCrMo alloy. The underlying oxide layer was mainly composed of  $\text{Cr}_2\text{O}_3$ . Sulfur was detected in the low-carbon alloy, which was attributed to the possible formation of  $\text{CoS}_2$  [121].  $\text{CoS}_2$  is similar to  $\text{MoS}_2$  which, because of its weak interlamellar bonds, reduces friction. The formation of the adsorbed protein layer was found to affect the wettability of the surface. After polishing, the contact angle of high- and low-carbon alloys was greater than  $90^\circ$  ( $94^\circ$  and  $98^\circ$ , respectively). The contact angle dropped rapidly immediately after the surface was immersed in serum solution, and after 1 h had reached almost a constant value between  $20^\circ$  and  $30^\circ$ . It seems that the formation of thick films of proteins with metal ions can efficiently reduce the friction of the surface and lubricate the contact zone.

On the other hand, proteins bind to metal ions, which likely increased the corrosion rate [119]. Even though proteins and adsorbed protein layers can lubricate material surfaces, the total degradation was enhanced by the increased corrosion process. The presence of proteins increased the total specific wear rate under abrasion-corrosion test conditions [122]. A microabrasion tester was designed so that the working electrode made of cast CoCrMo alloy was loaded against the roughened zirconia ball surface to improve particle entrainment and

test repeatability. The wear-enhanced corrosion process was deduced from the electrochemical current noise measurements. Tests were conducted in 0.9% NaCl, phosphate-buffered saline solution (PBSS), and 25% and 50% bovine serum solution with either 0 or  $1 \text{ g cm}^{-3}$  SiC for “sliding-corrosion” (SC) and “abrasion-corrosion” (AC) tests. The former condition without externally introduced abrasives is closer to the scenario of two-body metal-on-metal articulation in a hip bearing in the steady state, whereas the AC condition represents an extreme condition where a high volume of third-body abrasive particles (e.g., fractured carbides, bone cements, metal debris, etc.) are produced during the running-in period of the implant [123]. The corrosion rate deduced from potentiodynamic polarization curves measured under static condition was higher in bovine solution than in inorganic solutions, which was attributed to the formation of metal–protein complexes that can be effectively transported away under static conditions (see Fig. 1.13). Conversely, electrochemical noise measurements under abrasion conditions indicated that average anodic current levels were appreciably lower (1.3–3 times) for the proteinaceous solutions when compared with the inorganic solutions. In this case the proteins can become completely denatured in the tribological contact, which could result in the formation of a lubrication layer that reduces the friction of the tribological contact. Three-body abrasive wear gave significantly higher wear rates compared to two-body sliding wear. Total wear constitutes material loss from pure mechanical wear ( $W_o$ ), material loss from corrosion-enhanced wear under AC conditions ( $W_c$ ), and material loss from wear-enhanced corrosion under AC conditions ( $C_w$ ). For the abrasion-corrosion condition, pure mechanical wear ( $W_o$ ) was a major cause of the material loss in all four solutions (Fig. 1.20). The presence of proteins increased corrosion-enhanced wear ( $W_c$ ). It seems that proteins enhance wear both chemically and mechanically, i.e., influencing the surface mechanical properties and forming an adhesive layer enhancing the particle entrapment.

A severely deformed nanocrystalline layer was identified immediately below the worn surface for both solutions [122]. The layer was formed by a recrystallization process or strain-induced phase transformation that occurs during microabrasion. In the former scenario, repetitive formation and breaking of asperities junctions results in surface damage and wear debris formation. These particles or unbroken junctions can be further deformed and incorporated into the CoCrMo surface. The distinct subsurface structure containing a mechanically mixed nanocrystalline layer could be a mixture of the

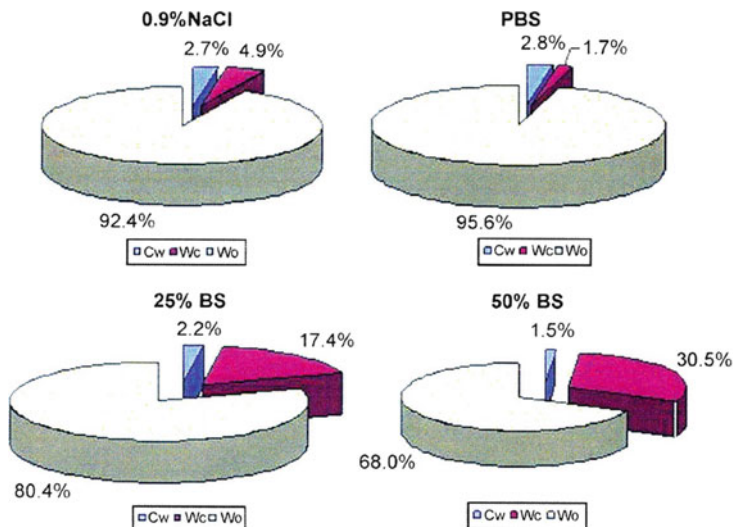


**Fig. 1.20** Percentage of volume loss for CoCrMo in four test solutions:  $C_w$ , material loss from wear-enhanced corrosion;  $W_c$ , material loss from corrosion-enhanced wear; and  $W_o$ , material loss from pure mechanical conditions (Reprinted from D. Sun, J.A. Wharton, R.J.K. Wood, L. Ma, and W.M. Rainforth, *Tribology International* 42 (2009) 99, with permission from Elsevier [122])

substrate metal, oxide layers, and possibly surrounding biological species (e.g., denatured proteins) [124].

Such a layer was found at the surface of a retrieved hip joint [125, 126]. It was suggested that this layer may reduce the effect of three-body abrasion by increasing the resistance against surface fatigue. This layer also helps to explain the origin of the nanometer-sized metallic debris. Two types of nanometer-sized debris originating from the femoral head and the acetabular inlay of the metal-on-metal prostheses were identified: Cr-based and CoCr-based particles [126]. An example is given for CoCr-based, needle-shaped particles 40–80 nm in length, seen as black elongated particles in Fig. 1.21. Co and Cr were identified from the EDS spectrum as alloying elements, together with oxygen, calcium, phosphorus, and other elements originating from the tissue or solution during digestion.

Another possible process that may occur within the nanocrystalline layer is strain-induced phase transformation (SIT) [124]. The severely deformed alloy surface has been subjected to high strain levels and

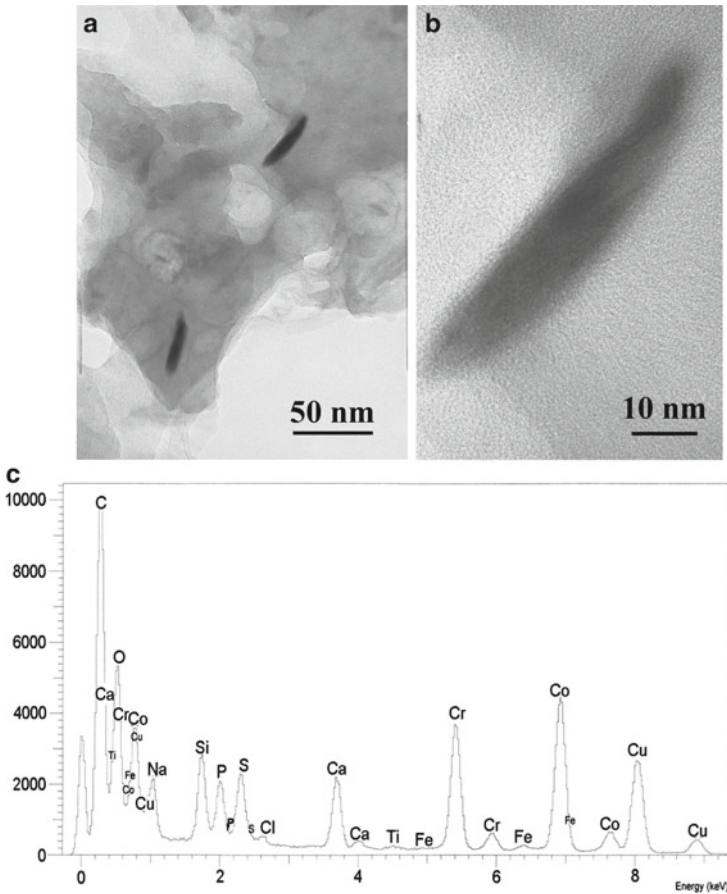


**Fig. 1.21** High-resolution transmission electron microscopy (TEM) images (a, b) and EDS spectrum (c) of CoCr-based particles isolated from periprosthetic tissue of hip prostheses with metal-on-metal bearing using the papain digestion procedure. (a)  $\times 200,000$ ; (b)  $\times 1,000,000$

could transform from the meta-stable face-centered cubic (FCC) structure into a hexagonal close-packed (HCP) phase [124, 127]. SIT has been described as a local phenomenon of nucleation and growth surrounding the stacking fault. In this case, the stress concentration near the defects could have exceeded the yield strength of the CoCrMo ( $\sim 500$  MPa) and significantly increased the driving force for the structural change [128–130].

## 1.8 Corrosion Processes In Vivo: Galvanic, Crevice, and Fretting Corrosion

Early retrieval studies already showed that a certain number of implants exhibited damage caused by corrosion. In the 1950s, various retrieved metal components were examined [131]. Corrosion was detected only on ferrous-based components. In some cases the corrosion was stated as the reason for removal resulting from pain, inflammation, and swelling. The most common site for corrosion was the junction between components. In another study the authors examined implants made of stainless steel, CoCrMo, or Ti [132]. With stainless steel, there was obvious corrosion. With the CoCrMo alloy, component fretting with some corrosion occurred at the interfaces. With stainless steel and CoCrMo alloys, the corrosion was probably preceded by fretting or mechanical erosion of surfaces. With Ti components, mechanical erosion or fretting was seen.

Because of the stable passivity of the alloys used, it has also been argued that galvanic corrosion poses no risk in a biomedical device [27]. Gruen and Amstutz published the first histopathological and metallurgical description of a failed hip prosthesis consisting of dissimilar metals: a vitallium acetabular cup and a stainless steel femoral head (so-called metal-on-metal combination) [133]. The reason for removal was ascribed to severe abrasive wear and fretting corrosion. This combination should not be used as a bearing in the body.

Since then, the quality of material and design has significantly changed. Retrieval studies reviewed recently confirmed that the CoCrMo alloy may be subjected to various types of localized corrosion *in vivo*, e.g., galvanic corrosion from the contact of two metals, fretting corrosion caused by the micromotions of the metal components, and crevice corrosion from occluded areas in certain parts of the implant components [10, 112].

Galvanic corrosion occurs when dissimilar metals are in direct electrical contact in corrosive solutions or atmospheres [112]. Enhanced corrosion of the less noble metal takes place, whereas the corrosion rate of the more noble metal is reduced or even completely suppressed. However, once the metal or alloy is covered by a protective passive layer, the corrosion potential is typically that of a more noble metal than that of the bare metal surface. Therefore, judging solely by the standard potential values, one would overestimate the danger of galvanic corrosion. Because passive films act as very

efficient barriers to corrosion, the danger of galvanic corrosion is lower for passive materials than for the coupling of actively corroding metals. Relative movement between the implant and the tissue, for example, at a bearing surface or on a cyclically loaded implant, will cause mixing at the interface, will modify the composition of the electrolyte, and, consequently, may modify the surface of the alloy [6]. Charge imbalance thus created will result in sustained corrosion.

Surgical steel should not be used in contact with cobalt-based implants, because the relatively poor corrosion resistance of steel can lead to rapid galvanic corrosion if the stainless steel suffers pitting corrosion. However, if the conditions are not aggressive enough to trigger pitting or crevice corrosion of the stainless steel, and both materials remain in the stable passive state, coupling of the two materials will not lead to any significant change of the corrosion behavior of the materials; i.e., there was no appreciable risk for a crevice corrosion caused or amplified by galvanic coupling [134]. This situation was confirmed for spinal implants where galvanic corrosion between a titanium alloy and stainless steel was insignificant [135].

Although generally the combination with ferrous alloys should be avoided, the combination between titanium and cobalt alloys was predicted to be safe [20]. However, this prediction turned out to be not completely valid *in vivo*. The processes of localized corrosion became more and more important as from the mid-1980s an increasing number of modular components were introduced into total joint replacements. It appeared that the solution of the Co alloy head on a Ti stem was satisfactory for both press-fit and biological in-growth applications [136]. The Ti alloy stem provided reduced stiffness when compared with identical stems of Co alloy, and the tougher Co alloy femoral head provided improved wear resistance against the polyethylene. Moreover, variable neck lengths through separate heads and stems could be mated at the time of surgery. Under the conditions of modularity, the processes of localized corrosion become more pronounced as several processes can be operative simultaneously: crevice, galvanic, and fretting corrosion.

In 1992 was reported that 17 of 30 retrieved modular prostheses presented evidence of corrosion along the matching tapers [137]. No specimen was corroded unless it has been less than 9 months in the body, but all that had been in place for more than 40 months were damaged. The authors ascribed the damage to galvanically accelerated

corrosion rather than to fretting. The corrosion was in the form of deep pits and was observed only in mixed-metal prostheses. In other studies, however, similar damage as in mixed alloys was observed between similar alloys although in lower percentage [138–141]. In mixed-metal combinations (Ti6Al4V/CoCrMo), 16% of necks and 35% of heads showed corrosion damage, whereas in similar metal combinations (CoCrMo/CoCrMo) the corrosion damage was observed in 14% of necks and 23% of heads [138]. Corrosion and fretting scores tend to be higher for heads than for necks [140].

Some authors observed a correlation between the degree of prostheses with moderate to severe corrosion and the duration of implantation [138, 140], while others found no correlation [141, 142]. The majority of cases were graded as mild (superficial scratches, burnishing, or localized pitting) and moderate (larger region of superficial pitting or significant abrasion or galling covering less than 25% of the interface). Bobyn et al. pointed out that all head–neck junctions in retrieved modular prostheses showed some evidence of surface modifications or fretting wear, but mainly class A (none or negligible) or class B (mild burnishing) were observed [142]. Corrosion at the head–neck junction was observed in only 1 of 17 retrieved prostheses, which supports the conclusion that galvanic-induced corrosion is not an inevitable consequence of mixed-metal taper but that probably other factors influence chemical stability, i.e., crevice corrosion conditions and fretting. Corrosion was more common in stems in which there was no bone ingrowth histologically [141]. Modularity may provoke corrosion damage even when combining the same materials but of different metallurgical conditions [140].

The corrosion process *in vivo* thus may occur as a result of mechanical–electrochemical interactions in the taper crevice [138]. Oxide film fracture caused by mechanical fretting and the restricted crevice environment of the taper induced the changes in the solution chemistry of the fluid inside the taper, including pH drop and increase in chloride concentration. On the other hand, mechanical loading is not a prerequisite for some level of crevice corrosion to occur in these tapers because fluid ingress into the taper crevice alone significantly alters the crevice solution chemistry. However, these changes are inadequate by themselves to autocatalyze the crevice corrosion process. Taper fretting crevice corrosion is induced when the modular taper is loaded at physiological level. Fretting corrosion is most likely present in tapers, which results in oxide fracture and the repassivation

process, which hydrolyzes water to form metal oxide and hydrogen ions. With lower pH and increased chloride concentration, repassivation time constants increase, slowing the oxide reformation rate, and lower potentials. Under these conditions the oxide film becomes thinner and less capable of resisting corrosion attack. Consequently, large-scale etching and other localized corrosion features are seen in retrieved prostheses [138, 141, 143–145]: these features included pitting corrosion and fretting [144], interdendritic and intergranular attack [138], and intergranular corrosion-fatigue failure [145]. The latter failure was noted in two cases retrieved for fracture in the neck region of the stem. The fractures occurred at the grain boundaries and appeared to be the result of three factors:

1. Porosity at the grain boundaries
2. Intergranular corrosive attack, initiated both at the head–neck taper and at the free surface
3. Any cyclic fatigue-loading of the stem

It seems that the intergranular porosity, which may have weakened the prosthesis, provided a pathway for intergranular attack.

Fretting corrosion can be reduced by design changes that increase the stability of the interface [142, 146]. A correlation existed between corrosion and length of neck extensions [146]. Longer head neck extensions may be more susceptible to fretting corrosion because of an instability at the interface. Short-term mixed-metal corrosion studies demonstrated that the coupling of Co and Ti alloys did not render the interface more susceptible to corrosion. On the other hand, a larger-diameter neck will increase neck stiffness and may reduce fretting and subsequent corrosion of the taper interface [138]. These benefits must be balanced with the resulting decreased range of motion and joint instability associated with larger taper diameters. Furthermore, giving the close relationship between tolerances and fretting, the machining tolerances should be set very low to minimize the possibility of mechanical failure and adverse biological response induced by the increased generation of wear debris particles [142].

In vitro cyclic loading fretting tests on a prototype of a cementless, modular neck prosthesis confirmed that some fretting microdamage on the tapered surface was produced under all test conditions analyzed [147]. The amount of abraded material increased almost linearly with the applied load magnitude but not with the number of load cycles. Weight loss ranged from  $0.28 \pm 0.10$  mg for small stem bodies

loaded 5.5 million times up to 2,300 N to  $2.54 \pm 0.53$  mg for large stem bodies loaded 20 million times up to 3,300 N. It was calculated that a modular neck tapered joint would produce on average 0.6 mg per year of metal debris. The authors suggested that this amount should not have any significant effect clinically because a normal and stable prosthesis is likely to produce less than 10 mg per year of metal debris.

Large amounts of corrosion products being formed and particulate accumulation could result in loss of mechanical integrity of the implants *in vivo*, create particles for third-body wear, and release particles and metal ions into the surrounding tissue [138, 148]. The products of corrosion identified at the modular junctions of various prostheses examined were similar regardless of the implant design or the materials coupled (CoCrMo/CoCrMo,  $\text{Al}_2\text{O}_3$ /CoCrMo, CoCrMo/Ti6Al4V) [149, 150]. Two distinct varieties of corrosion products were found: one was a highly crystalline interfacial layer of mixed oxides and chloride intimately associated with the site of corrosion within the crevice formed by the mated head and neck, and the other was an amorphous chromium orthophosphate hydrate-rich material deposit just outside the crevice, apparently as a precipitate of chromium with phosphorus from the fluids of the joint cavity. Particles of corrosion product from the crevice were found only rarely in the surrounding tissues, but abundant, fine particulate debris of the chromium orthophosphate was observed in most of the periprosthetic tissues examined as a result of its ready access to the joint cavity. Migration of particulate chromium phosphate particles to sites remote from their origin was also demonstrated [150].

Abundant black corrosion product was observed at the head-neck junction between a femoral neck made of Ti-6Nb-7Al alloy and a femoral head made of Co-28Cr-6Mo alloy (Fig. 1.22), consisting of Cr- and Ti-oxides and chlorides. It was reported recently that there may be a connection between the simultaneous presence of corrosion products and hypersensitivity-associated tissue reaction [151]. The corrosion product consisted of green- to yellow-colored particles in fibrotic capsular tissue containing Cr, P, and O peaks, which is consistent with the formation of chromium orthophosphate observed by other authors [126, 150]. None of the investigated deposits revealed the presence of cobalt. Tissue reactions of various intensity characteristic of immune response were observed in all cases [151].

Because of all these potential problems described, the use of modular systems should be judicious in primary hip arthroplasty [152].

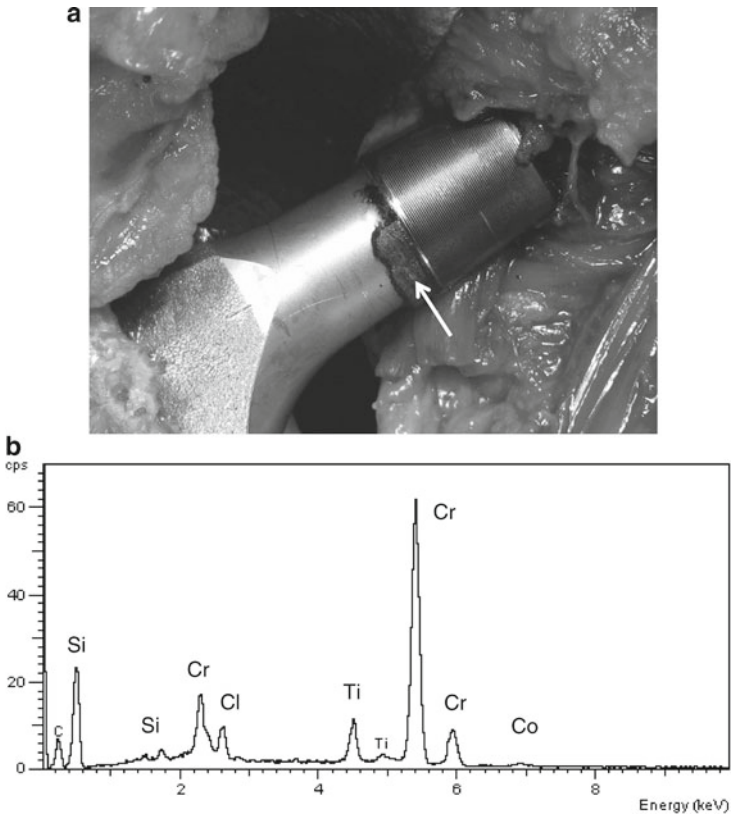


**Fig. 1.22** (a) Crevice, fretting, and possibly galvanic corrosion between a femoral neck made of Ti-6Nb-7Al alloy and a femoral head made of Co-28Cr-6Mo alloy. Corrosion product is denoted by the *arrow*. The prosthesis was revised because of aseptic loosening after 13 years in situ. (Reprinted from I. Milošev, *Pure Appl. Chem.* 83 (2011) 309, with permission from IUPAC [10]). (b) EDS spectrum of the corrosion product deposit denoted by *arrow*

Modularity beyond the head and neck junction should be reserved for those cases where a comparable monolithic implant would not suffice. Alternatives to the conventional mating of dissimilar metals at the head-neck junction would be to use a Ti alloy sleeve press-fit into a CoCr head, which appears to eliminate fluid intrusion and galvanic corrosion at the critical interface between dissimilar metals [153]. In such an arrangement, almost no signs of corrosion were

detected. Other alternatives to modular systems would be to use a hardened Ti head or ceramic head on a Ti alloy stem [153]. No evidence of corrosion was noted in the group consisting of Co alloy head and stem and in the group consisting of Co alloy head and a Ti stem coupled via a shrink fit [154].

In addition to classical modular hip design comprising a stem with a proximal taper and modular head, recently there is an increasing number of double-taper designs including double-taper proximal neck and modular head [155]. The clinical advantages of such a design include intraoperative adjustment of leg length via the neck–head taper and femoral anteversion via the neck–stem taper. The retrieval study demonstrated that even in modern taper designs modularity can lead to fretting and crevice corrosion. Metal ion generation and particulate debris may contribute to periprosthetic osteolysis and loosening. The authors also reported boundary corrosion and intergranular/transgranular corrosion ascribed to the chromium carbide phase.

In addition to modular prostheses, corrosion damage was observed in other systems, e.g., in cemented prostheses. Willert et al. described the mechanism of crevice corrosion of a cemented Ti–6Al–4V alloy stem and recommended that Ti alloys can be no longer recommended for cementation but only for cementless applications [156]. The authors proposed that the process proceeds in four steps: partial debonding of cement and metal stem, initiation of crevice corrosion, further propagation of crevice corrosion and debonding, and termination and recurrence of crevice corrosion-induced pain caused by diffusion of acid. This hypothesis is thought to be valid for stems that remain firmly fixed distally while debonding and abrasion occur proximally. The degradation of CoCrMo cemented hip implants after implantation in sheep was investigated [157]. Auger depth profiles confirmed the presence of a Cr-rich oxide, which was thinner on the retrieved prostheses than on virgin surface. The ratio of chemical elements at the metal surface was not significantly changed, but the ratio in the surrounding tissue showed preferential dissolution of cobalt. Although a clear correlation was observed between the clinical evaluation of the implant stability or fixation and the metal concentrations in the interface tissue, no such correlation was observed for the concentrations in the joint capsule membrane. It was suggested that the mode and degree of mass transport might depend on the presence of cracks and defects in the cement mantle as well as on the local physiological conditions [157].

## 1.9 Conclusions

In this chapter, some aspects of the processes occurring at the surface of CoCrMo alloy exposed to simulated physiological conditions in *in vitro* measurements and *in vivo* as identified on retrieved metal components were described. The behavior is rather complex, and even minor changes in the composition of the alloy, composition of the medium, physicochemical conditions, load and motion of the components, etc., may lead to significant changes in the composition, structure, and thickness of the surface layer. Related studies were reviewed herein, starting from the early days of use of CoCrMo as an orthopedic alloy to the present. In the past, emphasis has been given to corrosion stability in saline medium. It is now clear that the interactions of the alloy surface with various biomolecules *in vitro*, as well as the conditions of load, motion, and design of the prosthesis, are crucial for its long-term performance *in vivo*. For in-depth understanding, these processes should be studied further. Both *in vitro* experiments as well as studies of retrieved components being exposed to the *in vivo* environment are equally important. Furthermore, the biological impact of metal ions, which is not reviewed herein, should also be carefully examined for the safe use of metal components *in vivo*.

**Acknowledgments** The valuable technical assistance of Mr. Gregor Žerjav is gratefully acknowledged. High-resolution TEM experiments on CoCr-based particles were carried out by Dr. Maja Remškar. The author thanks the orthopedic surgeons at the Valdoltra Orthopedic Hospital for collaboration on retrieval studies. The financial support by the Slovene Research Agency is greatly appreciated (grants No. P2-0148 and J1-2243).

## References

1. Williams DF (1981) The properties and clinical use of cobalt-chromium alloy. In: Williams DF (ed) *Biocompatibility of clinical implant materials*, vol I. CRC Press, Boca Raton, FL, p 99
2. International standard ISO 5832-4-1996, 2nd edn. *Implants for surgery – Metallic materials – Part 4: Cobalt-chromium-molybdenum casting alloy*
3. International standard ISO 5832-12-2007, 2nd edn. *Implants for surgery – Metallic materials – Part 12: Wrought cobalt-chromium-molybdenum alloy*
4. International standard ISO 5832-5-2005, 3rd edn. *Implants for surgery – Metallic materials – Part 5: Wrought cobalt-tungsten-nickel alloy*

5. International standard ISO 5832-6-1997, 2nd edn. Implants for surgery – Metallic materials – Part 6: Wrought cobalt-nickel-chromium-molybdenum alloy
6. Hallab NJ, Jacobs JJ, Katz JL (2004) Orthopedic applications. In: Ratner BD, Hoffman AS, Schoen FJ, Lemons JE (eds) *Biomaterials science: an introduction to materials in medicine*. Elsevier, London, p 526
7. Brunski JB (2004) Metals. In: Ratner BD, Hoffman AS, Schoen FJ, Lemons JE (eds) *Biomaterials science: an introduction to materials in medicine*. Elsevier, London, p 137
8. Ring PA (1971) *J Bone Joint Surg Br* 53B:344
9. Charnley J (1971) *J Bone Joint Surg Br* 53B:342
10. Milošev I (2011) *Pure Appl Chem* 83:309
11. Hoar TP, Mears DC (1966) *Proc R Soc London* 294:486
12. Hanks JH, Wallace RE (1949) *Proc Soc Exp Biol Med* 71:196
13. Kuhn AT (1981) *Biomaterials* 2:68
14. Espevik S (1978) *Acta Odontol Scand* 36:113
15. Mueller HJ, Greener EH (1970) *J Biomed Mater Res* 4:29
16. Cahoon JR, Hill LD (1978) *J Biomed Mater Res* 12:805
17. Galante J, Rostoker W (1972) *Clin Orthop* 86:237
18. Rostoker W, Galante JO, Lereim P (1978) *J Biomed Mater Res* 12:823
19. Lucas LC, Buchanan RA, Lemons JE (1981) *J Biomed Mater Res* 15:731
20. Kummer FJ, Rose RM (1983) *J Bone Joint Surg Am* 165-A:1125
21. Griffin CD, Buchanan RA, Lemons JE (1983) *J Biomed Mater Res* 17:489
22. Thompson NG, Buchanan RA, Lemons JE (1979) *J Biomed Mater Res* 13:35
23. Lucas LC, Buchanan RA, Lemons JE, Griffin CD (1982) *J Biomed Mater Res* 16:799
24. Syrett BC, Wing SS (1978) *Corrosion* 34:379
25. Cohen J (1962) *J Bone Joint Surg* 44-A:307
26. Süry P (1977) *Corrosion Sci* 17:155
27. Mears DC (1975) *J Biomed Mater Res* 9:133
28. Igual Muñoz A, Mischler S (2007) *J Electrochem Soc* 154:C562
29. Hodgson AWE, Kurz S, Virtanen S, Fervel V, Olsson C-OA, Mischler S (2004) *Electrochim Acta* 49:2167
30. Metikoš-Huković M, Babić R (2007) *Corros Sci* 49:3570
31. Kocijan A, Milošev I, Merl DK, Pihlar B (2004) *J Appl Electrochem* 34:517
32. Metikoš-Huković M, Babić R, Omanović D, Milošev I (2007) *ECS Trans* 2:43
33. Milošev I, Strehblow HH (2003) *Electrochim Acta* 48:2767
34. Metikoš-Huković M, Pilić Z, Babić R, Omanović D (2006) *Acta Biomater* 2:693
35. Kocijan A, Milošev I, Pihlar B (2003) *J Mater Sci Mater Med* 14:69
36. Milošev I, Strehblow H-H (2000) *J Biomed Mater Res* 52:404
37. Milošev I (2002) *J Appl Electrochem* 32:311
38. Kocijan A, Milošev I, Pihlar B (2004) *J Mater Sci Mater Med* 15:643
39. Valero Vidal C, Igual Muñoz A (2008) *Corrosion Sci* 50:1954
40. Valero Vidal C, Olmo Juan A, Igual Muñoz A (2010) *J Colloids Surf B Biointerfaces* 80:1
41. Karimi S, Nickchi T, Alfantazi A (2011) *Corrosion Sci* 53:3262

42. Ouerd A, Alemany-Dumont C, Normand B, Szunerits S (2008) *Electrochim Acta* 53:4461
43. Sato N, Ohtsuka T (1978) *J Electrochem Soc* 125:1735
44. Burke LD, Lyons ME, Murphy OJ (1982) *J Electroanal Chem* 132:247
45. Ismail KM, Badawy WA (2000) *J Appl Electrochem* 30:1303
46. Badawy WA, Al-Kharafi FM, Al-Ajmi JR (2000) *J Appl Electrochem* 30:693
47. Foelske A, Strehblow H-H (2000) *Surf Interface Anal* 29:548
48. Kudo K (1978) In: Frankenthal P, Kruger J (eds) *Passivity of metals*. Electrochemical Society, Princeton, NJ, p 918
49. Heusler KE (1978) In: Frankenthal P, Kruger J (eds) *Passivity of metals*. Electrochemical Society, Princeton, NJ, p 771
50. Gervasi CA, Biaggio SR, Vilche JR, Ariva AJ (1989) *Corros Sci* 29:427
51. Povey AF, Metcalfe AA (1977) *J Electroanal Chem* 84:73
52. Wang K, Li Y-S, He P (1998) *Electrochim Acta* 43:2459
53. Moffat TP, Latanision RM (1992) *J Electrochem Soc* 139:1869
54. Haupt S, Strehblow H-H (1987) *J Electroanal Chem* 228:365
55. Melendres CA, Pankuch N, Li YS, Knight RL (1992) *Electrochim Acta* 37:2747
56. Schmuki P, Virtanen S, Davenport AJ, Vitus CM (1996) *J Electrochem Soc* 143:3997
57. Seo M, Saito R, Saho N (1980) *J Electrochem Soc* 127:1909
58. Pourbaix M (1974) *Atlas of electrochemical equilibria in aqueous solutions*, 2nd edn. NACE, Huston
59. Bardwell JA, Sproule GI, MacDougall B, Graham MJ (1992) *J Electrochem Soc* 139:371
60. Metikoš-Huković M, Ceraj-Cerić M (1987) *J Electrochem Soc* 134:2193
61. Lorang G, Da Cunha Belo M, Simoes AMP, Ferreira MGS (1994) *J Electrochem Soc* 141:3347
62. Olefjord I, Brox B, Jelvestam U (1985) *J Electrochem Soc* 132:2854
63. Piao T, Park S-M (1997) *J Electrochem Soc* 144:3371
64. Li Y-S, Wang K, He P, Huang BX, Kovacs P (1999) *J Raman Spectrosc* 30:97
65. Codaro EN, Melnikov P, Ramires I, Guastaldi AC (2000) *Russ J Electrochem* 36:1117
66. Pound BG (2010) *J Biomed Mater Res A* 94A:93
67. Gilbert JL (1998) *J Biomed Mater Res* 40:233
68. Haeri M, Goldberg S, Gilbert JL (2010) *Corros Sci* 53:582
69. Gilbert JL, Bai Z, Beringer J, Megremis S (2004) *Medical device materials: Proceedings of the materials and processes for medical devices conference*. ASM International, Anaheim, p 139
70. Smith SM, Gilbert JL (1994) In: Kovacs P, Istephanous NS (eds) *Proceedings of the symposium on compatibility of biomedical implants*, 94-15. The Electrochemical Society, Pennington, NJ, p 229
71. Brown SA, Farnsworth LJ, Merritt K, Crowe TD (1988) *J Biomed Mater Res* 22:321
72. Özçelik F, Gülen J, Akdoğan A, Pişkin S (1999) *Prakt Metallogr* 36:385
73. Lewis AC, Heard PJ (2005) *J Biomed Mater Res* 75A:365
74. Urban RM, Jacobs JJ, Gilbert JL, Galante JO (1994) *J Bone Joint Surg Am* 76-A:1345

75. Ouerd A, Alemany-Dumont C, Berthomé G, Normand B, Szunerits S (2007) *J Electrochem Soc* 154:C593
76. Black J (1992) *Biological performance of materials*. Dekker, New York
77. Smith RM, Martell AE (eds) (1977) *Critical stability constants*, vol 3. Plenum, New York
78. Peters T Jr (1996) *All about albumin*. Academic Press, San Diego, CA
79. Sugio S, Kashima A, Mochizuki S, Noda M, Kobayashi K (1999) *Protein Eng* 12:439
80. Omanovic S, Roscoe SG (1999) *Langmuir* 15:8315
81. Omanovic S, Roscoe SG (2000) *J Colloid Interface Sci* 227:452
82. Stupnišek-Lisac E, Metikoš-Huković M, Lenčić D, Forkapić-Furac K (1992) *Corrosion* 48:924
83. Jackson DR, Omanovic S, Roscoe SG (2000) *Langmuir* 16:5449
84. Alfonso MLCA, Villamil Jaimés RFV, Arêas EPG, Capri MR, Oliveira E, Agostinho SML (2008) *Colloids Surf A Physicochem Eng Asp* 317:760
85. Giacomelli CE, Esplandiú MJ, Ortiz PI, Avena MJ, De Pauli CP (1999) *J Colloid Interface Sci* 218:404
86. Kopac T, Bozgeyik K, Yener J (2008) *Colloids Surf A Physicochem Eng Asp* 322:19
87. Ithurbide A, Frateur I, Galtayries P, Marcus P (2007) *Electrochim Acta* 53:1336
88. Pradier CM, Kármán F, Telegdi J, Kálman E, Marcus P (2003) *J Phys Chem B* 107:6766
89. Reyes L, Bert J, Fornazero J, Cohen R, Heinrich L (2002) *Colloids Surf B* 25:99
90. Lu DR, Park K (1991) *J Colloids Interface* 144:271
91. Svare CW, Belton G, Korostoff E (1970) *J Biomed Mater Res* 4:457
92. Brown SA, Merritt K (1980) *J Biomed Mater Res* 14:173
93. Williams RL, Brown SA, Merritt K (1988) *Biomaterials* 9:181
94. Merritt K, Brown SA (1988) *J Biomed Mater Res* 22:111
95. Clark GCF, Williams DF (1982) *J Biomed Mater Res* 16:125
96. Yamauchi O, Odani A (1996) *Pure Appl Chem* 68:469
97. Yang J, Black J (1994) *Biomaterials* 15:262
98. Woodman JL, Black J, Jiminez SA (1984) *J Biomed Mater Res* 18:99
99. Merritt K, Brown SA, Sharkey NA (1984) *J Biomed Mater Res* 18:991
100. Merritt K, Brown SA, Sharkey NA (1984) *J Biomed Mater Res* 18:1005
101. Hallab NJ, Skipor A, Jacobs JJ (2003) *J Biomed Mater Res A* 65:311
102. Hallab NJ, Jacobs JJ, Skipor A, Black J, Mikecz K, Galante JO (2000) *J Biomed Mater Res* 49:353
103. Contu F, Elsener B, Böhni H (2002) *J Biomed Mater Res* 62:412
104. Contu F, Elsener B, Böhni H (2003) *J Biomed Mater Res* 67A:246
105. Hiromoto S, Noda K, Hanawa T (2002) *Corrosion Sci* 44:955
106. Hiromoto S, Onodera E, Chiba A, Asami K, Hanawa T (2005) *Biomaterials* 26:4912
107. Hsu RW-W, Yang C-C, Huang C-A, Chen Y-S (2005) *Mater Chem Phys* 93:531
108. Hanawa T, Hiromoto S, Asami K (2001) *Appl Surf Sci* 183:68
109. Lin H-Y, Bumgardner JD (2004) *Biomaterials* 25:1233

110. Lewis AC, Kilburn MR, Heard PJ, Scott TB, Hallam KR, Allen GC, Learmonth ID (2006) *J Orthop Res* 24:1587
111. Landolt D, Mischler S, Stemp M (2001) *Electrochim Acta* 46:3913
112. Virtanen S, Milošev I, Gomez-Barena E, Trebše R, Salo J, Kontinen YT (2008) *Acta Biomater* 4:468
113. Contu F, Elsener B, Böhni H (2003) *J Electrochem Soc* 150:B419
114. Hiromoto S, Onodera E, Chiba A, Asami K, Hanawa T (2005) *Biomaterials* 26:4912
115. Igual Muñoz A, Mischler S (2011) *J Mater Sci Mater Med* 22:437
116. Mischler S (2008) *Tribol Int* 41:573
117. Igual Muñoz A, Casabán Julián L (2010) *Electrochim Acta* 55:5428
118. Casabán Julián L, Igual Muñoz A (2011) *Tribol Int* 44:318
119. Yan Y, Neville A, Dowson D (2007) *Tribol Int* 40:1492
120. Yan Y, Neville A, Dowson D, Williams S (2006) *Tribol Int* 39:1509
121. Yan Y, Neville A, Dowson D (2006) *J Phys D Appl Phys* 39:3206
122. Sun D, Wharton JA, Wood RJK, Ma L, Rainforth WM (2009) *Tribol Int* 42:99
123. Band T, Metcalf J, Jones H (2001) *J Bone Joint Surg* 86-B:402
124. Bücher R, Fisher A (2003) *Materialwissenschaft Werkstofftechnik* 234:966
125. Wimmer MA, Loos J, Nassutt R, Heitkemper M, Fischer A (2001) *Wear* 250:250
126. Milošev I, Remškar M (2009) *J Biomed Mater Res A* 91A:1100
127. Bücher R, Tager G, Dudinski W, Gleising B, Wimmer MA, Fisher A (2005) *J Biomed Mater Res B* 72:206
128. Svanson SAV, Freeman MAR (1977) *The scientific basis of joint replacement*. Wiley, New York
129. Salinas-Rodriguez A (1999) *ASTM Spl Techn Publ* 1365:108
130. Levitas VI (2004) *Europhys Lett* 66:687
131. Scales JT, Winter GD, Shirley HT (1959) *J Bone Joint Surg* 41-B:810
132. Scales JT (1971) *J Bone Joint Surg Br* 53-B:344
133. Gruen TA, Amstutz HC (1975) *J Biomed Mater Res* 9:465
134. Reclaru L, Lerf R, Eschler P-Y, Blatter A, Meyer J-M (2002) *Biomaterials* 23:3479
135. Serhan H, Slivka M, Albert T, Kwak SD (2004) *Spine J* 4:379
136. Collier JP, Surprenant VA, Jensen RE, Mayor MB, Suprenant HP (1991) *Clin Orthop Relat Res* 271:305
137. Collier JP, Surprenant VA, Jensen RE, Mayor MB, Suprenant HP (1992) *J Bone Joint Surg* 74-B:511
138. Gilbert JL, Buckley CA, Jacobs JJ (1993) *J Biomed Mater Res* 27:1533
139. Gilbert JL, Jacobs JJ (1997) *The mechanical and electrochemical processes associated with taper fretting crevice corrosion: a review*. In: Marlowe DE, Parr JE, Mayor MB (eds) *Modularity of orthopaedic implants*. ASTM publication, STP 1301, West Conshohocken, PA, p 45
140. Goldberg JR, Gilbert JL, Jacobs JJ, Bauer TW, Paprosky W, Leurgans S (2002) *Clin Orthop Relat Res* 401:149
141. Cook SD, Barrack RL, Baffes GC, Clemow AJT, Serekian P, Dong N, Kester M (1994) *Clin Orthop Relat Res* 298:80

142. Bobyn JD, Duyovne AR, Krygier JJ, Young DL (1993) In: Morrey BF (ed) *Biological, material, and mechanical considerations of joint replacement*. Raven, New York, p 287
143. Mathiesen EB, Urban Lindgren J, Blomgren GA, Reinholt FP (1991) *J Bone Joint Surg Br* 73-B:569
144. McKellop HA, Sarmiento A, Brien W, Park SH (1992) *J Arthroplasty* 7:291
145. Gilbert JL, Buckley CA, Jacobs JJ, Bertin KC, Zernich MR (1994) *J Bone Joint Surg* 76-A:110
146. Brown SA, Flemming CAC, Kawalec JS, Placko HE, Vassaux C, Merritt K, Payer JH, Kraay MJ (1995) *J Appl Biomater* 6:19
147. Viceconti M, Baleani M, Squarzone S, Toni A (1997) *J Biomed Mater Res* 35:207
148. Salvati EA, Lieberman JR, Huk OL, Evans BG (1995) *Clin Orthop Relat Res* 319:85
149. Urban RM, Jacobs JJ, Gilbert JL, Rice SB, Justy M, Bragdon CR, Galante JO (1997) Characterization of solid products of corrosion generated by modular-head femoral stems of different designs and materials. In: Marlowe DE, Parr JE, Mayor MB (eds) *Modularity of orthopaedic implants*. ASTM publication, STP 1301, West Conshohocken, PA, p 33
150. Urban RM, Jacobs JJ, Gilbert JL, Galante JO (1994) *J Bone Joint Surg* 76-B:1345
151. Huber M, Reinisch G, Trettenhahn G, Zweymüller K, Lintner F (2009) *Acta Biomater* 5:172
152. McCarthy JC, Bono JV, O'Donnell PJ (1997) *Clin Orthop Relat Res* 344:162
153. Yerby SA, Taylor JK, Park J, Shackelford JF (1996) *J Arthroplasty* 11:157
154. Lieberman JR, Rimnac CM, Garvin KL, Klein RW, Salvati EA (1994) *Clin Orthop Relat Res* 300:162
155. Kop AM, Swarts E (2009) *J Arthroplasty* 24:1019
156. Willert H-G, Brobäck L-G, Buchhorn GH, Jensen PH, Köster G, Lang I, Ochsner P, Schenk R (1996) *Clin Orthop Relat Res* 333:51
157. Hodgson AW, Mischler S, Von Rechenberg B, Virtanen S (2007) *Proc IMechE H* 221:291

# Chapter 2

## Electroless Synthesis of Metallic Nanostructures for Biomedical Technologies

Luca Magagnin, Paula Cojocar, and Francesco Secundo

### 2.1 Introduction

The electroless deposition of metals has emerged as one of the leading growth areas in surface engineering and metal finishing, and, recently, it is gaining interest for the synthesis of metallic nanostructures for biomedical technologies. In this perspective, the fundamental aspects underlying the autocatalytic deposition (ACD) and immersion plating are briefly reviewed, establishing the unique identity of galvanic displacement among electrochemical processes in general, and electroless processes in particular. Numerous biological and biomedical phenomena occur at the nanometer level, and the current research focus of many fields is nanotechnology. Nanostructured metallic systems can provide the ability to probe the sub-optical, molecular level and are becoming powerful tools to study biomolecular processes. Metal nanosystems also hold great promise for the field of nanomedicine, where nanostructures are designed to diagnose and provide therapy at the single-cell level. The exploitation of the electroless methods as an amazingly simple and effective route for generating metal nanostructures will be reviewed within the frame of

---

L. Magagnin (✉) • P. Cojocar  
Dip. Chimica, Materiali e Ing. Chimica G. Natta Politecnico di Milano,  
Via Mancinelli, 7, 20131, Milano, Italy  
e-mail: luca.magagnin@polimi.it; paula.cojocar@polimi.it

F. Secundo  
Istituto di Chimica del Riconoscimento Molecolare, CNR,  
via Mario Bianco 9, 20131, Milano, Italy

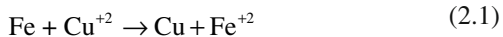
biomedical technologies, discussing the applications in sensors and microdevices, the preparation and use of nanostructured metals for supporting and wiring biomolecules, for DNA analysis and disease screening. The use of nanostructures such as nanorods and nanoparticles, as these structures show interesting optical, electrical, and mechanical properties, will be analyzed in view of their potential applications in nanobiotechnology.

## 2.2 Electroless Deposition

The galvanic displacement plating process is sometimes generally, but not satisfactorily, defined as the deposition of a metallic coating on a substrate from a solution that contains the ions of the coating material. This definition of the displacement mechanism is misleading because it can be applied to most of the plating processes from aqueous phase. Also the expression, plating, denoting a general application of a metallic coating, is commonly used to indicate the deposition of metallic films through electrochemical processes. Even if they are commonly grouped together under electrochemical methods or electrodeposition processes, distinctions between electrolytic and electroless deposition processes must be made [1]. By the application of an external voltage or current flow between two electrodes, one of these consisting of the base material, an electrolytic process allows the modification of a substrate surface in an aqueous or nonaqueous electrolytic environment. The deposition of a metallic coating on a substrate through an electroless plating processes without the use of an external voltage or current are commonly referred to as chemical rather than electrochemical methods in order to emphasize the absence of an external power supply. Their mechanisms can be explained by taking account of their electrochemical redox potential. Among the electroless plating processes, a distinction is required to select autocatalytic and galvanic displacement methods. The autocatalytic method is an electroless process in which the reduction of the metallic ions in solution and film deposition can be carried out through the oxidation of a chemical compound present in the solution itself, i.e., of a reducing agent. The oxidation of the reducing agent can start or become self-sustained only at the depositing metal surface; for some noncatalytic base materials, the activation of the

deposition with catalytic metals such as palladium is required [2, 3]. Examples of an autocatalytic process are the well-known electroless nickel deposition from hypophosphite-based solution [2]. In comparison to electrodeposition, ACD avoids current distribution, improves thickness uniformity, and allows film deposition with a thickness that mainly depends on the deposition time.

Galvanic displacement or immersion plating (sometimes also called cementation) on a substrate takes place when the base material is displaced by a metallic ion in solution that has a lower oxidation potential than the displaced metal ion [4–15]. The base material is dissolved into the solution and the metallic ions in solution are reduced on the surface of the base material. Such a mechanism differs completely from ACD because, in immersion plating, reducing agents are not required to reduce the metal ions to metal, as the base material behaves as the reducing agent. Perhaps the most commonly discussed example of immersion plating is the deposition of copper onto steel in a copper sulfate acid solution through the following reaction:



Even similar reactions should sometimes be avoided in metallic finishing; galvanic displacement deposition processes are widely used, since they yield high value finishes on a variety of metals. The following characteristics of the galvanic displacement process can be pointed out: the thickness of the deposited film obtained by immersion plating is limited (typically, in the range of hundreds of nanometers), because the deposition stops when the entire surface of the base metal is coated. Due to the nature of the displacement process, the deposition occurs by downward growth. The surface of the coating reproduces almost exactly that of the base material, both in contour and in location, avoiding current distribution issues and the absence of electrical connections among areas of the substrate. Immersion plating is a part of many finishing processes, ranging from decorative or functional coatings to integrated circuit soldering. Zinc immersion plating on aluminum is required to reduce the activity of the aluminum surface, as a sort of sacrificial layer, which is partially dissolved during the immersion in acidic hexavalent chromium-based electrolytes [2]. Many decorative films of the noble or platinum group metals on copper and copper alloys can be deposited through immersion plating, producing adherent, wear-resistant, and tarnish-free coatings [16, 17].

### ***2.2.1 Autocatalytic Deposition of Metallic Nanostructures***

Nickel, cobalt, copper, silver, gold, and palladium are commonly deposited by ACD for applications in electronics, corrosion and decorative fields, and biomedical sector [18]. Electrolytes for ACD processes are typically constituted from the sources of metallic ions, the complexing and reducing agents, stabilizers, and inhibitors. For further information on ACD, the reader is referred to [19–22].

Nanostructured materials, such as nanoparticles, nanowires, and nanoarrays, have attracted much attention due to their interesting electronic, optical, and chemical properties. Electroless deposition has shown initial promise for fabricating nanostructures in this emerging field of research. As an alternative technique, electroless deposition is of great interest due to its simplicity (solution-based process, no complex instrumentation), economical aspect, and effectiveness to form certain desired film thicknesses, morphologies, and nanostructures on a wide variety of substrates for biomedical applications. A current trend in materials design and production is to produce materials with characteristics like multi-components, multi-scales, multi-structures, multi- and hybridized functions, biocompatibility, etc. While the production of such materials remains a great challenge for material scientists, materials with sophistication, hierarchical organizations, function hybridization, miniaturization, environment resistance, and adaptability have been provided by nature. Learning from nature is an efficient route to produce materials that answer up the challenges. Biomimicking includes mimicking natural structures, functions, mechanisms, and/or the whole system. Biomimicking brings improvements to human technology and life by allowing us to approach modern technical problems with effective and ingenious solutions. An emerging field in the biomimicking of natural materials is biomorphic mineralization—a technique that produces materials with morphologies and structures resembling those of nature living things through employing bio-structures as templates for mineralization [23]. On the border between displacement and electroless, in situ metal reduction processes are applied to a range of templates like biomolecules, viral particles, silks, eggshell membrane, plant and animal materials for biomorphic mineralization (Fig. 2.1).

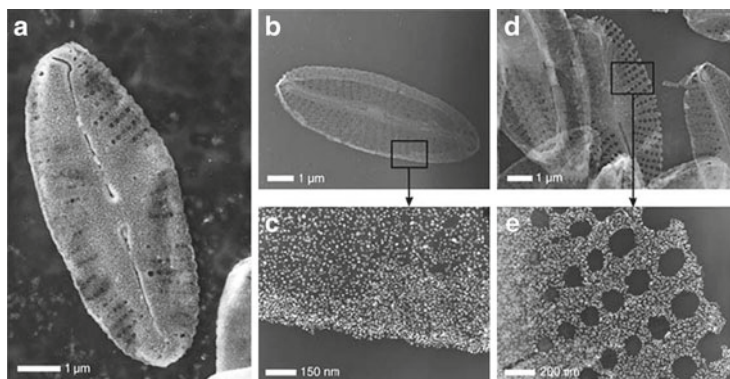
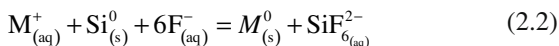


**Fig. 2.1** Electron microscope images of DNA-functionalized *Navicula* diatoms densely coated with one layer of DNA-modified 13 nm gold particles. (a) SEM and (b, c) TEM images revealing a dense outer coating of nanoparticles on the *Navicula* surface. (d, e) Further show the homogeneous nanoparticle coating on the highly symmetric and nanoscopically detailed *Navicula* templates under different magnifications. Reprinted with permissions from Wiley-VCH (Rosi et al. [24])

### 2.2.2 Galvanic Displacement of Nanostructured Metals on Silicon

Galvanic displacement on Si from solutions containing HF is a redox reaction in which both anodic and cathodic processes occur simultaneously at the Si surface while the charge may be exchanged through the substrate [25–30]. Fluoride ions in solution help sustain the reaction by dissolving the silicon substrate as silicon hexafluoride, avoiding the formation of silicon oxide, thus exposing new silicon surface. As commonly reported, the global chemical reaction of the redox couple is as follows:



where aq and s indicate the aqueous and solid phases, respectively.

Silicon is dissolved in solution as silicon hexafluoride, while the metal is deposited. The oxidation of silicon followed by the galvanic displacement of the metal ions in solution is believed to initiate at defects on the surface such as kinks, steps, contaminated sites, or areas chemically more reactive than H-terminated regions. Doping of the silicon substrate, due to the transfer of the charged carriers

through the substrate during displacement, can affect the deposition mechanism [31]. Galvanic displacement is thermodynamically more favorable for metals with higher redox potential values, e.g., for gold or palladium than for copper or nickel. Considering that the redox potential for metal reduction is much more negative than for hydrogen evolution (e.g.,  $-0.48$  V SHE in 40 %  $\text{NH}_4\text{F}$  and  $-0.12$  V in 0.5 % HF) and for noble and platinum group metal deposition, cathodic reactions must include the following one:

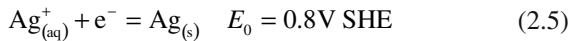


The efficiency of the metal deposition on the silicon surface is expected to vary according to the composition and the pH of the solution [25, 32]. The reducing behavior of elemental silicon toward noble metal ions in aqueous solutions containing fluoride ions has long been known [33–39]. Contamination by metallic ions can lead to undesirable deposition of noble metal impurities on the Si surface, compromising the performance of electronic devices [40–42]. The deposition of metal films from fluoride-containing solutions on both silicon (Cu, Au) and germanium (Au) was studied by Balashova et al. and Krikshtopaitis et al. about 30 years ago [43, 44]. A reduction in the metal precipitation rate was observed with time for both silicon and germanium. The evaluation of the germanium potential during deposition indicated that the reduction of gold ions took place predominantly by charge transfer through the valence zone of the electrode. Magagnin et al. studied Au films deposited on Si(111) and on Ge(111) surfaces by the galvanic displacement method in fluoride-containing solutions [45]. While the Au/Si interface was characterized by weak adhesion, the Au films adhered very strongly to the surface of Ge, even in the thick film regime. Adhesion of the gold films on germanium was related to the formation of a chemical bond between Au and Ge atoms. This was confirmed from the valence band (VB) region of the X-ray photoelectron spectra obtained from germanium coated with gold. In particular, the spectrum showed a shift in the main peak toward higher binding energies as well as an increased density of states at binding energy  $\text{BE}=0$ . Such a shift was attributed to the interaction of the metal with the germanium substrate, with the formation of a stoichiometric compound at room temperature, such as in the case of palladium and platinum on silicon and germanium [45–47].

Silver galvanic displacement on silicon has been employed to achieve nanostructured films, such as nanopillars, for surface-enhanced Raman scattering (SERS) analysis [48]. Galvanic displacement of silver can be carried out in silver nitrate and hydrofluoric acid solutions [48–50]. The displacement reaction is as follows:

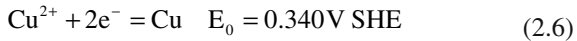


Considering the metal reduction reaction,



The process is thermodynamically favorable, with a standard cell potential of 2 V. There are a large number of possible steps, and in principle any one of these could be rate determining (1) diffusion of  $\text{Ag}^+$  to the silver surface; (2) adsorption of  $\text{Ag}^+$  and charge transfer to yield silver on silver; (3)  $\text{F}^-$  diffusion, charge transfer, and reaction at the Si surface to yield  $\text{SiF}_6^{2-}$ ; (4) desorption of  $\text{SiF}_6^{2-}$ ; and (5) diffusion of  $\text{SiF}_6^{2-}$  away from surface. The overall growth rate was observed to be diffusion controlled by silver species [48].

Several studies have been carried out on the galvanic deposition of copper from fluoride- containing solutions, providing an attractive deposition method for copper interconnects or seed layers for subsequent metallization [51]. Galvanic displacement is also a promising avenue for the integration of metals in micromechanical devices, due to its conformal nature and high substrate selectivity [45]. In the case of copper, the displacement reaction involves the following one:



Typically, copper deposition has been carried out from a copper sulfate and hydrofluoric acid-based solution [33–39, 52, 53]. A crucial issue is the lack of adhesion between the copper and the Si substrate with severe constrains in its application [54]. Magagnin et al. reported a new process for the galvanic deposition of copper films with high reflectivity and smoothness onto silicon from ammonium fluoride-containing solutions [55]. The deposition was carried out at room temperature in a solution consisting of ammonium fluoride ( $\text{NH}_4\text{F}$  40 %) 50 % vol., copper sulfate ( $\text{CuSO}_4 \cdot 5\text{H}_2\text{O}$ ) 0.01 M, ascorbic acid ( $\text{C}_6\text{H}_8\text{O}_6$ ) 0.01 M, sodium potassium tartrate ( $\text{KNaC}_4\text{H}_4\text{O}_6 \cdot 4\text{H}_2\text{O}$ )

0.005 M, and methanol 30 % vol. The authors observed that the adhesion of the copper film to the substrate could be tailored through the addition of ascorbic acid in solution, due to the hydrogen-scavenging action of the ascorbic acid [56]. The nucleation and growth followed a 3D island growth mechanism with nucleation of metal clusters and subsequent growth of a film. The initial displacement was characterized by an extremely fast nucleation with a large number of nuclei. The 3D structure was found to be permeable to fluoride ions, resulting in long plating times and thick deposits. Regarding adhesion, peeling of the deposited copper film was never observed, independently of the substrates (i.e., p- or n-type, single- or poly-crystalline silicon) and film thickness, demonstrating a high degree of adhesion to the substrate and resistance to scratching. The coating process was demonstrated to be suitable for plating free-standing polycrystalline silicon micromachined devices.

Several properties shared among the platinum group metals (and some of their oxides as well) make them attractive for technological and commercial applications. These include their exceptional catalytic activity, their high resistance to wear, tarnish and chemical attack, and their stability at high temperatures. These metals are suitable for the immersion plating of semiconductors, and indeed, the galvanic displacement of Pt and Pd on Si and Ge has been observed [32, 50, 57–59]. In the case of Ge, deposition occurs even in the absence of fluorides or complexing agents, due to the solubility of GeO in aqueous environments [58]. The best studied case is the displacement of Pt on Si, using either Pt(II) or Pt(IV) salts. Gorostiza et al. investigated the early stages of Pt(IV) galvanic displacement on Si(100) from HF solutions. Nucleation of polycrystalline platinum silicides was observed, along with the etching of the substrate surface. A subsequent study aimed to clarify the reaction mechanism of Pt(II) on Si in the presence of fluorides [32]. Galvanic displacement of palladium films on silicon has received less attention compared to platinum. Most studies employ the displacement of palladium nuclei for subsequent electroless metallization. Karmalkar et al. reported on the palladium activation of silicon surfaces achieved using a solution of PdCl<sub>2</sub> and NH<sub>4</sub>F in dilute HF. The activation layer showed poor adhesion to the substrate, even though a silicide layer was readily formed. This characteristic may make this process preferable over other activation methods in applications where a Schottky-type contact is required [60].

## 2.3 Electroless Gold for Biomedical Applications

Gold is the metal with the highest number of biomedical applications. Indeed, it is commonly used in restorative dentistry. As salts and radioisotopes gold is of pharmacological value. Injectable gold has been proven to help to reduce the pain and swelling of rheumatoid arthritis and tuberculosis. Furthermore, gold salts have anti-inflammatory properties [61]. As elemental (metallic) gold has low cytotoxicity and is inert to almost all chemicals it encounters inside the body [62]. However, if this property is a prerequisite of gold to be a good candidate for both *in vitro* and *in vivo* applications, new properties such as controllable surface chemistry, localized surface plasmon resonance (LSPR), and morphology arise from the preparation of metallic gold in nanostructured forms expanding the potential applications [63]. The most commonly prepared shapes are spheroids, triangular prisms, rods, and cubes. All of these shapes are based on the reduction of a metal salt to produce nanoparticles with varied shapes and sizes. Another form of core-shell particles has a metal shell surrounding a dielectric center. These particles are functionalized with silane and then reacted with small gold nanoparticles. The gold particles provide nucleation sites for the growth of the metallic shell from metal salts in solution [64]. Surface chemistry of gold nanostructures offers the possibility to tail a particular gold nanostructure (i.e., Au nanoparticles) for a specific biomedical application. Gold colloids were studied in humans in the 1950s as radiotracers for sentinel lymph node biopsy, and more recently a phase I clinical trial has been completed for gold nanosphere as drug carrier [65, 66]. The surface of gold is well-known for forming strong, stable gold-thiolate bonds (Au-S, ~50 kcal/mol) to molecules with thiol (-SH) or disulfide groups (S-S) [67]. This binding has been extensively employed to form—through adsorption of alkanethiols and a self-assembling process—a highly ordered monolayer onto a gold surface (self-assembled monolayers). The functional group at the distal end of the molecule adsorbed on the gold surface allows the formation of a well-defined interface on the gold nanostructure that might favor (or depress) the interaction with cells and biomolecules in specific ways. On the other hand, it has to be considered that also nonspecific adsorption of biological molecules on gold nanostructures can occur, affecting cell/gold (or target molecule/gold) interactions in a biological environment [68]. Poly(ethylene glycol) (PEG) is the most used

biocompatible polymer to modify the surface of gold nanostructures for *in vivo* applications. PEG obstacles nonspecific protein adsorption and particle aggregation. It also delays the inclusion of circulating gold nanostructures into the reticuloendothelial system (RES). This latter effect makes possible a greater accumulation of gold nanostructures in tumors through passive targeting [69]. Passive targeting or enhanced permeability and retention (EPR) effect is the result of the combination of the higher growth and porosity of blood vessels in tumors and the reduced lymphatic drainage from tumors than in healthy tissue. Consequently, nanostructures increase their concentration in tumors, a situation that can be advantageously exploited for cancer therapy or imaging. Pegylation of gold nanostructures is relatively easily carried out by replacement with an excess of thiol-terminated PEG of surfactants, capping agents, or stabilizers used for nanoparticle synthesis and that bind less strongly compared with gold–thiolate interactions [70]. The development of metal nanostructured materials conjugated to biomolecule that are highly specific with regard to intermolecular interactions has promising applications in drug delivery, cell targeting, protein epitope mapping, and protein–protein interactions. Conjugation of metal nanostructures to tumor cell complementary moieties (e.g., antibodies, peptides, and folate, among others), via PEG or directly on the nanostructure surface via a thiolate–gold bond, it will generate a modified gold (metal) nanostructure able to bind to cancer cells as they circulate, increasing their concentration in the desired region. Surface modification through thiolate binding and polymer adsorption can also be addressed to control the charge of a gold nanostructure, which is an important factor for both the cellular uptake and biodistribution of nanostructures. Positively charged nanostructures have been shown to have enhanced affinity to negatively charged cell surfaces and are most likely to cross cellular membranes and enter the cytoplasm of cells, an important aspect to consider in delivery applications [68, 71]. It is also possible to use the thiol group to attach oligonucleotides for sensing applications, smart polymers or drugs for stealth delivery, as well as a wide variety of other types of molecules (Fig. 2.2) [73, 74].

Particular optical properties of gold nanostructures arise from their interaction with an electromagnetic radiation by the phenomenon called LSPR. This later originates when the delocalized conduction electrons of the metal begin to oscillate collectively relative to the lattice of positive nuclei with the frequency of the incoming light.

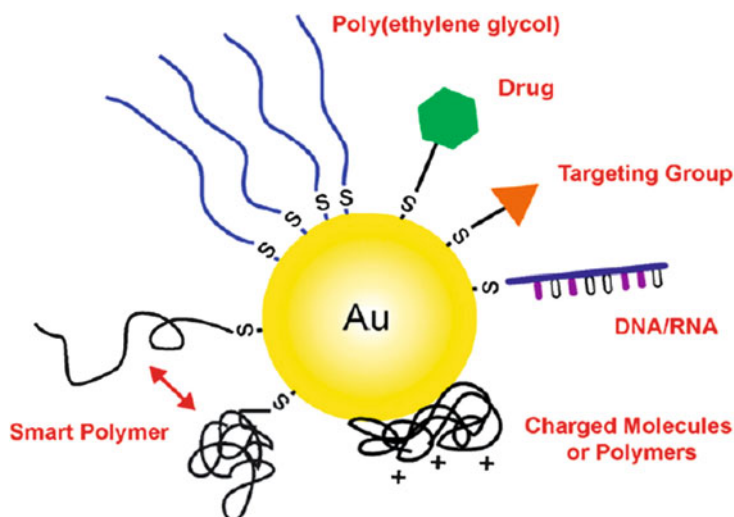


**Fig. 2.2** Gold nanostructures can be conjugated with a wide variety of functional moieties, both through the gold–thiolate bond and by passive adsorption. Reprinted with permissions from RCS Publishing (Cobley et al. [72])

Upon interaction with the gold nanostructure, the radiation can be scattered (e.g., reflected in all direction at the same wavelength) or absorbed causing vibration of the lattice and observed as heat. Furthermore, LSPR also generates strong electric near fields close to the surface of the particle. Size, shape, and morphology of the nanostructure, as well as the dielectric environment are factors that affect LSPR response of gold nanostructures [75–77]. On the basis of the interaction taken into account, different techniques have been developed and employed for biomedical applications. Light-scattering phenomenon is exploited in imaging techniques such as optical coherence tomography (OCT) and dark-field microscopy. In both techniques, the presence of scattering particles allows an enhancement of the image contrast [72]. Absorption is at the base of a variety of techniques that, through the photothermal effect, exploit the transformation of the energy of the radiation of a laser in heat when absorbed by gold nanostructures. The so-produced heat can be used to allow the release in drug delivery systems, enhance contrast in optical imaging techniques like photoacoustic imaging, and provide photothermal treatment [72]. Particularly interesting for biomedical applications of gold nanostructures is their absorption and scattering in

the near-infrared region (NIR, 650–900 nm) due to the low scattering from tissue and low absorption from blood and water in this spectral region (the so-called “water-window” region), allowing light to penetrate deeply into the biological tissues. Frequency and intensity of absorption of NIR and scattering depend on the aspect ratio of gold nanostructures. To this end, different electroless procedures that start from a dissolved gold salt (i.e.,  $\text{HAuCl}_4$ ) have been employed for the preparation of gold nanostructures with various morphologies as gold nanospheres, gold nanorods, gold nanoshells, and gold nanocages. The last three kinds show an augmented LSPR in the NIR region. An example of nanoparticles preparation for SPR uses sodium borohydride as reducing agent: 0.2 mL of 1 % aqueous sodium citrate was added into 10 mL of 0.01 % aqueous  $\text{HAuCl}_4$  with vigorous stirring. After 1 min, 0.2 mL of 0.075 % (w/v)  $\text{NaBH}_4$  in sodium citrate was added. The solution was stirred for 5 min and stored at 4 °C before use [78].

Structural and chemical stability is also a crucial factor that has to be carefully considered when NIR-absorbing branched gold nanoparticles are used for clinical applications, in fact the instability of nanoparticles' morphology causes spectral shift of their plasmon absorption band and limits their use in real applications. However, stabilization of branched structure was achieved by exchanging the initial capping agent for different alkanethiols and disulfides. The strong electric near field from LSPR can enhance the Raman or the infrared signals of molecules adsorbed on the surface of a gold or silver nanostructure by several orders of magnitude and the techniques developed are known as SERS and surface-enhanced infrared absorption (SEIRA) spectroscopy, respectively. Both techniques have been used for biosensor analysis based on antibody–antigen interactions. Furthermore, theoretical calculations and experimental measurements have shown that the number of absorption peaks and effective spectral ranges for SERS are strongly dependent upon the exact morphology displayed by metal nanostructures [72]. These techniques require the preparation of metal nanoplates. The procedures usually adopted for preparing metal nanoplates are mainly based on solution-phase chemical reactions with the assistance of various surfactant molecules, for instance, polymeric chains (e.g., poly(vinyl pyrrolidone) (PVP) or polyamines), micellar assemblies (e.g., cetyltrimethylammonium bromide (CTAB) or bis-(2-ethylhexyl) sulfosuccinate (AOT)), and coordinating molecules [72]. Nevertheless, the presence of surfactants

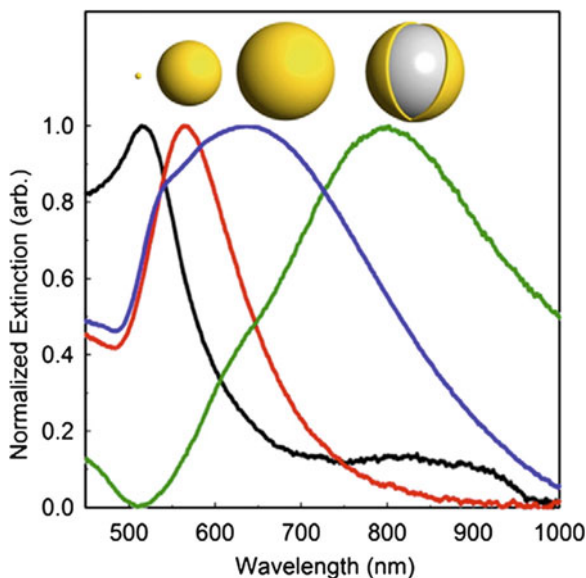


**Fig. 2.3** Size-dependent gold nanoparticle extinction spectra. Plasmon absorption depends on nanoparticle size and composition; shown are the extinction spectra of solid gold nanoparticles (*black*= 10 nm dia., *red*= 100 nm dia., *blue*= 150 nm dia.) and the red-shifted silica core gold nanoshell spectrum (*green*= 150 nm dia.). Nanoparticle illustrations above each corresponding spectra are drawn to relative scale and spectra have been normalized to ease viewing of relative peak positions. Reprinted with permissions from Elsevier (Cherukuri et al. [80])

molecules on the plate surface can negatively affect the surface-enhanced spectroscopies (i.e., they can alter the biomolecule stability or hinder the adsorption on the metal surface decreasing the enhancement of the observed signal).

Gold nanoparticles are simply solid gold nanospheres that can range from 2 nm to several 100 nm in diameter. Gold nanoparticles have characteristic extinction spectra due to plasmonic absorptions. Recent advances have produced gold–silica nanoshells which are composite nanoparticles composed of an inner silica (glassy) core ~100 nm diameter and a thin outer layer of gold (10–15 nm thick) [79]. The gold shell thickness to core diameter ratio can be adjusted and be used to tune the absorption characteristics of the nanoparticle synthetically (Fig. 2.3) [80].

The ability to construct nanoscale materials with specific plasmon absorption characteristics provides the pharmaceutical chemist a new

tool in their chemotherapeutic arsenal. Nanotube membrane-based biosensors allow a highly sensitive detection based on electrochemical methods. To prepare the Au nanotubes, monodisperse gold is deposited by an electroless procedure onto the pore walls of a polycarbonate membrane; i.e., the pores act as templates for the nanotubes. The so-made membranes have inside diameter approaching molecular dimensions. The so-made biosensor can detect the analyte species by measuring a change in transmembrane current when the analyte is added to the nanotube-based cell. Potential applications for these biosensors are in fields such as bioanalytical, biomedical, pharmaceutical, and drug discovery. A single conical Au nanotube in a PET membrane was used to design a new type of protein biosensor. The nanotubes were modified with various biochemical molecular recognition agents (MRAs) to detect analytes in solution with an on/off response [72]. Like the above experiments utilizing the resistive-pulse sensing method, this sensing protocol also involves passing an ion current through the single nanotube. However, current-pulse translocation events are not observed in this case. Instead, as the analyte binds to the surface-bound MRAs the current flowing through the nanopore is permanently shut off. Blockage of the ion current occurs because the diameter of the analyte is of comparable dimensions to that of the nanotube tip. The conical nanopores in PET were electrolessly plated with Au to yield conical Au nanotubes. Attachment of the MRAs to the nanotube surface was carried out using Au-thiol chemistry. The functionalized nanotube membranes were mounted in an electrochemical cell and a transmembrane potential was applied across the nanotube. The ion current flowing through the nanotube was monitored using current-voltage curves. The unique properties of gold nanoparticles to provide a suitable microenvironment for biomolecules immobilization retaining their biological activity, and to facilitate electron transfer between the immobilized proteins and electrode surfaces, have led to an intensive use of this nanomaterial for the construction of electrochemical biosensors with enhanced analytical performance with respect to other biosensor designs. Chen et al. proposed an innovative microfluidic device for hyaluronic acid (HA) extraction and electrochemical detection utilizing PMMA-based microchip integrated with gold nanoelectrode ensemble (GNEE) [81]. GNEE is fabricated using electroless deposition in a thin polycarbonate (PC) film and then directly bonded onto the PMMA substrate for high-performance electrochemical detection [81]. Lu et al. studied the preparation of bioinspired masks using a soft-templating route and

used to confine a chemical reaction (e.g., electroless gold deposition) to a select area (e.g., the chemical reactor) [82]. By using smaller bacteria or viruses as biotemplates, channels (rod-shaped wells) that are nanometer in size can be formed. These submicron-sized chemical reactors can then be used to grow arrays of nanoparticle-like wires that are truly nanometers in width and/or length. By controlling the concentration of bacteria in the original suspension and the orientation of the electric field lines, the density and direction of the nanoparticle-like wires with respect to each other can be controlled. It is envisioned that these nanoparticle arrays can be used as building blocks to create multidimensional nanostructures, confine proteins/antibodies to specific locations on a patterned surface, and in chemical sensing. Alternatively, these rod-shaped wells could be used to direct and control the growth of chemical entities such as protein crystals or other nanostructures [82].

Magnetic nanoparticles (MPs) are another group of nanostructured metal materials particularly interesting for the numerous potential medical applications. Magnetic nanoparticles can be used as support for protein and enzyme immobilization, as agents in magnetic resonance imaging (MRI), for the separation and sorting of proteins and cells, as carriers for drugs delivery systems, in the hyperthermia treatment for cancerous tumors and immunoassays [72, 83, 84]. They can be synthesized by numerous electroless procedures as microemulsions, sol-gel syntheses, sonochemical reactions, hydrothermal reactions, hydrolysis and thermolysis of precursors, flow injection syntheses, and electrospray syntheses [83, 84]. The synthesis of superparamagnetic nanoparticles is a complex process due to the fact that must be found experimental conditions that allow to obtain a monodisperse population of magnetic grains of suitable size by a reproducible process that can be industrialized without any complex purification procedure, such as ultracentrifugation, size-exclusion chromatography, magnetic filtration, or flow field gradient [83, 84]. These methods have been used to prepare particles with homogeneous composition and narrow size distribution. However, the most common method for the production of magnetite nanoparticles is the chemical coprecipitation technique of iron salts. The increasing requirements of the multifunctional nanostructures for many technical applications in biomedicine and bioelectronics have brought to the synthesis of multifunctional nanostructures based on the combination of metallic and magnetic nanostructures, where the magnetic nanoparticles can provide MRI contrast and direct the nanostructure to the

target by exterior magnetic field. Gold (Au) nanoshells with magnetic nanoparticles have been synthesized, where magnetic nanoparticles were entrapped in the center of silica sphere by the well-known Stöber method [85]. Furthermore, the so-prepared nanostructured metal material fuse the broad NIR absorption property and superparamagnetic property into one particle that can be applied as magnetic-field-targeted photothermal therapy agents and multimodal molecular probes. The biorecognition of a target DNA bound a DNA-modified nanoparticles by a probe DNA linked to gold nanoparticles can be exploited for biosensing purposes. Interestingly, electroless deposition of silver on the surface of the gold probes results in particle growth, which increases their scattering efficiency with time and can be correlated with target concentration [74, 83–86].

The interest in electroconductive textiles has tremendously increased over the last few years. By functionalizing textile surfaces with thin layers of metal, electrical conductivity can be combined with flexibility and pliability. This approach was used to deposit a thin layer of soft gold onto polypyrrole- and copper-coated *para*-aramid yarns in an electroless way. A deposition solution was used which contained a gold salt, sulfite, and thiosulfate to result in a smooth and homogenous gold layer. Performance tests showed that the coated yarns offered an excellent electrical conductivity combined with good mechanical properties and satisfying resistance to washing. In addition, electrochemical impedance measurements revealed that the gold-coated yarns are promising electrode materials to measure biomedical signals [87].

## 2.4 Electroless Silver for Antibacterial Applications

Silver coating may be an effective viable route to prevent device-related infections due to its good antimicrobial activity and low toxicity [88, 89]. The biocidal activity of silver is related to the biologically active silver ion released from silver coatings [88, 89]. In general, metallic silver appears to be inert and have no antibacterial action. Silver ions ( $\text{Ag}^+$ ), however, bind to and react with proteins and enzymes, thereby causing structural changes in the bacterial cell wall and membranes, leading to membrane permeability damage, cellular

disintegration and death of the bacterium [88, 89]. The silver-coated medical devices, such as dressings, heart valves, central venous catheters, and urinary catheters, have been proved to reduce the infections effectively. The silver-coated silicone Foley catheters are effective at reducing the incidence of catheter-associated urinary tract infections and resistant organisms in an acute care hospital [90]. It has been reported that the surface energy of coatings also has significant influence on initial bacterial adhesion [91–93]. Silver can be electrolessly deposited by using different reducing agents. The reducing agents had a significant influence on the morphology and surface energy of the silver coatings. Shao et al. evaluated four types of silver coatings on stainless steel plates using  $\text{AgNO}_3$ -based electroless plating solutions with four different reducing agents, formaldehyde, hydrazine, glucose, and potassium sodium tartrate tetrahydrate, respectively. The silver coating produced with formaldehyde exhibited a rougher nanostructure as compared to the other three silver coatings. The number of bacteria adhered to the rougher coating was higher than that of the smooth silver coatings produced with hydrazine, glucose, or potassium sodium tartrate tetrahydrate. Bacterial adhesion decreased with decreasing total surface energy of the coatings and with increasing surface energy component of the coatings. All the silver coatings performed much better than stainless steel in reducing bacterial attachment [88]. Gray et al. investigated the biological efficacy of silver deposited by a conventional electroless plating technique on polyurethane. A bacteriostatic effect was noticed for silver-coated polyurethane samples where a slight reduction in bacterial growth in the growth medium compared to the control samples was observed [94]. Zhao et al. studied a metal–polymer composite coatings based on silver electroless deposition: the main composition of the electroless Ag–PTFE solution included silver nitrate ( $\text{AgNO}_3$ ), sodium hydroxide ( $\text{NaOH}$ ), ammonia ( $\text{NH}_3\text{H}_2\text{O}$ ), glucose ( $\text{C}_6\text{H}_{12}\text{O}_6$ ), tartaric acid ( $\text{C}_4\text{H}_6\text{O}_6$ ), ethanol ( $\text{C}_2\text{H}_5\text{OH}$ ), and PTFE emulsion [95]. The Ag–PTFE composite coating with corrosion-resistant properties showed a tremendous potential for reducing biofouling in medical devices or industrial equipment [93, 95]. Lee et al. reported on a process for the production of stable and optically tunable Ag films by soaking glass substrates in ethanolic solutions of  $\text{AgNO}_3$  and butylamine [96, 97]. These Ag films showed an excellent homogenous morphology and SERS activity. They also demonstrated a procedure for depositing stable silver nanoparticles onto cotton fabrics for

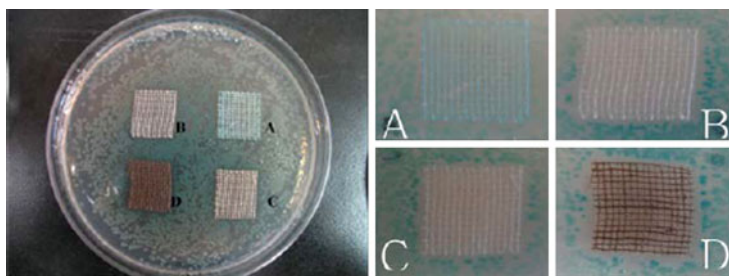


**Fig. 2.4** Growth inhibition of *E. coli* by silver-coated cotton fabric on an agar plate with X-gal selection. (a) Cotton fabric. (b, c and d) Silver nanocoated fabric with low, medium and high loading levels, respectively. Reprinted with permissions from The Royal Society of Chemistry (Lee et al. [98])

biomedical applications by using the same principle of Ag films (Fig. 2.4). The practicality of this procedure was shown in clinical usages, since it could be produced by a one-pot reaction that requires only  $\text{AgNO}_3$ , butylamine, and absolute ethanol [98]. In addition to its simplicity, the loading levels of silver nanoparticles on cotton fabrics were completely controlled by varying the concentration of the reactants.

The novel fabric exhibited excellent bactericidal effects on pathogenic bacteria found in wounded skin, for example *S. aureus*, opening the use for the medical treatment of skin burns or cuts. Antibacterial efficiency of  $\text{Ag/SiO}_2$  grafted on wool has been investigated by Wang et al. [98]. Oh et al. have also prepared  $\text{Ag/SiO}_2$  and investigated its antibacterial and antifungal effectiveness [99]. Fu et al. have produced multilayer composite films from heparin/chitosan/nanosilver for biomedical applications [100]. Twu et al. extended a method using a basic chitosan suspension with simultaneous stabilizing and reducing effect to synthesize silver/chitosan nanocomposites from an aqueous  $\text{AgNO}_3$  solution [101, 102].

## 2.5 Biomedical Applications of Electroless Nickel, Cobalt, and Copper

Yang et al. introduced electroless nickel in microtubule-associated proteins demonstrating the stability of microtubules during the process of electroless plating with Ni and the final nanowire network [103].

They showed that electroless plating of microtubule-associated proteins in a bath containing nickel acetate (50 g/L), sodium citrate (25 g/L), lactic acid 85 % (25 g/L), and a reducing agent–DMAB (dimethylamine borane complex, 2.5 g/L), stabilized microtubules resulted in the formation of a continuous network of metallic nanowires. The metal coating consisted of small, crystalline Pt clusters embedded in an amorphous metal matrix composed of Ni distributed along the entire surface of the microtubules [103]. Lu et al. reported a synthesis of monodisperse water-soluble magnetic Co nanoparticles using a facile reduction method in aqueous media in the presence of alkyl thioether end-functionalized poly(methacrylic acid) (PMAA-DDT) ligands [104]. Co nanoparticles were prepared by reduction of  $\text{Co}^{2+}$  in water in the presence of the polymer ligand. In a typical procedure, the reductant  $\text{NaBH}_4$  and the polymer were added to a flask. The size and the shape of the nanoparticles were both tunable by varying synthesis conditions. The Co nanoparticles were readily water-soluble and could be used directly for biomedical assays such as an MRI contrast enhancer. In addition, the PMAA-DDT polymer coating could be conjugated directly with biomolecules via the carboxylic groups, potentially exploiting further for other biomedical applications (e.g., magnetic separation, immunoassays, stem cell tracking, cancer metastasis monitoring using MRI, targeted drug delivery, and hyperthermia cancer treatment) [104]. Kristian et al. studied the preparation of PtCo/C electrocatalysts using redox transmetalation reaction at different pH. Carbon-supported PtCo nanoparticle catalysts with core-shell structure via reduction method and subsequent electroless deposition [105].

A copper sulfate solution containing acetic acid as a complexant and ascorbic acid as reducing agent was used by Valenzuela et al. to metalize self-assembling protein-based microtubules in order to produce nanowires for interconnects [106]. A copper electroless plating bath containing 30 g/L of  $\text{CuSO}_4$ , 140 g/L of sodium potassium tartrate, 20 g/L of NaOH, and 10 mL/L of formaldehyde was used to demonstrate a facile method of fabricating copper nanowires using DNA molecules as templates. The fabrication takes advantage of the electroless plating of copper including activation with palladium. The diameter of the nanowires can be easily controlled by the plating time [107]. Copper and nickel electroless deposition was used over the pre-anodized titanium substrates in order to produce anodes for the process of the electrochemical degradation in wastewater [108].

## 2.6 Metal Nanostructures by Galvanic Displacement

This simple reaction can be used with a wide variety of metal templates and salt precursors and is limited by little more than the requirement of an appropriate difference in the electrochemical potentials between the two metals. Based on fundamental chemistry, this reaction provides a straightforward and versatile route to a broad range of simple and complex structures including hollow nanocrystals, alloyed nanostructures with controllable elemental compositions, and nanoparticles with tunable optical properties [63]. The alloying and dealloying processes involved in a galvanic displacement reaction also have a strong impact on both the structures and properties of the final products [109, 110]. In recent years, the synthesis of solid metal nanocrystals having a wide variety of shapes and sizes has been achieved through careful control of the reaction conditions such as temperature, the concentrations of trace ions, and surfactant choice [111]. Many of these nanocrystals can be used as templates for galvanic displacement reactions, making it possible to use this technique to synthesize hollow nanostructures with well-defined and controllable sizes and shapes.

A typical example can be found in the reaction between Ag nanocubes and  $\text{HAuCl}_4$ . When more than one type of facets are present on the surface of the initial Ag nanocubes, it is possible to synthesize Au nanocages with controlled pores at the corners, as shown in Fig. 2.5 [112, 113]. It is also possible to use this method to generate hollow nanotubes with diameters of 100 nm and lengths of several microns. One of the most useful features of nanostructures synthesized with a galvanic displacement reaction is the highly tunable optical properties that result from the tunable shift in the ratio between the inner and outer particle diameters (i.e., the wall thickness). Galvanic displacement allows for straightforward tuning of the LSPR peak of nanostructures across the visible region and into the NIR due to the coupling between the surface plasmons of the inner and outer surfaces [63].

Galvanic displacement can find applications in the development of new electrochemical sensors. Sensors are the devices which are composed of an active sensing material with a signal transducer. Among these, electrochemical sensors have more advantage over the others because, in these, the electrodes can sense the materials which are

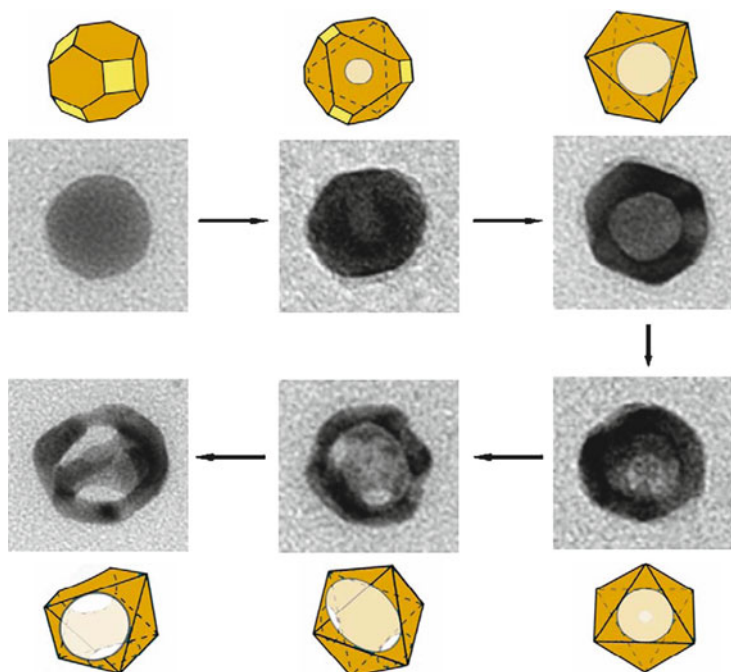


**Fig. 2.5** Schematics and TEM images showing the different stages of a galvanic displacement reaction between  $\text{HAuCl}_4$  and 24-nm Ag spheres. *Yellow and orange colors* indicate  $\{1\ 0\ 0\}$  and  $\{1\ 1\ 1\}$  facets, respectively. Reproduced with permission from American Chemical Society (Kim et al. [112])

present within the host without doing any damage to the host system [114]. Within these sensors, the active sensing material on the electrode should act as a catalyst and catalyze the reaction of the target compounds to obtain the output signals. The selection and development of an active material is a challenge. The recent development in the nanotechnology has paved the way for large number of new materials and devices of desirable properties which have useful functions for numerous electrochemical sensor and biosensor applications [115]. Basically by creating nanostructure, it is possible to control the fundamental properties of materials even without changing their chemical composition. In this way the attractive world of low-dimensional systems, together with the current tendencies on the fabrication of functional nanostructured arrays could play a key role in the new trends of nanotechnology. A good method for generating any kind of

nanostructures should enable simultaneous control of the dimensions, properties, and morphology. The creation of an indented surface, i.e., modification of a surface by nanostructures, is essential for effective enlargement of the surface area. It is expected that the enlargement of the surface area of sensing electrodes will result in a significant increase in microsensor sensitivity. This is one of the reasons why nanostructures are considered promising in the field of sensing technology. Metal nanostructures are especially promising in biosensing applications. The reducing behavior of elemental silicon toward noble metal ions in aqueous solutions containing fluoride ions has long been known. The following reagents were used to prepare the basic aqueous solution: gold sulfite solution 0.01 M, sodium fluoride 0.1 M, sulfuric acid to pH=2; single crystalline (100) silicon, p-type, was used as a substrate [116]. The preparation of a protein monolayer can be a crucial step in the development of bionanodevices that find applications in the field of biomaterials, biocoatings, biofuel cells, and solar cells based on the use of natural photosynthetic complexes. Most of these nanotechnological applications require the formation of a protein monolayer on a conductive support in a correct conformation and orientation. The preparation of a monolayer of the flavoenzyme monooxygenase from *Thermobifida fusca* on a gold film prepared by galvanic displacement on silicon in the sulfite–fluoride solution was reported [116, 117]. This enzyme can be applied in the field of biocatalysis and its immobilization on conductive supports could be an approach for improving its performance also in biosensors [118, 119]. The goodness of the Au film for enzyme adsorption was evaluated by comparison of the enzyme-specific activity and of the enzyme-loading capacity. The gold films obtained by immersion of the silicon substrate into a basic chloride solution were characterized by very poor adhesion. The deposits were easily abraded with soft paper and peeled off with scotch tape. The use of sulfite produced metallic films resistant to abrasion by soft paper and to peeling by scotch tape. The deposits were smooth, highly reflective, and continuous across the gold/silicon interface, even if the film structure is characterized by coarsening of clusters due to the three-dimensional growth. In Fig. 2.6, the phenylacetone monooxygenase PAMO adsorption of the gold surface is reported in comparison with the control.

In the case of gold surfaces from sulfite-based solutions, a large increase in the adsorption with respect to the control sample without enzyme was observed. The same increase was not detected for samples from chloride-based solutions.

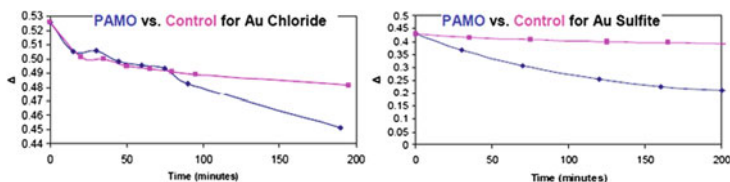


**Fig. 2.6** PAMO adsorption  $\Delta$  (Abs at 341 nm–Abs at 440 nm) vs. control for gold from chloride and sulfite. Reproduced with permission from The Electrochemical Society (Magagnin et al. [116])

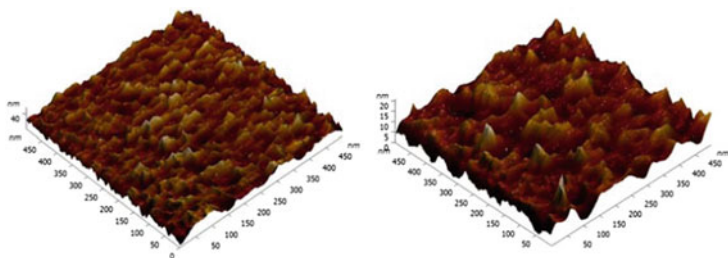


**Fig. 2.7** AFM image for gold from sulfite before (Average roughness 4.8 nm) and after (Average roughness 1.3 nm) enzyme adsorption. Reproduced with permission from The Electrochemical Society (Magagnin et al. [116])

Adsorption was also confirmed by the change in the morphology and roughness of the gold surface from sulfite solution before and after treatment, as it can be observed in Fig. 2.7. Galvanic displaced gold was used for enzyme adsorption for biosensor application; the formulation of the electrolyte allows to tune and to improve also the interaction with the enzymes [116].

## 2.7 Conclusions

Electroless deposition and galvanic displacement demonstrate to be a viable route for the synthesis of metallic nanostructures with successful exploitation in biomedical applications. Renewed and upcoming research in this area is required in order to find and illuminate new processes and to deeply understand the mechanisms of the deposition process and its control. The nanomaterials generated through these methods, combining advanced nanostructuring and multifunctional

building blocks, will play a fundamental role in the designing of nanobiosystems able to interact with the biological systems at the nanolevel.

## References

1. Carraro C, Maboudian R, Magagnin L (2007) *Surf Sci Rep* 62:499
2. Schlesinger M, Paunovic M (2000) *Modern electroplating*, 4th edn. Wiley, New York
3. Kanani N (2005) *Electroplating: basic principles, processes and practise*. Elsevier Science, Amsterdam
4. Johnson RW (1961) *J Electrochem Soc* 108:632
5. Werbicki JJ (1971) *Plating* 58:763
6. Ma DH, Levy DJ (1978) *J Electrochem Soc* 125:1741
7. Kovac Z, Tu K-N (1984) *IBM J Res Dev* 28:726
8. Monteiro FJ, Barbosa MA, Gabe DR, Ross DH (1989) *Plat Surf Finish* 76:86
9. Keping H, Jingli F (1996) *Trans Inst Met Finish* 74:95
10. Stoyanova E, Stoychev D (1997) *J Appl Electrochem* 27:685
11. Wei Z-L, Tang D, Wang X, You S-X (2005) *Jinshu Rechuli/Heat Treat Met* 30:262
12. Meeh P (2005) *Circuit World* 31:28
13. Hashimoto S, Kiso M, Oda Y, Otake H, Milad G, Gudacauskas D (2006) *Circuit World* 32:16
14. Yang L, Luan B (2005) *J Electrochem Soc* 152:C474
15. Brevnov DA, Olson TS, Lopez GP, Atanassov P (2004) *J Phys Chem B* 108:17531
16. Guenther B (2000) *Trans IMF* 78:143
17. Lee D-J, Lee HS (2006) *Microelectron Reliab* 46:1119
18. Djokic SS (2002) In: Conway BE, White RE (eds) *Modern aspects of electrochemistry*, No. 35. Kluwer Academic/Plenum, New York, p 51
19. Laser D, Bard AJ (1976) *J Electrochem Soc* 123:1828
20. Laser D, Bard AJ (1976) *J Phys Chem* 80:459
21. Nozik AJ (1980) *Faraday Discuss Chem Soc* 70:7
22. Magagnin L, Cojocaru P, Cavallotti PL (2011) *ECS Trans* 33:1
23. Fan T-X, Chow S-K, Zhang D (2009) *Prog Mater Sci* 54:542
24. Rosi NL, Thaxton CS, Mirkin CA (2004) *Angew Chem Int Ed* 43:5500
25. D'Asaro LA, Nakahara S, Okinaka Y (1980) *J Electrochem Soc* 127:1935
26. Ting CH, Paunovic M, Pai PL, Chiu G (1989) *J Electrochem Soc* 136:462
27. Nagahara LA, Ohmori T, Hashimoto K, Fujishima A (1992) *J Electroanal Chem* 333:363
28. Nagahara LA, Ohmori T, Hashimoto K, Fujishima A (1993) *J Vac Sci Technol A* 11:763
29. Dryfe RAW, Walter EC, Penner RM (2004) *Chem Phys Chem* 5:1879

30. Lide DR (2007) CRC handbook of chemistry and physics, 87th edn. Taylor and Francis, Boca Raton, FL
31. Gorostiza P, Diaz R, Sanz F, Morante JR (1997) *J Electrochem Soc* 144:4119
32. Gorostiza P, Allongue P, Diaz R, Morante JR, Sanz F (2003) *J Phys Chem B* 107:6454
33. Chyan OMR, Chen JJ, Chien HY, Sees J, Hall LJ (1996) *Electrochem Soc* 143:92
34. Jeon JS, Raghavan S, Parks HG, Lowell JK, Ali I (1996) *J Electrochem Soc* 143:2870
35. Lee MK, Wang HD, Wang JJ (1997) *J Solid State Electron* 41:695
36. dos Santos FSG, Martins LFO, D'Ajello PCT, Pasa AA, Hasenack CM (1997) *Microelectron Eng* 33:59
37. dos Santos FSG, Pasa AA, Hasenack CM (1997) *Microelectron Eng* 33:149
38. Lee MK, Wang JJ, Wang HD (1997) *J Electrochem Soc* 144:1777
39. Li G, Kneer EA, Vermiere B, Parks HG, Raghavan S, Jeon JS (1998) *J Electrochem Soc* 145:241
40. Srinivasan R, Suni II (1998) *Surf Sci* 408:L698
41. Srinivasan R, Suni II (1999) *J Electrochem Soc* 146:570
42. Rossiter C, Suni II (1999) *Surf Sci* 430:L553
43. Balashova NA, Eletsii VV, Medyntsev VV (1965) *Elektrokhimiya* 1:274
44. Krikshtopaitis IB, Kudzhmauskaite ZP (1971) *Elektrokhimiya* 7:1579
45. Magagnin L, Maboudian R, Carraro C (2002) *J Phys Chem B* 106:401
46. Perfetti P, Katnani AD, Zhao T-X, Margaritondo G, Bisi O, Calandra C (1982) *J Vac Sci Technol* 21:628
47. Calandra C, Bisi O, Ottaviani G (1985) *Surf Sci Rep* 4:271
48. Liu F-M, Green M (2004) *J Mater Chem* 14:1526
49. Peng K, Zhu J (2004) *Electrochim Acta* 49:2563
50. Aizawa M, Buriak JM (2006) *J Am Chem Soc* 128:5877
51. Dhingra S, Sharma R, George PJ (1999) *Solid State Electron* 43:2231
52. Cheng X, Li G, Kneer EA, Vermiere B, Parks HG, Raghavan S, Jeon JS (1998) *J Electrochem Soc* 145:352
53. Ogata YH, Sasano J, Itoh T, Sakka T, Rayon E, Pastor E, Parkhutik V (2005) *J Electrochem Soc* 152:C537
54. Oskam G, Long JG, Natarajan A, Searson PC (1998) *J Phys D Appl Phys* 31:1927
55. Magagnin L, Maboudian R, Carraro C (2001) *Electrochem Solid State Lett* 4:C5
56. Xu J, Jordan RB (1990) *Inorg Chem* 29:2933
57. Gorostiza P, Diaz R, Servat J, Sanz F (1997) *J Electrochem Soc* 144:909
58. Porter LA Jr, Choi HC, Schmeltzer JM, Ribbe AE, Elliott LCC, Buriak JM (2002) *Nano Lett* 2:1369
59. Ye XR, Wai CM, Zhang D, Kranov Y, McIlroy DN, Lin Y, Engelhard M (2003) *Chem Mater* 15:83
60. Karmalkar S, Banerjee J (1999) *J Electrochem Soc* 146:580
61. Messori L, Marcon G (2004) In: Sigel A (ed) *Metal ions and their complexes in medication*. CRC, Boca Raton, p 280
62. Lewinski N, Colvin V, Drezek R (2008) *Small* 4:26

63. Cobley CM, Xia Y (2010) *Mater Sci Eng R* 70:44
64. Stuart DA, Haes AJ, Yonzon CR, Hicks EM, Van Duyne RP (2005) *IEE Proc Nanobiotechnol* 152:13
65. Sherman AI, Ter-pogossian M (1953) *Cancer* 6:1238
66. Paciotti GF, Myer L, Weinreich D, Goia D, Pavel N, McLaughlin RE, Tamarkin L (2004) *Drug Deliv* 11:169
67. Love J, Estroff L, Kriebel J, Nuzzo R, Whitesides G (2005) *Chem Rev* 105:1103
68. Alkilany AM, Nagaria PK, Hexel CR, Shaw TJ, Murphy CJ, Wyatt MD (2009) *Small* 5:701
69. Peer D, Karp JM, Hong S, Farokhzad OC, Margalit R, Langer R (2007) *Nat Nanotechnol* 2:751
70. Au L, Zhang Q, Cobley CM, Gidding M, Schwartz AG, Chen J, Xia Y (2010) *ACS Nano* 4:35
71. Cho EC, Au L, Zhang Q, Xia Y (2010) *Small* 6:517
72. Cobley CM, Chen J, Chul Cho E, Wang LV, Xia Y (2011) *Chem Soc Rev* 40:44
73. Daniel M-C, Astruc D (2004) *Chem Rev* 104:293
74. Yavuz MS, Cheng Y, Chen J, Cobley CM, Zhang Q, Rycenga M, Xie J, Kim C, Song KH, Schwartz AG, Wang LV, Xia Y (2009) *Nat Mater* 8:935
75. Kreibitz U, Vollmer M (1995) *Optical properties of metal clusters*, vol 25, Springer series in material science. Springer, Berlin
76. Kelly K, Coronado E, Zhao L, Schatz GC (2003) *J Phys Chem B* 107:668
77. Wiley BJ, Im SH, Li Z-Y, McLellan J, Siekkinen AR, Xia Y (2006) *J Phys Chem B* 110:15666
78. Lei Y, Chen H, Dai H, Zeng Z, Lin Y, Zhou F, Pang D (2008) *Biosens Bioelectron* 23:1200
79. Samanta B, Yan H, Fischer NO, Shi J, Jerry DJ, Rotello VM (2008) *J Mater Chem* 18:1204
80. Cherukuri P, Glazer ES, Curley SA (2010) *Adv Drug Deliv Rev* 62:339
81. Chen C-M, Yeh M-L, Chien C-S, Chuang Y-T, Lin C-H (2009) *IEEE SENSORS Conf* 2009:1788
82. Lu Z-X, Wood LF, Ohman DE, Collinson MM (2009) *Chem Commun* 4200
83. Laurent S, Forge D, Port M, Roch A, Robic C, Vander Elst L, Muller RN (2008) *Chem Rev* 108:2065
84. Pankhurst QA, Thanh NKT, Jones SK, Dobson J (2009) *J Phys D Appl Phys* 42:224001
85. Suzuki D, Kawaguchi H (2005) *Langmuir* 21:8175
86. Suzuki D, Kawaguchi H (2005) *Langmuir* 21:12016
87. Schwarz A, Hakuzimana J, Kaczynska A, Banaszczyk J, Westbroek P, McAdams E, Moody G, Chronis Y, Priniotakis G, De Mey G, Tseles D, Van Langenhove L (2010) *Surf Coat Technol* 204:1412
88. Shao W, Zhao Q (2010) *Surf Coat Technol* 204:1288
89. Schierholz JM, Lucas LJ, Rump A, Pulverer G (1998) *J Hosp Infect* 40:257
90. McArdle P (2005) *Am J Infect Control* 33:130
91. Zhao Q, Liu Y, Wang C, Wang S, Müller-Steinhagen H (2005) *Chem Eng Sci* 60:4858
92. Zhao Q, Liu Y (2006) *J Food Eng* 72:266

93. Zhao Q, Wang C, Liu Y, Wang S (2007) *Int J Adhes Adhes* 27:85
94. Gray JE, Norton PR, Alnouno R, Marolda CL, Valvano MA, Griffiths K (2003) *Biomaterials* 24:2759
95. Zhao Q, Liu Y, Wang C (2005) *Appl Surf Sci* 252:1620
96. Park HK, Yoon JK, Kim K (2006) *Langmuir* 22:1626
97. Kim K, Kim HS, Park HK (2006) *Langmuir* 22:8083
98. Lee HY, Park HK, Lee YM, Kim K, Park SB (2007) *Chem Commun* 29:2959
99. Oh SD, Lee S, Choi SH, Lee IS, Lee YM, Chun JH, Park HJ (2006) *Colloids Surf A Physicochem Eng Asp* 275:228
100. Fu J, Ji J, Fan D, Shen J (2006) *J Biomed Mater Res A* 79A:665
101. Twu YK, Chen YW, Shih CM (2008) *Powder Technol* 185:251
102. Dastjerdi R, Montazer M (2010) *Colloids Surf B Biointerfaces* 79:5
103. Yang Y, Constance BH, Deymier PA, Hoying J, Raghavan S, Zelinski BJJ (2004) *J Mater Sci* 39:1927
104. Lu LT, Tung LD, Robinson I, Ung D, Tan B, Long J, Cooper AI, Fernig DG, Thanh NTK (2008) *J Mater Chem* 18:2453
105. Kristian N, Yu Y, Lee J-M, Liu X, Wang X (2010) *Electrochim Acta* 56:1000
106. Valenzuela K, Raghavan S, Deymier PA, Hoying J (2008) *J Nanosci Nanotechnol* 8:3416
107. Kudo H, Fujihira M (2006) *IEEE Trans Nanotechnol* 5:90
108. Mahmoud SS (2009) *J Alloys Compd* 472:595
109. Skrabalak SE, Chen J, Sun Y, Lu X, Au L, Cogley CM, Xia Y (2008) *Acc Chem Res* 41:1587
110. Lu X, Chen J, Skrabalak SE, Xia Y (2008) *Proc Inst Mech Eng N* 221:1
111. Xia Y, Xiong Y, Lim B, Skrabalak SE (2009) *Angew Chem Int Ed* 48:60
112. Kim MH, Lu X, Wiley BJ, Lee EP, Xia Y (2008) *J Phys Chem C* 112:7872
113. Chen J, McLellan J, Siekkinen A, Xiong Y, Li Z-Y, Xia Y (2006) *J Am Chem Soc* 128:14776
114. Wilson GS, Gifford R (2005) *Biosens Bioelectron* 20:2388
115. Hubalek J, Hradecky J, Adam V, Krystofova O, Huska D, Masarik M, Trnkova L, Horna A, Klosova K, Adamek M, Zehnalek J, Kizek R (2007) *Sensors* 7:1238
116. Magagnin L, Cojocar P, Raygani A, Brivio D, Secundo F, Turolla A, Ottolina G (2011) *ECS Trans* 33:59
117. Fraaije MW, Wu J, Heuts D, van Hellemond EW, Spelberg J, Janssen DB (2005) *Appl Microbiol Biotechnol* 66:393
118. Lansdown ABG (2002) *J Wound Care* 11:125
119. Wang S, Hou W, Wei L, Jia H, Liu X, Xu B (2007) *Surf Coat Technol* 202:460

# Chapter 3

## Biodegradable Mg Alloys: Corrosion, Surface Modification, and Biocompatibility

Sannakaisa Virtanen

### 3.1 Introduction

Metallic materials used in biomedical applications traditionally are highly corrosion resistant, in order to prevent degradation of permanent implants and to diminish possibly harmful metal ion release. Therefore, metallic materials used for instance in orthopaedic applications include Ti base alloys, stainless steels, or Co–Cr–Mo alloys. As these materials are passive in the human body, only a quite small amount of metal ions is released into the surroundings by electrochemical corrosion. A very different approach is the use of low-corrosion-resistant metals for biodegradable, temporary implants. Biodegradable (or bioabsorbable) implants are of interest for applications, in which from medical point of view the implant is not required to stay in the body permanently. An example of such an application is stenting, where remodeling of the arterial wall is expected to take place and a continuous presence of the stent becomes unnecessary. For biodegradable metals, once implanted, the device would stay in human body only for the time it takes to heal, and then it will spontaneously dissolve away. Permanent metallic implants can lead to certain biocompatibility problems related to continuous physical/mechanical irritation and long-term release of metallic

---

S. Virtanen (✉)

Department of Materials Science and Engineering (WW-4),  
Institute for Surface Science and Corrosion, University of Erlangen-Nuremberg,  
Martensstrasse 7, Erlangen 91058, Germany  
e-mail: Virtanen@ww.uni-erlangen.de

ions and/or particles through corrosion or wear processes. Moreover, implantation in children would require an additional surgery in order to remove the permanent implant which cannot adapt to growth of the human body. Such problems could be avoided using a bioabsorbable implant.

Due to their non-toxic nature and easiness of corrosion, Mg- and Fe-based materials have been considered as promising candidates for biodegradable implants. This chapter will only discuss Mg alloys as biodegradable implant material. Recent reviews on the development of biodegradable stents, including a description of the state-of-the-art for both Fe and Mg alloys, are provided by [1, 2]. Alloy design concepts for Fe- and Mg-based biodegradable metals are given in [3–5].

Mg alloys have been considered for use as biomaterials suitable for both degradable bone implants [6] and bioabsorbable cardiovascular stents [7]. In addition to the non-toxicity of Mg ions (which belong to the most abundant cations in the human body), Mg takes part in many metabolic reactions, and hence the use of Mg alloys in biodegradable implants could even trigger some desired physiological reactions. At high concentrations Mg becomes toxic, but Mg toxicity by corrosion of implants is not expected to be a problem as it is expected that homeostatic mechanisms should efficiently control the free concentration. For orthopedic applications an interesting fact is the relatively low elastic modulus of Mg alloys, which is significantly nearer to the mechanical properties of bone than is the case for other traditional metallic implant materials. Hence, less stress shielding effects would be expected when using Mg alloys.

The idea to use magnesium alloys as biodegradable implant is not new, as discussed in review on the history of Mg-based implants [8]. Due to different type of problems related to the state of materials, such as high-corrosion rates because of large amounts of impurities in the early alloys, their use was stopped shortly after their introduction. Nowadays, a better control of the alloy chemistry (alloying and impurities) as well as a better understanding of the critical factors in Mg alloy corrosion exists. The state-of-the-art of magnesium alloys as biomaterials is summarized in a recent review in [9]. Corrosion behavior of Mg alloys in view of their use in biomedical applications is summarized in [10, 11]. General information on Mg alloy corrosion can be found in [12–14].

### 3.2 Basics of Magnesium Corrosion in View of Biocompatibility Considerations

Magnesium has a very low electrochemical potential ( $E^\circ = -2.4$  V vs. SHE) indicating its very high tendency to oxidation. Figure 3.1 shows the potential–pH diagram for Mg, illustrating the wide region of active dissolution [15]. As Mg passivation is only possible in alkaline environments and in the absence of aggressive species such as chlorides, active dissolution of Mg takes place in most natural environments. The low electrochemical potential of Mg also leads to a high risk of galvanic corrosion, when Mg is in contact with most other technologically important metals and alloys. Moreover, most impurities and alloying elements of Mg are nobler than the Mg matrix, and hence internal galvanic corrosion is a typical corrosion mode of non-pure Mg. This is especially significant as the kinetics of the cathodic hydrogen evolution reaction is relatively low on pure Mg; hence a strong acceleration of the active dissolution rate of Mg is encountered in the presence of impurity inclusions or second-phase particles enriched in the alloying elements—these particles then act as efficient cathodes coupled with the Mg matrix anode. Such internal galvanic

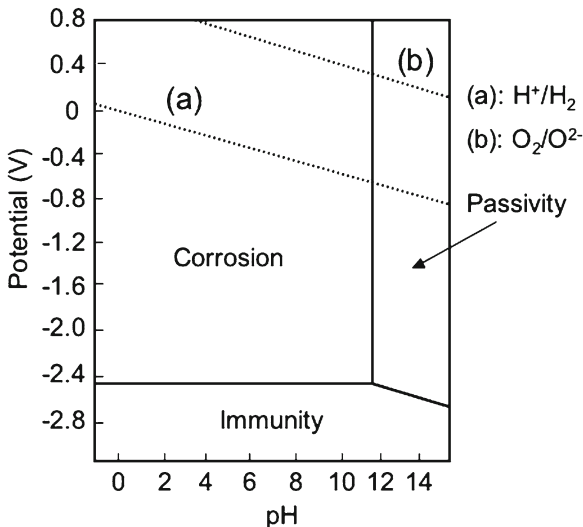


Fig. 3.1 Potential–pH (Pourbaix) diagram for Mg in  $H_2O$

corrosion not only accelerates dissolution of the Mg matrix, but it moreover often leads to a highly non-homogeneous dissolution morphology, as the cathodic and the anodic sites are separated. For any application based on controlled metal degradation, a layer-by-layer uniform dissolution would be easier to use for life-time prediction than highly non-uniform dissolution mode. Moreover, in biomedical applications, where the device may experience mechanical loading, non-uniform dissolution can lead to the formation of non-uniform stresses in the device and in worst case to pre-mature mechanical failure.

The low electrochemical potential also indicates that Mg corrosion is always coupled with hydrogen gas evolution: the anodic Mg oxidation reaction is coupled with reduction of hydrogen from water; see Eqs. (3.1) and (3.2) for Mg corrosion.

Anodic reaction



Cathodic reaction



The hydrogen gas evolution as a coupled reaction to Mg oxidation can be of significance for the use of Mg alloys in biomedical applications, as questions arise on the absorption/transport of hydrogen gas in tissues. If the local hydrogen generation rate is too high, hydrogen accumulation leading to gas pockets can take place. Of course, any approaches to control the Mg corrosion rate, will reduce the hydrogen evolution rate. Due to the significance of the hydrogen gas production in the biomedical application, many researchers interested in biodegradable Mg alloys use the  $\text{H}_2(\text{g})$  collection experiments as a measure to the corrosion rate. Even though the volumetric detection of gas production as such is a simple tool to monitor corrosion as a function of time, such measurements do not give information on the mechanisms of corrosion. For instance, if a newly developed alloy shows lower rates of hydrogen gas evolution than a reference alloy, conclusions cannot be made if the alloying elements influence the kinetics of the cathodic or anodic reactions.

Another issue of significance in view of biocompatibility is the fact that Mg corrosion leads to an alkaline shift of the pH value in the

vicinity of the corroding surface. This alkaline pH shift results from the fact that  $\text{Mg}^{2+}$  cation is weak cation acid, and hence do not react with water under production of protons. Therefore, formation of  $\text{Mg}^{2+}$  in the anodic reaction cannot neutralize the alkaline pH shift due to the cathodic reaction [in the case of Mg corrosion, mostly reduction of hydrogen ions, see (3.2)]. It is noteworthy that the alkaline pH shift can be beneficial for surface passivation of Mg, considering the Pourbaix diagram shown in Fig. 3.1. However, in view of the use of Mg in the human body, the alkalization of the environment can be harmful for the biological environment. Even though the body fluids are buffered, pH increase is possible in the vicinity of the surface of the Mg implant. This has been demonstrated in the laboratory [16–18], details of the pH behavior of the solution during Mg corrosion of course depend very strongly on the experimental conditions such as the ratio of the Mg sample surface to the volume of the electrolyte. In the biomedical applications in vivo, the situation is more complex. For instance, blood flow can refreshen the electrolyte, and hence less strong pH effects would be expected than under stagnant conditions. On the other hand, if the Mg alloy surface is covered by cell-adherent layers or by tissue, local chemistries may evolve on the surface, as mass transfer is hindered. Even though information is hardly available on in vivo observations on local pH values in the vicinity of Mg implants, it is noteworthy to point out that cell death has been demonstrated to take place in in vitro experiments due to Mg corrosion-induced pH increase in medium [18].

For some applications targeted, the corrosion rate of conventional (commercial) alloys seems to be too high. This statement, however, is mostly based on in vitro investigations in simulated body fluids (SBFs), and the choice of the SBF can drastically influence the measured corrosion rates (see e.g., [19, 20]) as well as be very different to the in vivo case (see e.g., [21]). One challenge in the field of Mg alloy biodegradation is that relatively little in vivo information on the degradation rates is still available. For stents, where the dimensions of the structures are quite small, the initial fast corrosion rate may lead to too fast degradation of the device. On the other hand, for other types of applications such as bone plates, the dimensions are significantly larger. It is therefore possible that the initial corrosion rate is high but the formation of sparingly soluble corrosion products can slow down dissolution and even prevent complete bioabsorption of the implant with time. These considerations illustrate that in any

case measures to control the corrosion rate are required; in best case leading to a desired time-dependence of degradation, for instance sufficiently slow dissolution in the beginning, then faster dissolution leading to complete disappearance of the device after desired time.

One approach to control the corrosion rate would be the development of novel Mg alloys. It should be recognized, however, that Mg alloying is a highly challenging task, as Mg has a low solubility for many elements. Therefore alloying often leads to the formation of second-phase particles, which may be desired for mechanical strengthening of the alloy, but as already mentioned, in most cases this can lead to the formation of galvanic couples on the alloy surface and accelerates dissolution of the less noble Mg matrix. Moreover, in the case of development of biodegradable Mg alloys, alloying elements of course should be non-toxic.

Another route to modify the corrosion behavior of any material is the use of different types of surface modification techniques or coatings. Any coating that would decrease Mg dissolution rate, would automatically also reduce the issues of concern of the coupled hydrogen evolution reaction and the surface alkalization. In the case of biodegradable Mg alloys, the coating behavior should be compatible with the biomedical application; depending on the targeted application the specifications for coatings vary. The coatings by no means should provide a too perfect barrier for dissolution, as biodegradation is still desired. For imperfect coatings, however, care should be taken that strong localized dissolution at coating defects should not lead to undermining and possibly flaking off of the coating.

### **3.3 Critical Factors in Mg Alloy Corrosion**

#### **3.3.1 *Impurity Content***

The detrimental effect of small amounts of certain impurities, such as Fe, Ni, Cu, on the corrosion rate of Mg alloys is well known. For these elements, tolerance limits have been determined, below which the corrosion rate remains low but drastically increases upon exceeding the tolerance limit. It is important to point out that these tolerance limits depend on the alloy composition. The effects of these impurities are mostly explained to be due to internal galvanic coupling effects, in

that the impurities form efficient local cathodes for the hydrogen evolution coupled with the less noble matrix. Recent studies on the effect of Fe impurity in Mg and Mg–Al alloys indicate that the corrosion behavior of the alloys can be dominated by the Fe impurities, and that Fe-rich particles in the microstructure are responsible for the strong acceleration of the dissolution rate upon exceeding the tolerance limit [22]. Therefore, in order to truly compare the corrosion behavior of different alloys, the impurity content should be reported. Figure 3.2 shows an example on the influence of purity of Mg and Mg–Al alloys, specifically of the Fe content, on the dissolution behavior in 3% NaCl measured as hydrogen evolution volume [22]. The low-purity Mg shows the highest corrosion rates of all alloys studied, whereas the high-purity Mg shows very low dissolution rates. Moreover, comparing the behavior of the different Mg–Al alloys (with a variation in Al and Fe content), the authors concluded that the differences in the corrosion behavior are mainly due to the increase in the impurity content, and cannot be directly attributed to the Al-content of the alloy.

### 3.3.2 Alloy Composition

Commercial Mg alloys often contain Al and Zn as major alloying elements. Other alloying elements of interest are Y, Zr, and rare earths.

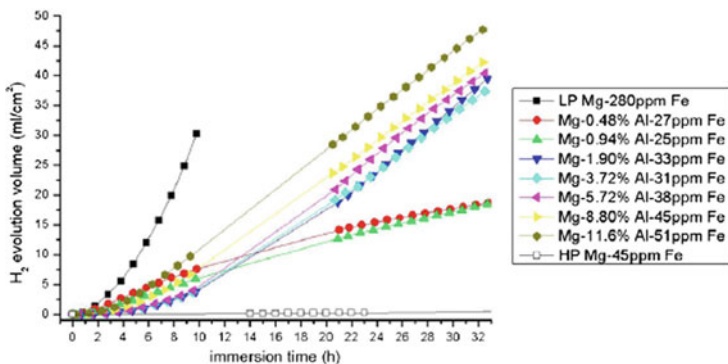


**Fig. 3.2** Corrosion behavior, measured as hydrogen gas evolution, for high-purity (HP) and low-purity (LP) Mg as well as some Mg–Al alloys in 3% NaCl. Reprinted from [22], with permission from Elsevier

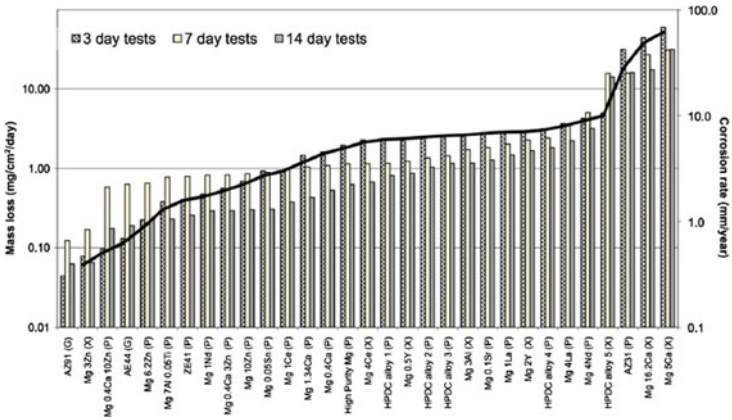


**Fig. 3.3** Corrosion rates for a variety of Mg alloys determined in MEM (Minimum Essential Medium) at 37°C. Reprinted from [24], with permission from Elsevier

Exploratory alloys for use in biodegradable implants include for instance Mg–Ca and Mg–Ca–Zn alloys. For the use of Mg alloys in biomedical applications, new boundary conditions for the choice of alloying arise, in that the alloying elements should be non-toxic. Hence, for instance a commercial alloy AZ91 (9% Al, 1% Zn) with good mechanical and corrosion behavior may not be an optimum choice for biodegradable implants, due to the high Al content. The role of the alloying elements is, in addition to modifying the corrosion behavior, to improve the mechanical properties of the alloys. In solid solution, the alloying elements can influence the anodic dissolution rate of Mg. Most Mg alloys of interest, however, are heterogeneous, multi-phase alloys. This is of major significance for the corrosion behavior: The alloying elements are enriched in intermetallic particles, and as typically the conventional alloying elements are more noble than Mg, internal galvanic coupling similar to the above discussed effects of impurities is resulting. This may lead to non-uniform corrosion morphology, as the anodic and cathodic sites are locally separated. On the other hand, hydrogen evolution kinetics is relatively slow on pure Mg, and can be significantly faster on many of the intermetallic phases present in the alloys—this is an additional corrosion-accelerating effect [23]. A survey of the biocorrosion behavior of commercial and exploratory Mg alloys demonstrates that the dissolution rate of different alloys can vary by three orders of magnitude; this variation in dissolution rates by alloying is unexceptionally high, see Fig. 3.3 [24].

### 3.3.3 *Effect of Simulated Body Solution Composition on Mg Alloy Corrosion*

It is important to note that the choice of SBF for in vitro assessment of the corrosion behavior of Mg alloys can have a very striking influence on the results obtained. From chemical point of view, the corrosive environment of body fluids consists of a 0.9% NaCl solution with small amounts of other inorganic salts (such as  $\text{Ca}^{2+}$ ,  $\text{PO}_4^{3-}$ , and  $\text{HCO}_3^-$ , for more details see [25, 26]), at a temperature of  $37^\circ\text{C}$ . The chemical environment of blood plasma is highly aggressive for Mg and its alloys, due to the high concentration of chloride ions. Other ions in the body fluids, especially phosphates and carbonates, form relatively sparingly soluble compounds with Mg cations. Hence corrosion product layers are precipitated on the surface; these layers provide only limited corrosion protection, as they are often porous. Recent studies demonstrate the important role of  $\text{HCO}_3^-$  ions in the formation of compact and well-protecting surface layers on Mg [27]; measurements of corrosion rates in SBFs with different  $\text{HCO}_3^-$  concentrations led to a variation of the degradation rate by a factor of 10. In addition to the exact ionic composition of different SBFs [25, 26], different buffers [e.g., tris(hydroxymethyl)aminomethane (TRIS), 4-(2-hydroxyethyl)-1-piperazineethanesulfonic acid (HEPES),  $\text{CO}_2/\text{HCO}_3^-$ ] are used and these not only have different buffer capacities but the choice of buffer can moreover influence the degradation behavior of Mg. These examples clearly demonstrate that the choice of electrolyte for Mg degradation studies very strongly influences the results obtained. In any case a simple physiological saline solution cannot simulate the behavior of Mg in the body, neither as concerns the degradation rate nor the composition of the surface layers forming during corrosion.

In addition to inorganic species, body fluids contain different types of biomolecules and cells, which may adsorb or adhere to the biomaterial surface and thereby affect the corrosion behavior. To better simulate the biological environment, the effect of proteins on the corrosion behavior of Mg alloys has been explored.

Most of these experiments studied the effect of albumin (typically BSA: bovine serum albumin) on Mg alloy corrosion, since albumin is the most abundant blood protein. Mueller et al. studied the effect of albumin addition to PBS (phosphate buffered saline) solutions on the corrosion behavior of pure Mg and the alloys AZ31 and LAE442

**Table 3.1** Composition of some relevant alloys studied in the field of biodegradable Mg alloys (concentrations are given on for the major alloying elements is given in the table)

Alloy	Mg (wt%)	Al (wt%)	Zn (wt%)	Li (wt%)	Rare earths
AZ31	Balance	2.5–3.5	0.6–1.4		
AZ91	Balance	8.0–9.5	0.3–1.0		
LAE 442	Balance	ca. 4		ca. 4	ca. 2

[28]. For the alloy AZ31, albumin addition showed relatively little effect on the electrochemical behavior (potentiodynamic polarization curves), but for pure Mg and the alloy LAE442 albumin additions strongly accelerated anodic dissolution. Table 3.1 shows the chemical composition of the alloys used in these studies. The effect of albumin was also found to be concentration dependent. On the other hand, corrosion inhibition by albumin addition has been reported for the AZ91 alloy (see Table 3.1.) in SBF [29], as well as for Mg–Ca alloy in water and in NaCl solutions [30]. Moreover, a change of albumin effect with time has been observed, in that initially higher polarization resistance ( $R_p$ ) values (corresponding to lower corrosion rates) were measured for a rare-earth metal containing Mg alloy in albumin-containing SBF as compared with albumin-free SBF, but after some hours of immersion the  $R_p$ -values were lower for samples in albumin-containing solution [31]. These examples indicate that albumin (and most probably other proteins, as well) certainly has an influence on the corrosion behavior of Mg and its alloys, but this influence can be alloy- and time-dependent. It should be pointed out, moreover, that the exact mechanisms in play have not been elucidated. Generally, protein adsorption layers could act as an additional barrier between the metal surface and the surroundings, hence inhibiting corrosion. On the other hand, proteins may complex metal cations and therefore could accelerate dissolution. Also, the formation of a biofilm on the metal surface could lead to a “crevice-like” situation on the surface, hindering mass transfer with the bulk electrolyte and hence enforcing chemical changes taking place (e.g., pH increase). In the case of Mg, the nature of the protein adsorption layer on the surface could change with time, for instance due to Mg corrosion and related effects. In how far the pH increase on Mg surface can, for instance, lead to denaturation or even de-adherence of proteins is not clear from the present knowledge-state.

Experiments with the addition of serum in SBFs have also been carried out. In this case, interactions between different biomolecules

and the metal surface are more complex than indicated by the single protein studies. Also in this case, alloy- and time-dependent complex behavior has been observed [32]: for Mg–Ca alloys, serum proteins increased the corrosion rate, for AZ31 alloy in the initial 3 days immersion the serum proteins increased the corrosion rate and thereafter decreased it, whereas for the AZ91 alloy a reduced corrosion rate was observed upon addition of serum to medium. Yamamoto and Hiromoto have carried out a thorough and systematic study on the effect of inorganic salts, amino acids, and proteins of the degradation behavior of pure magnesium [33]: amino acids were found to accelerate dissolution of Mg, which was explained by the chelating effect of the Mg cations, and the presence of serum proteins was found to retard magnesium degradation.

Even though many open questions still exist on the exact mechanisms and interactions between the constituents of SBFs and the Mg alloy surface, it seems clear that the corrosion product layers formed on Mg alloy surfaces in more complex solutions than simple saline solutions can play a significant role in the degradation process. These conversion layers mostly contain large amounts of Ca, Mg, P, O, and C. In [34], the layers formed on a rare-earth containing Mg alloy in m-SBF solution were described as amorphous, hydrated, carbonated (Ca,Mg)-phosphate, based on XRD, EDX, and FT-IR characterization. The layers formed on Mg and Mg alloys in typical compositions of SBF are not highly protective in nature, as indicated for instance by electrochemical impedance spectroscopy measurements [31], this is most probably due to high porosity of these layers. The degradation process of Mg in SBFs hence not only leads to the release of soluble Mg cations, but moreover corrosion product layers are precipitated on the surface. Therefore, a gradual conversion of metallic Mg into Mg-containing corrosion product layers takes place. As discussed in [24], non-soluble and voluminous corrosion products could raise some problems in biomedical applications.

Apart from different SBF solutions, cell culture medium [for instance, Dulbecco's Modified Eagle's cell culture medium (DMEM), with or without addition of fetal bovine serum (FBS)] has also been used as electrolyte for Mg degradation studies. Different authors have demonstrated that Mg alloy corrosion is significantly slower under cell culture conditions than in other types of simulated physiological solutions (e.g., Hank's solution, SBF) [20, 32, 35]. This may be related to surface "passivation" by formation of insoluble Mg-carbonate layers, as has been discussed in [27, 32, 33, 36]. As

carbonate ions seem to be of a high significance for surface reactions of Mg alloys, experiments carried out under CO<sub>2</sub> purging (e.g., cell incubator) as compared with experiments open-to-air can be expected to lead to different behaviors with otherwise same chemical exposures.

Finally, there is emerging evidence that cell-adherent layers on Mg surface can slow down corrosion processes; this was indicated by electrochemical impedance spectroscopy as well as pH measurements in the absence and presence of cells on Mg alloy AZ91 surfaces [18].

### **3.4 Biocompatibility Assessment of Corroding Mg Surfaces**

Different aspects of biocompatibility are addressed by different types of testing methodology. In addition to still relatively few *in vivo* animal studies on Mg alloys and emerging clinical studies, an increasing number of *in vitro* cell studies on corroding Mg surfaces have been published in recent years. It should be mentioned that the alkaline pH shift as well as H<sub>2</sub> gas evolution on corroding Mg alloys surface can drastically affect *in vitro* cell culture testing. *In vitro* cell culture experiments on fast corroding cp-Mg (cp-Mg: commercially pure Mg) surfaces have indicated that without any surface pre-treatments or coatings, cp-Mg surface can be too reactive for cells to adhere and grow; for the static cell culture experiment and for the sample material used for these studies [17, 35]. After simple surface treatments, such as passivation in NaOH or soaking in SBF or in cell culture medium, cells could adhere and spread on Mg surface, as the initial surface reactivity decreased by these surface treatments. For long-term cell behavior, other factors such as continuous increase of alkalinity in the vicinity of the cells can, however, strongly reduce the viability of cells [17].

Recently, an increasing number of cell culture studies on corroding Mg surfaces have been published [37–43]. However, relatively conflicting reports can be found in the literature indicating both survival and death of cells on Mg surfaces. As the types of alloys and cell lines used for these experiments are not identical, it is difficult up to now to draw any generalizing conclusions on the critical factors influencing cell behavior on Mg alloy surfaces. Moreover, it has been

discussed in the literature that current *in vitro* test procedures for cytotoxicity, cell viability, and proliferation may not be suitable for Mg alloys, and new protocols should be carefully evaluated [44].

### **3.5 Surface Modification Approaches to Tailor Degradation and Biocompatibility**

Depending on the targeted application, different types of surface modification techniques have been explored to optimize the performance of Mg alloys. For traditional applications of Mg alloys, the focus in coating development has been almost solely on corrosion protection. Reviews on coatings for Mg alloys can be found in [45, 46]. Surface modification of magnesium alloys in view of biomedical applications has been reviewed in [47]. For Mg alloys as biodegradable implants, surface modifications target a combination of improved degradation behavior and biocompatibility. This of course leads to additional requirements for the desired coating characteristics, as the coating itself also should be non-toxic (or biocompatible) as well as biodegradable—hence, the coating should only slow down dissolution to the desired rate but not provide a too strong passivating effect.

Surface modification and coating of Mg alloys are challenging, due to the high reactivity of the Mg surface. Coating adhesion is therefore of a very high significance, to prevent undermining and delamination of coatings upon initiation of corrosion at defects. To prevent such failures, typically pre-treatment of the Mg surface is crucial [46]. Chemical and electrochemical surface modification approaches in aqueous environments must be designed in a way to prevent too strong dissolution of the substrate during the surface treatment.

Depending on the type of biomedical applications, different types of surface modification approaches may be beneficial. It should be mentioned in this context that only in relatively few studies indeed the biological performance of the surface modified Mg alloys has been studied; the claim for an improved biocompatibility is often based on simple dissolution studies in SBFs. As it is hardly surprising that almost any type of surface coating will to a certain degree slow down corrosion reactions, such an approach cannot truly lead to a novel biocompatibility assessment of the system. In the following, an

overview of different types of surface modification approaches is given, classified according to the coating type. As far as possible, critical assessment of the achievements in view of the biomedical application will be discussed.

### 3.5.1 Calcium–Phosphate Based Coatings

For orthopedic applications, calcium–phosphate coatings are of interest, as they are biocompatible and can improve osteoinduction of implants; this has been demonstrated on titanium surfaces (e.g., [48] and references therein). Also for Mg alloys, preparation of calcium–phosphate coatings has been explored, for instance by ion-beam-assisted deposition [49], or by various types of electrochemical and chemical treatments [50–63]. The corrosion rate of Mg alloys can be influenced by the calcium–phosphate coatings, but the resulting degradation rate depends on the detailed nature of the coating. Different types of calcium–phosphates exist, and depending on the coating preparation route, the resulting layer can be for instance hydroxyapatite  $[\text{Ca}_{10}(\text{PO}_4)_6(\text{OH})_2]$  or amorphous calcium–phosphate  $[\text{Ca}_3(\text{PO}_4)_2 \cdot n\text{H}_2\text{O}]$ . The different calcium–phosphate phases exhibit varying solubility (as a function of temperature and pH) but moreover also differ in their biocompatibility, osteo-induction, and osteo-conduction properties. In addition, the morphology of the calcium–phosphate coatings depends on the coating methodology. This in its turn not only may influence the degradation behavior, but surface morphology also affects the biological performance.

The most simple preparation routes are based on biomimetic, spontaneous precipitation of calcium–phosphate phases on Mg and Mg alloy surfaces upon exposure to simulated biofluids. In SBF solutions, the layer that forms spontaneously on Mg alloys is mostly not hydroxyapatite, but instead an amorphous mixed (Mg,Ca)-phosphate (which can be carbonated and hydrated). As hydroxyapatite is the major mineral component of bone, research has been targeted to find ways for direct, biomimetic formation of hydroxyapatite on Mg surfaces. Use of optimized solution chemistry, temperature, and in some cases specific surface pre- or post-treatments have been indeed demonstrated to lead to direct formation of

hydroxyapatite (or Mg-substituted hydroxyapatite) on Mg by immersion treatments [58, 59, 61].

In addition to the biomimetic approach of coating Mg alloys with calcium–phosphate, sol–gel coating technique [64], or electrodeposition routes [65] are being explored. For more corrosion-resistant biomaterials, such as titanium, these methodologies have been well studied. However, in the case of Mg alloy substrates, it may be necessary to modify and optimize the protocols for coating methodologies, especially if the coating process is typically carried out in aqueous solutions, due to the high reactivity of the Mg alloy surfaces. An ethanol-based sol–gel technique was reported to be successful to prepare thick ( $\approx 50\ \mu\text{m}$ ) calcium–phosphate coatings on a Mg alloy Mg-4Y [64]. As the coatings were porous and contained many cracks, the degradation rate of the substrate could not be reduced. However, *in vitro* cell culture testing with osteoblasts indicated a significantly improved cytocompatibility compared with non-coated substrates, and cell growth was strongly enhanced. These findings are in line with studies on  $\beta$ -TCP ( $\beta$ -tricalcium phosphate) coated Mg—prepared by a chemical immersion treatment combined with an alkali-heat treatment—indicating good cell adherence and proliferation [53]. Moreover, continuous formation of bone-like apatite was observed during biodegradation testing in Hank's solution. Also  $\text{CaHPO}_4 \cdot 2\text{H}_2\text{O}$  coated Mg alloy was reported to lead to significant improvement of cell adherence, growth, and proliferation [56]. These coatings were further investigated by *in vivo* implantation, and promotion of early bone growth at the implant/bone interface was observed for the coated Mg alloy implants. *In vitro* mineralization behavior of electrodeposited Ca–P coatings on a Mg-6Zn alloy demonstrate that bone-like apatite formation kinetics from SBFs depends on the type of calcium–phosphate coating, which in its turn can be tailored by the electrodeposition parameters [65]. The results indicate promotion of nucleation of bone-like apatite by hydroxyapatite and fluoridated hydroxyapatite coatings, whereas brushite coatings delayed formation of bone-like apatite. Therefore, even though until now only few reports can be found on the biological performance of Mg alloys coated with different types of calcium–phosphate layers, these reports mostly indicate an improved bioactivity of the coated substrates. It should be mentioned once more that the different coating methodologies not only influence the calcium–phosphate chemistry and crystal structure, but moreover the morphology of the

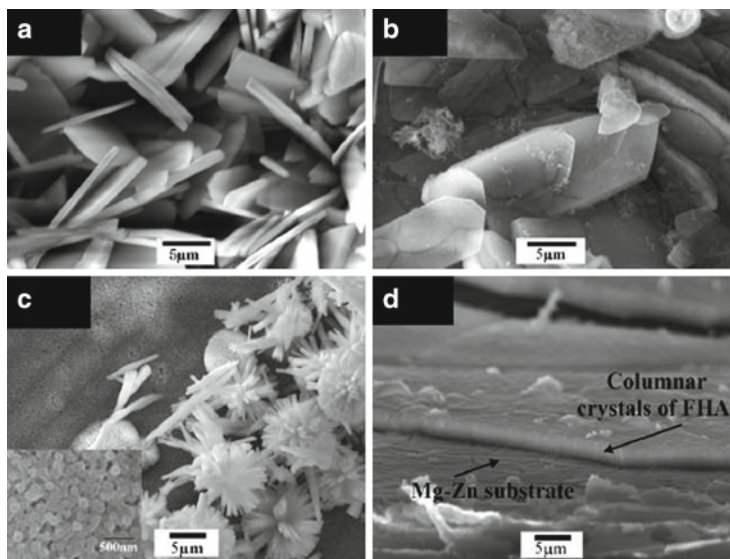


**Fig. 3.4** SEM images showing the morphology of electrodeposited Ca-P coatings on a Mg-Zn alloy: (a) brushite coating; (b) hydroxyapatite coating; (c) fluoridated hydroxyapatite (FHA) coating; (d) cross-section of the FHA coating. Reprinted from [65], with permission from Elsevier

coatings varies. Examples of surface morphologies of different types of Ca-P coatings prepared by electrodeposition on Mg are shown in Fig. 3.4 [65]. Both these factors, chemistry and phase of Ca-P and the morphology, influence both the degradation and biological performance.

### 3.5.2 Electrochemical Anodization

As oxide films on metals and alloys often grow according to the high-field model, the oxide layer thickness is proportional to voltage upon anodic polarization in an electrolyte. Anodization therefore can be used to thicken native oxide layers on metals and alloys. Especially in the case of so-called valve metals (e.g., Al, Ti, Ta, etc.), the oxide layers are blocking under anodic bias, and anodization is possible up to high voltages; hence thick oxides can be formed on the surface. At potentials above the dielectric breakdown voltage, sparking takes place

resulting in the formation of porous oxide layers. Sparking results in current and/or voltage oscillations in the electrochemical response.

In the case of Mg alloys, many commercial anodization methods have been developed. These methods lead to formation of highly corrosion-resistant surface layers, but have the drawback of often containing environmentally hazardous species such as chromates. More environmentally friendly electrolytes for anodization are based on potassium hydroxide, phosphate, fluoride, borate, or silicate containing electrolytes. The electrolytes often are of a relatively complex nature, containing many inorganic compounds; the exact effects of the different electrolyte constituents have not been unambiguously clarified. One reason to use such complex electrolytes is the empirical observation that in these solutions the dissolution of the Mg alloy substrates is reduced during anodization. Moreover, incorporation of the electrolyte species in the anodic oxide layers can make the layers more electrically blocking, reducing anodic oxygen evolution during anodization, which often is observed as a side reaction for anodization of Mg in simple alkaline solutions. However, anodization of Mg is also possible in simple NaOH solutions; by adjusting the electrochemical parameters, formation of compact or porous anodic oxide layers takes place [51, 66–68]. In this case the layers consist of only  $\text{Mg}(\text{OH})_2$  or  $\text{MgO}$ , hence no other compounds which might raise questions on biocompatibility are introduced to the surface. According to Hiromoto and Yamamoto, the degradation rate of pure Mg in cell culture medium can be adjusted by anodizing at different voltages in NaOH [67]. Moreover, the authors demonstrated that steaming (autoclaving) the anodized layers led to a further reduction of the degradation rate, due to sealing of the pores. It is noteworthy that by using the correct anodization parameters, occurrence of localized corrosion of Mg could be suppressed. In addition to the effect of anodic layers on Mg on the biodegradation behavior, it has been demonstrated that calcium–phosphate precipitation on Mg surface from artificial plasma can be enhanced by prior anodization of Mg [51].

As already mentioned, anodization above the dielectric breakdown potential (so-called spark-anodization, micro-arc oxidation) leads to formation of porous oxide layers on the surface. As surface morphology is one key factor for cell adhesion and tissue integration, tailoring the surface morphology (together with surface chemistry and degradation rate) may be a promising route for optimizing the biological performance of Mg alloys. In the case of Ti-based implants, such

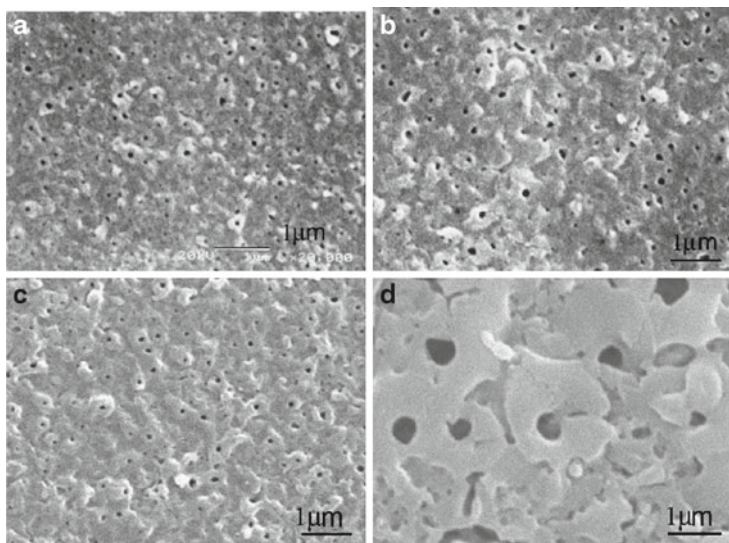


**Fig. 3.5** Morphology of anodic oxide films grown on Mg alloy AZ91 in 4 M NaOH depending on the anodization current density and final voltage: (a) anodization with 113 mA/cm<sup>2</sup> up to 70 V; (b) anodization with 700 mA/cm<sup>2</sup> up to 70 V; (c) anodization at 100 mA/cm<sup>2</sup> up to 90 V; (d) anodization with 560 mA/cm<sup>2</sup> up to 90 V. Reprinted from [68], with permission from Elsevier

microporous layers prepared by spark-anodization have been demonstrated to lead to strong and fast bone integration [69, 70]. In the case of Mg alloys, the biological performance of spark-anodized surfaces still needs to be systematically elucidated. A typical image of porous oxide layer formed on Mg by spark-anodization is shown in Fig. 3.5.

On the other hand, it is interesting to note that Mg coated by micro-arc oxidation was reported to keep its antibacterial behavior [71], which is generally related to the pH increase in the bacterial suspension. Other types of coatings studied in this work, fluorine- and silicon-containing conversion coatings, which were much denser and led to stronger suppression of Mg corrosion, led to loss of the antibacterial effect against *Escherichia coli* and *Staphylococcus aureus*.

### 3.5.3 *Other Surface Modification Techniques*

MgF<sub>2</sub> conversion coatings have been discussed as feasible surface modification to improve the biodegradation behavior of Mg and its alloys [72–77]. The coating approach is based simply on the formation of insoluble MgF<sub>2</sub> on the surface upon immersion of Mg in concentrated HF solutions. Depending on the F<sup>-</sup> concentration, a mixed Mg(OH)<sub>2</sub> and MgF<sub>2</sub> layer, or a hydroxide-substituted MgF<sub>2</sub> layer can be formed on Mg alloys by immersion. In 48% HF, uniform and dense MgF<sub>2</sub> layers can be formed on Mg. The MgF<sub>2</sub> surface layer is not stable in the absence of the high concentration of fluoride, such as in the biological environment. However, the layer can efficiently slow down biodegradation in the initial time of exposure, as for instance demonstrated in an *in vivo* study [76]. In that study, MgF<sub>2</sub> coated LAE442 (see Table 3.1) cylinders were implanted in rabbits. Even the uncoated sample showed in the rabbit model an acceptable host response and a low corrosion rate, but the degradation rate could be further reduced by the MgF<sub>2</sub> coating. The MgF<sub>2</sub> coating was found to be an effective method to reduce the initial corrosion rate *in vivo* (first 4 weeks after implantation) and therefore to retard temporarily the release of alloying elements. On the other hand, the MgF<sub>2</sub> coating showed irritation of the local synovial tissue during its dissolution. As the authors discuss, the local release of MgF<sub>2</sub> depends on the coating thickness, which in its turn influences the dissolution rate. Therefore, optimization of such MgF<sub>2</sub> coatings in view of their biocompatibility and influence on the degradation behavior is possible, also in view of the specific biomedical application.

The degradation behavior of Mg alloys can also be significantly influenced by self-assembled monolayers (SAMs) [78–82]. For instance, organosilanes that are known to be able to covalently bond to metal hydroxide surfaces have been deposited on Mg alloy surfaces [78, 79]. In addition, SAM layers of carboxylate salts [80], as well as of alkanolic and phosphonic acids [81, 82] have been prepared on Mg alloy surfaces, and significant corrosion protection effects could be observed. The SAM approach could be especially attractive in view of the biological response of the surface, as by changing the functional head group of the molecules, the surface functionality could be modified to desired behavior. For instance, protein adsorption and cell adhesion are generally influenced by surface wettability. Surface modification of Mg alloys by suitable organic molecules

could hence be used for instance to enhance protein binding on a hydrophobic surface. Formation of a super-hydrophobic Mg surface by self-assembled stearic acid has been reported [83]. Until now, SAMs layers have not yet been explored on Mg alloys in view of optimizing the biological performance.

Molecular functionalization of Mg surfaces can also be carried out by pre-adsorbing proteins on the surface. Protein adsorption on Mg will spontaneously take place upon contact with serum, blood, or any protein-containing solution, but it has been demonstrated that a more compact protein (albumin) layer can be formed on Mg surface, using silane coupling chemistry [84]. The same approach could be used to bind any desired protein on Mg surface, and hence to prevent non-specific adsorption of proteins from the body fluids. In addition to tailoring the biological performance to match the requirements of the specific application targeted, such protein layers were found to strongly suppress dissolution of Mg [84]. The role of the linker molecule (3-Aminopropyltriethoxysilane, APTES, in the present case [84]) is not only to provide better binding of the proteins on the Mg surface. As proteins such as albumin are only soluble in aqueous media, a direct protein-coating by soaking a bare Mg surface in the protein-containing solution suffers from relatively strong dissolution of the substrate in the coating solution. As adsorption of the linker molecules can be done in non-aqueous solvents, Mg dissolution during the first step of coating is prevented. The linker molecule adsorption layers then sufficiently protect the Mg surface in the second step of coating in the aqueous protein-containing solution, enabling a formation of denser protein adsorption layers than in the direct coating approach.

In addition, organic coatings, especially those based on biodegradable polymers [85–88], are of interest for surface modification of Mg alloys in view of applications in medicine, as they could combine corrosion protection with other functionalities, such as drug delivery [89]. In addition to organic coatings, also development of different types of composite coatings (e.g., polymer/bioglass composites) on Mg surfaces is in focus of interest. A special challenge is to achieve good adhesion of the coating, which often requires optimized surface pre-treatments. In case of insufficient adhesion and onset of corrosion in coating defects, filiform type of corrosion is known to be a risk for organic-coated Mg samples (see e.g., [90]).

In contrast to other metallic biomaterials, for Mg alloys surface nanostructuring for improving cell adhesion has hardly been explored. For instance in the case of Ti, drastic influence of nanotubular  $\text{TiO}_2$  layers on the cell behavior have been reported as compared with compact  $\text{TiO}_2$  layers [91]. Moreover, such nanotubular surface layers were found to enhance the formation of hydroxyapatite on the Ti surface [92]. In the case of Mg, electrochemical anodization approaches to achieve similar surface morphologies as reported for Ti have been explored, and even though nanoporous [93] as well as nanotubular [94] surface layer has been reported, these nanostructures until now show a poor order. Moreover, possible enhancement of biological functionalities by such nanostructured surface layers still needs to be explored.

### 3.6 Conclusions

Surface modification of Mg alloys by electrochemical, chemical, or biological approaches is promising for tailoring the degradation and biological performance in view of use of the materials in biodegradable implants. Challenges are given by the fact that coatings should be biocompatible, should degrade in a controllable manner, and also be compatible with the surgical and medical procedures. However, as temporary implants are expected to degrade in a relatively short time as compared with many other engineering applications, there is less concern on preparation of defect-free, robust coatings for a long-term corrosion protection.

The effects of different types of coatings on Mg alloys on the biological performance have not been systematically studied, in view of determining critical surface parameters (e.g., morphology, chemistry, or wettability of the surface). Therefore, effects observed cannot be directly attributed to the specific nature of the coating. The improved biological performance by coatings could in many cases be due to the reduced corrosion rate. Hence, the biological environment is less disturbed by strong hydrogen gas evolution or the alkaline pH shift resulting from Mg alloy corrosion.

Many surface modification approaches change simultaneously more than one surface parameter, for instance the chemical composition, morphology, and reactivity of the surface. It is therefore difficult

to attribute the biological response to one single surface parameter. Dominant surface parameters for tailored biocompatibility of Mg alloys need to be further studied.

A further challenge in determining critical surface parameters on the biological performance in the case of Mg alloys is that most surface modifications lead to a reduced surface reactivity, but not to a complete passivation of the surface. Such a behavior is of course required, as the coated system still should degrade in the body. Nevertheless, the highly dynamic nature of the modified Mg alloy surfaces makes it difficult to assess the origin of effects observed. A key issue for preventing undesired biological reactions seems to be that the initial surface reactivity should be slowed down. With time, a complete degradation of the device (including the coating) should take place.

## References

1. Hermawan H, Dubé D, Mantovani D (2010) *Acta Biomater* 6:1693
2. Moravej M, Mantovani D (2011) *Int J Mol Sci* 12:4250
3. Schinhammer M, Hänzi AC, Löffler JF, Uggowitzer PJ (2010) *Acta Biomater* 6:1705
4. Hänzi AC, Sologubenko AS, Uggowitzer PJ (2009) *Int J Mater Res* 100:1127
5. Hänzi AC, Dalla Torre FH, Sologubenko AS, Gunde P, Schmid-Fetzer R, Kuehlein M, Löffler JF, Uggowitzer PJ (2009) *Philos Mag Lett* 89:377
6. Staiger MP, Pietak AM, Huadmai J, Dias G (2006) *Biomaterials* 27:1728
7. Heublein B, Rohde R, Kaese V, Niemeyer M, Hartung W, Haverich A (2003) *Heart* 89:651
8. Witte F (2010) *Acta Biomater* 6:1680
9. Witte F, Hort N, Vogt C, Cohen S, Kainer KU, Willumeit R, Feyerabend F (2008) *Curr Opin Solid State Mater Sci* 12:68
10. Virtanen S, (2011) *Mater Sci Eng B* 176:1600–1608
11. Xin Y, Hub T, Chu PK (2011) *Acta Biomater* 7:1452
12. Song GL, Atrens A (1999) *Adv Eng Mater* 1:11
13. Song GL, Atrens A (2003) *Adv Eng Mater* 5:837
14. Song GL, Atrens A (2007) *Adv Eng Mater* 9:177
15. Pourbaix M (1974) *Atlas of electrochemical equilibria in aqueous solutions*, 2nd edn. NACE, Houston
16. Quach N-C, Uggowitzer PJ, Schmutz P (2008) *CR Chimie* 11:1043
17. Lorenz C, Brunner JG, Kollmannsberger P, Jaafar L, Fabry B, Virtanen S (2009) *Acta Biomater* 5:2783
18. Seuss F, Seuss S, Can Turhan M, Fabry B, Virtanen S (2011) *J Biomed Mater Res B* 99B:276–281

19. Mueller W-D, Lucia Nascimento M, Fernández Lorenzo M (2010) *de Mele. Acta Biomater* 6:1749
20. Xin Y, Hu T, Chu PK (2010) *J Electrochem Soc* 157:C238
21. Witte F, Fischer J, Nellesen J, Crostack H-A, Kaese V, Pisch A, Beckmann F, Windhagen H (2006) *Biomaterials* 27:1013
22. Liu M, Uggowitzner PJ, Nagasekhar AV, Schmutz P, Easton M, Song G-L, Atrens A (2009) *Corros Sci* 51:602
23. Südholz AD, Kirkland NT, Buchheit RG, Birbilis N (2011) *Electrochem Solid-State Lett* 14:C5
24. Kirkland NT, Lespagnol J, Birbilis N, Staiger MP (2010) *Corros Sci* 52:287
25. Müller L, Müller FA (2006) *Acta Biomater* 2:181
26. Oyane A, Kim HM, Furya T, Kokubo T, Miyazaki T, Nakamura T (2003) *J Biomed Mater Res* 65A:188
27. Xin Y, Hub T, Chu PK (2011) *Corros Sci* 53:1522
28. Mueller W-F, de Mele MFL, Nascimento ML, Zeddier M (2009) *J Biomed Mater Res* 90A:487
29. Liu C, Xin Y, Tian X, Chu PK (2007) *J Mater Res* 22:1806
30. Liu CL, Wang YJ, Zheng RC, Zhang XM, Huang WJ, Chu PK (2010) *Corros Sci* 52:3341
31. Rettig R, Virtanen S (2008) *J Biomed Mater Res* 85A:167
32. Gu XN, Zheng YF, Chen LJ (2009) *Biomed Mater* 4:1
33. Yamamoto A, Hiromoto S (2009) *Mater Sci Eng C* 29:1559
34. Rettig R, Virtanen S (2009) *J Biomed Mater Res* 88A:359
35. Keim S, Brunner JG, Fabry B, Virtanen S (2011) *J Biomed Mater Res B* 96:84
36. Xin Y, Huo K, Tao H, Tang G, Chu PK (2008) *Acta Biomater* 4:2008
37. Li L, Gao J, Wang Y (2004) *Surf Coat Technol* 185:92
38. Zhang Y, Tao H-R, He YH, Zou G-Y, Jian Y, Zhang S-X, Zhang B-L, Li J-N, Zhao C-L, Zhang X-N (2008) *J Clin Rehabil Tissue Eng* 12:8162–8166
39. Gu X, Zheng Y, Cheng Y, Zhong S, Xi T (2009) *Biomaterials* 30:484
40. Zhang E, Yin D, Xu L, Yang L, Yang K (2009) *Mater Sci Eng C* 29:987
41. Zhang S, Li J, Song Y, Zhao C, Zhang X, Xie C, Zhang Y, Tao H, He Y, Jiang Y, Bian Y (2009) *Mater Sci Eng C* 29:1907
42. Yun Y, Dong Z, Yang D, Schulz MJ, Shanov VN, Yarmolenko S, Xu Z, Kumta P, Sfeir C (2009) *Mater Sci Eng C* 29:1814
43. Xin Y, Jiang J, Huo K, Tang G, Tian X, Chu PK (2009) *J Biomed Mater Res A* 89:717
44. Fischer J, Prosenc MH, Wolff M, Hort N, Willumeit R, Feyerabend F (2010) *Acta Biomater* 6:1813
45. Gray JE, Luan B (2002) *J Alloys Compd* 336:88
46. Chen XB, Birbilis N, Abbot TB (2011) *Corrosion* 67:03005–1
47. Yang J, Cui F, Lee IS (2011) *Ann Biomed Eng* 39:1857
48. Narayanan R, Seshadri SK, Kwon TY, Kim KH (2008) *J Biomed Mater Res* 85B:279
49. Yang JX, Jiao YP, Cui FZ, Lee I-S, Yin QS, Zhang Y (2008) *Surf Coat Technol* 202:5733
50. Song YW, Shan DY, Han EH (2008) *Mater Lett* 62:3276
51. Hiromoto S, Shishido T, Yamamoto A, Maruyama N, Somekawa H, Mukai T (2008) *Corros Sci* 50:2906

52. Zhang Y, Zhang G, Wei M (2008) *J Biomed Mater Res* 89B:408
53. Geng F, Tan LL, Jin XX, Yang JY, Yang K (2009) *J Mater Sci Mater Med* 20:1149
54. Wen C, Guan S, Peng L, Ren C, Wang X, Hu Z (2009) *Appl Surf Sci* 255:6433
55. Wang Y, Wei M, Gao J (2009) *Mater Sci Eng C* 29:1311
56. Xu L, Pan F, Yu G, Yang L, Zhang E, Yang K (2009) *Biomaterials* 30:1512
57. Cortes DA, Lopez HY, Mantovani D (2007) *Mater Sci Forum* 539–543:589
58. Hiromoto S, Yamamoto A (2009) *Electrochim Acta* 54:7085
59. Gray-Munro JE, Strong M (2009) *J Biomed Mater Res* 90A:339
60. Tomozawa M, Hiromoto S, Harada Y (2010) *Surf Coat Technol* 204:3243
61. Chen X-B, Birbilis N, Abbott TB (2011) *Corros Sci* 53:2263
62. Waterman J, Pietak A, Birbilis N, Woodfield T, Dias G, Staiger MP (2011) *Mater Sci Eng B* 176:1756–1760
63. Pietak A, Shadanbaz S, Walker J, Staiger MP, Dias GJ, *Mater Sci Eng B* (in press)
64. Roy A, Singh SS, Datta MK, Lee B, Ohodnicki J, Kumta PN (2011) *Mater Sci Eng B* 176:1679
65. Song Y, Zhang S, Li J, Zhao C, Zhang X (2010) *Acta Biomater* 6:1736
66. Ono S, Kijima H, Masuko N (2002) *J Surf Finish Soc Jpn* 53:406 (in Japanese)
67. Hiromoto S, Yamamoto A (2010) *Mater Sci Eng C* 30:1085
68. Peixoto Barbosa D, Knörrschild G (2009) *Surf Coat Technol* 203:1629
69. Sul YT (2003) *Biomaterials* 24:3893
70. Sul YT, Johansson C, Byon E, Albrektsson T (2005) *Biomaterials* 26:6720
71. Ren L, Lin X, Tan L, Yang K (2011) *Mater Lett* 65:3509
72. Chiu KY, Wong MH, Cheng FT, Man HC (2007) *Surf Coat Technol* 202:590
73. Yan T, Tan L, Xiong D, Liu X, Zhang B, Yang K (2010) *Mater Sci Eng C* 30:740
74. Drynda A, Hassel T, Hoehn R, Perz A, Bach F-W, Peuster M (2010) *J Biomed Mater Res A* 93:763
75. Pereda MD, Alonso C, Burgos-Asperilla L, Del Valle JA, Ruano OA, Perez P, Fernández Lorenzo De Mele MA (2010) *Acta Biomater* 6:1772
76. Witte F, Fischer J, Nellesen J, Vogt C, Vogt J, Donath T, Beckmann F (2010) *Acta Biomater* 6:1792
77. Ye X-Y, Chen M-F, You C, Liu D-B (2010) *Front Mater Sci China* 4:132
78. Scott A, Gray-Munro JE (2009) *Thin Solid Films* 517:6809
79. Scott AF, Gray-Munro JE, Shepherd JL (2010) *J Colloid Interface Sci* 343:474
80. Liu Y, Yu Z, Zhou S, Wu L (2006) *Appl Surf Sci* 252:3818
81. Ishizaki T, Okido M, Masuda Y, Saito N, Sakamoto M (2011) *Langmuir* 27:6009
82. Ishizaki T, Teshima K, Masuda Y, Sakamoto M (2011) *J Colloid Interface Sci* 360:280.s
83. Wang Y-H, Zhong L, Liu Y-Y, Jiang Q-L, Guo X-Y, Wang J (2010) *Corros Sci Prot Technol* 22:329
84. Killian M, Wagener V, Schmuki P, Virtanen S (2010) *Langmuir* 26:12044

85. Gray-Munro JE, Seguin C, Strong M (2009) *J Biomed Mater Res* 91A:221
86. Wong HM, Yeung KWK, Lam KO, Tam V, Chu PK, Luk KDK, Cheung KMC (2010) *Biomaterials* 31:2084
87. Gu XN, Zheng YF, Lan QX, Cheng Y, Zhang ZX, Xi FT, Zhang DY, *Biomed Mater* 4 (2009) Article number 044109
88. Li JN, Cao P, Zhang XN, Zhang SX, He YH (2010) *J Mater Sci* 45:6038
89. Lu P, Fan H, Liu Y, Cao L, Wu X, Xu X (2011) *Colloids Surf B Biointerfaces* 83:23
90. Williams G, Grace R (2011) *Electrochim Acta* 56:1894
91. Park J, Bauer S, von der Mark K, Schmuki P (2007) *Nano Lett* 7:1686
92. Tsuchiya H, Macak JM, Müller L, Kunze J, Müller F, Greil P, Virtanen S, Schmuki P (2006) *J Biomed Mater Res A* 77A:534
93. Brunner J, Hahn R, Kunze J, Virtanen S (2009) *J Electrochem Soc* 156:C62
94. Turhan MC, Lynch RP, Jha H, Schmuki P, Virtanen S (2010) *Electrochem Commun* 12:796

# Chapter 4

## Microcantilever Sensors: Electrochemical Aspects and Biomedical Applications

Lana Norman, Garima Thakur, and Thomas Thundat

### 4.1 Introduction

Microfabricated cantilevers, similar to those used in Atomic Force Microscopy (AFM), are generating growing interest as a sensor platform for label-free detection of chemical and biological molecules [1–17]. Using recent advances in surface microfabrication, it is possible to design and fabricate cantilevers and cantilever arrays with extremely high sensitivity for mass or surface stress. These cantilevers are generally fabricated from silicon or silicon nitride by top-down micromachining methods and can be produced efficiently and affordably. Although the cantilevers have micrometer dimensions, their responses are in nanometer-scale, which lends itself to their reference as nanomechanical transducers. The cantilever can be made in different shapes and sizes allowing for flexibility in the design, which renders the resulting cantilevers ideal candidates for the possible incorporation in microfluidic and miniaturized lab-on-a-chip devices. Generally, these cantilevers are operated in either the static deflection mode or the dynamic resonant mode. The basic principle for the static mode is that a chemical or physical event occurring at the functionalized surface of one side of the cantilever generates a surface stress difference (between the active functionalized and passive non-functionalized sides) that

---

L. Norman (✉) • G. Thakur • T. Thundat  
Department of Chemical and Materials Engineering,  
University of Alberta, 9107 116 Street, Edmonton, AB, Canada T6G 2V4  
e-mail: norman@ualberta.ca; garima@ualberta.ca; thundat@ualberta.ca

causes the cantilever to bend away from its resting position. Whereas in the resonant mode, a binding event occurring on the cantilever increases the overall mass thus decreasing the resonant frequency, which is similar to quartz crystal microbalances. In general, when a force is applied to the end of a free standing cantilever a vertical bending will result. As described by Hooke's Law ( $F = -k_{\text{spring}} \Delta z$ ), the bending or deflection ( $\Delta z$ ) of the cantilever is directly proportional to the applied force  $F$ , and the cantilever spring constant  $k_{\text{spring}}$  is the proportionality factor. The cantilever spring constant dictates the flexibility and sensitivity of the cantilever and is defined by its dimensions and material constants. For a rectangular-shaped cantilever,  $k_{\text{spring}}$ , is given by [18]

$$k_{\text{spring}} = \frac{Ewt^3}{4l^3} \quad (4.1)$$

where  $E$  is the elasticity or Young's modulus,  $w$  is the cantilever width,  $t$  its thickness, and  $l$  its length. If the cantilever is set to oscillate, its resonance frequency  $f_{\text{res}}$  is related to  $k_{\text{spring}}$  by [19]

$$f_{\text{res}} = \frac{1}{2\pi} \sqrt{\frac{k_{\text{spring}}}{m^*}} \quad (4.2)$$

where  $m^*$  is an effective mass which takes into consideration the cantilever geometry and mass distribution along the cantilever. A compelling feature of cantilevers is that they can be operated in either mode within vacuum, air or liquid depending on the specific application.

## 4.2 Microcantilever Sensors: Working Principles

### 4.2.1 Cantilever Modes of Operation

The response signal from a cantilever sensor is either beam bending (static) or changes in its resonance response (resonance frequency, amplitude, phase, and  $Q$ -factor), dynamic mode. Illustrated in Fig. 4.1 are the three basic modes of operation for microcantilever-based systems: heat (bimaterial) mode, dynamic (resonant) mode, and static (surface stress) mode [12, 14, 19, 20]. In static mode, only one of the faces of the microcantilever is rendered environmentally

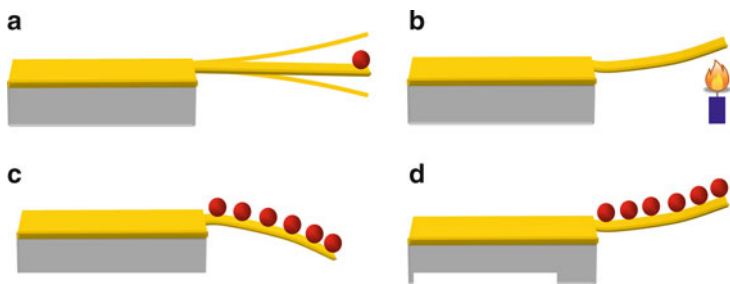


**Fig. 4.1** Cantilever modes of operation: (a) Dynamic mode detects mass changes on the cantilever via changes in the resonance frequency; (b) Bimetallic mode detects temperature changes by a static bending due to the different thermal expansion coefficients of the metal layer and silicon cantilever; and (c, d) Surface stress mode, where asymmetric physical or chemical events occurring at the cantilever's functionalized surface leads to an overall cantilever bending. For example, adsorption on the top surface can either cause a compressive stress (c), resulting in a bending of the cantilever downward or a tensile stress (d), which results in a bending of the cantilever upward

or stimuli responsive. Conversely, each mode differs from the other in terms of the principle of transduction, functionalization, and detection mechanisms. In this section, a brief introduction to the major modes of operation will be provided, while highlighting in more detail the static or surface stress mode used predominantly in electrochemical microcantilever investigations. In the mode of operation referred to as the heat or bimaterial mode, the cantilever is coated with a metal layer so that differences in the thermal expansion of the cantilever and coating (i.e., silicon–gold composite) will influence the cantilever bending as a function of temperature (see Fig. 4.1b). Heat changes can result from an external influence (i.e., changes in temperature), occur directly on the surface by exothermal reactions (catalysis), or are due to the material properties of a sample attached to the apex of the cantilever (micromechanical calorimetry). In comparison to traditional calorimetric methods performed on milligram samples, the sensitivity of the cantilever heat mode is orders of magnitudes higher, requiring only nanogram amounts of sample with which sensitivities in the range of nanojoules to femtojoules have been achieved [21–23]. Another interesting example employing the bimaterial effect is known as photothermal deflection spectroscopy [24]. In this technique the absorption of light energy by the adsorbed material on the bimaterial

cantilever results in cantilever bending due to a fraction of the absorbed energy (nonradiative decay) being converted to heat [25]. A cantilever bending plot as a function of illuminating wavelength resembles the absorption spectrum of the adsorbate molecules. This method offers extremely high selectivity for molecular recognition when operated in the mid infrared (IR) region. Therefore, the cantilever bending due to photothermal heating, when illuminated by IR radiation in a sequential fashion (as a function of the light wavelength) can provide spectroscopic data about the material found at the interface of the microcantilever. Thundat et al. have used this technique to detect and characterize explosive materials adsorbed at the microcantilever interface [24], as well as to investigate and characterize spectroscopic results for microcantilevers coated with *Bacillus anthracis* or *Bacillus cereus* [26]. The search for an appropriate detection mechanism of airborne *Bacillus anthracis*, which is an etiology agent of anthrax, has gained interest because of anthrax-based terrorist threats. Detection of terrorist weapons such as explosive materials, chemical agents, and deadly pathogens would have grave consequences on society in general and microcantilever-based sensing systems offer a path for the development of miniature sensor systems to facilitate sensitive and selective detection of these materials.

In the dynamic or resonance mode (Fig. 4.1a), cantilevers are excited close to their resonance frequency, which is typically on the order of tens of kHz to a few MHz. The resonance frequency changes when an additional mass is adsorbed to the oscillating cantilever. For a rectangular cantilever, the change in mass ( $\Delta m$ ) can be calculated from the variation in the resonance frequency:

$$\Delta m = \frac{k_{\text{spring}}}{4\pi^2} \left( \frac{1}{f_1^2} - \frac{1}{f_0^2} \right) \quad (4.3)$$

where the resonance frequency before and during the experiment is  $f_0$  and  $f_1$ , respectively [1]. With optimized cantilever geometries and under ultra-high vacuum, it is possible to measure mass changes down to the single molecule level in the resonant mode when operated at very high frequency [7]. Unfortunately, the detection of molecules in solution is hindered by the inherent dampening of the cantilever oscillation in a liquid environment, which decreases the mass resolution and requires a more sophisticated setup [12]. Recently, Manalis and coworkers have developed an innovative

way to avoid viscous dampening by placing the liquid sample inside a hollow cantilever rather than oscillating the cantilever in a liquid environment [27]. This method eliminates viscous damping while at the same time preserves the mass resolution of the nanomechanical resonator [27]. Manalis' group has used the resonating devices embedded in microfluidic channels to measure the mass of single cells during their growth cycle [28, 29], detect IgG protein [27] and weigh individual bacteria [27]. With the growth and development of this technology, it is expected that detection of lower mass entities in solution should be readily realized having greater implications in the implementation of this mechanism of detection in biomedical devices. A general review of mechanical nanobiosensors can be found in an article by Waggoner and Craighead [16].

By far the most commonly employed cantilever mode of operation, specifically when investigating bio-related processes, is known as the static or surface stress mode (Fig. 4.1c, d). As previously mentioned, the basic principle arises from a chemical or physical event occurring on one face of the microcantilever generating a surface stress change that is manifested as a nanometer-scale bending away from the equilibrium position. The transduction mechanism can be monitored in real-time with considerable sensitivity via an optical beam reflected from the free end of the microcantilever. The deflection is directly proportional to the surface stress through a modified form of Stoney's equation [30]. By definition, a *compressive stress* corresponds to an expansion of the microcantilever, whereas a *tensile stress* corresponds to a contraction [31–34]. In accordance with common sign convention, a compressive stress is generally expressed with a negative value, while a tensile stress is expressed with a positive one [35].

### 4.2.2 Cantilever Deflection

The optical beam deflection technique is the most frequently employed approach to monitor cantilever displacements as a result of asymmetrical changes in the surface stress. In this configuration, a laser beam is focused on the apex of the microcantilever and the reflected beam is monitored with a position sensitive detector (PSD). The measurement scheme used to correlate the cantilever deflection,  $\Delta z$ , to the change in signal,  $\Delta S$ , observed at the PSD is depicted in

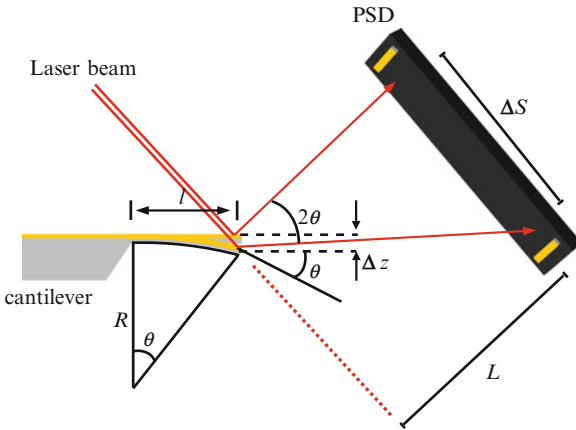


**Fig. 4.2** Illustration of the beam deflection parameters used to determine the microcantilever bending with nanometer accuracy

Fig. 4.2. It can be assumed that the bending angle of the deflected laser beam is equal to twice that of the cantilever bending angle since all the angles are very small. The cantilever deflection  $\Delta z$  is calculated from the microcantilever bending angle  $\theta$  [32–34]

$$\theta = \frac{\Delta S}{L} \quad (4.4)$$

and the cantilever length  $l$  by

$$\Delta z = \frac{\theta}{4} l \quad (4.5)$$

where  $L$  is the distance between the PSD and the cantilever and for small deflections  $L \approx L \pm \Delta z$ , since  $L \gg \Delta z$  [32–34]. The combination of Eqs. (4.4) and (4.5) relates the actual microcantilever deflection to the PSD signal: [32–34, 36]

$$\Delta z = \frac{l}{4L} \Delta S. \quad (4.6)$$

Equation (4.6) is valid for laser beam deflection measurements carried out in air. If the cantilever is immersed in a liquid, then the reflected laser path is modified according to Snell's law. In order to correct for

the change in angle resulting from the reflected laser beam passing through an aqueous solution, the following relationship is used [34]:

$$\Delta S = \frac{\Delta S'}{n_{\text{liquid}}} \frac{1}{\left(1 - \frac{d}{L} + \frac{d}{n_{\text{liquid}}L}\right)} \quad (4.7)$$

where  $n_{\text{liquid}}$  is the index of refraction of the solution and  $d$  is the distance between the optical window and the cantilever. Unfortunately, this consideration is often neglected in current scientific studies when considering fluidic systems using an optical deflection mechanism and gives rise to an overapproximation of the observed deflection leading to considerable error in the reported surface stress values [33, 34].

### 4.2.3 Quantifying Surface Stress

It is common practice to report surface stress values, which are independent of cantilever spring constant, instead of absolute deflections so that the results of cantilever experiments with different geometries or materials can be directly compared [37]. In many cases, the physically or chemically induced deformations of microcantilevers have been assessed with the classic formula derived by Stoney [30], which simply relates the induced radius of curvature,  $R$  (see Fig. 4.2), of the microcantilever to the change in surface stress,  $\Delta\sigma$ :

$$\Delta\sigma = \frac{Et^2}{6R(1-\nu)} \quad (4.8)$$

where  $E$  is Young's modulus,  $t$  is the thickness of the cantilever, and  $\nu$  is Poisson's ratio. However, there has been much debate in the recent literature about the application of Stoney's equation to microcantilevers [4, 32, 38–46]. This not only arises from an inconsistency between the experimental and modeled systems, but also from large discrepancies in the reported experimental parameters. For example, it was established by Grütter and coworkers that a considerable uncertainty is introduced when using Stoney's formula due to the large range of values reported for Young's modulus of silicon nitride ( $E \approx 130\text{--}385$  GPa) [28, 30, 45, 47, 48]. To compensate, they derived

a formula starting with Hooke's law that relates the energy stored in a deflected microcantilever to its spring constant. This calculation eliminates the need to know the elastic modulus and requires only knowledge of the geometry, spring constant, and Poisson's ratio of the microcantilever. The formulas for the differential surface stress derived in their work for a rectangular microcantilever [32–34]

$$\Delta\sigma = \frac{4}{3(1-\nu)} \frac{l}{wt} k_{\text{rect}} \Delta z \quad (4.9)$$

and for a triangular microcantilever [32–34]

$$\Delta\sigma = \frac{4}{3(1-\nu)} \frac{l^2}{\left[ wt l_1 + \frac{tb}{4l} (l-l_1)^2 \right]}. \quad (4.10)$$

The numerical constants in the above formulas account for the microcantilever beam curvature resulting from a uniform surface stress, as opposed to a concentrated load applied to the tip. And an independent assessment of  $k_{\text{rect}}$  and  $k_{\Delta}$  should be carried out to increase the accuracy of the calculated surface stress change.

#### 4.2.4 Interpretation of the Measured Surface Stress

In microcantilever experiments, the interpretation of the origin of the surface stress is not trivial. It is known that the absolute bending signal is a convolution of specific and non-specific adsorption events and the corresponding surface stress change may not necessarily correlate with the amount of adsorbed material. In particular, microcantilevers functionalized with biomolecules have been successfully used to translate bimolecular interactions into nanomechanical motion, based on phenomena such as DNA hybridization [49–55], protein–protein recognition [49, 54, 56, 57], and cell adhesion [58, 59]. These systems offer significant advantages given the highly specific molecular recognition reactions which evolve under mild, aqueous conditions. However, steric and electrostatic repulsions, configuration entropy, hydration forces, conformational changes, and changes in osmotic pressure have all been proposed to contribute to the resulting surface stress. Moreover, these contributions may compete with each other rendering the nontrivial interpretation of the surface stress arising from multiple

interactions at the cantilever interface. This is supported by ongoing debates in the literature [49, 53, 54, 60–63]. Given the inherent complexity involved of biomolecular interactions it is difficult to ascertain the exact origin of the surface stress which limits the ability of synthetic chemists to harness these materials for device applications.

Microcantilevers, in general, are also highly susceptible to vertical deflections that may be caused by extraneous interactions, particularly when operating in liquids. Thermal drift, non-specific physical adsorption of molecules from the surrounding liquid or changes in the index of refraction near the sensing surface can contribute to the drift [49, 52, 53, 56, 62, 64]. To circumvent this problem and extract the surface stress changes arising from specific physico-chemical reactions, simultaneous measurements of reference cantilevers aligned in the same array as the responsive cantilevers are often employed. To obtain reliable data under these circumstances, not only do the microcantilever properties have to be independently characterized but the reference interface must be truly inert [52, 53, 56, 62, 65].

The parallel optical detection and surface functionalization of multiple cantilevers in an array format are not always easily realized. When single cantilever experiments are employed, the combination of the surface stress measurements with a complementary technique can enable the interpretation of the measured surface stress. For example, Grütter et al. have developed a differential cantilever-based sensor equipped with an adaptor sensor capable of complementary ellipsometric measurements [66]. The combined cantilever–ellipsometer instrument is capable of simultaneous in situ surface stress and film thickness measurements associated with molecular events occurring at the microcantilever interface. Electrochemical techniques are particularly attractive since they offer the ability to address the entire sample rapidly by an electrochemical perturbation or control the redox state of “individual” molecules by an applied potential scan. The integrated aspect of the combined electrochemical microcantilever instrument provides the surface and interfacial characterization capabilities required for the interpretation of the vertical deflection response.

#### **4.2.5 *Electrochemical–Microcantilever Setup***

To date, combined electrochemical–cantilever measurements have predominately employed custom-built, reflecting laser beam deflection

setups connected to an external potentiostat to monitor the static deflection of the microcantilever as a function of the electrochemical interfacial processes. In other words, the modified cantilever is the mechanical transducer enabling simultaneous, *in situ*, and real-time measurements of the interfacial stress changes accompanying electrochemical methods. In these experiments, the metal-coated microcantilever chip serves as both the working electrode (in a conventional three-electrode cell configuration) and the reflective platform of the optical setup. The counter and reference electrodes are chosen based on the particular investigation or application of the electrochemical–microcantilever system. Generally, the functionalized microcantilever is clamped and immersed into an electrochemical cell filled with the appropriate electrolyte solution. Micropositioners are generally used in order to control the immersion surface area of the active electrode as well as to avoid the possibility of electrochemical reactions occurring at the electrical contact points. While such setups described herein function well for fundamental investigations operating in a laboratory setting, the design of a robust and flexible system is paramount for repeatability, stability, and eventually device operation.

Recently, Boisen et al. have designed, fabricated, and demonstrated the capabilities of an electrochemical-cantilever hybrid platform system equipped with a microfluidic flow cell [67]. The integrated cantilever-electrode system addresses the electrical sensing requirements, while the flow cell encloses and seals the fluidic chamber and is designed to provide electrical and fluidic connections [67]. A brief description of the device is given here but more details can be found elsewhere [67]. The silicon chip measures 15 mm × 15 mm and contains two large openings that are connected by a 1 mm wide channel allowing for fluid input and output (see Fig. 4.3). The input/output wells and the connecting channel are etched in such a manner that when combined with flow cell components a 2  $\mu$ l chamber results. The connecting channel contains six cantilevers having different length dimensions giving rise to multiple available spring constants, which should in turn, help in the investigation of a range of interactions resulting in different magnitudes of responses and improve the signal-to-noise ratio. Furthermore, each cantilever is capable of acting as an independent working electrode which means individual responses should be accessible. At the edge of the channel, opposite to the cantilevers, are two independent large-area reference and counter electrodes.

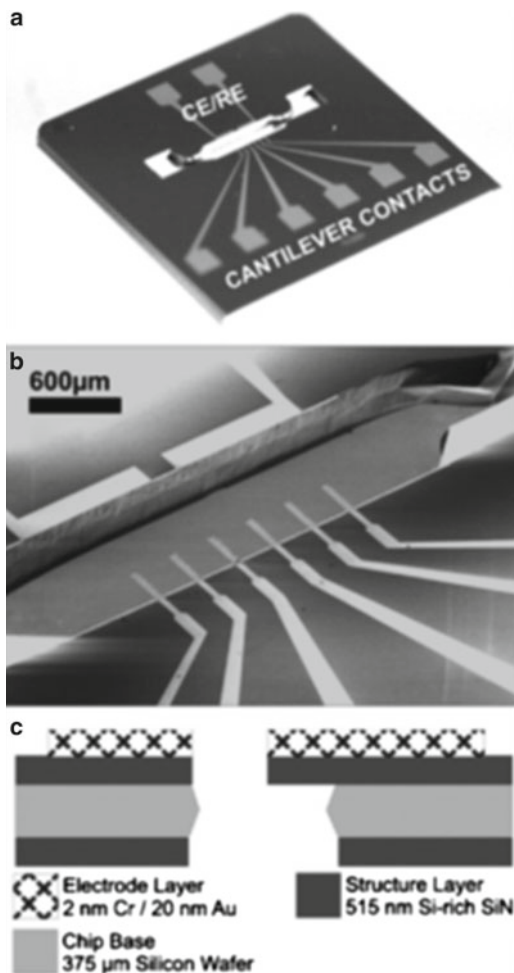


**Fig. 4.3** (a) A photograph of the ECC chip, with clearly visible contact pads for the cantilever working electrodes (WE), as well as the counter (CE) and reference (RE) electrodes. (b) A SEM image of the 300- $\mu\text{m}$ -long cantilevers and electrodes in the channel. (c) A profile fabrication diagram depicting the layers of the ECC chip. Layer thickness is not drawn to scale. Reprinted from [67] with permission from Elsevier

By integrating cantilevers with electrodes in a microfluidic channel, Boisen and coworkers were able to address several of the issues often associated with simultaneous electrochemical-microcantilever measurements, such as stability and device compatibility with readout systems [63].

To test the feasibility of the electrochemical-microcantilever hybrid platform, the electrochemical-deflection behavior of the gold-coated cantilevers in ionic solutions was investigated. In a solution of 30 mM  $\text{KNO}_3$ , also containing 30  $\text{NH}_4\text{CH}_3\text{COO}$  to maintain the pH at 6.8, a compressive surface stress change of 7–8  $\text{mN m}^{-1}$  was consistently observed with potential steps of 0.1 V. Here, after each potential step the current quickly returns to zero because the associated charge is a result of the change in the double layer and not a redox event. Since no current is flowing across the electrolyte-electrode interface, the authors attribute the motion of the cantilever to be a result of the well-known charge-induced surface stress established by both Haiss and Ibach [31, 35].

When the potential is scanned from +0.5 V to -0.5 V in the presence of the redox couple  $[\text{Fe}(\text{CN})_6]^{3-/4-}$ , the shape of the cyclic voltammogram is similar to that obtained under diffusion-limited conditions. The corresponding surface stress change is observed to reach a maximum as the potential passes the reduction wave, and then decreases slightly when the potential becomes more negative. The cantilever returns to its resting position on the reverse scan. Here, it is believed that the motion of the cantilever results from a combination of the electrical double layer plus the accumulation of charge corresponding to Faradaic events occurring at the cantilever interface. These results are similar to that observed by Thundat and coworkers which will be discussed later in the chapter [68].

### 4.3 Applications of Specifically Fabricated Microcantilevers

Microcantilevers are most commonly fabricated from isotropic materials such as silicon or silicon nitride [69]. In this section, a simple and accessible electrochemical approach for the fabrication of nanostructured microcantilevers will be discussed. Recent microfabrication advances have allowed for the introduction of cantilevers made

from polymeric materials giving rise to flexibility in design and availability of alternative structures with interesting applications. An example of an electrochemically SU8 cantilever employed in microfluidics will be given here. Finally, an electrochemical patterning tool where electrodeposition of metals onto a conductive substrate facilitated by microcantilevers will be introduced.

### ***4.3.1 Anodic Aluminum Oxide Microcantilevers: Electrochemical Etching***

Microcantilevers with anodic aluminum oxide (AAO) nanochannels have been recently prepared [10, 70]. In this section, a brief description of the fabrication and selective use of electrochemical etching involved in this process is given. The fabrication process of AAO cantilevers with nanochannels consists of multiple steps (a) the formation of an AAO layer on top of aluminum substrate by a two-step anodization, (b) patterning of the microcantilever array by photolithography, (c) fabrication of the suspended beam structures by anisotropic etching of the AAO layer, and (d) removal of the layer below AAO using electrochemical etching.

Hexagonally ordered nanochannels having a 40 nm diameter on the microcantilever surface were accomplished by the electrochemical fabrication process. As listed above, the first step in the fabrication of microcantilevers involves the formation of an AAO layer on top of aluminum. In this step, the channel diameter is optimized by varying the anodization conditions such as applied voltage, temperature, and reaction time. Formation of patterns on aluminum by conventional photolithography proceeds in the second step. Here, a thin layer of aluminum was deposited on the AAO layer followed by the spin coating of a photoresist layer. The desired microcantilever patterns are formed on the photoresist using a photomask. The third step involved immersion of the microcantilever into a phosphoric acid solution for the selective removal of exposed AAO. Finally, the suspended cantilevers are fabricated by removing the aluminum under the patterns without damaging the AAO. A major advantage of electrochemical etching over conventional fabrication methods is that the fabrication process is considerably simplified. Furthermore, electrochemical etching permits the fabrication of

AAO suspended microcantilevers where the aluminum is removed without damaging the AAO.

Electrochemical etching can be defined as a surface finishing process based on anodic dissolution of a metal or an alloy in an appropriately chosen etching solution. Experimentally, a solution of perchloric acid and ethanol (1:4, v/v) was utilized for electrochemical etching at 7°C for 2 h. The initial anodization proceeded at +40 V in a 0.3 M oxalic acid solution for 8 h at 15°C. During the second anodization process, the AAO layer was etched away with an alumina etching solution at 20°C for 2.5 h. A second anodization step was carried out to form a new AAO layer under identical conditions; however, a shorter time duration of 20 min was used here.

The AAO microcantilever has vertically parallel pores or nanochannels having a diameter up to 50 nm, which were fabricated using the electrochemical process described above. As suggested by the unique design and properties of these nanochannels, it was proposed that these AAO cantilevers can be used to deposit a sensing material with a special affinity for a specific analyte. For example, a strand of DNA may attach to the analyte without interference by other DNA molecules [70]. In this way, the fabrication of microcantilevers where one can control the structure of the device using electrochemical parameters has been demonstrated successfully.

### ***4.3.2 Electrochemically Actuated SU8 Cantilevers in Microfluidics***

Microvalves are one of the most researched subjects in microfluidics because of their myriad of uses in various microfluidic applications [71–73]. Integrated microvalves are required in internal flow regulations, various chemical analysis techniques, gas/liquid sample injections, mixing, micro-gas chromatograph systems, and in lab-on-a-chip devices [72, 74, 75]. Bubble-based electrochemical valves show a great potential in some of the above-mentioned applications because of their compact, localized actuation with fast response, and most significantly their low integration costs and significant driving power. Recently, a device introducing electrochemical SU8 microvalves featuring a cantilevered structure has been investigated [76]. This device containing an electrochemically actuated SU8 cantilever

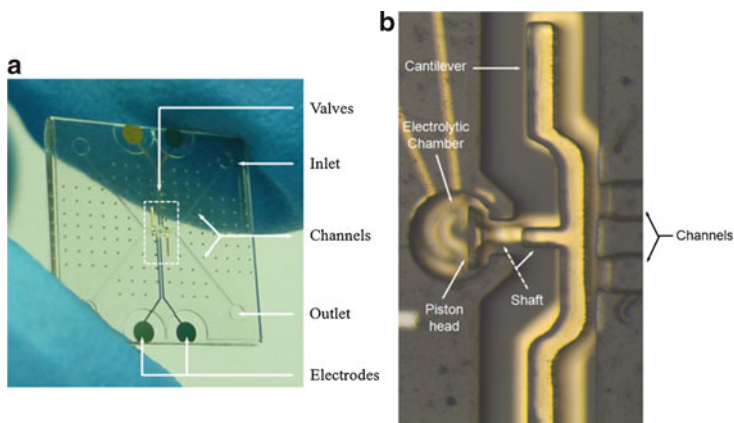


**Fig. 4.4** (a) General view of the fabricated device on a  $1 \text{ cm}^2$  die, showing the main components for two separate valves. (b) Close-up view of the cantilever head, the channels and the electrocatalytic actuator. Reprinted from [76] with permission from Elsevier

valve showed very low dead volume and had low power requirements. A brief description of the device will be presented in this section; however, the architecture and the working principle of the device have been more thoroughly described by Ezkerra et al. [76]. As per the design, the valve consists of a cantilever placed next to an electrolytic actuator, where a bubble is generated due to the water electrolysis using phosphate buffer saline (PBS) as an electrolyte. The bubble starts pushing the cantilever body against the channels, by means of a piston, and blocks them once it reaches a critical size. The valve incorporates minimized leakage and helps prevent contact between the cantilever and the cover. The gasket is a  $15 \mu\text{m}$  intermediate SU8 layer that also seals the channels thereby providing a  $15 \mu\text{m}$  clearance for the cantilever to move as shown in Fig. 4.4. The valve actuator also consisted of a pair of interdigitated electrodes and the circular shape of the chamber favored a faster actuation by providing a maximum actuation area while enhancing coalition of small bubbles ahead of the cantilever. A close-up view of the valve with its different components is shown in Fig. 4.4b.

After the fabrication process was accomplished, the electrochemical valves were tested under a range of pressure driven flows to determine regulation capabilities. The electrodes were actuated with a power source, the flow pressure was regulated, and the flow rate was

measured using a fluidic bench. The motion of the cantilever was monitored using a high speed camera. The circuit was filled at a pressure of 5 kPa using PBS buffer (pH 7.4) and the bubble was grown to block the channel. A fast response time of only 0.2 s to close at a voltage of +5.5 V was observed. The sequence of these quick events taking place in the valve could be described as:

- (a) Filling up of the valve chamber with PBS leaving bubbles in the dead space.
- (b) Actuation of electrodes leading to growth of the bubble ( $t=30$  s).
- (c) Pushing the cantilever by the bubble and moving it in dead spaces to the back of the chamber resulting in the closing of the channels ( $t=200$  ms).
- (d) Continuous expansion of bubbles in the chamber ( $t=230$  s) and switching the electrodes off.

Upon closing of the valve the flow pressure was varied between 0 and 40 kPa and the flow rate was measured where very low leakage was observed in this device. These results showed the potential of using soft materials like SU8 for fabrication of movable structures and have valid applications for use as electrochemical actuators in microfluidic devices.

### ***4.3.3 Microcantilever Array: Patterning Conducting Surface Using Electrodeposition***

A patterning tool that allows an electrochemical reaction to occur inside microdroplets was used for the electrodeposition of copper onto a conducting gold substrate [77]. An array of ten pen-like shaped silicon cantilevers was placed on a PC-controlled motion stage for spatial positioning. Each cantilever incorporates a fluidic channel that enables the direct transfer of a loaded liquid onto the deposition surface simply by contact of the cantilevers' tip with the substrate. The device allowed the electrochemical reaction to take place inside the microdroplet of the electrolyte, having a typical volume of the order of microliters, deposited on the conducting surfaces. The voltage was applied between the cantilever electrode and the conducting gold surface thus leading to the electrodeposition of the desired species present in the electrolyte. The amount of

deposited material was readily monitored and controlled by the voltage pulse and the electrodeposition time.

The experimental setup consisted of a microspotter, a potentiostat, cupric sulfate solution, and a gold-coated silicon substrate for the electrodeposition of copper. The electrodes were connected to the potentiostat where the microcantilevers were anodically polarized (counter electrode), the sample surface was cathodically polarized (working electrode) and the reference electrode was shunted to the counter electrode. As mentioned above, copper deposition as surface bumps was achieved by bringing the cantilever tip in contact with the surface to create microdroplets of cupric sulfate based solution and then applying a set voltage. The optimized potential value was +1.9 V, which ensured the reduction of copper ions onto the gold sample surface. The factors which contributed to the systematic and ordered arrangement of the patterns include (a) geometry of the cantilever where a constant distance of 6  $\mu\text{m}$  was maintained between the electrode and the surface on which the metal was deposited and (b) the parallel arrangement of the array of ten microcantilevers ensured that each spotting step introduced deposition of ten spots reproducibly. The current flowing through the ten parallel cells was recorded as a function of time using a potentiostat, resulting in a conventional chronoamperogram plot. The electrodeposition of the matrices of copper spots was analyzed using SEM and AFM.

#### **4.4 Surface Stress Change Investigated for Gold-Coated Microcantilevers under an Applied Potential**

Electrochemical–microcantilever systems have been used to investigate the surface stress generated with the under potential deposition (UPD) of a metal, which involves the formation of one or more metal monolayers at a potential positive of the reversible Nernst potential for bulk deposition. The adsorption of a species on the surface can be expected to alter the surface stress, since the local interactions of each adsorbate will vary the bond strength between neighboring atoms on the surface. The surface stress response associated with the reversible electrochemical deposition of a metal monolayer at a gold-cantilever interface has been reported in the literature for several

UPD systems, including Cu [78], Pb [78, 79], and Ag [80]. Not only has metal electrodeposition been investigated, but an example of nonmetallic materials will also be given in the following section.

Moreover, sensor development for a number of heavy metal ions (e.g.,  $\text{Hg}^{2+}$ ,  $\text{Cu}^{2+}$ ,  $\text{Pb}^{2+}$ ,  $\text{Cd}^{2+}$ ), which are known to be toxic species in groundwater, is required. This group of metal ions can be electrochemically reduced resulting in an electrodeposition of the metal, which is a property that has been utilized for sensing. The development of reliable, sensitive, and low-cost sensor systems to analyze water-based toxins using electrochemical methods in concert with microcantilevers is an area of considerable interest.

#### ***4.4.1 Detection of Lead (Pb) with a Gold-Coated Microcantilever Electrode***

Welland et al. have investigated the electrodeposition and stripping of Pb on an Au (111) surface [79]. A significant change in the surface stress was observed at the potential corresponding to the rotational phase transition of the Pb. The results showed that surface stress changes varied in a complicated manner with the applied potential. The observed surface stress changes associated with deposition of bulk Pb were smaller than the ones described for monolayer processes. The compressive stress was related to lattice mismatches between the gold surface, the strained Pb monolayer, and the unstrained bulk Pb. A plausible explanation for the observed differential stress could arise from the different adlayer structures present in different regions of the potential cycle [79].

#### ***4.4.2 Detection of Copper (Cu) with a Gold-Coated Microcantilever Electrode***

Microcantilevers coated with gold have been used as working electrodes on which copper has been deposited and anodically stripped in an aqueous solution, while the differential surface stress at the microcantilever electrodes has been concomitantly measured. Surface stress as a function of time was investigated during copper electrodeposition on a gold-coated microcantilever at  $-0.4$  V vs. Ag (QRE,

quasi-reference electrode) in a 0.1 M  $\text{NaNO}_3$  supporting electrolyte with varying  $\text{Cu}^{2+}$ . Electrodeposition of copper leads to an obvious change in surface stress of the gold-coated microcantilever. A threshold concentration of  $10^{-11}$  M  $\text{Cu}^{2+}$  was established for these sensing systems [78].

Stripping analysis is an electrochemical technique in which an application of a cathodic pulse leads to a deposition of a species from solution onto an electrode surface [81]. The species of interest is then redissolved or stripped from the electrode surface using linear sweep voltammetry or another voltammetric technique in which the voltage is increased linearly with time from the deposition potential to more anodic values. As the species of interest is oxidized, the current is observed to reach a peak value and then decrease. For equal deposition conditions the peak current is then proportional to the concentration of electroactive species in solution. Following deposition of copper at  $-0.4$  V from a 0.1 M  $\text{NaNO}_3$  electrolyte solution containing  $\text{Cu}^{2+}$ , the potential was increased at a rate of  $40 \text{ mV s}^{-1}$ . The current and the surface stress were simultaneously measured as a function of the anodic stripping potential.

As previously mentioned, there has been a great deal of work on the UPD of different metals onto gold [82]. Some work has been reported on the simultaneous measurement of stress at a (macro) cantilever electrode during the UPD of metals. For example, research by Haiss and coworkers is particularly relevant to the deposition and stripping of  $\text{Cu}^{2+}$  [20, 64, 74]. Haiss and coworkers followed the surface stress evolution during copper UPD on gold in the presence of bromide ion. During the cathodic scan an increasing amount of  $\text{Cu}^{2+}$  ions is adsorbed on the bromide-covered gold surface. A tensile surface stress of about  $0.4 \text{ N m}^{-1}$  was observed during the cathodic scan at potentials between  $+0.3$  and  $+0.1$  V. Haiss has attributed this to the adsorption of positively charged copper ions. The surface stress evolution in this potential region scaled linearly with the charge density on the surface. Haiss attributed this as an indicator of a pronounced charge transfer from the adsorbed copper to the underlying gold surface. Upon monolayer completion, further adsorption of copper ions is observed giving rise to an observed compressive stress at the cantilever surface.

As discussed above, a microcantilever-based sensor seems to be capable of detecting  $\text{Cu}^{2+}$  at a concentration of about  $10^{-11}$  M based on microcantilever surface stress alone. Selectivity will be imparted to

the sensor by the choice of the deposition potential. Good selectivity can be obtained by conducting stripping analysis of the electrodeposited copper. Identification of copper can be achieved from the potential dependence of the partial derivative of the surface stress with respect to potential. Unfortunately, the researchers found that the concentration of  $\text{Cu}^{2+}$  in solution required for good selectivity is four orders of magnitude higher than that needed for sensitive detection in the absence of interfering species. This potential-controlled electrochemical method offers the promise of achieving chemical selectivity for microcantilever sensor applications in liquid environments for a variety of analytes while still maintaining high sensitivity.

#### **4.4.3 *Surface Stress Induced in Microcantilever Electrodes in a $\text{K}_3\text{Fe}(\text{CN})_6/\text{NaNO}_3$ Solution***

In this section, gold-coated microcantilevers were used as working electrodes and their mechanical response under an applied potential was investigated in  $\text{NaNO}_3$  and  $\text{K}_3\text{Fe}(\text{CN})_6/\text{NaNO}_3$  containing electrolyte solutions. The current–potential response, the normal output of the cyclic voltammetry experiment, and the microcantilever surface stress response were measured simultaneously to investigate the effect of a controlled potential on the surface stress of microcantilever electrodes [68].

Presented in Fig. 4.5a are the surface stress and simultaneously recorded cyclic current–potential response obtained in 0.1 M  $\text{NaNO}_3$  (pH=3.8) in the potential range of  $-0.1$  to  $0.8$  V with potential sweep rates of 5, 10, and 20  $\text{mV s}^{-1}$ . During the cathodic scan, a downward surface stress of the microcantilever increased as the potential decreased, corresponding to an increasing compressive stress. whereas, an upward surface stress of the microcantilever corresponding to an increasing tensile stress occurred during the anodic potential sweep.

In a  $\text{NaNO}_3$  solution without an electroactive species present, there should be no Faradic electrochemical reactions taking place at the electrode surface. This was verified by cyclic voltammetry as indicated in Fig. 4.5a, which shows voltammograms with simultaneous determination of microcantilever deflection, as the potential scan rate was varied from 5 to 20  $\text{mV s}^{-1}$ . The results indicate that the change in surface stress is nearly independent of both potential and

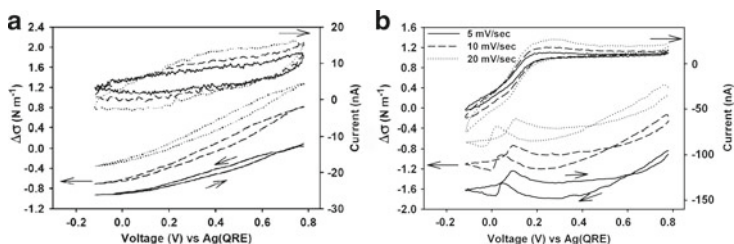


**Fig. 4.5** (a) Microcantilever surface stress (*bottom*) and current (*top*) vs. the electrode potential in a  $\text{NaNO}_3$  solution. (b) Microcantilever surface stress (*bottom*) and current (*top*) vs. potential in a  $\text{K}_3\text{Fe}(\text{CN})_6/\text{NaNO}_3$  solution. Sweep rates are  $5 \text{ mV s}^{-1}$  (*solid line*),  $10 \text{ mV s}^{-1}$  (*broken line*), and  $20 \text{ mV s}^{-1}$  (*dotted line*). Plots of microcantilever surface stress vs. potential are offset to clarify the presentation. Reprinted from [68] with permission from Elsevier

the potential sweep rate within the specified potential region. This suggests that the observed surface stress on the electrode was induced only by the change in electrochemical potential. The observed result can be explained by a change in electrostatic force acting on the electrode surface with potential. As the potential increases, charges accumulate around the electrode surface through diffusion of electrolyte resulting in the formation of the classical double layer at the metal–solution interface. This increasing charge density in the double layer results in an increase in electrostatic forces acting on the plane of the gold surface, which causes increasing compressive stresses on the gold surface indicated by a bending away from the gold-coated side of the microcantilever. During a cathodic scan, the decrease in charge density in the double layer reduces the electrostatic forces acting on the gold surface and the cantilever returns to its resting position.

The effect of electrochemical potential on surface stress of the microcantilever electrode was also determined in the presence of the well-studied reversible redox couple  $\text{Fe}(\text{CN})_6^{3-}/\text{Fe}(\text{CN})_6^{4-}$ . Microcantilever deflection and potential-induced current were investigated in a solution of  $0.05 \text{ M K}_3\text{Fe}(\text{CN})_6$  in a  $0.1 \text{ M NaNO}_3$  as the support electrolyte ( $\text{pH}=3.8$ ). Figure 4.5b shows the microcantilever surface stress and current vs. potential dependencies simultaneously obtained using a  $\text{K}_3\text{Fe}(\text{CN})_6/\text{NaNO}_3$  solution within the range of potentials  $-0.1$  to  $0.8 \text{ V}$  and sweep rates of  $5$ ,  $10$ , and  $20 \text{ mV s}^{-1}$ . The microcantilever electrode shows behavior that is characteristic of a microelectrode in which the diffusion layer is large in relation to the dimensions of the electrode. The behavior indicates that the diffusion

rate of the ionic species around the microcantilever electrode is relatively fast compared with the rates of reduction and oxidation reactions. This suggests that the ionic adsorption and desorption at the microcantilever electrode plays an important role in generation of the observed surface stress change. It is possible that voltammetry with simultaneous stress measurement at relatively high sweep rates will be required to separate the effects of ion adsorption/desorption and electron transfer-induced surface charge density on surface stress. To summarize, the results presented for the  $K_3Fe(CN)_6/NaNO_3$  system indicated that the differential surface stress of microcantilever was introduced by electrochemically induced changes in charge density due to both ion adsorption/desorption and electron transfer on the electrode surface.

#### 4.5 Detection of $NO_2$ with a Resonating Microcantilever

In an entirely unique approach, a setup similar to Kelvin probe technique was utilized as a sensitive sensor platform for gases (as shown in Fig. 4.6) [83–85]. Koley et al. have investigated the sensing behavior of various materials for  $NO_2$  detection using the aforementioned highly sensitive potentiometric technique [83]. The experimental and analysis procedure involved a topographic signal for monitoring the

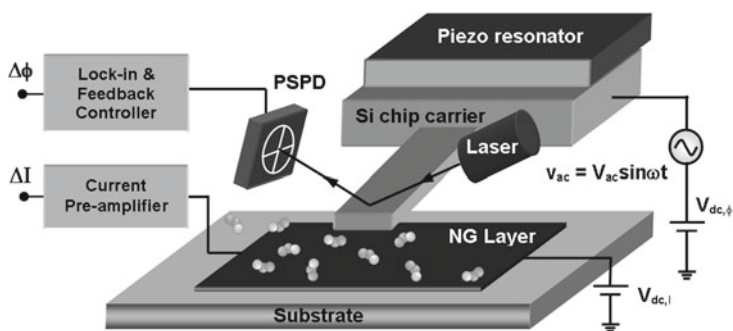


**Fig. 4.6** Schematic diagram of the surface work function based  $NO_2$  detection setup [83]

cantilever oscillation, where a silicon cantilever was used and excited at frequency,  $\omega$ , that was close to its resonance frequency,  $\omega_0$ , in non-contact mode using the piezo-actuator. System software was used to check the amplitude of the sinusoidal topography signal which varied with change in surface work function as the target molecules get adsorbed on the functionalization layers [83].  $\text{NO}_2$  sensing experiments were conducted on thin films of transition metals, such as  $\text{In}_2\text{O}_3$  and  $\text{Sn}_2\text{O}_3$ , ZnO nanowires, and carbon based nanostructured layer deposited on Si wafer. To analyze  $\text{NO}_2$  sensing, adsorption induced surface work function change of the sensing layer was observed by examining sensitivity of microcantilever. The amperometric measurements were conducted using a current preamplifier, with metal press contact placed at the two ends of the nanostructured film of graphite.

To understand the principle behind this technique one needs to consider the force between the cantilever and the sensing surface which consists of two components the electrostatic and the capacitive [86]. It was assumed that the electrostatic charges on the surface were constant and electrostatic force component was considered to be zero. Hence, the total force was considered to be capacitive. If the external ac and dc bias was  $V_{\text{ac}} \sin \omega t$  and  $V_{\text{dc}}$ , respectively, and  $\Delta\phi$  was the surface work function difference between the cantilever and sensing surface then the total force was given by the following equation:

$$F_{\text{total}} = F_{\text{cap}} = \frac{1}{2} \frac{\partial C}{\partial z} (V_{\text{ac}} \sin \omega t + V_{\text{dc}} - \Delta\phi) \quad (4.11)$$

where  $\partial C/\partial z$  is the capacitance gradient of the cantilever. The oscillating amplitude of cantilever can be given by the following expression: [87]

$$A = \left( \frac{F_{\text{total}}}{k} \right) Q \quad (4.12)$$

where  $k$  and  $Q$  are the spring constant and the quality factor of the cantilever, respectively. The  $\omega$ -component was dominant because  $\omega$  was close to the resonance frequency and due to high quality factor of the cantilever at the resonance frequency. The obtained electrical signal (oscillating amplitude) is proportional to

$$\left[ \frac{\partial C}{\partial z} (V_{\text{dc}} - \Delta\phi) V_{\text{ac}} \right] \quad (4.13)$$

As shown by the relation (4.13), the oscillation amplitude was dependent on the capacitance gradient, quality factor, spring constant, and the ac voltage amplitude. In this technique, dc and ac sensitivity of the cantilever was determined to analyze the  $\text{NO}_2$  sensing [83]. The sensitivity of the cantilever was calculated as the rate of change of amplitude with dc bias and expressed as  $\text{nm mV}^{-1}$  (obtained as  $360 \text{ nm mV}^{-1}$  for Si cantilever). The root mean square noise was calculated as a standard deviation of the beat amplitude as a function of time for constant ac and dc biases (approximately 20 nm for the Si cantilever at  $360 \text{ nm mV}^{-1}$  of sensitivity). Hence, the minimum surface work function was obtained as  $55 \mu\text{V}$  from the above-mentioned values ( $20/360 \text{ mV}$ ).

The surface work function change of cantilever was measured upon flow of  $\text{NO}_2$  at sub-ppm range. The potentiometric measurements indicated that the transition metal oxides, such as  $\text{In}_2\text{O}_3$  and  $\text{SnO}_2$ , had approximately similar work function response at 80 and  $100 \mu\text{V s}^{-1}$ , respectively. Significant work function response was observed for ZnO nanowires at an initial rate of  $64 \mu\text{V s}^{-1}$ . Whereas, change in surface work function for nanostructured graphite (NG) layer was approximately 25 mV as compared to 11 mV for nanocrystalline graphite (NCG) in the time period of 100 s.  $\text{NO}_2$  detection up to 60 ppm was possible on NG layer using this technique.

This method seems as a promising approach for simultaneous use of potentiometric and conductance measurements for sensing volatile chemicals or gases such as  $\text{NO}_2$  [83].

## 4.6 Electrochemical–Microcantilever Artificial Muscle Systems

Nanoscale actuators that are capable of converting chemical or electrical energy into mechanical motion are needed for a wide range of applications such as robotics, artificial muscles, prosthetic devices, micromechanical, and microfluidic devices. To date, a number of nanomechanical systems that employ microcantilevers have been successful in transferring molecular phenomena into macroscopic-scale motion. For example, stimuli-responsive conducting polymers have received considerable attention due to their similarity to micro-artificial muscles [88, 89]. Furthermore, they can be operated under

physiological conditions making them particularly well suited for biomedical applications [90]. Several groups have grafted polymers to one face of the cantilever which enables a wide range of responses that can be achieved due to conformational changes between two states [91–95]. Stoddard and coworkers have tethered a linear molecular motor based on a bistable rotaxane structure to the gold-coated microcantilevers where the supramolecular interlocked molecules enabled a controlled nanomechanical response under chemical and electrochemical stimuli [96–98]. The basic principle of all these systems arises from a chemical or physical event, occurring on one face of the microcantilever generating a differential surface stress change that is manifested as a bending of the nanometer-scale variation away from the equilibrium position (static mode). The surface stress can be compressive where the cantilever experiences an expansion, or it can be tensile where a contraction is experienced at the cantilever interface. The elicited response depends on the properties and interactions of the functionalized-microcantilever interface with the environment. Moreover, the above aforementioned systems employ a novel nanomechanical transduction mechanism integrating “bottom-up” molecular design with “top-down” microfabrication and several of these examples will be discussed below.

#### ***4.6.1 Microcantilever-Conducting Polymers Systems***

Conjugated polymers as actuators have a number of key features that make them particularly attractive for their use as artificial muscles. First, they exhibit large actuation strains from a few percent to over 30%, where the strain can be exploited to elicit responses on the micro- or macro-scale, respectively. This strain can be exploited in linear, volumetric, or bending actuations. They have high strength where stresses are 1,000 times as great as skeletal muscle [90]. Not only can the actuators be switched between fully expanded and contracted states, but they can also be held at a precise intermediate state, which allows the actuators not only to move, but also to be carefully positioned and held in a desired fixed place. This is important for devices like catheters or microsurgical tools, and is a feature that is not shared by most other artificial muscle materials. The standard operating solution for conjugated polymers is aqueous electrolytes, meaning that they can perform well in blood, urine, or other

bio-fluids. This is in contrast to most other actuators which require a protective shield to avoid corrosion. Finally, conducting polymers can be electrically addressed, where they only consume current when switching between states (contracted/expanded), which readily allows for their integration with standard control systems.

The redox-induced deflection of polyaniline- and polypyrrole-coated cantilevers has been independently investigated [33, 88, 89]. In both cases, electropolymerization at the gold-coated microcantilever interface (working electrode) gives rise to a physically adsorbed conducting polymer system. For these macromolecular systems, under an applied potential the mechanism of actuation can be divided into two contributing factors including conformational changes induced by the charge density in the polymer backbone and an osmotic (or volume) expansion due to insertion of ions and their solvation shells [33, 88, 89, 99, 100]. However, the underlying gold substrate may be exposed to anions where the polymer film does not properly adhere to the microcantilever. In addition, through defects in the polymer matrix the gold substrate may be exposed to the anions, giving rise to the well-known charge-induced surface stress addressed by both Haiss and Ibach [31, 35]. The charge-induced contribution makes the quantification and reproducibility of the electrochemically induced surface stress difficult to ascertain and is beyond the scope of this discussion [97, 101]. More importantly, in order for these systems to be used as conventional microactuators, it is important to characterize their properties, particularly potential-induced surface stress changes as a function of film thickness, electrolyte, and lifetime.

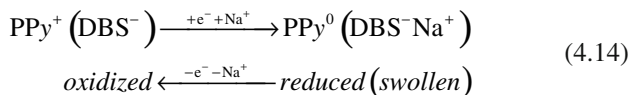
In the case of polyaniline (PAN), the microcantilevers were functionalized via electropolymerization of aniline on the gold-coated surface carried out in a 0.1 M  $\text{H}_2\text{SO}_4/0.5$  M  $\text{Na}_2\text{SO}_4$  solution in the presence of the aniline monomer under the application of a constant potential of 0.8 V vs. a Ag-QRE. Under these conditions, the resulting polymer film adhered to one face of the microcantilever was found to have a film thickness of 190 nm. The PAN-coated cantilevers were then subject to a multipotential-step chronoamperometric experiment in a mixture of 0.1 M  $\text{H}_2\text{SO}_4/0.5$  M  $\text{Na}_2\text{SO}_4$ . The potential steps from  $-0.2$  V to 0.8 V resulted in an electrochemically induced transition from the reduced polymer (PAN) state to the oxidized polymer (PAN<sup>2+</sup>) state, whereas the reduced polymer PAN-state was regenerated with potential steps from 0.8 V to  $-0.2$  V. The integration of

the resulting current responses indicated that the charge associated with the oxidation of PAN to PAN<sup>2+</sup> is independent of the oxidation–reduction time-width, meaning that the total oxidation to PAN<sup>2+</sup> proceeded within a 5 s time frame. A reversible cantilever surface stress response was observed to accompany the electrochemical oxidation and reduction of the polymer with the cyclic multistep potential changes. A compressive surface stress was observed with the oxidation of the PAN to PAN<sup>2+</sup> when the potential was stepped from –0.2 V to 0.8 V. On the reverse potential step (0.8 V to –0.2 V, PAN<sup>2+</sup> → PAN), the PAN-functionalized microcantilever returned to its original resting position. Interestingly, when the PAN gold-coated microcantilever was subject to a 50 s or 5 s pulse width, an instantaneous increase in the stress on the cantilever having a value of approximately –2.3 N m<sup>–1</sup> was observed. The rapid increase in surface stress change was then followed by a gradual increase to a surface stress change maximum which was potential pulse-width dependent. The authors attribute the rapidly observed change in surface stress ( $\Delta\sigma = -2.3 \text{ N m}^{-1}$ ) to electrostatic repulsive and steric interactions as a result of the electrogeneration of PAN<sup>2+</sup> and corresponding ion pairing events. This conclusion is in agreement with their finding that the concentration of PAN<sup>2+</sup> remains constant regardless of pulse width length [88, 102]. The gradual increase in surface stress response with increasing potential pulse time-width, reaching a maximum change in surface stress of –3.9 N m<sup>–1</sup> at 50 s, was contributed to the well-known polymer swelling phenomena accompanying redox-transformations in polymeric systems [88, 102]. A more detailed kinetic analysis of the PAN-functionalized-microcantilever response revealed deflection rates of  $k = 2.8 (\pm 0.3) \times 10^{-4} \text{ s}^{-1}$ , which agreed nicely with the swelling response rate ( $k_{\text{sw}} = 3.0 (\pm 0.3) \times 10^{-4} \text{ s}^{-1}$ ) of a PAN film of similar thickness adsorbed at a gold-coated surface observed in a surface plasmon resonance study [88]. As discussed above, not only can the PAN-microcantilever actuator be switched between fully expanded and contracted states eliciting a maximum and minimum response, but they can also be held in an intermediate state, allowing for movement control where the system can be held in a desired fixed position.

Grütter et al. have measured the surface stress induced by electrochemical transformations of a thin polypyrrole (PPy) polymer film electrodeposited on the gold-coated face of a silicon microcantilever [33, 89]. PPy is particularly unique among artificial muscles because of its applications as a biomaterial. These polymeric systems exhibit

excellent *in vitro* and *in vivo* biocompatibility, they can be doped with and can release biomolecules, and they are widely studied as biosensors [90]. Moreover, they are compatible with aqueous media and operate at low voltages, unlike conventional piezoelectric actuators. Here, the PPy(DBS) film was electropolymerized from an aqueous solution containing 0.1 M Py and 0.1 M sodium dodecyl benzene sulfonate (NaDBS) at a constant potential of 0.55 V (vs. Ag/AgCl) onto the gold-coated face of the microcantilever. The potential value was chosen to ensure that a uniform polymer film was deposited at the microcantilever interface. A film thickness of ~300 nm was verified by AFM measurements where a 3% deviation was found for a set of PPy films physisorbed on different microcantilevers. This result shows the consistency of the electropolymerization implemented method for defining the working electrode and allows for direct comparison of results observed for the polymer films deposited on different microcantilevers.

Similar to the PAn-microcantilever, the microcantilever serves as both the working electrode (in a conventional three-electrode cell configuration) and as the mechanical transducer for simultaneous real-time measurements of the current and interfacial stress changes. Sweeping the film's potential between +0.30 V and -0.85 V in an electrolyte solution (0.1 M NaDBS) results in the electrochemical switching between the oxidized (PPy<sup>+</sup>, doped) and reduced (PPy, neutral) states of the PPy film:



Accompanying the redox reaction is the well-known reversible volume change of the conjugated polymer, which in turn causes the cantilever to bend. A typical cyclic voltammogram and corresponding surface stress change response obtained for microcantilevers modified with a PPy film are depicted in Fig. 4.7. A maximum compressive surface stress change of approximately  $-2 \text{ N m}^{-1}$  was observed at the switching potential +0.3 V. The authors attributed the stress changes to the physical swelling of the physically adsorbed polymer matrix (due to the incorporation of counterions and solvent) and the interaction of the supporting electrolyte ions with the underlying exposed metal surface.

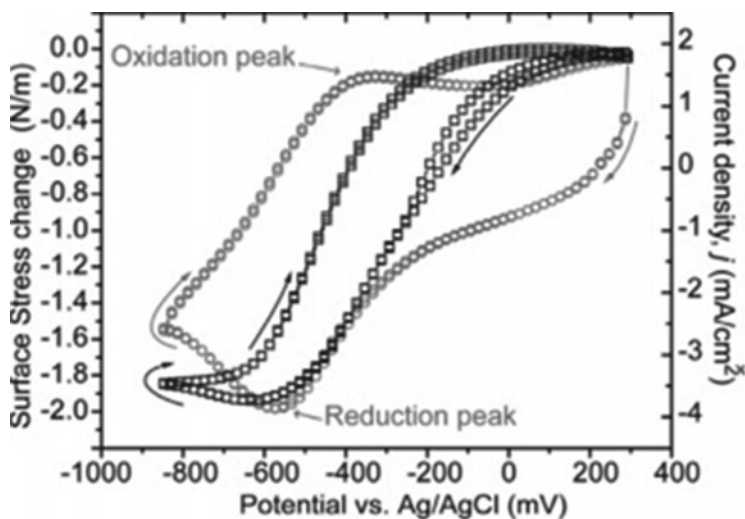


**Fig. 4.7** Surface stress (*black square*) and current (*gray circle*) vs. potential measured simultaneously during two consecutive cyclic voltammetric scans in 0.1 M NaDBS solution. The potential is swept at  $100 \text{ mV s}^{-1}$  between  $-0.85$  and  $+0.30 \text{ V}$ . A change in surface stress of about  $2 \text{ N m}^{-1}$  is observed when going between the anodic and the cathodic peaks. Reprinted with permission from [89], ©2005 American Chemical Society

To investigate the long-term stability of the PPy-microcantilever actuators, the system was subjected to consecutive doping/dedoping cycles. The cyclic voltammetry experiments were carried out in two different electrolyte solutions, 0.1 M NaDBS and 0.1 M NaCl, where the potential was cycled between  $+0.3 \text{ V}$  and  $-0.8 \text{ V}$  (vs. Ag/AgCl). In both cases, the microcantilever deflections were monitored as a function of number of cycles. When the PPy-microcantilever was actuated in the presence of 0.1 M NaDBS, a noticeable decrease in the amplitude of actuation was observed already after 50 scans, indicating an irreversible change in the polymer film. In contrast, when the PPy-microcantilever was actuated in the presence of 0.1 M NaCl, the peak-to-peak surface stress amplitude slightly increased until reaching a maximum value of  $-1.9 \text{ N m}^{-1}$ , which was relatively stable over 500 cycles. This value is comparable in magnitude with the initial stress change observed in NaDBS electrolyte. It is obvious that for this microcantilever-based actuating system, the choice of electrolyte is of important consideration when considering the long-term actuating capabilities.

A comparison of the results reported for polyaniline- [88] and polypyrrole- [90] coated microcantilevers reveals that the surface stress change per charge density generated multilayer polymer films is  $\sim 300 \text{ N m}^{-1}/\text{C cm}^{-2}$  (polyaniline; 190 nm thick) and  $\sim 20 \text{ N m}^{-1}/\text{C cm}^{-2}$  (polypyrrole; 300 nm thick). Larger deflections are theoretically obtainable by building thicker films of conducting polymers (i.e., increase the number of redox sites per square area), meaning that the system properties can be tailored to produce a larger actuation. Therefore, microcantilevers functionalized with conducting polymers are potentially promising electroactuating systems for such applications as nanomechanics, nanotweezers, and micromechanical elements, where there is a strong preference for actuation in a constant chemical environment.

#### 4.6.2 *Microcantilever–Polymer Brush Systems*

Several groups have grafted nonconducting polymers to one face of the cantilever which enables a wide range of responses that can be achieved depending on changes in the environmental conditions [91, 92, 95, 103–106]. However, polymer brushes require chemical diffusion for the actuation stimulus, which often involves a change in the sensing environment rendering the cantilevers prone to well-known turbulences such as thermal drift or mechanical bending by hydrodynamic forces or changes in the dielectric constant of the liquid. To circumvent this problem, Huck and coworkers employed an approach where the systems environment remains constant (i.e., solvent, electrolyte concentration, temperature, and pH), while using an active stimulus, such as an applied bias to trigger specific conformational changes [93]. Here, the researchers have grafted ultrathin poly(2-methacryloyloxy)ethyltrimethyl ammonium chloride (PMETAC) brushes onto gold-coated microcantilever interfaces where electroactuation capabilities were exhibited when an alternating positive (+0.5 V) and negative (−0.5 V) potential bias was applied in a static electrolyte solution (1 mM  $\text{NaNO}_3$ ). In this case, the mechanism of actuation is not based on redox cycles but on reversible perturbations of the electrical double layer associated with ion transport in and out of the polymer brush. Nonetheless, the pressure exerted on the cantilever includes contributions from the osmotic pressure from free ions,

lateral interactions of brush segments, and the electric field strength giving rise to a compressive surface stress change.

On further investigation of the deflection profile, the electroactuation of the cantilever modified brushes was found to depend strongly on the potential, scan rates, and salt concentration. Very interesting about this particular system is that it is reminiscent of recent studies on conformational changes of surface-bound, strongly charged, single stranded DNA molecules. In this case, the counterion distribution and orientation of the polymer chains have also been shown to be strongly influenced by electric fields [107–109]. While nature provides sophisticated and highly specific examples of molecular interactions, their inherent complexity which generates the nanomechanical response has rendered the origin of the surface stress difficult to ascertain. By varying the parameters independently, as the researchers have done, these polymer brush systems have the potential to provide insight into the much more complex behavior exhibited by natural occurring systems assembled on microcantilevers having greater implications in their potential use as biomedical devices.

### 4.6.3 *Microcantilevers–Linear Molecular Machines Systems*

An important class of artificial molecular muscles or so-called “molecular machines” are based on interlocked molecular structures. In general, the supramolecular assemblies are composed of a discrete number of molecules connected through noncovalent bonds. An inherent property of these systems that can be used to exert linear forces is that the molecular components can move relative to one another while still remaining part of the molecule. A good example includes redox switchable rotaxanes that have been specifically designed as molecular analogs to skeleton muscles and can “expand” and “contract” linearly in response to chemical or electrochemical stimuli. The bistable donor–acceptor rotaxane is composed of two  $\pi$ -electron poor tetracationic macrocycle cyclobis (paraquat-*p*-phenylene) (CBPQT<sup>4+</sup>) rings and in the unoxidized state of the rotaxane are found encircling the redox-active tetrathifulvalene (TTF) stations, approximately 4.2 nm apart from each other (Fig. 4.8, upper diagram). The supramolecular assembly also contains two  $\pi$ -electron-rich naphthalene (NP) stations.

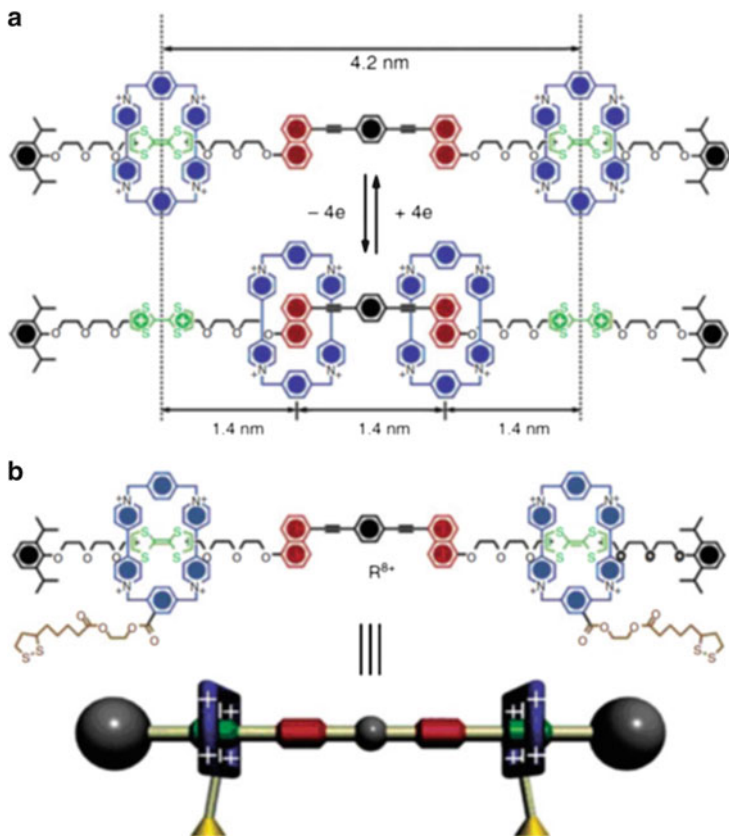


**Fig. 4.8** (a) Structural formulas of the extended (*top*) and the contracted (*bottom*) states of a prototypical molecular muscle based on doubly bistable [3] rotaxanes. In the relaxed state, cyclobis(paraquat-*p*-phenylene) (CBPQT<sup>4+</sup>) rings (*blue*) encircle the electron-rich tetrathiafulvalene (TTF) stations (*green*), approximately 4.2 nm apart. With chemical or electrochemical oxidation of TTF stations, CBPQT<sup>4+</sup> rings move inward to the secondary naphthalene (NP) stations (*red*), approximately 1.4 nm apart, effecting a 67% reduction in distance between CBPQT<sup>4+</sup> rings (*blue*). (b) Structure formula and graphical representation of a disulfide-tethered bistable molecular muscle used in subsequent cantilever bending experiments. Reprinted with permission from [101], ©2005 American Chemical Society

Oxidation of TTF to either the radical TTF<sup>•+</sup> or dicationic TTF<sup>2+</sup> results in electrostatic repulsion between it and the CBPQT<sup>4+</sup> forcing the macrocycles to move to the more favorable and weaker alternate NP station, effectively placing the rings at a distance of 1.4 nm

(Fig. 4.8, upper diagram). This movement represents a molecular contraction of approximately 67% between the two rings. By tethering these bistable donor–acceptor rotaxanes to a gold-coated microcantilever, which was achieved by incorporating disulphide moieties on the CBPQT<sup>4+</sup> rings (Fig. 4.8, middle diagram), Stoddard et al. were successful in harnessing the collective efforts of an ensemble of these linear molecules to exert forces resulting in a nanomechanical response [97, 101]. In their study, the controlled movement of the rings between the two switched states in response to the cycled additional of chemical redox reagents induced a reversible contractile (tensile) strain in the surface of the microcantilever. The reversibility of the actuation is limited by the degradation of either the gold–thiol bond or the rotaxane itself, either of which would be a likely source of the gradual decrease observed in the response amplitude.

The contraction/relaxation of these surface-tethered molecular muscles can also be controlled electrochemically. Again, the gold-coated microcantilever was used as a working electrode in a modified three-electrode cell. When a constant potential high enough to oxidize the TTF component (0.4 V vs. Ag/AgCl in 0.1 M aqueous NaClO<sub>4</sub>) is applied, a deflection toward the gold-coated microcantilever occurred. Conversely, the relaxation of the functionalized microcantilever is achieved when the potential is held at a value capable of reducing the oxidized TTF but low enough not to reduce CBPQT<sup>4+</sup>. The system was also found to be only partially reversible under electrical stimuli. In both these redox-controlled processes, where linear artificial molecular muscles are tethered to the gold-coated microcantilever, a collective movement of the rings along the dumbbell induced the contractile strain on the surface of the microcantilever which caused it to bend [97, 101].

It is important to note that a number of investigations employing gold-coated microcantilevers modified with functionalized self-assembled monolayers (SAMs) have attributed the observed micromechanical deflection to *collective* in-plane molecular interactions [49, 53, 54, 96, 97]. For example, the micromechanical motion arising from the hybridization of complementary oligonucleotides has also been attributed to collective phenomena within the biomolecular layer [49, 51–54]. Other work involving the pH titration of microcantilevers functionalized with carboxylic acid-terminated alkanethiolate SAMs has demonstrated that the in-plane surface forces, which dictate the magnitude and nature of the surface stress associated with protonation/

deprotonation reactions, and are sensitive to the solution pH, ionic strength, solution ion composition [49, 62], as well as the alkyl chain length [110]. These findings with acidic SAMs are of broader relevance to understanding the molecular origins of surface stress at charged solid interfaces and in biological interactions. Key to the development and implementation of microcantilever-based sensing and actuating technologies is the ability to control the directional motion with known precision and amplitude. This level of control requires a comprehensive understanding of the origin of the surface stress generated in the (bio-)chemical system under investigation, which is the subject addressed in the next section.

#### **4.7 Origin of the Surface Stress Observed for Electroactive Self-Assembled Monolayers Functionalized Microcantilevers**

Chemically well-defined SAMs provide a relatively simple and versatile system with tailorable interfacial chemistry enabling one to probe specific molecular events that would permit insight into the fundamental mechanisms of surface stress generation. Several studies have demonstrated that the selectivity and sensitivity of microcantilever systems rely heavily on the reproducible formation of a functional layer on one surface of the cantilever [111–118]. For example, investigations of the evolution of the surface stress during the chemisorption of *n*-alkanethiols onto gold-coated cantilevers have provided some much needed insight into the experimental factors and chemical interactions that drive the self-assembly process and determine the predominant structural phase adopted by the alkanethiolates [6, 112, 113, 117, 119, 120]. To this end, Badia et al. have investigated the mechanism of the redox-induced deflection of microcantilevers using model SAMs of electroactive ferrocene-terminated alkythiols [37, 121, 122].

Ferrocenylalkylthiol SAMs are probably the most studied electroactive monolayers and their faradaic electrochemistry is extensively documented in the literature [123–134]. This is largely because ferrocene SAMs exhibit relatively straightforward electrochemistry meaning that with the appropriate experimental parameters every surface-tethered ferrocene can undergo a one-electron reversible redox reaction. Furthermore, for a compact ferrocene SAM, the dense molecular packing confines the

electrogeneration of ferrocenium cations and their complexation with the counterions to the monolayer/solution interface and non-specific ion/solvent permeation across the dielectric monolayer is predominantly inhibited. Electrochemical transformations of surface-confined ferrocenylalkylthiols have previously been shown to elicit dramatic changes in interfacial properties through molecular reorganization or ion complexation controlled/triggered by small external changes in the applied potential [135, 136]. In the study discussed herein, gold-coated microcantilevers are functionalized with the redox-active ferrocenylalkylthiols and the origin of the dynamically controlled actuation and surface stress properties are investigated.

The authors clearly demonstrate that the electrochemical transformation of a redox moiety (ferrocene) in the *monomolecular* organic film can generate a surface stress change of a sufficient magnitude to deflect a microcantilever. A characteristic cyclic voltammogram and microcantilever stress profile observed for the redox reaction of a ferrocene-terminated monolayer in a typical electrolyte solution is shown in Fig. 4.9. Oxidation of the ferrocenes-terminated SAM in perchlorate electrolyte generated a compressive surface stress change of  $-0.20 \pm 0.04 \text{ N m}^{-1}$ , and cantilever deflections ranging from  $0.8 \mu\text{m}$

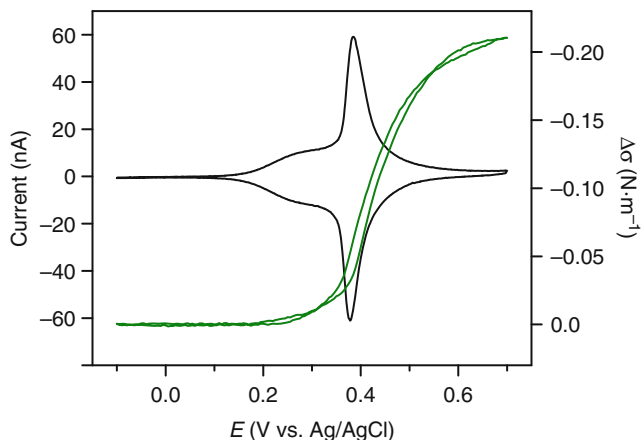


**Fig. 4.9** Typical CVs (left axis, black solid line) and corresponding differential surface stress,  $\Delta\sigma$  (right axis, green solid line), responses for ferrocenes alkanethiol modified microcantilever substrates in 0.10 M  $\text{NaClO}_4/0.01 \text{ M HClO}_4$ . Scan rate =  $5 \text{ mV s}^{-1}$ . Reprinted with permission from [37], ©2009 American Chemical Society

to 60 nm for spring constants between  $\sim 0.01$  and  $\sim 0.8$  N m<sup>-1</sup>. The results strongly suggest that the microcantilever deflection is driven by the lateral tension resulting from molecular reorientation/volume expansion accompanying the charge-transfer and ion-pairing events. To verify this hypothesis, mixed SAM-modified microcantilevers, in which the electroactive ferrocenes are isolated from one another by an inert *n*-alkylthiolate matrix, were investigated. Under an applied potential, a faradaic current was measured, but no microcantilever beam deflection was observed. This finding confirms that the cantilever responds to the lateral pressure exerted by an ensemble of re-orienting ferrocenium-bearing alkylthiolates upon each other rather than to individual anion pairing events, meaning collective interactions are only possible if there is a sufficient number of neighboring ferroceniums. Interactions between ferroceniums (vs. isolated non-interacting ferroceniums) are detected electrochemically in binary SAMs when the surface mole fraction of ferrocene is  $\geq 0.2$ , due to the presence of domains or clusters of ferrocene alkanethiolates [128, 131]. In single-component FcRSAu, the oxidation of a ferrocene next to an already oxidized ferrocenium cation is unfavorable due to electrostatic or Coulombic repulsion between the charged moieties, so that a critical number of electrogenerated ferroceniums may be needed for neighboring interactions [137, 138]. Furthermore, Badia and Norman were able to exploit these findings to control the magnitude of the cantilever response by varying either the molecular structure or electrolyte anion used to generate the surface stress change [122].

As stated above, the cantilever responds to the lateral pressure exerted by an ensemble of re-orienting ferrocenium-bearing alkylthiolates upon each other rather than individual anion pairing events. This finding has general implications for using SAM-modified microcantilevers as (bio-)sensors because it indicates that the cantilever responds to collective in-plane molecular interactions rather than reporting individual (bio-)chemical events.

#### **4.8 Microcantilevers Using Electrochemistry: Biosensing Applications**

The microcantilever surface can be electrochemically functionalized. One of the examples is electrodeposition of chitosan, an aminopolysaccharide, on the microcantilever surface [139]. It is worthwhile

to mention that chitosan has three important properties namely, pH responsiveness (from pH 6 to 6.5), formation of films using a pH switch, and its nucleophilicity [139–141]. These properties are useful in the electrodeposition of chitosan. Briefly, the deposition was carried out by immersing the chip in a chitosan solution and applying a negative potential to the working electrode relative to a counter electrode in the solution. A pH gradient was established at the cathode due to a net hydrogen ion consumption. At pH 6.5, chitosan was solidified at the cathode because of its insolubility at this pH. Also, a slow rate will help in the uniformity of the electrodeposited film.

Moreover, using this thick chitosan functionalized (1.5  $\mu\text{m}$ ) cantilever it was possible to selectively detect the neurotransmitter dopamine from ascorbic acid through a mechano-transduction of electrochemical oxidation reaction [139]. Firstly, the chitosan-coated cantilever bending was measured prior to any electrochemical reactions. Next, the cantilever was placed in a solution of ascorbic acid and an anodic potential was applied in order to oxidize the solution at the electrode surface and no substantial change in bending was observed. However, when a similar procedure was carried out in the presence of dopamine, a bending of approximately 800 nm was observed upon oxidation of dopamine at the chitosan-functionalized cantilever. It was inferred that chitosan forms a crosslinked hydrogel upon oxidation of dopamine resulting in an estimated stress of 1.7 MPa. However, more extensive studies are required to find out the detection limit comparable to that in biological samples, as a relatively high concentration (100  $\mu\text{M}$ ) of dopamine was required in these experiments.

In another example, cyclic voltammetry was used for the electrodeposition of streptavidin on a microcantilever device having nano-integrated electrodes (Nano-IDEs) [142]. Streptavidin embedded in polyscopoletin was deposited on the Nano-IDEs from a solution containing streptavidin and scopoletin in 0.1 M NaCl. The thickness of the streptavidin/scopoletin layer was found to be a function of the number of cyclic voltammetry scans used. Fluorescein-conjugated biotin was also coupled to the surface of the working electrode. The fluorescence intensity was also found to increase with increasing cyclic voltammetry scans.

Xia et al. have investigated the adsorption of dopamine and the interaction of iron (III) ions with dopamine on gold-coated microcantilevers [143]. Dopamine is of particular interest owing to its postulated

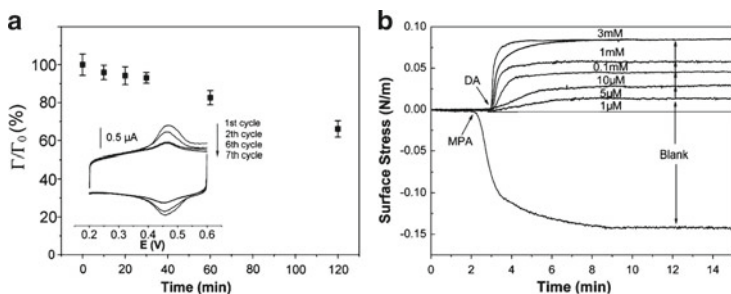


**Fig. 4.10** (a) The plot of normalized surface coverage ( $\Gamma/\Gamma_0$ ) of dopamine-modified electrodes vs. dipping time in a 10 mM NaCl bland solution (pH=2.5). The surface coverage was obtained from the voltammogram at the first potential cycle and normalized to that of dopamine-modified electrode without dipping in the blank solution. The *inset* is the voltammograms with repetitive potential cycling after dipping 10 min in blank solution. The scan rate is  $0.02 \text{ V s}^{-1}$ . (b) Surface stress changes vs. time in a flow blank solution with sequential injections of 0.001, 0.005, 0.01, 1.0, and 3.0 mM dopamine solutions and 1 mM 3-mecroptopropionic acid. Reprinted from [143] with permission from Elsevier

role in Parkinson's and Alzheimer's disease [144]. Dopamine is known to reversibly and weakly adsorb on a gold interface. In their study, Xia et al. first monitor the adsorption characteristics of dopamine at the gold-microcantilever interface [143]. The magnitude of the observed surface stress was found to depend on the dopamine injection concentration, reaching a maximum stable surface stress change with concentrations greater than 1 mM (Fig. 4.10). The microcantilever exhibited a tensile stress or a bending toward the gold-coated surface. It was not possible to model the dopamine adsorption according to the Langmuir approach, suggesting that multilayer formation or intermolecular interactions were the dominant forces in this process. Therefore, the surface stress change was attributed to the presence of intermolecular hydrogen bonds of dopamine and the charge transfer effect between adsorbates and the substrate.

The surface coverage ( $\Gamma$ ,  $\text{mol cm}^{-2}$ ) of dopamine was readily determined according to the equation  $\Gamma = Q/nFA$ , where  $Q$  is the coulometric charge ( $C$ ) and is obtained from the integration of the anodic peak,  $A$  is the area of electrode ( $\text{cm}^2$ ),  $n$  is the number of electrons transferred ( $n=2$ ), and  $F$  is Faraday's constant ( $96,485 \text{ C mol}^{-1}$ ). Dopamine adsorbates at the gold-microcantilever were found to be relatively stable over a time period of 30 min as indicated by the small decline ( $\sim 6.5\%$ ) in the normalized surface concentration (Fig. 4.10a).

The dopamine-modified gold-coated microcantilevers were then used to investigate interactions between dopamine and  $\text{Fe}^{3+}$ . The authors found that the deflection response was dependent on both concentration of  $\text{Fe}^{3+}$  and the interaction time which was controlled by subsequent injections of a blank solution. A two-step deflection profile was observed at relatively high concentrations of  $\text{Fe}^{3+}$ . Here,  $\text{Fe}^{3+}$  initially reacted with dopamine molecules found in the outer layers and the complexes were removed with subsequent injects. Then  $\text{Fe}^{3+}$  reacted further with dopamine molecules forming a surface complex in the first layer next to the gold. When the concentration of  $\text{Fe}^{3+}$  was kept relatively low, only the first stage was observed as indicated by the absence in variation in the cantilever response. In all cases, a compressive stress was observed until the dopamine-modified surface was regenerated.

A notable example of microcantilever biosensors includes their use for the detection of glucose [145–148]. Diabetes is among one of the most prevalent diseases in the world and its diagnosis and management requires daily monitoring of blood glucose levels. In the first examples, microcantilever-based glucose biosensors were modified by poly-L-lysine or glutaraldehyde with glucose oxidase (GOx) [145, 146]. The cantilever was observed to bend on the exposure to solutions containing glucose. A theoretical study on the reaction energetics and expected heat response of the cantilever indicated that the cantilever deflection is not simply a result of reaction-generated heat, but likely a consequence of the surface stress induced by the specific interactions of glucose with the GOx enzyme [145, 146]. These results were later confirmed by Ji et al., where a systematic study was undertaken to investigate the flow rate, glucose concentration, reproducibility, selectively, effect of pH, and  $\text{H}_2\text{O}_2$  on the GOx-functionalized-microcantilever response [148]. In their study, a multilayer film was assembled on one face of the microcantilever using a layer-by-layer approach. The cantilever biosensing system showed a 10% reproducibility in the glucose measurements. Selectivity was readily demonstrated since the multilayer GOx-modified microcantilever did not respond to the same concentrations of mannose, fructose, and galactose. This extensive study provided evidence that the cantilever response did indeed arise primarily from protein conformational changes as a result of the glucose binding event [148]. In a more recent study, glucose responsive polymer brushes were synthesized on gold substrates in a microcantilever array format [147].

The stimuli–response properties of the polymer brush–microcantilever system were evaluated by exposing them to varying concentrations of glucose for a range of pH values, while simultaneously measuring the corresponding surface stress change. A large, reversible swelling response in the presence of free glucose at physiologically relevant concentrations was easily observed. Moreover, the deflection and surface stress response of the micromechanical cantilevers, functionalized with polymer brushes, are substantially larger and faster than that of their glucose sensing SAM-functionalized-microcantilever counterparts. In all cases, the combination of the microcantilever platform with glucose sensing components provides a unique approach for investigating glucose levels.

## 4.9 Conclusion

To date, combined electrochemical–cantilever measurements involving different systems with characteristic features remains in its infancy. This chapter has provided an overview of the current existing literature. The electrochemically induced motion of free-standing microcantilevers is attracting growing interest as micro-/nano-actuators and robotic devices. This is not only due to their growing accessibility and affordability, but also because these devices exhibit fast and reliable detection of small concentration of molecules in air and solution. However, the development and implementation of these cantilever-based actuating technologies requires a molecular-level understanding of the origin of the surface stress that causes the cantilever to bend. Electron transfer kinetics at a metal–liquid interface under electrochemical control is of immense interest. An understanding of the dependence of surface stress on potential at the solid–electrolyte interface is an important and challenging problem, and could lead to a better understanding of processes occurring at an electrified interface in solution. Furthermore, in order to achieve improved performance for biomedical application, the development and improvement of microcantilever sensors that allow for measurements in complex real-life samples remains a critical issue that needs to be addressed.

**Acknowledgments** This research is supported by Canada Excellence Research Chair Program.

## References

1. Thundat T, Warmack RJ, Chen GY, Allison DP (1994) *Appl Phys Lett* 64:2894
2. Gimzewski JK, Gerber C, Meyer E, Schlittler RR (1994) *Chem Phys Lett* 217:589
3. Chen GY, Thundat T, Wachter EA, Warmack RJ (1995) *J Appl Phys* 77:3618
4. Butt H-J (1996) *J Colloid Interface Sci* 180:251
5. Thundat T, Oden PI, Warmack RJ (1997) *Microscale Thermophys Eng* 1:185
6. Berger R, Delamar E, Lang H-P, Gerber C, Gimzewski JK, Meyer E, Güntherodt H-J (1997) *Science* 276:2021
7. Raiteri R, Grattarola M, Butt H-J, Skládal P (2001) *Sens Actuators B* 79:115
8. Lang HP, Hegner M, Gerber C (2005) *Mater Today* 8:30
9. Sepaniak M, Datskos P, Lavrik N, Tipple C (2002) *Anal Chem* 74:568A
10. Hansen KM, Thundat T (2005) *Methods* 37:57
11. Lang HP, Baller MK, Berger R, Gerber C, Gimzewski JK, Battiston FM, Fornaro P, Ramseyer JP, Meyer E, Güntherodt HJ (1999) *Anal Chim Acta* 393:59
12. Ziegler C (2004) *Anal Bioanal Chem* 379:946
13. Lavrik NV, Sepaniak MJ, Datskos PG (2004) *Rev Sci Instrum* 75:2229
14. Goeders KM, Colton JS, Bottomley LA (2008) *Chem Rev* 108:522
15. Raiteri R, Grattarola M, Berger R (2002) *Mater Today* 5:22
16. Waggoner PS, Craighead HG (2007) *Lab Chip* 7:1238
17. Singamaneni S, LeMieux MC, Lang H-P, Gerber C, Jiang H, Naik RR, Bunning JJ, Tsukruk VV (2008) *Adv Mater* 20:653
18. Sader JE (2002) In: Hubbard A (ed) *Encyclopedia of surface and colloid science*. Marcel Dekker, New York, p 846
19. Fritz J (2008) *Analyst* 133:855
20. Baller MK, Fritz J (2004) In: Kambhampati D (ed) *Protein microarray technology*. Wiley-VCH, Weinheim, p 195
21. Berger R, Lang HP, Gerber C, Gimzewski JK, Fabian JH, Scandella L, Meyer E, Güntherodt H-J (1998) *Chem Phys Lett* 294:363
22. Barnes JR, Stephenson RJ, Woodburn CN, O'Shea SJ, Welland ME, Rayment T, Gimzewski JK, Gerber C (1994) *Rev Sci Instrum* 65:3793
23. Bachels T, Tiefenbacher F, Schäfer R (1999) *J Chem Phys* 110:10008
24. Krause AR, Van Neste C, Senesac L, Thundat T, Finot E (2008) *J Appl Phys* 103:094906
25. Barnes JR, Stephenson RJ, Welland ME, Gerber C, Gimzewski JK (1994) *Nature* 372:79
26. Wig A, Arakawa ET, Passian A, Ferrell TL, Thundat T (2006) *Sens Actuators B* 114:206
27. Burg TP, Godin M, Knudsen SM, Shen W, Carlson G, Foster JS, Babcock K, Manalis SR (2007) *Nature* 446:1066
28. Bryan AK, Goranov A, Amon A, Manalis SR (2010) *Proc Natl Acad Sci* 107:999
29. Godin M, Delgado FF, Son S, Grover WH, Bryan AK, Tzur A, Jorgensen P, Payer K, Grossman AD, Kirschner MW, Manalis SR (2010) *Nat Methods* 7:387
30. Stoney GG (1909) *Proc R Soc London Ser A* 82:172
31. Haiss W (2001) *Rep Prog Phys* 64:591

32. Godin M, Tabard-Cossa V, Grütter P, Williams P (2001) *Appl Phys Lett* 79:551
33. Tabard-Cossa V, Godin M, Beaulieu LY, Grütter P (2005) *Sens Actuators B* 107:233
34. Tabard-Cossa V, Godin M, Beaulieu LY, Grütter P (2006) *Sens Actuators B* 119:352
35. Ibach H (1997) *Surf Sci Rep* 29:195
36. Lang HP, Gerber C (2008) In: Samori P (ed) *STM and AFM studies on (bio)molecular systems: unravelling the nanoworld*, vol 285. Springer, Heidelberg, p. 1.
37. Norman LL, Badia A (2009) *J Am Chem Soc* 131:2328
38. Evans DR, Craig VSJ (2006) *J Phys Chem B* 110:5450
39. Freund LB, Floro JA, Chason E (1999) *Appl Phys Lett* 74:1987
40. Jeon S, Thundat T (2004) *Appl Phys Lett* 85:1083
41. Klein CA (2000) *J Appl Phys* 88:5487
42. Mertens J, Álvarez M, Tamayo J (2005) *Appl Phys Lett* 87:234102
43. Rasmussen PA, Hansen O, Boisen A (2005) *Appl Phys Lett* 86:203502
44. Sader JE (2001) *J Appl Phys* 89:2911
45. Sader JE, Larson I, Mulvaney P, White LR (1995) *Rev Sci Instrum* 66:3789
46. Zhang Y, Ren Q, Zhao Y-p (2004) *J Phys D Appl Phys* 37:2140
47. Miyatani T, Fujihira M (1997) *J Appl Phys* 80:7099
48. Khan A, Philip J, Hess P (2004) *J Appl Phys* 95:1667
49. Fritz J, Baller MK, Lang HP, Rothuizen H, Vettiger P, Meyer E, Güntherodt H-J, Gerber C, Gimzewski JK (2000) *Science* 288:316
50. Fritz J, Cooper EB, Gaudet S, Sorger PK, Manalis SR (2002) *Proc Natl Acad Sci* 99:14142
51. Mukhopadhyay R, Lorentzen M, Kjems J, Besenbacher F (2005) *Langmuir* 21:8400
52. Shu W, Liu D, Watari M, Riener CK, Strunz T, Welland ME, Balasubramanian S, McKendry RA (2005) *J Am Chem Soc* 127:17054
53. McKendry RA, Zhang J, Arntz Y, Strunz T, Hegner M, Lang HP, Baller MK, Certa U, Meyer E, Güntherodt H-J, Gerber C (2002) *Proc Natl Acad Sci* 99:9783
54. Wu G, Ji H, Hansen K, Thundat T, Datar R, Cote R, Hagan MF, Chakraborty AK, Majumdar A (2001) *Proc Natl Acad Sci* 98:1560
55. Stachowiak JC, Yue M, Castelino K, Chakraborty AK, Majumdar A (2006) *Langmuir* 2006:263
56. Backmann N, Zahnd C, Huber F, Bietsch A, Plückthun A, Lang H-P, Güntherodt H-J, Hegner M, Gerber C (2005) *Proc Natl Acad Sci* 102: 14587
57. Savran CA, Knudsen SM, Ellington AD, Manalis SR (2004) *Anal Chem* 76:3194
58. Park J, Ryu J, Choi SK, Seo E, Cha JM, Ryu S, Kim J, Kim B, Lee SH (2005) *Anal Chem* 77:6571
59. Ilic B, Yang Y, Craighead HG (2004) *Appl Phys Lett* 85:2604
60. Álvarez M, Carrascosa LG, Moreno M, Calle A, Zaballos Á, Lechuga LM, Martínez-A C, Tamayo J (2004) *Langmuir* 20:9663
61. Khaled A-RA, Vafia K, Yang M, Zhang X, Ozkan CS (2003) *Sens Actuators B* 94:103
62. Watari M, Galbraith J, Lang H-P, Sousa M, Hegner M, Gerber C, Horton MA, McKendry RA (2007) *J Am Chem Soc* 129:601

63. Hagan MF, Majumdar A, Chakraborty AK (2002) *J Phys Chem B* 106:10163
64. Zhang J, Lang HP, Huber F, Bietsch A, Grange W, Certa U, McKendry RA, Güntherodt H-J, Hegner M, Gerber C (2006) *Nat Nanotechnol* 1:214
65. Ndieyira JW, Watari M, Barrera AD, Zhou D, Vögli M, Batchelor M, Cooper MA, Strunz T, Horton MA, Abell C, Rayment T, Aeppli G, McKendry RA (2008) *Nat Nanotechnol* 3:691
66. Godin M, Laroche O, Tabard-Cossa V, Beaulie LY, Grütter P, Williams PJ (2003) *Rev Sci Instrum* 74:4902
67. Fischer LM, Pedersen C, Elkjær K, Noeth N-N, Dohn L, Boisen A, Tenje M (2011) *Sens Actuators B* 157:321
68. Tian F, Pei JH, Hedden DL, Brown GM, Thundat T (2004) *Ultramicroscopy* 100:217
69. Ansari MZ, Cho C (2009) *Sensors* 9:6046
70. Lee P-S, Lee J, Shin N, Lee K-H, Lee D, Jeon S, Choi D, Hwang W, Park H (2008) *Adv Mater* 20:1732
71. Sharma G, Svensson S, Ogden S, Klintberg L, Hjort K (2011) *J Micromechanics Microeng* 21, 075010
72. Lee W-B, Chen Y-H, Lin H-I, Shiesh S-C, Lee G-B (2011) *Sens Actuators B Chem* 157:710
73. Ogilvie IRG, Sieben VJ, Cortese B, Mowlem MC, Morgan H (2011) *Lab Chip* 11:2455
74. Ricciardi C, Canavese G, Castagna R, Ferrante I, Ricci A, Marasso SL, Napione L, Bussolino F (2010) *Biosens Bioelectron* 26:1565
75. Avila M, Zougagh M, Escarpa A, Rios A (2009) *Electrophoresis* 30:3413
76. Ezkerra A, Fernández LJ, Mayora K, Ruano-López JM (2011) *Sens Actuators B Chem* 155:505
77. Leichle T, Nicu L, Descamps E, Corso B, Mailley P, Livache T, Bergaud C (2006) *Appl Phys Lett* 88:254108
78. Bange AF, Brown GM, Senesac LR, Thundat T (2009) *Surf Sci* 603:L125
79. Brunt TA, Rayment T, O'Shea SJ, Welland ME (1996) *Langmuir* 12:5942
80. Brunt TA, Chabala ED, Rayment T, O'Shea SJ, Welland ME (1996) *J Chem Soc Faraday Trans* 92:3807
81. Bard AJ, Faulkner LR (2001) *Electrochemical methods fundamentals and applications*, 2nd edn. Wiley, New York
82. Herrero E, Buller LJ, Abruña HD (2001) *Chem Rev* 101:1897
83. Qazi M, Koley G (2008) *Sensors* 8:7144
84. Mandeles A, Christofides C (1993) *Physics, chemistry and technology of solid state gas sensor devices*. Wiley, New York, NY
85. Koley G, Qazi M, Lakshmanan L, Thundat T (2007) *Appl Phys Lett* 90:173105
86. Koley G, Spencer MG (2001) *J Appl Phys* 90:337
87. Sasaki N, Tsukada M (1998) *Jpn J Appl Phys* 2(37):L533
88. Lahav M, Durkan C, Gabai R, Katz E, Willner I, Welland ME (2001) *Angew Chem Int Ed* 40:4095
89. Tabard-Cossa V, Godin M, Grütter P, Burgess I, Lennox RB (2005) *J Phys Chem B* 109:17531
90. Smela E (2003) *Adv Mater* 15:481
91. Bumbu G-G, Kircher G, Wolkenhauer M, Berger R, Gutmann JS (2004) *Macromol Chem Phys* 205:1713

92. Bumbu G-G, Wolkenhauer M, Kircher G, Gutmann JS, Berger R (2007) *Langmuir* 23:2203
93. Zhou F, Biesheuvel PM, Choi E-Y, Shu W, Poetes R, Steiner U, Huck WTS (2008) *Nano Lett* 8:725
94. Zhou F, Huck WTS (2006) *Phys Chem Chem Phys* 8:3815
95. Zhou F, Shu W, Welland ME, Huck WTS (2006) *J Am Chem Soc* 128: 5326
96. Liu Y, Flood AH, Bonvallet PA, Vignon SA, Northrop BH, Tseng H-R, Jeppesen JO, Huang TJ, Brough B, Baller M, Magonova S, Solares SD, Goddard WA, Ho C-M, Stoddard JF (2005) *J Am Chem Soc* 127:9745
97. Huang TJ, Brough B, Ho C-M, Liu Y, Flood AH, Bonvallet PA, Tseng H-R, Stoddard JF, Baller M, Magonova S (2004) *Appl Phys Lett* 85:5391
98. Juluri BK, Kumar AS, Liu Y, Ye T, Yang Y-W, Flood AH, Fang L, Stoddard JF, Weiss PS, Huang TJ (2009) *ACS Nano* 3:291
99. Bay L, Jacobsen T, Skaarup S, West K (2001) *J Phys Chem B* 105:8492
100. Roemer M, Kurzenknabe T, Oesterschulze E, Nicoloso N (2002) *Anal Bioanal Chem* 373:754
101. Liu Y, Flood AH, Bonvallet PA, Vignon SA, Northrop BH, Tseng H-R, Jeppesen JO, Huang TJ, Brough B, Baller M, Magonov S, Solares SD, Goddard WA, Ho C-M, Stoddard JF (2005) *J Am Chem Soc* 127:9745
102. Chegel V, Raitman O, Katz E, Gabai R, Willner I (2001) *Chem Commun* 10:883
103. Howse JR, Topham P, Crook CJ, Gleeson AJ, Bras W, Jones RAL, Ryan AJ (2006) *Nano Lett* 6:73
104. Zhaliev A, Abu-Lail NI, Lim DW, Chilkoti A, Zauscher S (2007) *Langmuir* 33:339
105. Igarashi S, Itakura AN, Toda M, Kitajima M, Chu L, Chifen AN, Förch R, Berger R (2006) *Sens Actuators B* 117:43
106. Abu-Lail NI, Kaholek M, LaMattina B, Clark RL, Zauscher S (2006) *Sens Actuators B* 114:371
107. Rant U, Arinaga K, Fujita S, Yokoyama N, Abstreiter G, Tornow M (2004) *Nano Lett* 4:2441
108. Rant U, Arinaga K, Fujita S, Yokoyama N, Abstreiter G, Tornow M (2006) *Org Biomol Chem* 4:3448
109. Shen G, Tercero N, Gaspar MA, Varughese B, Shepard K, Levicky R (2006) *J Am Chem Soc* 128:8427
110. Sushko ML, Harding JH, Shluger AL, McKendry RA, Watari M (2008) *Adv Mater* 20:3848
111. Tabard-Cossa V, Godin M, Burgess IJ, Monga T, Lennox RB, Grütter P (2007) *Anal Chem* 79:8136
112. Kohale S, Molina SM, Weeks BL, Kare R, Hope-Weeks LJ (2007) *Langmuir* 23:1258
113. Godin M, Williams PJ, Tabard-Cossa V, Laroche O, Beaulie LY, Lennox RB, Grütter P (2004) *Langmuir* 20:7090
114. Headrick JJ, Sepaniak MJ, Lavrik NV, Datskos PG (2003) *Ultramicroscopy* 97:417
115. Lavrik NV, Tipple CA, Sepaniak MJ, Datskos PG (2001) *Chem Phys Lett* 336:371
116. Hansen AG, Martensen MW, Anderson JET, Ulstrup J, Kuhlue A, Garnæs J, Boisen A (2001) *Probe Microsc* 2:139

117. Desikan R, Lee I, Thundat T (2006) *Ultramicroscopy* 106:795
118. Mertens J, Calleja M, Tarín A, Tamayo J (2007) *J Appl Phys* 101:034904
119. Berger R, Delamarche E, Lang HP, Gerber C, Gimzewski JK, Meyer E, Güntherodt H-J (1998) *Appl Phys A* 66:S55
120. Desikan R, Armel S, Meyer HM III, Thundat T (2007) *Nanotechnology* 18:424028
121. Quist F, Tabard-Cossa V, Badia A (2003) *J Phys Chem B* 107:10691
122. Norman LL, Badia A (2011) *J Phys Chem C* 115:1985
123. Finklea HO (1996) In: Bard AJ, Rubinstein I (eds) *Electroanalytical chemistry*, vol 19. Marcel Dekker, New York, p 109
124. Weber KS, Creager SE (1998) *J Electroanal Chem* 458:17
125. Valincius G, Niaura G, Kazakevičienė B, Talaikytė Z, Kažemėkaitė M, Butkus E, Razumas V (2004) *Langmuir* 20:6631
126. Kazakevičienė B, Valincius G, Niaura G, Talaikytė Z, Kažemėkaitė M, Razumas V, Plaušinitis D, Teišerskienė A, Lisauskas V (2007) *Langmuir* 23:4965
127. Ju H, Leech D (1999) *Phys Chem Chem Phys* 1:1549
128. Lee LYS, Sutherland TC, Rucareanu S, Lennox RB (2006) *Langmuir* 22:4438
129. Sato Y, Mizutani F, Shimazu K, Ye S, Uosaki K (1999) *J Electroanal Chem* 474:94
130. Kondo T, Okamura M, Uosaki K (2001) *J Organomet Chem* 637–639:841
131. Auletta T, van Veggel FCJM, Reinhoudt DN (2002) *Langmuir* 18:1288
132. Kazakevičienė B, Valincius G, Niaura G, Talaikytė Z, Kažemėkaitė M, Razumas V (2003) *J Phys Chem B* 107:6661
133. Viana AS, Jones AH, Abrantes LM, Kalaji M (2001) *J Electroanal Chem* 500:290
134. Weber KS, Hockett LA, Creager SE (1997) *J Phys Chem B* 101:8286
135. Sondag-Huethorst JAM, Fokkink LGJ (1994) *Langmuir* 10:4380
136. Luk Y-Y, Abbott NL (2003) *Science* 301:623
137. Calvente JJ, Andreu R, Molero M, Lopez-Perez G, Domínguez M (2001) *J Phys Chem B* 105:9557
138. Smith CP, White HS (1992) *Anal Chem* 64:2398
139. Koev ST, Powers MA, Yi H, Wu LQ, Bentley WE, Rubloff GW, Payne GF, Ghodssi R (2007) *Lab Chip* 7:103
140. Payne GF, Wu LQ (2004) *Trends Biotechnol* 22:593
141. Payne GF, Yi HM, Wu LQ, Bentley WE, Ghodssi R, Rubloff GW, Culver JN (2005) *Biomacromolecules* 6:2881
142. Lee JA, Yun JY, Lee SS, Lee KC (2006) *Key Eng Mater* 326–328:1359
143. Xu Y, Zhang B, Wu S, Xia Y (2009) *Anal Chim Acta* 649:117
144. Fasano M, Bergamasco B, Lopiano L (2006) *J Neurochem* 96:909
145. Pei J, Tian F, Thundat T (2004) *Anal Chem* 76:292
146. Subramanian A, Oden PI, Kennel SJ, Jacobson KB, Warmack RJ, Thundat T, Doktycz MJ (2002) *Appl Phys Lett* 81:385
147. Chen T, Chang DP, Liu T, Desikan R, Datar R, Thundat T, Berger R, Zauscher S (2010) *J Mater Chem* 20:3391
148. Yan X, Xu KX, Ji H-F (2005) *Anal Chem* 77:6197

# Chapter 5

## Surface Treatments with Silver and Its Compounds for Biomedical Applications

Stojan S. Djokić

### 5.1 Introduction

Selection of materials to be used for medical devices depends on the targeted application. For instance, in wound-healing applications, the most commonly used materials as topical dressings are various textile materials, polymeric foams, alginate, carboxy methyl cellulose (CMC) or other types of gels, and sometimes adhesives. Among textile materials, usually fabrics made of natural (e.g., cotton) or synthetic (e.g., high-density polyethylene (HDPE), nylon, polyester, etc.) fibres are used. For catheters, polymers such as polyurethane, silicone, latex or similar are applied as tubes.

All devices suffer a common problem of device-related infection. Increasingly, new materials are being developed which are described as *anti-infective*, *bioactive* or *anti-microbial*.

Medical device-related infection is often caused by formation of bio-film adhering to the surface. Administration of antimicrobial agents by systemic or oral routes generally fails to reach the microbial bio-film. A successful antimicrobial treatment in such cases is markedly improved by maintaining sufficiently high concentrations of the antimicrobial agent for a site-specific activity [1–3].

Antimicrobial properties of silver and its compounds have been utilized for a long time. Surfaces treated with silver and its compounds find applications in medical devices used as topical wound dressings,

---

S.S. Djokić (✉)  
Elchem Consulting Ltd, Edmonton, AB, Canada T5X 6B3  
e-mail: sdjokic@telus.net

urinary catheters, endotracheal tubes, cardiac valves, surgical masks, implantable devices, water filtration, etc. [4–12].

A treatment of various surfaces e.g., textile, polymers or metals with silver or its compounds is carried out due to antimicrobial action of silver ions. The aim of this chapter is to analyze and review the achievements in the area of treatments of various surfaces with silver and/or its compounds for biomedical applications.

## 5.2 Historical Overview

The germicidal properties of silver have been utilized since the early Mediterranean cultures. According to Russell, Alexander the Great was advised by Aristotle in 350 BC to store water in silver vessels and to boil it before use [13]. It has been known since 1000 BC that water kept in silver vessels, exposed to light or filtered, could be rendered potable. The first topical applications of silver nitrate were for the treatment of chronic wounds and ulcers [14]. For an extensive review on early uses of silver in the treatments of burns, the reader is referred to the article by Klasen and references therein [14].

Silver nitrate or as often mentioned in the classical literature as *lapis infernalis* was also used for treatments of fresh burns [15, 16]. For this purpose, burns were treated with a “silver nitrate pencil” or linen soaked in 0.5–2%  $\text{AgNO}_3$ .

Developments in microbiology have strongly stimulated researchers to further investigate effects of various compounds on the growth of microorganisms. Because of the empirical use of silver nitrate, Behring was interested in its effects on anthrax, typhoid, and gonorrhoea [17]. His experiments showed that silver in blood or fluids of similar composition exhibited antiseptic properties. In broth and gelatin, silver was significantly less active.

Credé introduced the use of silver nitrate solutions (less than 2%) as eye-drops to prevent *ophthalmia neonatorum* caused by gonococci [18].

The effect of metallic silver on growth of staphylococci and streptococci under laboratory conditions was investigated by Credé and Beyer [19]. They observed that when pieces of metallic silver were removed from an inoculated plate after 24 h, growth of microorganisms was not observed on the spot where silver metal was placed. Also, if that spot was re-inoculated, no microorganisms grew.

On the basis of this observation Credé and Beyer postulated that metabolic products of bacteria reacted with silver metal-producing compounds with an antiseptic effect. In further explanations, they assumed that the lactic acid, which was present in high concentrations in the wound, reacted with metallic silver. As a consequence, the concentration of the lactic acid decreased. They suggested that lactic acid was needed for the growth of microorganisms and that if this were not present, the silver would remain as an indifferent metal.

According to Credé and Beyer, the first step in the bactericidal process of silver would be the formation of silver salt. Silver salts effective for antimicrobial purposes included silver nitrate, silver lactate, silver tartrate, and silver citrate. Notably, silver lactate and silver citrate with dilutions (1:3,800) killed staphylococci and streptococci in 10 min. They further reported that if these compounds were present on the plate in concentrations of about 12.5 ppm, they inhibited the bacterial growth.

Credé also reported on silver-based dressings known as “white silver dressings” and “gray silver dressings.” The “white silver dressing” was consisted of cotton mesh on which silver foil was mounted. The “gray silver dressing” which was brought on the market consisted of sterilized cotton impregnated with metallic silver.

Other forms of silver such as coatings for the prevention of beverages from spoilage or plates and foils in the surgical treatments of wounds and broken bones have been used within the past three centuries.

The lethal effects of metals toward bacteria and lower life forms were investigated by Ravelin [20] and von Naegeli [21]. von Naegeli reported that a concentration of silver ions which were derived from metallic silver in the order of magnitude of  $9.2 \times 10^{-9}$  M would kill common fresh-water *Spirogyra*. At concentrations of  $5.5 \times 10^{-6}$  M, the germination of *Aspergillus niger* spores was prevented. This phenomenon was described by von Naegeli as *oligodynamic effect*. The term oligodynamic effect is typically restricted to describing solutions in which the metal ion concentration is several orders of magnitude lower than that which would be lethal for higher organisms [22].

The observations by the early Mediterranean civilizations and later by Credé, Beyer, Ravelin, and Naegali related to the activity of silver and its compounds continued to attract surgeons [14]. At the beginning of the twentieth century a gauze soaked in a 1% silver nitrate solution was used by German army surgeons for both fresh and operation wound treatments [23].

The literature data from the nineteenth and early twentieth century suggest that the use of silver and/or its compounds was exclusively empirical. There was no reasonable scientific explanation at that time about the antimicrobial activity of silver and its compounds.

Many developments in the science and technology of that time, in general, were not well advanced. For example, electrochemistry as a science was at its early stage. Credé and Beyer were obviously pioneers who clearly demonstrated that silver compounds exhibit antimicrobial activity [19]. They also observed that pure metallic silver is not antimicrobially active. Their brilliant experiments strongly supported their conclusions. At the later stages of developments, it was actually shown that only silver ions are responsible for the antimicrobial activity of silver or its compounds. Credé and Beyer were probably not aware of Arrhenius's theory of electrolytic dissociation [24] and existence of ions in solutions, which was published approximately at the same time as their work. The findings about the antimicrobial activity of silver are discussed in later sections of this chapter.

Acél was the first who attributed the antimicrobial properties of silver to the liberation of  $\text{Ag}^+$  from materials [25]. The oligodynamic activity of silver was studied in detail and published by a Canadian bacteriologist, James Gibbard [26].

Gibbard observed that if the metallic silver is cleaned with abrasive cloth or paper it becomes inactive. Also, if molten silver is allowed to cool in an atmosphere of hydrogen, no antimicrobial activity appeared. Contrarily, when the molten silver was cooled in air, antimicrobial activity was observed. In general terms, on the basis of the experiments performed by Gibbard, the pure silver is devoid of antimicrobial activity but tarnished and/or surface oxidized silver was active.

As a result of many experiments with metallic silver, colloidal silver (which nowadays is referred to as silver *nanoparticles* or similar), and silver oxide, Gibbard concluded that silver possesses bactericidal action due to liberation of  $\text{Ag}^+$  ions, probably from silver oxide. He, furthermore, confirmed that this antimicrobial action was suppressed in the presence of glucose.

This experimental observation is consistent with the fact that glucose is a reducing agent of  $\text{Ag}^+$  ions. Glucose is frequently used in the electroless deposition of silver. Consequently, Gibbard's observation can be explained as follows. In the presence of glucose dissociated  $\text{Ag}^+$

ions will be reduced to elemental silver, which is not antimicrobially active. Importantly, Gibbard wrote that “the bactericidal activity of silver is due entirely to ionized silver.”

Additionally, Gibbard observed that silver nitrate and “electrically” dispersed silver, when diluted on the basis of silver concentration, all possess a similar bactericidal or oligodynamic activity. The bactericidal activity of silver oxide was markedly reduced by the presence of proteins and glucose.

In 1965, Moyer revived interest in silver nitrate solution for wound-healing applications [27, 28]. He found that the lowest concentration of silver nitrate active against *Pseudomonas aeruginosa* and *Escherichia coli*, both in vitro and in vivo was 0.5%. Notably, the silver nitrate was administered via thick cotton gauze dressing covering the wound. The gauze was kept continuously moist by wetting the dressing with  $\text{AgNO}_3$  solution every 3–4 h.

Another silver-based formulation, silver sulfadiazine was introduced by Fox [28]. Silver sulfadiazine is produced from silver nitrate and sodium sulfadiazine by substituting a silver atom for a hydrogen atom in the sulfadiazine molecule. Silver sulfadiazine remains as the most widely used substance for burn treatments even nowadays.

Although silver nitrate solution was used successfully in burn treatments, it has disadvantages such as hypotonicity and methaemoglobinaemia [29]. Butcher et al. [30] recommended the use of silver lactate and silver acetate. The antimicrobial activity was good and, importantly, they observed a reduced frequency of black spots on walls, floors and clothing as a further advantage compared with silver nitrate.

In the latter part of the twentieth century intensive research on treatments of various dressing with silver and/or silver-based compounds due to their antimicrobial activity was carried out for the wound-healing applications. Two silver-coated nylon products were studied in vitro [31]: silver-coated nylon (SN) and woven heavy rip stop (HRS) containing 26% metallic silver. The results showed that the silver-coated nylon materials were active against many microorganisms.

In order to increase the concentration of silver ions at the wound surface, a weak direct current was applied with silver-coated nylon being the anode [32]. The antimicrobial activity of silver-coated nylon markedly increased due to oxidation of silver and a consequent release of silver ions.

Similar experiments were performed using silver-coated nylon cloth [33, 34]. The experimental animals whose burns had been inoculated with a lethal dose of *P. aeruginosa* were treated. A silver needle was inserted under the burn wound and served as a cathode. A direct current of 0.4–40 mA was then applied from an external source. The maximum voltage varied from 0.1 to 0.86 V. When the silver-coated nylon was used as an anode and silver needle as cathode, a therapeutic antimicrobial effect was achieved. Contrarily, when silver-coated nylon was used as the cathode, the antimicrobial effect was not produced.

The experimental observations described in publications [33, 34] confirm that a presence of  $\text{Ag}^+$  ions is essential for the antimicrobial activity. It is obvious from these experiments that when silver-coated nylon served as an anode the electrochemical oxidation takes place, producing  $\text{Ag}^+$  ion. When the silver needle was used as an anode, no antimicrobial activity was observed. One can assume that in this case, due to significantly smaller surface of the silver needle in comparison with the surface of silver-coated nylon gauze, much lower concentrations of silver ions would be released, leading in this way to an insufficient or no antimicrobial activity.

At the end of the twentieth and the beginning of the twenty-first centuries, significant research on the surface treatments of various textile and polymeric materials with silver and its compounds for use in wound healing, catheters and other biomedical applications was carried out. In the past few decades several topical dressings containing silver have been developed for wound care, and they are available on the market under different trade names.

With the appearance of nanotechnology as a separate engineering discipline, many so-called nanomaterials, nanoparticles, nanocrystals, etc. have attracted researchers worldwide. One of the products that particularly attracted market and health care workers is available under the trade name Acticoat. This product is used in clinical settings and is described as “nanocrystalline silver dressing” [35, 36]. Acticoat is produced by the physical vapor deposition of silver, under the conditions of reactive sputtering, i.e., in the presence of oxygen, as described in the US Patent 6,238,686 B1 [37]. It is important to note that this “nanocrystalline silver” represents a mixture of pure silver,  $\text{Ag}_2\text{O}$ , and  $\text{Ag}_2\text{CO}_3$  as documented by a careful analysis of this material [38].

A multilayer wound dressing representing a multi-ply nylon fabric plated with silver by an electroless deposition process [39, 40] is known under the trade name Silverlon. It is claimed that the dressing can be used for prophylactic and therapeutic care, treatments of skin

infections and surface wounds including surgical incisions. Furthermore, the authors claimed that the product has antibacterial, antifungal, and analgesic properties.

Another product, based on chemical deposition of silver oxysalts onto high-density polyethylene (HDPE) [41–43], was recently introduced. Silver oxysalt  $\text{Ag}_7\text{O}_8\text{NO}_3$  is deposited onto HDPE from an aqueous solution containing  $\text{AgNO}_3$  as a source of silver ions and persulfate  $\text{S}_2\text{O}_8^{2-}$  as an oxidizing agent of  $\text{Ag}^+$  ions. The final product,  $\text{Ag}_7\text{O}_8\text{NO}_3$ -coated HDPE, contains silver ions in the higher oxidation states, for which it is believed that they may exhibit a stronger antimicrobial activity. On the basis of the published literature [41–43], silver oxysalts exhibited reasonable antimicrobial activity. Media and internet sources have announced that this product, “Exsalt,” is now available on the market.

In addition, a patent issued by Antelman [44] refers to a high performance of the silver (I, III) oxide-coated antimicrobial articles. In this invention, deposition of “tetrasilver tetroxide” ( $\text{Ag}_4\text{O}_4$ ) crystal or interstitial precipitation onto fabrics was proposed.

### 5.3 Surface Modification with Silver and Its Compounds for Biomedical Purposes

When applied in vivo, all devices suffer a common problem of device-related infection. The first step in infection is adherence of microorganisms to the medical device surface. Adherence of microorganisms on the medical device surfaces and their further colonization may result in tissue destruction, dysfunction of the device, and systemic dissemination of the pathogen [1].

Although specific data are lacking, it is likely that the increasing prevalence of antibiotic resistance toward *Staphylococcus aureus*, *P. aeruginosa*, *Staphylococcus epidermidis*, and *E. coli* has further increased mortality and cost attributable to the medical device-associated infections [1, 45, 46].

Administration of antimicrobial agents by systemic or oral routes generally fails to reach the antimicrobial film formed at the surface of the medical device. A very successful way of antimicrobial treatment, in such cases, can be achieved by maintaining a sufficiently high concentration of the antimicrobial agent for the site-specific activity.

Surface treatment with silver and its compounds can be profitable in terms of achieving the desired antimicrobial activity due to the presence of silver ions.

Physicochemical modification of surfaces for biomedical applications may change the properties and consequently lead to different interactions with tissue, microbial cells, biological fluids, proteins, etc. Various surface functional groups having an antimicrobial activity may be applied to the surface thus leading to an improved behavior of the medical devices.

A treatment of various surfaces for biomedical applications e.g., textile, polymers or metals with silver or its compounds is carried out due to antimicrobial action of silver ions. There are several approaches in the production of medical devices used in order to achieve or improve the antimicrobial activity. These methods are based on:

1. Immersion
2. Coating
3. Matrix loading

The selection of a method for the surface treatment with silver or its compounds depends on the nature of material (e.g., textile, polymer, ceramic, metal, etc.) and their physicochemical properties.

Matrix loading involves the production of the composite materials, e.g., polymeric or ceramic matrices filled with silver or its compounds. As such, this method is out of the scope of this chapter, and it is not discussed here.

### **5.3.1 Immersion**

In the immersion method the material to be used for the medical device applications is immersed into a solution containing silver ions. It is expected that due to adsorption of silver ions at the surface of the device, the final product would exhibit the desired antimicrobial activity. This approach can be quite successful for hydrophilic materials with good adsorption properties, e.g., many textile materials or some polymer foams.

However, a treatment of compact polymeric, metallic (less noble than silver) or non-porous ceramic surfaces with silver ion containing solutions would not lead to their significant adsorption at the surface and thus poor, if any antimicrobial activity. If adsorbed at the surface,

silver ions and compounds, due to poor adhesion would rather be removed during the washing or rinsing procedures. On the other hand, a treatment of metallic surfaces which are less noble than silver with Ag(I)-containing solutions may lead to a deposition of the elemental silver via the galvanic displacement reaction [47]. For such treated surfaces, some antimicrobial activity may be observed, however, usually not at a significant level.

The immersion method has been used for a long time. Examples are wound dressings, such as gauze or similar, immersed into  $\text{AgNO}_3$  solution. However, disadvantages of this approach are numerous. If the immersion is carried out from a solution containing  $\text{Ag}^+$  ions it is difficult to maintain the concentration of the adsorbed silver ions at constant levels. Consequently, this could lead to a non-uniform release of silver ions, which may have a detrimental effect on the performance of the device. Furthermore, if the immersion is carried out in a slurry containing solid particles, which are expected to have antimicrobial activity, then a poor adhesion of these solid particles to the surface may cause many problems. Problems associated with poor adhesion may arise when a separation of solid particles from the surface of the medical device occur. When medical devices are applied in vivo, the solid particles may be released into the wound or body fluid resulting in catastrophic performance.

In clinical settings, suitable devices can be treated by immersion into solutions without solid particles. This offers flexibility and control to clinicians. In general terms, the immersion method for medical devices should be restricted to materials that are hydrophilic in nature and only for topical uses. Medical devices made of hydrophobic materials would exhibit limited or not at all attachment of silver ions at their surfaces. Consequently, they may perform poorly when applied in vivo.

### 5.3.2 *Coating*

Special coatings can be deposited onto medical devices in order to avoid biofilm formation and to provide protection from an infection or for other antimicrobial purposes. The main requirement for these coatings is to allow a continuous release of antimicrobially active agents to the desired place or to prevent the biofilm formation. Coating of medical devices with silver or its compounds may produce films at the surface that can provide sufficient concentrations of silver

ions in order to achieve the desired antimicrobial activity. Several processes for coating medical devices with silver or its compounds have been reported in literature.

Elemental silver can be deposited successfully onto the surface of medical devices, using different methods such as electrodeposition, electroless deposition, physical vapor deposition (PVD) and chemical vapor deposition (CVD). Silver compounds deposited onto a medical device surface may include most of the silver salts with a low solubility product,  $K_{sp}$ . These compounds may include  $\text{AgCl}$ ,  $\text{Ag}_2\text{SO}_4$ ,  $\text{Ag}_3\text{PO}_4$ ,  $\text{Ag}_2\text{CO}_3$ ,  $\text{Ag}_2\text{C}_2\text{O}_4$ ,  $\text{Ag}_2\text{C}_4\text{H}_4\text{O}_6$ ,  $\text{Ag}_7\text{O}_8\text{NO}_3$ ,  $\text{Ag}_3\text{C}_6\text{H}_5\text{O}_7$ , etc. Although these compounds have a very low solubility product, in contact with a biological media they can release silver ions thus leading to antimicrobial activity. Another class of silver compounds for topical applications may include silver oxides e.g.,  $\text{Ag}_2\text{O}$ ,  $\text{Ag}_2\text{O}_2$ ,  $\text{Ag}_3\text{O}_4$ , etc. Both silver oxides and silver salts are deposited onto the surface of medical device using chemical methods which are described in literature [37, 39–49].

All mentioned methods of deposition can produce at the surface of the medical device films of silver compounds with different composition and consequently, different physicochemical properties. These films can exhibit a good adhesion, uniform composition, continuous release of silver-containing ions and in this way achieve acceptable antimicrobial activity for the targeted applications.

Regularly, different methods of deposition of silver or its compounds onto the surface of the medical device include co-deposition of secondary elements and/or compounds, which significantly influences the results of the antimicrobial activity both in vitro and in vivo.

Other approaches of surface treatments for antimicrobial purpose may include  $\gamma$ -radiation, photo-chemical treatments or electrochemical oxidation.  $\gamma$ -radiation and photo-chemical treatments are beyond the scope of this chapter. The electrochemical oxidation of surfaces treated with silver may be attractive, and as such is discussed in the later sections.

## 5.4 Metallic Silver or Oxidized Silver Species

As mentioned above, the antimicrobial activity of the surfaces treated with silver or its compounds is determined by their physicochemical properties.

The leading factor for an antimicrobial activity of silver is the deliberation of silver ions from an appropriate material as originally recommended by Acél [25] and later confirmed by Gibbard [26].

Behavior of silver of various origin e.g., metallurgically obtained, physical vapor deposited and electroless deposited in physiological saline solutions and their antimicrobial activity were systematically investigated [50]. Methods such as open circuit potential (OCP) measurements in physiological saline solutions with and without presence of proteins, X-ray diffraction (XRD) and antimicrobial tests were employed in order to find out if elemental silver or oxidized silver species contribute to the antimicrobial activity.

When exposed to calf serum or to 0.85% NaCl solution, only certain samples produced by the physical vapor deposition exhibited a decay in the open circuit potential as a function of time. Pure metallurgical, electro deposited and electroless deposited silver specimens did not show significant changes in the open circuit potential vs. time curves. After the immersion of these samples in physiological solutions, the steady-state open circuit potential was established within the first 5 s.

Typical results for the OCP—time measurements for silver-containing samples produced by PVD on silicon or pure metallurgical silver in physiological saline and calf serum solutions are shown in Fig. 5.1.

The results as illustrated in Fig. 5.1 clearly show that the steady-state open circuit potential of pure silver (curves 3 and 4) was reached almost immediately upon the immersion into physiological solutions. Only certain samples of “silver” produced by the PVD showed a decrease in the open circuit potential upon immersion into physiological saline solutions (curves 1 and 2). As shown by the results presented in Fig. 5.1, the steady-state open circuit potential in 0.85% NaCl solution was achieved slightly faster compared to that of the physiological saline solutions containing calf serum.

The value of the steady-state potential after the decay depends on the substrate on which “silver” was deposited by PVD. The PVD “silver” samples on silicon substrates exhibited significantly more positive steady-state potentials in comparison with those deposited onto aluminum substrates. As shown in Fig. 5.2, the steady-state open circuit potential of PVD silver samples on aluminum substrates (curves 1 and 2) converges with that of an Al surface. This behavior is attributable to the porosity of deposited “silver” films. Curves 3 and

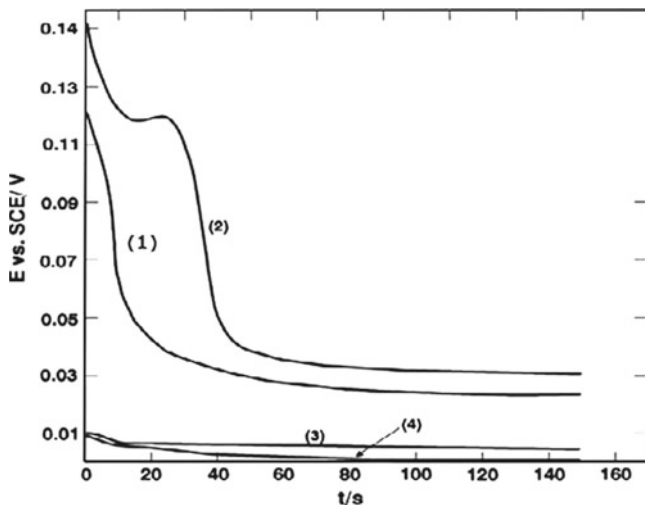


**Fig. 5.1** Comparison of the open circuit potential vs. time relationships for various silver electrodes in 0.85% NaCl and in calf serum: (1) silver sputtered on silicon, thickness 1,000 nm in 0.85% NaCl; (2) silver sputtered on silicon, thickness 600 nm in calf serum; (3) metallurgical silver in 0.85% NaCl; (4) metallurgical silver in calf serum [50]. Reprinted with permission from ECS—The Electrochemical Society

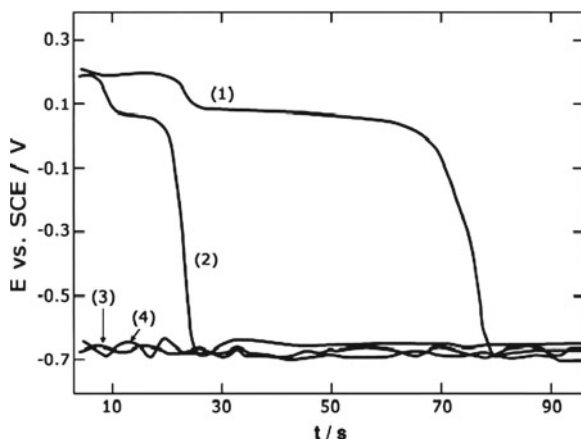


**Fig. 5.2** Comparison of the open circuit potential vs. time relationships for various silver electrodes in 0.85% NaCl and calf serum; (1) silver sputtered on Al, thickness 900 nm in calf serum; (2) silver sputtered on Al, thickness 900 nm in 0.85% NaCl solution; (3) aluminum electrode in calf serum; (4) aluminum electrode in 0.85% NaCl [50]. Reprinted with the permission from ECS—The Electrochemical Society

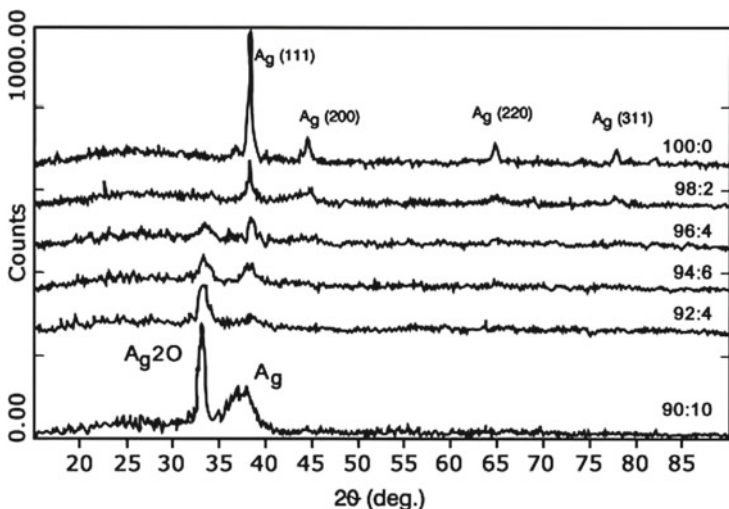


**Fig. 5.3** XRD patterns of silver films produced under different amounts of oxygen (from top to bottom: 0, 2, 4, 6, 8, and 10vol.% O<sub>2</sub>) in sputtering atmosphere [38]. Reprinted with permission from ECS—The Electrochemical Society

4 are related to the OCP of aluminum surfaces immersed in calf serum and 0.85% NaCl solution, respectively.

A decrease in the open circuit potential toward more negative values with an increase in the immersion time is attributed to the presence of silver oxide in the PVD samples. The presence of silver oxide in the PVD “silver” specimens is a consequence of the so-called reactive sputtering. These thin silver films were produced by PVD of silver in a reactive atmosphere containing 90–100% Ar, with the rest being oxygen. The procedures for deposition of such thin silver films are available in published literature [37, 38]. During the reactive sputtering in the oxygen-containing atmosphere, silver atoms react quickly with oxygen and form silver oxide [51].

The XRD analysis of sputtered thin silver films produced under the conditions of reactive sputtering in an Ar/O<sub>2</sub> atmosphere confirmed that they contain silver oxide [38, 50]. XRD patterns of “silver” films produced under different amounts of O<sub>2</sub> in the sputtering atmosphere are shown in Fig. 5.3.

Note that the samples produced by PVD from an atmosphere containing Ar only represent pure elemental silver. Silver peaks and respective Miller indices are shown for this sample in Fig. 5.3. Other

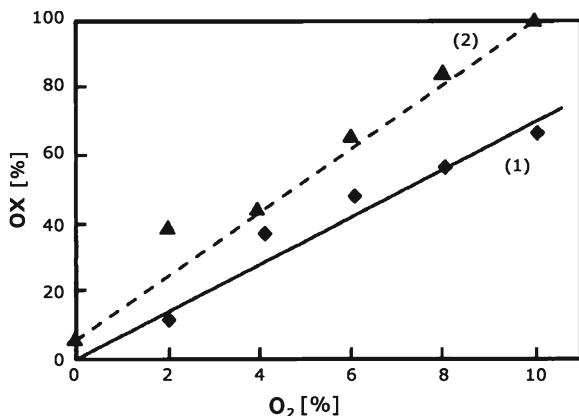


**Fig. 5.4** Dependence of the amount of oxidized species in sputtered silver films on the amount of oxygen in sputtering atmosphere (1) determined from cyclic voltammetry experiments, (2) determined by AAS [38]. Reprinted with permission from ECS—The Electrochemical Society

samples, as this figure illustrates, contain  $\text{Ag}_2\text{O}$  which is incorporated in silver films during the sputtering process. It is also obvious that with an increase in the  $\text{O}_2$  content in the sputtering atmosphere, the intensity of the  $\text{Ag}_2\text{O}$  peak in the XRD patterns increases, suggesting an increase in the  $\text{Ag}_2\text{O}$  content in the sputtered thin silver films.

This is confirmed by the electrochemical and atomic absorption analysis (AAS) [38]. As shown in Fig. 5.4, an increase in the content of  $\text{O}_2$  in sputtering atmosphere leads to an increase in the amount of  $\text{Ag}_2\text{O}$  in sputtered silver films. It seems that the sputtered samples produced from an atmosphere containing 90% Ar and 10%  $\text{O}_2$  are practically composed of  $\text{Ag}_2\text{O}$  only, with significantly smaller amounts being pure silver.

Importantly for the biomedical applications, only samples containing  $\text{Ag}_2\text{O}$  or other oxidized silver species exhibited the antimicrobial activity. The inhibition zone for microorganisms' growth was observed only for "silver" samples which had shown a decrease in the open circuit potential, i.e., for those that contained silver oxide. A typical photograph of the zone of inhibition for microorganisms e.g., *P. aeruginosa* grown with this type of sample is presented in Fig. 5.5.

As shown in Fig. 5.5, a clear zone of inhibition for the growth of *P. aeruginosa* was obtained. The test sample of sputtered silver on HDPE, containing 45wt.%  $\text{Ag}_2\text{O}$  was placed in the middle of a Petri

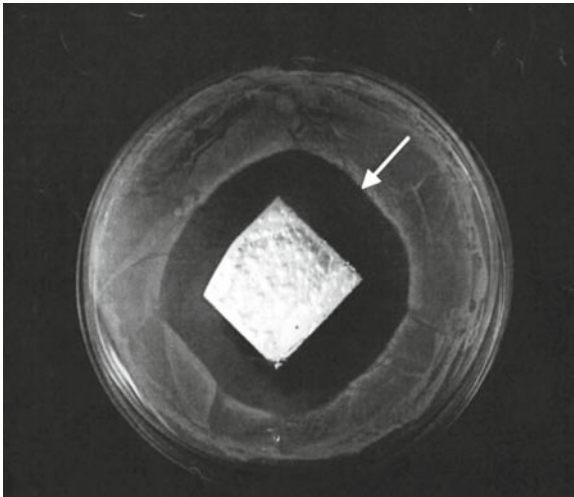


**Fig. 5.5** The inhibition zone for *Pseudomonas aeruginosa* growth (silver produced under the reactive sputtering) [50]. Reprinted with permission from ECS—The Electrochemical Society

dish. The clear zone of inhibition surrounding the test sample which is distinguished in Fig. 5.5 by an arrow was obtained after incubation at 37°C for 24 h. This result suggests that a growth of microorganisms, e.g., *P. aeruginosa* was inhibited. Similar behavior was always seen with the oxidized silver species, i.e., silver ions were present, as originally observed by Acél [25] and later confirmed by Gibbard [26].

When other silver samples, e.g., metallurgical, electrodeposited, electroless deposited or PVD samples produced in an inert atmosphere, such as pure Ar, were analyzed for the antimicrobial activity, no zone of inhibition appeared. The results obtained thus far strongly suggest that the element silver is not antimicrobially active.

Why is silver oxide ( $\text{Ag}_2\text{O}$ ) antimicrobial active? It is well known that  $\text{Ag}_2\text{O}$  has a solubility product of about  $2 \times 10^{-8}$  and that it increases with temperature [52]. Although  $\text{Ag}_2\text{O}$  has a relatively low solubility product, it dissolves in water according to the following reactions:



and



or



Reaction (5.3) predicts an increase in pH, after samples containing  $\text{Ag}_2\text{O}$  are exposed to water. After the immersion of samples produced by the reactive sputtering in water, an increase in pH from 6.5 to 11 was experimentally observed [50]. This increase in pH is attributable to the presence of  $\text{Ag}_2\text{O}$ .

Shorter transition times in the open circuit potential vs. time curves obtained when samples were exposed to NaCl solutions as compared to solutions containing calf serum can be attributed to serum proteins. Other reports [53, 54] disclosed that mechanisms and rates of corrosion of metals are modified when serum proteins are present in solutions. A presence of proteins may inhibit dissolution of  $\text{Ag}_2\text{O}$ . As a result, sputtered silver-based material exhibited longer transition times for which a steady-state potential was established when they were exposed to physiological saline-containing calf serum. On the other hand, respective transition times in 0.85% NaCl solution were obviously shorter.

In order to prove the concept that the sputtered coatings exhibit antimicrobial activity only because they contain silver oxide, pure metallic silver specimens were further electrochemically oxidized. The electrochemical oxidation of metallic silver in alkaline solutions leads to the formation of  $\text{Ag}_2\text{O}$  and in some cases  $\text{AgO}$  at the surface [55, 56].

A typical cyclic voltammogram of the metallic silver electrode is shown in Fig. 5.6. In the anodic branch of this cyclic voltammogram there are two main peaks which are attributed to the electrochemical oxidation of silver according to the following reactions:



with  $E^\circ = 0.342 \text{ V}$  [52].

At more positive potentials,  $\text{Ag}_2\text{O}$  is further oxidized to  $\text{AgO}$ , as described by the reaction below:



with  $E^\circ = 0.604 \text{ V}$  [52].

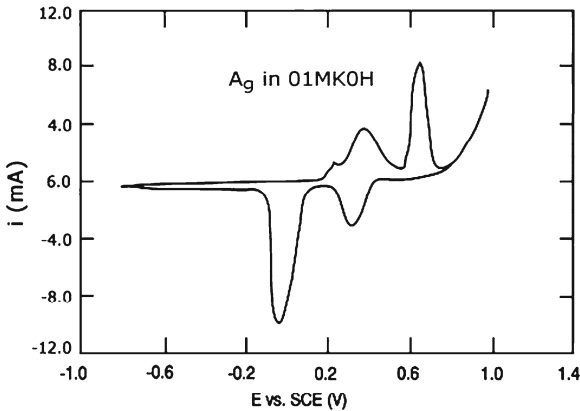


**Fig. 5.6** Cyclic voltammogram of silver electrode in 0.1-M KOH

The electrochemically oxidized metallurgical silver samples in 1-M KOH solution at potentials more positive than 300 mV vs. saturated calomel electrode (SCE) were analyzed by the XRD. For comparison, the results of XRD analysis of metallurgically obtained silver, sputtered silver obtained under the conditions of reactive sputtering (the presence of oxygen in the argon atmosphere), electrochemically oxidized metallic silver at +600 mV vs. SCE and silver oxide powder are presented in Fig. 5.7.

XRD patterns in Fig. 5.7 show clearly that films produced by the PVD from an argon atmosphere containing oxygen, electrochemically oxidized and of course silver oxide powders exhibited the  $\text{Ag}_2\text{O}$  peak.

Importantly, only samples that contained silver oxide, i.e., exhibited  $\text{Ag}_2\text{O}$  peak in the XRD patterns, showed antimicrobial activity. Specimens that did not contain the  $\text{Ag}_2\text{O}$  or other oxidized species were not antimicrobially active.

The inhibition zones for *P. aeruginosa* growth at the electrochemically oxidized metallurgical silver at +300 mV and at +700 mV for 500 s are shown in Fig. 5.8.

The clear zone (“bacteria free”) was obtained when electrochemically oxidized silver surfaces at +300 mV and +700 mV were exposed for 24 h at 37°C to an agar medium containing *P. aeruginosa*. Note a clear zone surrounding the dark circle of an electrochemically oxidized silver surface placed in the middle of a Petri dish. The zone is distinguished by an arrow.

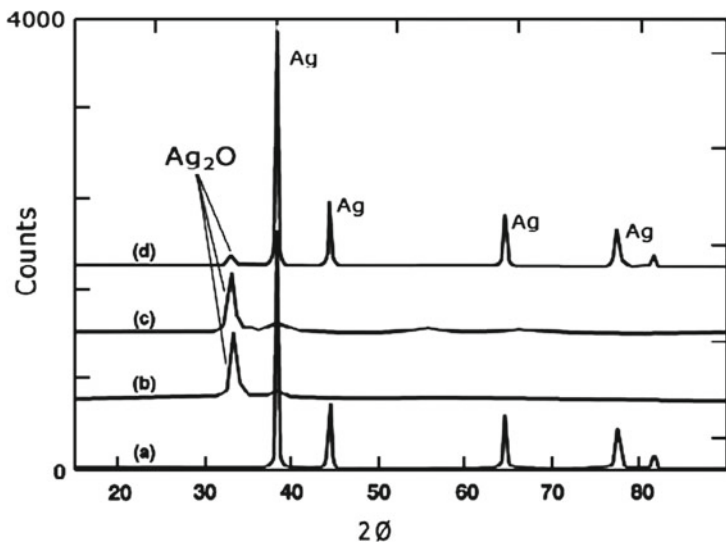


**Fig. 5.7** XRD patterns of (a) metallurgical silver (b) sputtered silver (c) Ag<sub>2</sub>O and (d) electrochemically oxidized Ag at 600 mV [50]. Reprinted with permission from ECS—The Electrochemical Society

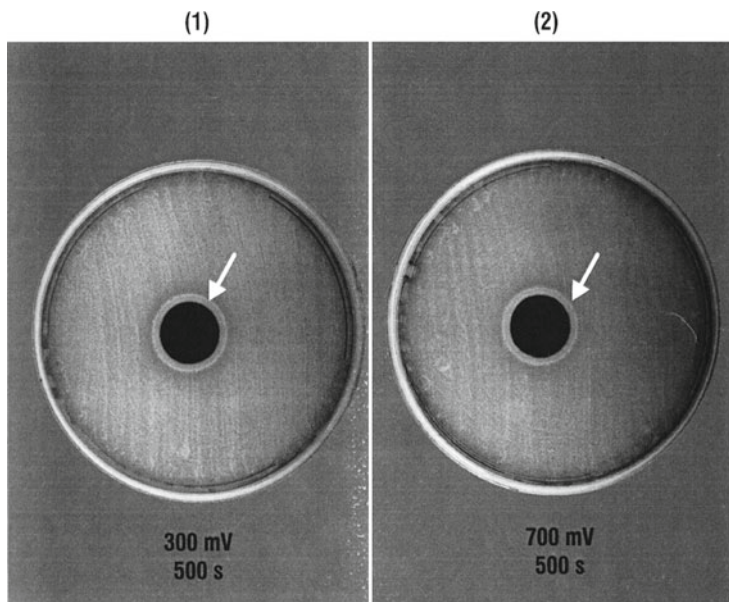


**Fig. 5.8** The inhibition zones for *Pseudomonas aeruginosa* growth at electrochemically oxidized silver electrode (1) at 300 mV for 500 s and (2) at 700 mV for 500 s [50]. Reprinted with permission from ECS—The Electrochemical Society

**Table 5.1** Bactericidal activity of silver specimens tested with *Pseudomonas aeruginosa* [57]

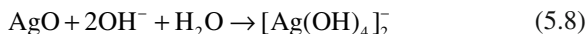
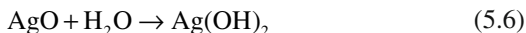
Sample	CFU/mL	Log reduction related to control
Anodized at 300 mV	$9.5 \times 10^2$	5.2
Anodized at 550 mV	$2.1 \times 10^3$	4.9
Anodized at 750 mV	$1.6 \times 10^3$	5
Ag metal (control)	$1.5 \times 10^8$	–

Reprinted with permission from ECS—The Electrochemical Society

Results on the bactericidal activity of electrochemically oxidized silver samples are presented in Table 5.1 [57].

It is obvious from Table 5.1 that electrochemically oxidized silver samples exhibited relatively high bactericidal activity. Approximately a “5-log reduction” was achieved with oxidized silver in comparison with pure silver samples. While the electrochemically oxidized silver samples were bactericidal, the results presented in Table 5.1 clearly show that pure silver is not.

As presented by the reaction (5.5) above, AgO is generated by the electrochemical oxidation of silver at potentials more positive than 600 mV. AgO is a very powerful oxidizing agent. Therefore, it is expected that AgO should exhibit greater antimicrobial activity than Ag<sub>2</sub>O [42]. However, the experimental results show no difference in antimicrobial activity among samples oxidized at different potentials (0.30, 0.55, and 0.75 V). AgO is a solid substance which is soluble in alkaline solutions [52]. Considering that these samples were produced during the electrochemical oxidation of silver in 1-M KOH solution, one can expect that as soon as the current is interrupted, or during the washing procedure, AgO will dissolve without decomposition according to the following reactions [52]:



Accordingly, at the electrode surface of samples oxidized at 0.6 V after the washing procedure, only the Ag<sub>2</sub>O could be expected. This was confirmed by XRD analysis. In the XRD pattern of samples oxidized at 0.6 V, only peaks related to Ag and Ag<sub>2</sub>O were observed

(Fig. 5.7). Consequently, no significant differences in the antimicrobial activity among samples oxidized at different potentials were observed.

The result of electrochemical oxidation shows without a doubt that a presence of soluble silver forms including silver oxide and/or silver salts is an essential factor leading to an antimicrobial activity of silver coatings. Elemental silver specimens did not show changes in the open circuit potential with time and, as a result, they did not exhibit antimicrobial activity.

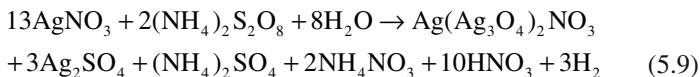
The electrochemically oxidized silver-coated nylon fabric can enhance the antimicrobial properties, as it was published by Deitch [32]. Silver-coated nylon fabric was electrochemically oxidized with direct current using metallic silver as cathode and tryptic soy broth as an electrolyte. The antimicrobial activity was significantly improved. Since an electrochemical oxidation produces silver oxide at the surface, this result strongly confirms that a presence of oxidized species, i.e., silver ions leads to the antimicrobial activity.

In order to achieve the best performance in terms of the antimicrobial activity, experimental observations strongly suggest that, if silver is aimed for this purpose, the medical devices for the topical applications should be coated with silver compounds. The examples include numerous textile materials (fabrics) used as wound dressings.

On the basis of the previous observations that only a presence of silver ions could lead to the antimicrobial activity, many attempts were made to produce medical devices used as topical wound dressings and coated with silver compounds. In this way, coating of fabrics to be used as topical wound dressings with silver oxysalts, silver chloride, silver sulfate, etc. have been investigated [41–44, 49].

Deposition of silver oxysalts such as  $\text{Ag}_7\text{NO}_{11} \cdot \text{Ag}_2\text{SO}_4$ , and  $\text{Ag}_7\text{NO}_{11}$  as powders or as coatings on HDPE mesh have been recently investigated for antimicrobial purposes [41]. This process is based on a reaction between  $\text{AgNO}_3$ , a source of  $\text{Ag(I)}$  ion and  $(\text{NH}_4)_2\text{S}_2\text{O}_8$  or  $\text{K}_2\text{S}_2\text{O}_8$  used as oxidizing agent of silver ions. In these reactions the silver oxysalts can successfully be produced as presented with the reactions below:

$\text{AgNO}_3$  and  $(\text{NH}_4)_2\text{S}_2\text{O}_8$ :



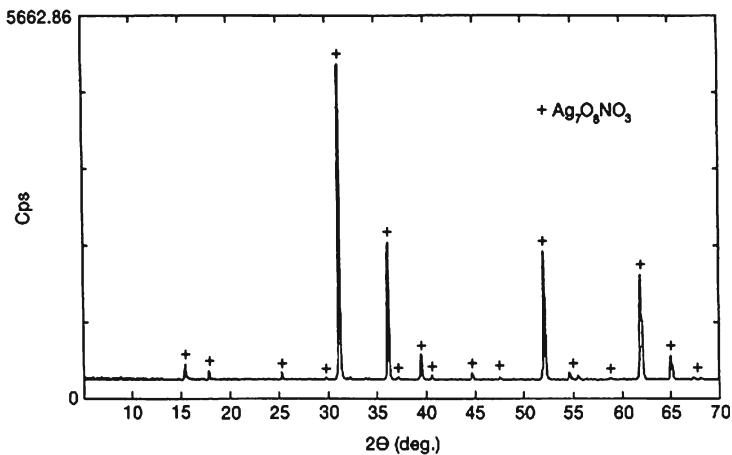
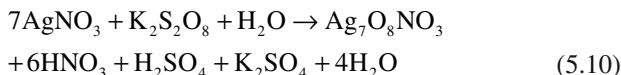


**Fig. 5.9** XRD pattern of the *grayish-black* precipitate produced by the reaction of  $\text{AgNO}_3$  and  $\text{K}_2\text{S}_2\text{O}_8$  [41]. Reprinted with permission from ECS—The Electrochemical Society

$\text{AgNO}_3$  and  $\text{K}_2\text{S}_2\text{O}_8$ :



In the reaction of  $\text{AgNO}_3$  with  $\text{K}_2\text{S}_2\text{O}_8$ , only  $\text{Ag}_7\text{NO}_{11}$  (or  $\text{Ag}_7\text{O}_8\text{NO}_3$ ) was deposited. As found by XRD analysis all the peaks in the pattern presented in Fig. 5.9 exactly match the compound of composition  $\text{Ag}_7\text{O}_8\text{NO}_3$ .

The SEM micrographs of  $\text{Ag}_7\text{O}_8\text{NO}_3$  produced by the chemical oxidation of  $\text{AgNO}_3$  with  $\text{K}_2\text{S}_2\text{O}_8$  are presented in Fig. 5.10. It appears that the particles are uniform and cubic in their shape. The size of these particles is estimated at about 2–5  $\mu\text{m}$ .

For the determination of antimicrobial activity, samples of HDPE were coated with silver oxysalts ( $\text{Ag}_7\text{O}_8\text{NO}_3$ ) as described in the literature [41]. The comparison of SEM micrographs of uncoated and coated HDPE mesh is presented in Fig. 5.11. As shown in Fig. 5.11b, the surface of HDPE is partially covered with  $\text{Ag}_7\text{O}_8\text{NO}_3$  particulates. The samples coated with  $\text{Ag}_7\text{O}_8\text{NO}_3$  particulates were tested for bioactivity against the bacteria *P. aeruginosa* and *S. aureus* or fungi *Candida albicans*.

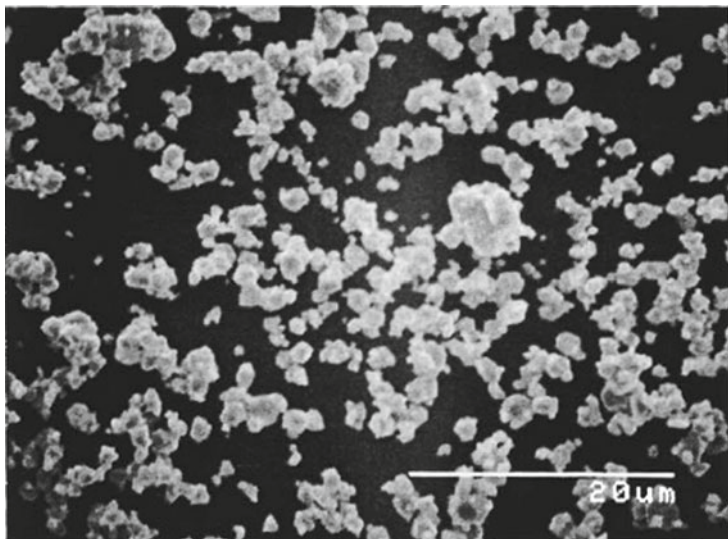


**Fig. 5.10** SEM micrograph of the *grayish-black* powder produced by the reaction of  $\text{AgNO}_3$  and  $\text{K}_2\text{S}_2\text{O}_8$  [41]. Reprinted with permission from ECS—The Electrochemical Society

As can be seen from the photographs shown in Fig. 5.12 clear zones surrounding the test samples, where a growth of tested microorganisms did not occur, were observed in all cases for *S. aureus* (a Gram-positive bacteria), *P. aeruginosa* (a Gram-negative bacteria) and *C. albicans* (a fungi). The size of the corrected zone of inhibition (CZOI), where the growth of tested microorganisms was not observed, was estimated at 3–5 mm for all the tested samples.

These results show that silver oxysalts have antimicrobial and antifungal properties. Furthermore, these results are in agreement with previously published results in which it was suggested that only oxidized silver species, and not metallic silver, exhibit an antimicrobial activity [25, 26, 50].

Production of silver oxysalt-coated dressings for the topical applications in the wound healing is patented [42] and available in North America on the market.

Biocidal and biostatic activities of HDPE treated with silver compounds were investigated in vitro [57]. For this purpose HDPE mesh was coated with  $\text{Ag}_2\text{CO}_3$ ,  $\text{Ag}_2\text{SO}_4$ ,  $\text{Ag}_2\text{O}$ ,  $\text{Ag}_7\text{O}_8\text{NO}_3$ ,  $\text{AgCl}$ ,  $\text{AgH}_2\text{PO}_4$ ,  $\text{Ag}_2\text{HPO}_4$ ,  $\text{Ag}_2\text{S}$ ,  $\text{Ag}_2\text{C}_2\text{O}_4$ , and  $\text{Ag}_2\text{C}_4\text{H}_4\text{O}_6$ . Coating of HDPE was

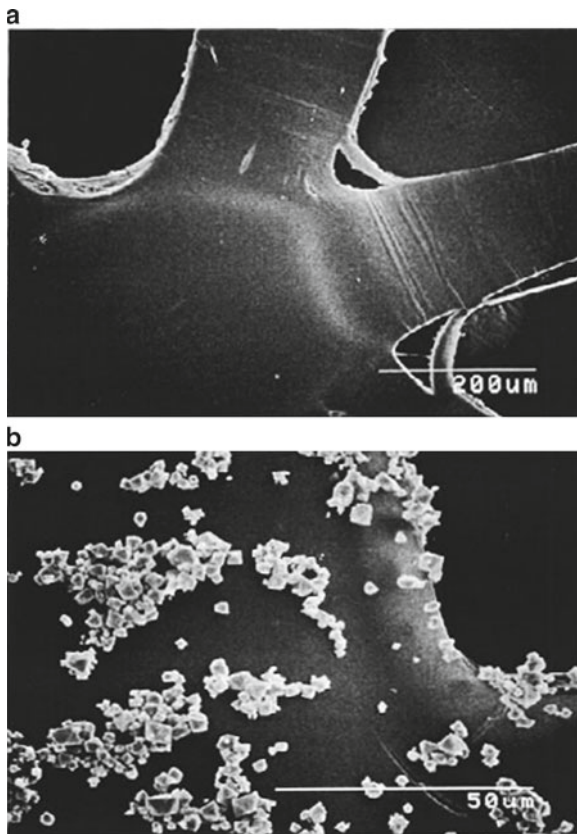


**Fig. 5.11** SEM micrographs for uncoated HDPE: (a) magnification 150 times and HDPE on which *grayish-black* powder was deposited (b) magnification 1,000 times [41]. Reprinted with permission of ECS—The Electrochemical Society

carried out by its simple immersion into solution or slurry, while mentioned compounds were synthesized *in situ* [58]. The results for biocidal and biostatic activities for HDPE samples coated with the mentioned oxides or silver-based salts are presented in Table 5.2.

The results in Table 5.2 show that samples coated with  $\text{Ag}_2\text{S}$  did not exhibit antimicrobial activity. Other HDPE samples coated with silver compounds showed more or less antimicrobial activity. The results described in Table 5.2 suggest that the antimicrobial activity is closely related to the ionization or solubility of respective silver compounds.

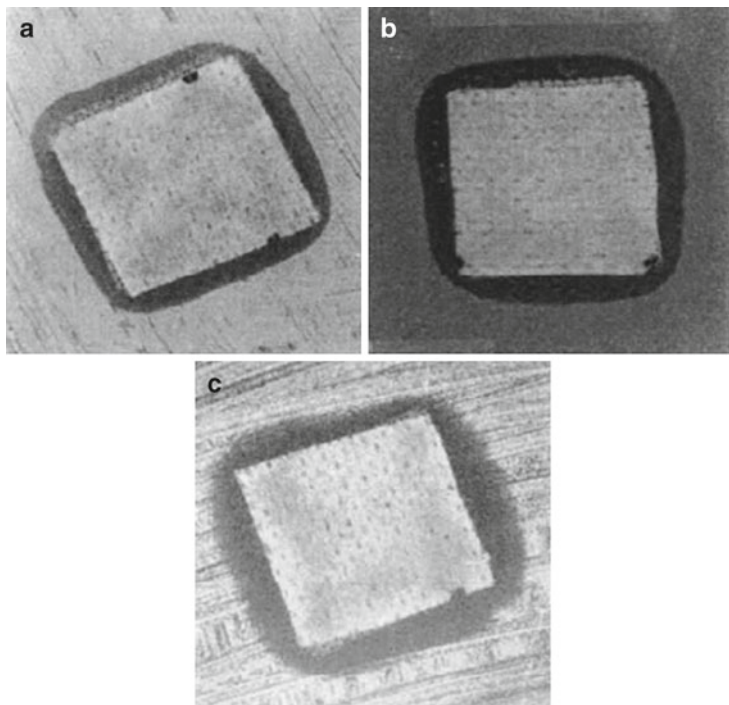


**Fig. 5.12** Controlled zones of inhibition of growth of microorganisms (a) *Staphylococcus aureus*, (b) *Pseudomonas aeruginosa* and (c) *Candida albicans* surrounding HDPE on which silver oxy-salts were deposited [41]. Reprinted with permission from ECS—The Electrochemical Society

No antimicrobial activity for  $\text{Ag}_2\text{S}$ -coated HDPE samples can be attributed to a very low solubility product of silver sulfide. The solubility product of  $\text{Ag}_2\text{S}$  is about  $10^{-50}$ . Consequently, when  $\text{Ag}_2\text{S}$ -coated HDPE is exposed to the medium containing microorganisms, silver ions are practically not available and antimicrobial activity of this particular sample is not observed.

Other silver compounds used in this work [58] have significantly higher solubility products. As such, upon the exposure to the medium containing microorganisms they can release silver ions and exhibit antimicrobial activity. Slightly less antimicrobial activity for  $\text{Ag}_2\text{SO}_4$ -coated HDPE can be attributed to an uneven distribution of this compound at the surface of the mesh.

**Table 5.2** Total silver content, biocidal and biostatic activities against *Staphylococcus aureus* for HDPE coated with various oxidized silver species [58]. Reprinted with permission from ECS—The Electrochemical Society

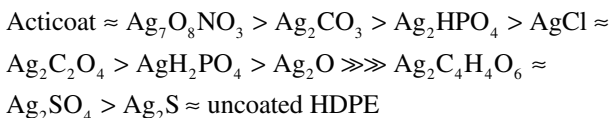
Sample	Total Ag (mgAg/cm <sup>2</sup> )	Bacteriostatic CZOI (mm)	Growth in tube Day 1		Bactericidal viable organisms (CFU)
			Day 2 (Y or N)		
AgCl	0.01	6.0	N	Y	$7.58 \times 10^4$
AgH <sub>2</sub> PO <sub>4</sub>	0.01	2.5	N	Y	$1.30 \times 10^5$
Ag <sub>2</sub> HPO <sub>4</sub>	0.01	8.0	N	Y	$1.37 \times 10^5$
Ag <sub>2</sub> S	0.01	0.0	Y	Y	TNTC
Ag <sub>2</sub> C <sub>2</sub> O <sub>4</sub>	0.01	6.0	N	Y	$1.95 \times 10^4$
Ag <sub>2</sub> C <sub>4</sub> H <sub>4</sub> O <sub>6</sub>	0.01	1.5	Y	Y	TNTC
Ag <sub>2</sub> CO <sub>3</sub>	0.01	10.0	N	N	$1.1 \times 10^5$
Ag <sub>2</sub> SO <sub>4</sub>	0.01	1.0	Y	Y	TNTC
Ag <sub>2</sub> O	0.01	3.0	N	Y	$2.75 \times 10^5$
Ag <sub>7</sub> O <sub>8</sub> NO <sub>3</sub>	0.03	12.0	N	N	$3.00 \times 10^3$
Acticoat	0.50	10.0	N	N	$2.00 \times 10^3$
Uncoated	0.01	No inhibition	Y	Y	$4.50 \times 10^8$

TNTC to numerous to count

Interesting behavior was found with HDPE samples coated with silver tartrate (Ag<sub>2</sub>C<sub>4</sub>H<sub>4</sub>O<sub>6</sub>). This sample exhibited a minor antimicrobial activity in comparison with other tested samples. A plausible explanation for this behavior can be attributed to tartrate ions. Tartrate ions (C<sub>4</sub>H<sub>4</sub>O<sub>6</sub><sup>2-</sup>) are well-known reducing agents of silver ions [59]. In this way, upon exposure of Ag<sub>2</sub>C<sub>4</sub>H<sub>4</sub>O<sub>6</sub>-coated HDPE mesh to the tested medium both Ag(I) and C<sub>4</sub>H<sub>4</sub>O<sub>6</sub><sup>2-</sup> ions will be produced due to the dissociation of silver tartrate. Furthermore, in an agar medium Ag(I) ions can be reduced to the elemental silver with tartrate ions. As a result, due to the formation of elemental silver, no bactericidal activity is seen as shown by the results in Table 5.2.

On the basis of the results shown in Table 5.2, most of the tested samples, except those coated with Ag<sub>2</sub>S, exhibited a clear zone of inhibition, thus indicating a positive bacteriostatic activity against *S. aureus*. Similarly, the bactericidal activity of HDPE coated with the mentioned silver compounds was positive for most tested samples.

The antimicrobial activity of HDPE samples coated with different compounds according to Table 5.2, qualitatively changes in the following order:



Acticoat is an antimicrobial wound dressing comprising of a mixture of  $\text{Ag}_2\text{O}$  and pure silver, which is available on the market. This product is widely used in the clinical settings. A better activity of Acticoat against *P. aeruginosa* when compared to other HDPE samples coated with different silver compounds should be attributed to the significantly larger amounts of total silver in the Acticoat specimens. As shown in Table 5.2, the Acticoat specimens contained 0.5 mg Ag/cm [2], which is 50 times more when compared to HDPE samples coated with other silver compounds. Interestingly, the samples coated with  $\text{Ag}_7\text{O}_8\text{NO}_3$  exhibited the antimicrobial activity comparable to that of Acticoat, although they contained approximately 15 times less silver than Acticoat.

The results shown in Table 5.2 suggest that not only the amount of Ag(I) present in medium, but also the nature of silver compounds plays a significant role in the antimicrobial activity. Silver compounds can be used as coatings on various surfaces in medical device industries. However, their use should be restricted on topical applications. In the external applications, problems related to the relatively high concentrations of silver can successfully be avoided.

When dealing with internal applications, e.g., catheters, implants or similar, where some activity of Ag(I)-based species is required, the use of silver compounds for these purposes should very carefully be examined. The presence of high concentrations of silver ions could rather be detrimental than beneficial [16]. It is well established that silver ions in high concentrations could be cytotoxic [16].

In the internal applications of medical devices coated with silver compounds, significant problems may arise due to the secondary reactions of Ag(I) ions and constituents of blood or body fluids.

For example contact of Ag(I) ions with Fe(II) ions from internal fluids could lead to the reaction:



Note that at a pH above 4.5,  $\text{Fe}^{3+}$  will be precipitated as  $\text{Fe}(\text{OH})_3$ . On the other hand, if  $\text{Ag}(\text{I})$  is reduced to elemental silver,  $\text{Ag}$ , then antimicrobial activity would not take place. Similarly, sufficient concentrations of  $\text{Ag}(\text{I})$  in the presence of  $\text{Cl}^-$  may form the  $\text{AgCl}$  precipitate, according to the following reaction:



Formation of  $\text{AgCl}$  or  $\text{Fe}(\text{OH})_3$  precipitates or solid  $\text{Ag}$  particles would not lead to a desired effect in the internal applications. One can only speculate what kind of consequences may occur when the precipitates such as  $\text{AgCl}$  or  $\text{Fe}(\text{OH})_3$  are formed, especially if this class of materials is targeted for intravenous catheters, urinary catheters or perhaps implant applications. The scenario could even be more complicated if the adhesion of silver compounds, including metallic silver, is poor. In this case, a separation of solid particles from the device inside the body could lead to the catastrophic problems.

Of course, an in-depth understanding of the behavior of silver or silver compounds coated devices for the internal use requires significant future studies.

## 5.5 Elemental Silver and Its Antimicrobial Activity

Like many other metals, silver can react with oxygen or other agents from the biological environment, forming at the surface oxide films. Oxidation process is the essential factor for the observation of the antimicrobial activity of medical devices coated with pure silver. Materials with pure metallic silver or metallic silver particles distributed within polymeric matrix were investigated for their antimicrobial activity [60]. Although this and other pure metallic silver materials produced poor inhibition zones in the agar diffusion tests commonly used to assess the activity of novel materials, they may show some antimicrobial activity in clinical studies, when tested in vivo.

A medical device coated with a homogenous layer of pure silver having an acceptable adhesion was exposed to interstitial fluids [61]. A bactericidal activity was seen as shown by the in vitro tests, enzyme linked immunosorbent assay (ELISA) techniques. The results showed

that the material significantly inhibited adherence and subsequent growth of *S. epidermidis*. The activity was not reduced after the exposure to blood proteins and persisted after 4 weeks pre-incubation in phosphate buffered saline solution [62].

Silver coatings on stainless steel SS 316 L substrates were prepared via electroless deposition from an alkaline  $\text{Ag}(\text{NH}_3)_2^+$  solution, using sodium potassium tartrate as a reducing agent [63]. The corrosion behavior was investigated in 0.9% NaCl solution and in artificial urine. The rate of corrosion in both 0.9% NaCl or in artificial urine was found to decrease with an increase in the thickness of silver coating. In 0.9% NaCl solution, the corrosion rate of silver coating was higher than that in the artificial urine. The number of bacteria (*P. aeruginosa*) adhering to the surface was significantly lower on the silver coatings than on bare stainless steel substrates. These results confirm that some antimicrobial activity of silver coatings was observed. This antimicrobial activity is attributable to the surface oxidation (corrosion) of silver-coated stainless steel and a consequent release of silver ions in the tested medium.

Metallic silver may exhibit some antimicrobial activity, when it is sufficiently long exposed to the interstitial fluids, suggesting that time is a very important parameter determining the corrosion rate. This leads to a conclusion that corrosion plays a significant role in the antimicrobial activity of pure silver. In catheter and/or implant applications it would be possible to oxidize the surface of silver metal in the presence of oxygen and various ions e.g.,  $\text{Cl}^-$ ,  $\text{SO}_4^{2-}$ , etc., from the interstitial fluids. Consequently, some “low” concentrations of  $\text{Ag}(\text{I})$  ions at the surface of the medical device could be present due to the corrosion of silver. The corrosion of silver leads to the appearance of the oligodynamic activity.

The devices coated with silver may contain naturally formed silver oxide at the surface. Or due to corrosion, while in contact with interstitial fluids, the surface of silver metal can be oxidized. A presence of oxidized silver species at the surface of the medical device could produce the concentrations of silver ions that are sufficient for the antimicrobial activity. In this way, an undesired infection and/or growth of a biofilm at the surface of the medical device would be possible to prevent.

For internal applications, devices coated with elemental silver would probably be safer to use due to lower concentrations of  $\text{Ag}(\text{I})$  released. The formation of precipitates such as  $\text{AgCl}$  or  $\text{Fe}(\text{OH})_3$ , as discussed

above, would probably be avoided with very low concentrations of Ag(I) released due to corrosion of silver. However, much experimental work is needed to prove this concept.

## 5.6 Conclusions

The results thus far have shown that a presence of silver ions on a biomedical device surface is an essential factor leading to antimicrobial activity. This fact is quite successfully used for wound-healing applications as topical dressings. A relatively fast release of silver ions in this case could lead to the desired antimicrobial activity.

Proper analysis of some devices coated with “nanocrystalline” silver showed that they are coated with silver oxide or other silver-based compounds. Medical devices coated with silver compounds e.g.,  $\text{Ag}_2\text{O}$ ,  $\text{Ag}_7\text{O}_8\text{NO}_3$ ,  $\text{Ag}_2\text{SO}_4$ ,  $\text{Ag}_2\text{CO}_3$ , etc., should very carefully be taken into consideration for the internal applications such as catheters and implants. “High” concentrations of the released silver ions may produce precipitates such as  $\text{AgCl}$  or  $\text{Fe}(\text{OH})_3$ , which could lead to dramatic consequences, especially when these devices are applied internally.

Silver in its elemental state does not exhibit significant antimicrobial activity due to very limited release of Ag(I) ions. If used in contact with interstitial fluids (implants or catheters), elemental silver may exhibit some antimicrobial activity due to corrosion and formation of surface oxides.

The formation of surface oxides may lead to the observation of an antimicrobial activity due to the release of Ag(I) ions.

## References

1. Tunney MM, Gorman SP, Patrick S (1996) *Rev Med Microbiol* 74:195
2. Elves AWS, Feneley RCL (1997) *Br J Urol* 80:1
3. Gorman SP, McGovern JG, Woolfson CG (2001) Adair and Jones. *Biomaterials* 22:2741
4. Rai M, Yadiv A, Gade A (2009) *Biotechnol Adv* 27:76
5. Djokić S (2008) *ECS Trans* 11(21):1
6. Yin H, Yamamoto T, Wang Y (2004) *Mater Chem Phys* 83:66

7. Zhu Z, Kai L, Wang Y (2006) *Mater Chem Phys* 96:447
8. Edelstein AS, Cammarata RC (1996) *Nanomaterials, synthesis, properties and applications*. Bristol and Philadelphia Publishers, Bristol
9. Leaper DL (2006) *Int Wound J* 3:282
10. Furno F, Morley KS, Wong B, Sharp BL, Howdle SM (2004) *Antimicrob Chemother* 54:1019
11. Li Y, Leung P, Song QW, Newton E (2006) *J Hosp Infect* 62:58
12. Jain P, Pradeep T (2005) *Biotechnol Bioeng* 90(1):59
13. Russell AD, Hugo WB (1994) In: Ellis GP, Luscombe DK (eds) *Progress in medicinal chemistry*, vol 31. Elsevier Science BV, Amsterdam, p 351
14. Klasen HJ (2000) *Burns* 26:117
15. Fricke JKG (1833) *Wochenschr gesammte Heilkunde* 1:14
16. Bernardi W (1847) *Z Erfahrungsheilkunst*, 2: 219
17. Behring E (1887) *Dtch Med Wochenschr* 13:805, **13** (1887) 830
18. Goodman L, Gelman A (1975) *The pharmacological basis of therapeutics*, 5th edn. Macmillan, New York
19. Credé B, Beyer JL (1896) *Silber und Silbersaltze als Antiseptika*. F.C. Vogel, Leipzig
20. Ravelin J (1869) *Sci Nat* 11:93
21. Naegeli V (1893) *Deutch Schr Schweiz Naturforsch Ges* 33:174
22. Thompson NR (1973), Silver In: Bailor JC Jr., Emelús HJ, Nyholm R, Trutman-Dickenson AF (eds), *Comprehensive Inorganic Chemistry*, Vol. III D, Pergamon Press, Oxford, UK, p.79
23. Wilms M (1916) *Wundbehandlung Beitrage Klin Chir* 98:608
24. Arrhenius S (1887) *Z Physik Chem* 1:631
25. Acél D (1920) *Z Biochem* 112:23
26. Gibbard J (1937) *J Am Public Health* 27:122
27. Moyer CA, Brentano L, Gravens DL, Monafó HW (1965) *Arch Surg* 90:812
28. Fox CL (1967) Silver sulfadiazine addendum to addendum therapy, in modern treatment. Harper and Row, Hoeber Medical Division, p 1259
29. Klasen HJ (2000) *Burns* 26:131
30. Butcher HR, Margraf HW, Gravens DL (1969) *J Trauma* 9:359
31. Deitch EA, Marino AA, Gillespie TE (1983) *Antimicrob Agents Chemother* 23:356
32. Deitch EA, Marino AA, Malakanok V, Albright JA (1987) *J Trauma* 27:301
33. Chu CS, McManus AT, Pruitt BA, Mason AD (1988) *J Trauma* 28:1488
34. Chu CS, McManus AT, Mason AD, Okerberg CV, Pruitt BA (1990) *J Trauma* 30:1044
35. Taylor PL, Usher AL, Burrell RE (2005) *Biomaterials* 26:7221
36. Taylor OL, Omotoso O, Wiskel JB, Mitlin D, Burrell RE (2005) *Biomaterials* 26:7230
37. Burrell RE, Morris LR (2001) Antimicrobial coating for medical device, US Patent 6,238, 686 B1
38. Djokić SS et al (2001) *J Electrochem Soc* 148:C191
39. A. B. Flick, Multilayer laminate wound dressing, US Patent 6, 087, 548 (2000).
40. Becker RO, Flick AB, Becker AJ (2006) Multilayer wound dressing, US Patent 7,005,556

41. Djokić SS (2004) *J Electrochem Soc* 151(6):C359
42. Djokić S (2007) Deposition products composite materials and processes for production thereof, US Patent 7,300,673 B2
43. Djokić S (2010) Deposition products composite materials and processes for production thereof, US Patent 7,867,076 B2
44. Antelman MS (2002) High performance silver (I, III) oxide antimicrobial textile articles, US Patent 6,436,420 A1
45. Johnson JR, Delavari P, Azar M (1999) Antimicrob Agents Chemother 49:2900
46. Gristina AG, Costerton JW (1985) *J Bone Joint Surg* 67:264
47. Djokić SS (2002) Electroless Deposition of Metals and Alloys, Chapter 2: In Conway BE, White RE and Bockris JO'M (eds), *Modern Aspects of Electrochemistry*, No.35, Kluwer Academic/Plenum Publishers, New York, p.51
48. Flick AB (2007), Multilayer conductive appliance having wound healing and analgesic properties. US Patent 7, 291,762.
49. Matson CJ (1988) Antimicrobial wound dressing, US Patent 4,728,323
50. Djokić SS, Burrell RE (1998) *J Electrochem Soc* 145:1426
51. Rizk A, Makar LN, Rizk S, Shinoda R (1990) *Vacuum* 40:285
52. Zhutaeva GV Shumilova NV (1985), Silver In Bard AJ, Parsons R, Jordan, J (eds) *Standard Potentials in Aqueous Solutions*, Marcel Dekker, New York, p.294
53. Brown SA, Merritt K (1980) *J Biomed Mater Res* 14:173
54. Clark GCF, Williams DF (1982) *J Biomed Mater Res* 16:125
55. Dirkse TP (1989) *Electrochim Acta* 35:647
56. Dirkse TP (1990) *Electrochim Acta* 36:1445
57. Djokić S (2010) *ECS Trans* 25(19):7
58. Djokić N et al (2008) *ECS Trans* 11(21):59
59. Koura N (1990), Electroless plating of silver, In Mallory GO, Hajdu JB (eds), *Electroless plating: fundamentals and applications*, AESFS, Orlando FL, p.441
60. Stickler DJ (2000) *Curr Opin Infect Dis* 13:389
61. Gluggebichler JP, Böswald M, Lugauer S, Krall T (1999) *Infection* 27(suppl 1): S16
62. Bechert T, Böswald M, Lugauer S (1999) *Infection* 27(suppl1):S24
63. Shao W, Zhao Q (2010) *Colloids Surf B Biointerfaces* 76:98

# Index

## A

Abrasion action, 52  
Abrasion-corrosion (AC), 56, 57  
Abrasive wear, 57, 60  
ACD. *See* Autocatalytic deposition (ACD)  
Activation energy, 31, 36–37  
Active/passive transition, 9–10, 13, 17, 18  
Actuation, 140–142, 151, 152, 155, 156, 159, 161  
Actuator, 141, 142, 149–153, 155, 166  
Adaptor sensor, 135  
Adsorption, 29, 33–38, 40–42, 45–47, 54, 56, 79, 81–83, 85, 94, 95, 110, 120, 129, 134, 135, 143, 145, 148, 149, 163, 164, 180  
Affinity, 36, 37, 43, 45, 46, 50, 82, 140  
 $\text{Ag}_2\text{C}_4\text{H}_4\text{O}_6$ , 182, 194, 196–198  
 $\text{Ag}_3\text{C}_6\text{H}_5\text{O}_7$ , 182  
 $\text{AgCl}$ , 11, 14, 21–23, 35, 36, 54, 55, 154, 155, 159, 161, 182, 194, 197–201  
 $\text{Ag}_2\text{CO}_3$ , 178, 182, 194, 197, 198, 201  
 $\text{Ag}_2\text{O}$ , 178, 185–191, 194, 197, 198, 201  
 $\text{Ag}_2\text{O}_2$ , 182  
 $\text{Ag}_3\text{O}_4$ , 182, 192  
 $\text{Ag}_4\text{O}_4$ , 179  
 $\text{Ag}_7\text{O}_8\text{NO}_3$ , 179, 182, 193, 194, 197, 198, 201  
 $\text{Ag}_3\text{PO}_4$ , 182  
 $\text{Ag}_2\text{SO}_4$ , 182, 192, 194, 196, 198, 201

Albumin, 2, 29, 32–38, 42–45, 52, 54, 109–110, 120  
Alginate, 173  
Alkaline environment, 103  
Alloy composition Mg–Al, 107–108  
Aluminum substrate, 139, 183  
Amino acids, 42, 47, 56, 111  
Anodic bias, 116  
Anodization, 116–118, 121, 139, 140  
Antibacterial behaviour, 118  
Anti-infective, 173  
Anti-inflammatory, 81  
Antimicrobial, 88, 173–183, 191–196  
  activity, 88, 176–183, 186, 187, 189, 191–193, 195, 196, 198–201  
  agents, 173, 179–180  
Antimicrobially active, 176–177, 181, 187, 189  
Artificial muscle, 150–160  
Au/Si interface, 78  
Autocatalytic deposition (ACD), 73, 75–77  
AZ 31, 106–111  
AZ 91, 108, 110–112, 118

## B

Bacteria, 87–90, 118, 131, 175, 189, 193, 194, 200  
Bending signal, 134  
Bioabsorbable, 101, 102

- Bioactive, 115, 173  
 Biocidal, 88, 194, 195, 197  
 Biocompatibility, 33, 38, 101–122,  
   153–154  
   assessment, 112–113  
 Biodegradable, 101–122  
   implant, 101, 102, 108, 113, 121  
   polymers, 120  
 Bioelectronics, 87  
 Biofilm, 45, 46, 110, 173, 181, 200  
 Bio-fluids, 114, 151–152, 180  
 Biological performance, 113–118,  
   120–122  
 Biomaterials, 36, 45, 49, 94, 102, 109,  
   115, 121, 153–154  
 Biomedical  
   applications, 1–67, 81–88, 90–91,  
   95, 101, 102, 104, 106, 108,  
   111, 113–114, 119, 127–166,  
   173–201  
   device, 60, 131, 157, 201  
   technologies, 73–96  
 Biomedicine, 87  
 Biomimetic, 114, 115  
 Biomimicking, 76  
 Biomolecules, 2, 32–51, 67, 74, 76,  
   81, 82, 85, 86, 91, 109–111,  
   134, 135, 153–154, 159  
 Biosensing, 88, 94, 162–166  
 Biosensors, 86, 88, 93–95, 154, 165  
 Biostatic, 194, 195, 197  
 Biotemplates, 87  
 Body fluids, 6, 48, 52, 53, 105, 109,  
   120, 181, 198  
 Bovine serum, 46–48, 50, 56, 57, 111  
 Bovine serum albumin (BSA), 33,  
   35–41, 109  
 BSA. *See* Bovine serum albumin  
   (BSA)
- C**  
 Calcium phosphate, 48, 50, 58,  
   114–117  
 Calf serum, 25, 29, 183–185, 188  
 Ca, Mg-phosphate, 111, 114, 115  
 Cancerous tumor, 87  
*Candida albicans*, 193, 194, 196  
 Cantilever, 127–133, 135–144,  
   147–154, 156–163, 165, 166  
 Carbonates, 109, 111–112, 114  
 Carboxy methyl cellulose (CMC), 173  
 Cast alloys, 4, 8  
 Catheters, 89, 151, 173–174, 178,  
   198–201  
 Cell-adherent layers, 105, 112  
 Cell-adhesion, 117, 119–121, 134  
 Cell-cultures, 46–51, 111, 112, 115,  
   117  
 Clinical settings, 178, 181, 198  
 CMC. *See* Carboxy methyl cellulose  
   (CMC)  
 Co(OH)<sub>2</sub>, 9, 11–14, 17, 50  
 Coating, 74, 75, 77, 80, 88–89, 91, 94,  
   106, 112–116, 118–122, 129,  
   139, 175, 180–182, 188, 192,  
   194–195, 198, 200  
 Cobalt–chromium (CoCr) implants,  
   46, 50  
 Cobalt–chromium–molybdenum  
   (CoCrMo) alloy, 1–67  
   developments, 3–4  
   in orthopedics, 1, 4–5  
   properties, 3–5  
 Cobalt oxide, 13, 24, 51  
 Colloidal silver, 176  
 Commercial anodization, 117  
 Commercial Mg alloys, 107, 112  
 Complexing agents, 2, 30–32, 42,  
   76, 80  
 Compressive stress, 129, 131,  
   144–147, 165  
 Conducting polymers, 150–156  
 Conformational changes, 38, 41, 134,  
   151, 152, 156, 157  
 Conversion layers, 111  
 CoO, 9, 12, 13, 21, 51  
 Copper films, 79–80  
 Corrosion  
   current, 29, 36, 47–48  
   mechanism, 29, 34  
   process *in vivo*, 2, 60–66  
   product layers, 109, 111  
   resistance, 2–5, 28, 46, 47, 61  
 CoS<sub>2</sub>, 56  
 Crevice corrosion, 6–8, 60–62, 66

$\text{Cr}_2\text{O}_3$ , 15–18, 20, 25, 27, 30, 50, 51, 56  
 $\text{CrPO}_4$ , 27, 50  
Current hysteresis, 8, 13, 15  
CVs. *See* Cyclic voltammograms (CVs)  
Cyclic voltammograms (CVs), 9, 10, 14, 15, 17, 18, 27, 154, 161, 188, 189  
Cytotoxicity, 81, 112–113

**D**

Decorative films, 75  
Deflection, 23, 127–133, 135–136, 138, 146, 147, 152, 153, 155–157, 159–162, 165, 166  
Degradation process, 111  
Delamination, 113  
Delivery applications, 82  
Deoxyribonucleic acid (DNA)  
  analysis, 74  
  hybridization, 134  
Detection, 25, 86–87, 104, 127, 129–131, 135, 144–146, 148–150, 163, 165, 166  
Dielectric breakdown, 116–117  
Disease screening, 74  
DNA. *See* Deoxyribonucleic acid (DNA)

**E**

EDTA. *See* Ethylenediaminetetraacetic acid (EDTA)  
Effect of protein, 2, 32–42, 109  
Eggshell membrane, 76  
Electroactuation, 145, 146, 156, 157, 160–162  
Electrochemical  
  anodization, 116–118, 121  
  cantilever, 135–136, 166  
  etching, 139–140  
  methods, 74, 144  
  oxidation, 17–18, 25, 153, 158, 163, 178, 182, 188, 191, 192  
  patterning, 139

Electrochemically functionalized, 162–163  
Electrochemically oxidized silver, 189–192  
Electrochemical studies  
  on chromium, 15–17  
  on cobalt, 9–14  
  on molybdenum, 14–15  
Electroconductive textiles, 88  
Electrodeposition, 74, 75, 115–116, 142–145, 153, 162–163, 182, 187  
Electroless  
  copper, 90–91  
  deposition, 73–80, 86, 87, 89, 91, 95, 178, 182, 200  
  gold, 81–88  
  nickel, 75, 90–91  
  silver, 88–90  
  synthesis, 73–96  
Electropolymerization, 152, 154  
Endothermic process, 38  
Enzyme immobilization, 87  
*Escherichia coli*, 90, 118, 177, 179  
Etching, 63, 80, 136, 139–140  
Ethylenediaminetetraacetic acid (EDTA), 30, 31, 42

**F**

Failures, 5–8, 63, 104, 113  
Ferrocenylalkylthiol, 160, 161  
Flavoenzyme, 94  
Fluoride containing, 78, 79  
Formaldehyde, 89, 91  
Fretting corrosion, 6–7, 44, 51, 60–66  
Friction, 5, 51, 56, 57

**G**

Galling, 62  
Galvanic corrosion, 7, 8, 60–66, 103–104  
Galvanic displacement, 74, 75, 77–80, 92–95, 181  
Germanium (Ge), 78, 80  
Germicidal, 174

Gold colloids, 81  
 Gold nanoparticles, 81, 85, 86, 88  
 Growth mechanism, 80

## H

HDPE. *See* High-density polyethylene (HDPE)  
 Hierarchical organizations, 76  
 High-density polyethylene (HDPE), 179, 186, 192–198  
 Highfield model, 15, 116  
 Homeostatic mechanism, 102  
 Hormones, 46  
 Human serum, 27, 33, 45, 46, 50  
 Hydrazine, 89  
 Hydrogen evolution volume, 107  
 Hydrophobic, 38, 40, 120, 181  
 Hydrolysis, 87  
 Hydrophilic, 38, 41, 180, 181  
 Hydrophobic surface, 38, 120  
 Hydroxide layer, 11–13, 15, 41, 50  
 Hydroxyapatite, 114–116, 121  
 Hyperthermia treatment, 19, 87  
 Hypotonicity, 177

## I

Immersion, 15, 17, 25, 29, 38–41, 43, 45, 48, 73, 75, 80, 94, 110, 111, 115, 119, 136, 139, 180–181, 183, 185, 188, 195  
     gold, 94  
     plating, 73, 75, 80  
 Immunoassays, 87, 91  
 Implant, 1, 5–8, 42–46, 50, 51, 60, 61, 64–66, 101, 102, 105, 108, 113–115, 117, 119, 121, 198–201  
 Implantable devices, 174  
 Impurity content, 106–107  
 Initiation of corrosion of implants, 66, 113  
 Insuline, 46  
 Internal application, 199–201  
 Intramuscular site, 44

## L

Lactic acid, 91, 175  
 LAE 442, 109–110, 119  
 Lattice mismatch, 144  
 Lethal effects, 175  
 Light scattering, 83  
 Linear molecule adsorption, 159  
 Low corrosion resistant, 101  
 Lubrication, 51, 57

## M

Magnesium (Mg)  
     alloy corrosion, 102, 106–112, 121  
     alloys, 101–122  
     cations, 109, 111  
     corrosion, 102–106, 110, 118  
     corrosion rate, 104–109, 111, 114, 119  
     dissolution rate, 103, 106, 108, 110, 119  
     ions, 102  
     matrix, 103, 104, 106, 107  
     toxicity, 102  
 Magnesium fluoride (MgF<sub>2</sub>) conversion coating, 118, 119  
 Magnetic filtration, 87  
 Magnetic nanoparticles (MPs), 87, 88  
 Magnetic resonance imaging (MRI), 87, 91  
 Matrix loading, 180  
 Medical devices, 23, 60, 89, 131, 157, 173, 179–182, 192, 198–201  
 Metal degradation, 45, 104  
 Metallic powders, 189  
 Metallic silver/oxidized silver, 88, 174–177, 182–200  
 Mg–Ca, 108, 110, 111  
 Mg–Ca–Zn, 108  
 Micro-arc oxidation, 117, 118  
 Microcantilever, 127–166  
 Microchip, 86, 136, 140  
 Microfluidic, 127, 131, 136, 138–142  
 Microfluidic device, 86, 142, 150  
 Microorganisms, 174, 175, 177, 179, 186, 187, 194, 196  
 Microsensors activity, 94  
 Microspotter, 143

Microvalves, 140  
Minituarization, 76, 127, 130  
Modified cantilever, 135, 136, 154,  
157, 159, 161, 162, 165  
Molecular functionalization, 120  
Molybdenum disulfide (MoS<sub>2</sub>), 56  
Molybdenum oxide, 14, 24, 48  
Monomolecular, 161  
Multifunctional nanostructures, 87, 95  
Multiphase alloys, 108

## N

Nanoarrays, 76, 87, 93  
Nanocrystalline, 57, 58, 178, 201  
Nanometer level, 73, 75  
Nanoscale actuators, 150  
Nanostructured materials, 76  
Nanostructures, 73–96, 121, 149, 150  
Nanotube membrane, 86  
Nanotubular TiO<sub>2</sub> layers, 121  
Nanowire network, 90  
Nanowires, 76, 87, 91, 149, 150  
Nernst potential, 143  
NO<sub>2</sub> detection, 148–150  
Nucleation, 59, 80, 81, 115

## O

OCP. *See* Open circuit potential (OCP)  
Oligodynamic effect, 175  
Open circuit potential (OCP),  
28–29, 34, 46–47,  
183–185, 188, 192  
Optical detection, 135  
Organic coatings, 120  
Organometallic compounds,  
2, 41–46  
Orthophosphate, 27, 64  
Osteoinduction, 114  
Oxide film, 9, 12–14, 16–18,  
21, 22, 26, 28, 62, 63,  
116, 118, 199  
Oxidized silver species, 182–200  
Oxidizing agent, 179, 191, 192

## P

Passive layer, 13, 15, 16, 19, 21–23,  
25, 30, 31, 50, 54, 60  
Passive region, 8–13, 15–17, 25, 28,  
29, 47–48, 54  
Passivity, 2, 6, 9, 11, 12, 14, 16, 17,  
22, 56, 60  
Patterning, 139, 142–143  
PBS. *See* Phosphate buffer solution  
(PBS)  
PEG. *See* Poly(ethylene glycol) (PEG)  
Permanent metallic implants, 101–102  
Phase diagram, 30, 32  
Phosphate buffer solution (PBS),  
9–17, 21, 23, 26–29, 33–35,  
38, 40, 51, 52, 54, 57, 109,  
141, 142  
Phosphate ions effect, 2, 26–29, 35  
Phosphorus, 36, 58, 64  
Photomask, 139  
Photoresist, 139  
pH shift, 105, 112, 121  
Physiological solutions, 2, 7, 9–20,  
24, 26, 31–51, 183  
Pitting, 6–8, 13, 16, 42, 48,  
61, 62  
Platinum group metals, 75, 78, 80  
Polarization curve, 7, 8, 18–20, 22, 23,  
33, 35, 57, 110  
Polarization resistance, 20, 46  
Polishing, 48, 51, 56  
Poly(ethylene glycol) (PEG), 81–82  
Polymer adsorption, 82  
Polymer brushes, 156–157,  
165–166  
Polymeric foams, 173  
Porous oxide layers, 117, 118  
Potentiometric measurements,  
148–150  
Pourbaix diagram, 103, 105  
Prosthesis, 1, 5, 60, 63, 65, 67  
Prosthetic grafted polymers, 151  
Protein adsorption, 38, 45, 56,  
110, 120  
Protein binding affinity, 43

*Pseudomonas aeruginosa*, 177–179,  
186–187, 189–191, 193, 194,  
196, 198, 200

## R

Radioisotopes, 81  
Raman scattering, 79  
Red cells, 44  
Reduction of hydrogen, 104, 105  
Release of chromium (Cr), 43, 46  
Repassivation, 6, 8, 51, 54, 62–63  
RES. *See* Reticuloendothelial system  
(RES)  
Reticuloendothelial system (RES), 82  
Rheumatoid arthritis, 81

## S

SAMs. *See* Self-assembled  
monolayers (SAMs)  
Schottky-type, 80  
Scratches, 6, 23, 54, 62, 80  
Selectivity, 79, 130, 145–146, 160, 165  
Self-assembled monolayers (SAMs),  
81, 119–120, 159–162, 166  
Self assembled performance, 120  
Sensing, 82, 86–87, 92–94, 130, 135,  
140, 144, 145, 148–150, 156,  
160, 166  
Sensing technology, 131  
Sensitivity, 64, 94, 127–129, 131, 146,  
149, 150, 160  
Sensor, 74, 84, 86, 92–95, 127–166  
Serum protein, 30, 33, 35, 43, 45–47,  
111, 188  
Silicon, 56, 77–80, 94, 127, 129, 133,  
136, 138, 142, 143, 149, 153,  
183, 184  
Silks, 76  
Silver, 11, 14, 21, 22, 35, 36, 54, 55,  
79, 88–90, 92, 93, 144, 152,  
154, 155, 159, 176, 178, 179,  
181, 190–192, 197–201  
Silver carbonate ( $\text{Ag}_2\text{CO}_3$ ), 178, 182,  
194, 197, 198, 201  
Silver nitrate ( $\text{AgNO}_3$ ), 79, 89, 90,  
174, 175, 177, 179, 181,  
192–194

Silver oxysalts ( $\text{Ag}_7\text{O}_8\text{NO}_3$ ), 179, 182,  
192–194, 197, 198, 201  
Silver sulfate ( $\text{Ag}_2\text{SO}_4$ ), 182, 192, 194,  
196–198, 201  
Silver tartrate ( $\text{Ag}_2\text{C}_4\text{H}_4\text{O}_6$ ), 175, 182,  
194, 197, 198  
Simulated body fluid solution, 52,  
105, 109–112  
Sliding conditions, 56  
Sonochemical reaction, 87  
Sputtered silver films, 186  
Stabilizers, 76, 82  
Stainless steel, 1, 4–8, 16, 30, 37, 42,  
60, 61, 89, 101, 200  
*Staphylococcus aureus* (*S. aureus*), 90,  
118, 179, 193, 194, 196, 197  
Stripping analysis, 145, 146  
Submicron-sized, 87  
Surface  
  fatigue, 58  
  modification, 62, 82, 101–122,  
  179–182  
  oxidized silver, 176  
  roughness, 95  
  stress, 127–129, 131  
  treatments, 112, 113, 173–201  
Surgery, 61, 102  
Surgical masks, 172  
Susceptibility, 7, 8, 42, 48, 56, 63, 135

## T

Temporary implants, 101, 121  
Tetrasilver tetroxide ( $\text{Ag}_4\text{O}_4$ ), 179  
Textile materials, 173, 180, 192  
Thick films, 56, 76, 78, 80, 135,  
152, 154  
Thiolate, 81–83, 159, 160, 162  
Ti, 7, 37, 42, 45, 46, 48, 60, 61,  
64–66, 116, 117, 121  
Ti-based alloys, 4, 6, 8, 45, 46, 61, 63,  
65, 66, 101  
Tissue, 6, 7, 27, 44, 58, 59, 61,  
64, 66, 84, 104, 105, 117,  
119, 179, 180  
Titanium surface, 114, 121  
Tomography, 83  
Topical dressings, 173, 178, 201  
Transducer, 92, 127, 136, 154

- Transfer resistance, 28, 29  
Transpassive, 12, 14–18, 22, 23, 25, 27, 47  
Tribocorrosion, 2, 51–59  
Tribological, 51, 54, 57  
Trivalent Molybdenum Metaphosphate ( $\text{Mo}(\text{PO}_3)_3$ ), 27
- U**  
Ultra-high vacuum, 130
- V**  
Viral particles, 76
- W**  
Wear, 2, 4, 5, 50–58, 61–63, 75, 80, 102
- Wear-enhanced corrosion, 57, 58  
White cells, 44  
Wound healing, 173, 177, 178, 194, 201
- X**  
X-ray diffraction (XRD)  
  analysis, 185, 189, 191, 193  
  patterns, 191  
X-ray photoelectron spectroscopy (XPS) analysis, 17, 36, 41
- Y**  
Young's modulus, 128, 133
- Z**  
Zone of inhibition, 186, 187, 194, 197